SANDIA REPORT
SAND2011-6801
Unlimited Release
Printed September 2011

Ductile Failure X-Prize

Brad L. Boyce, Joseph E. Bishop, Arthur Brown, Theresa Cordova, James V. Cox, Thomas B. Crenshaw, Kristin Dion, John M. Emery, John T. Foster, James W. Foulk III, David J. Littlewood, Alejandro Mota, Jakob Ostien, Stewart Silling, Benjamin W. Spencer, Gerald W. Wellman

Prepared by
Sandia National Laboratories
Albuquerque, New Mexico 87185 and Livermore, California 94550

Sandia National Laboratories is a multi-program laboratory managed and operated by Sandia Corporation, a wholly owned subsidiary of Lockheed Martin Corporation, for the U.S. Department of Energy's National Nuclear Security Administration.

Issued by Sandia National Laboratories, operated for the United States Department of Energy by Sandia Corporation.

Available to DOE and DOE contractors from
U.S. Department of Energy
Office of Scientific and Technical Information
P.O. Box 62
Oak Ridge, TN 37831

Telephone: (865) 576-8401
Facsimile: (865) 576-5728
E-Mail: reports@adonis.osti.gov
Online ordering: http://www.osti.gov/bridge

Available to the public from
U.S. Department of Commerce
National Technical Information Service
5285 Port Royal Rd.
Springfield, VA 22161

Telephone: (800) 553-6847
Facsimile: (703) 605-6900
E-Mail: orders@ntis.fedworld.gov
Online order: http://www.ntis.gov/help/ordermethods.asp?loc=7-4-0#online

SAND2011-6801
Unlimited Release
Printed September 2011

Ductile Failure X-Prize

Brad L. Boyce, Joseph E. Bishop, Theresa Cordova, James V. Cox, Thomas B. Crenshaw, Kristin Dion, Kevin Dowding, John M. Emery, John T. Foster James W. Foulk III, David J. Littlewood, Alejandro Mota, Jakob Ostien, Joshua Robbins, Stewart Silling, Benjamin W. Spencer, Gerald W. Wellman

Sandia National Laboratories
P.O. Box 5800
Albuquerque, New Mexico 87185-MS0889

Abstract

Fracture or tearing of ductile metals is a pervasive engineering concern, yet accurate prediction of the critical conditions of fracture remains elusive. Sandia National Laboratories has been developing and implementing several new modeling methodologies to address problems in fracture, including both new physical models and new numerical schemes. The present study provides a double-blind quantitative assessment of several computational capabilities including tearing parameters embedded in a conventional finite element code, localization elements, extended finite elements (XFEM), and peridynamics. For this assessment, each of four teams reported blind predictions for three challenge problems spanning crack initiation and crack propagation. After predictions had been reported, the predictions were compared to experimentally observed behavior. The metal alloys for these three problems were aluminum alloy 2024-T3 and precipitation hardened stainless steel PH13-8Mo H950. The predictive accuracies of the various methods are demonstrated, and the potential sources of error are discussed.

ACKNOWLEDGMENTS

The authors would like to thank the following managers for providing support through this effort: Dr. Joel Lash, Dr. Mike Chiesa, Dr. Alan Roach, Dr. Eliot Fang, Dr. John Aidun, Dr. Justine Johannes, Dr. Peter Wilson, and Dr. John Pott. This program was supported by the Advanced Scientific Computing program. BLB would also like to thank Sandra O'Canna for assistance in referencing the figure captions.

CONTENTS

FIGURES

TABLES

1. EXECUTIVE SUMMARY

The X-Prize Foundation has sponsored a series of technological challenges including the first private sector manned space flight (Anasari X-Prize), production-ready 100 mpg vehicles (Progressive X-Prize), and private sector moon landing (Google Lunar X-Prize). The X-Prize Foundation has demonstrated that competition drives innovation. We have borrowed the spirit of the X-Prize competitions to promote our own internal competition on the topic area of simulating ductile fracture scenarios. The purpose of the Sandia X-Prize competition is to facilitate an honest assessment of current prediction capabilities in the area of ductile fracture, and to identify avenues for improvement.

Ductile tearing of metallic materials is relevant to many Sandia applications but difficult to predict. This assessment effort has evaluated four different modeling paradigms for use in ductile failure predictions, specifically (1) peridynamics, (2) localization elements, (3) tearing parameters, and (4) extended finite elements (XFEM). This assessment has posed a series of three 'challenge' scenarios where the four modeling teams are asked to predict key quantitative failure metrics, such as the peak force prior to fracture and the critical stretch to cause fracture. After blind predictions were reported, experiments were conducted to confirm repeatable validation results.

The first challenge focused on predicting crack initiation of an inclined blunt notch in a thin plate of precipitation hardened stainless steel. The second challenge sought to predict conditions for both initiation and crack propagation from the same inclined blunt notch, but this time in a common aluminum alloy 2024-T3. Finally, the third challenge examined predictions of crack propagation in a side-grooved, fatigue-precracked compact-tension geometry, again made from 2024-T3.

Each of these challenges was chosen to be geometrically simple but mechanically difficult to predict. All three challenges investigated specimen thicknesses that were too thin to meet plane strain fracture requirements. The first two challenges involved blunted notches that deviated from sharp crack geometries needed for linear elastic fracture mechanics. These two challenges also involved an inclined crack with significant shear stresses during crack nucleation and mode mixity during crack propagation. Otherwise, the challenges should have been readily accessible: the loading conditions were simple pin loading with quasi-static strain rates. The materials were reasonably common. And the geometries were nominally extruded 2-dimensional geometries, although non-plane-strain fracture is inherently 3-dimensional.

None of the four modeling paradigms were able to consistently predict the conditions for crack initiation and propagation within the desired error margin of ±10%. In fact, while each method showed the promise of predictivity in certain challenges, they each also 'missed the mark' by factors of 2 or more in other challenges. This effort has clearly shown that there is no 'silver bullet' in place to predict ductile failure scenarios – the problem of fracture is not trivial. Even within the narrow application space represented by the X-Prize challenges, it is clear that these modeling tools each possess strengths and weaknesses that render their predictivity application specific.

After each of the blind predictions was compared to experimental results, the modeling teams were given a several months to assess the source(s) of error in their predictions. These sources of error can be generally divided into five categories: (1) physical model, (2) numerical implementation, (3) boundary conditions, (4) material properties, and (5) operator error. This fifth category operator error represents inappropriate assumptions, misinterpretation of the question, or misreporting of the results. While each of the five sources of error played a role in the competitions, it was surprising to see that the operator error category was often the overwhelming source of error.

IMPACT:

Sandia Failure Workshop
In 2008 Sandia held the first internal workshop on fracture, bringing together 30+ participants from several Sandia centers including 1400, 1500, 1800, and 8700. One of the key findings from this workshop was that Sandia lacked a strong strategic vision for its disparate fracture modeling efforts. As a result of this effort, the ASC Physics and Engineering Models campaign embarked on the ductile failure' X-Prize' internal competition. In 2010, the 2nd biennial Fracture Workshop was held in SNL/CA. The unifying nature of the X-Prize effort was evident: nearly all the talks in this 2-day workshop used the X-Prize challenges as illustrations of the strength and weaknesses of their methods. Clearly, the X-Prize effort has initiated a new era of communication, idea sharing, and honest evaluation on common ground to help move our fracture modeling capabilities forward.

Additional Internal Impact:
The X-Prize assessment activity has been highlighted in three internal reviews: the Fall Leadership Forum (2010), the Engineering Sciences External Review Panel (2010), and the Predictive Engineering Science Panel (2011). The X-Prize effort was selected as a Corporate Level 2 milestone for FY11, and this document provides evidence of fulfillment of that milestone. Futhermore, the X-Prize effort is being considered as a template from which to initiate a nation-wide ductile failure prediction assessment challenge.

DOE/NNSA/ASC Impact:
The X-Prize effort was highlighted at the 2010 ASC Predictive Science Academic Alliance Program (PSAAP) Workshop at the University of Texas, Austin. Also, the X-Prize effort was featured as the introductory presentation at a Tri-lab Damage Workshop. As a result of that workshop, the DOE is considering a Tri-lab validation exercise which bears similarity to the X-Prize effort as well as a similar JOWOG 42 effort. The first ASC Tri-lab challenge may involve predicting the deformation, damage, fracture, petaling, spalling, and fragmentation of a steel target impacted by a gas gun projectile.

2. INTRODUCTION

Making predictions of when and how a component will fail is a very challenging engineering problem. To address problems of ductile fracture, Sandia has fostered several parallel computational efforts. The present study provides an honest, quantitative assessment of the predictive capability of these emerging computational methods. To this end, the present study has adopted a series of three 'toy problems': relatively simple problems that are still challenging to predict. These toy problems have several key features: (a) no intuitively-obvious or closed-form solution exists, (b) the solution is unambiguous, (c) the boundary conditions are well defined and simple, (d) the geometry of the test piece is easily manufactured, easily measured, and easily tested, (e) there are no stress gradients or unusual surface conditions such as EDM'd surfaces, (f) the geometry is simple and relatively easy to mesh, and (g) the problem avoids buckling or other unwanted deformation modes.

For honest assessment, the X-Prize effort adopted a double-blind methodology. The simulation predictions were reported in the absence of any knowledge of the experimental outcome of the toy problem, or and knowledge of the predictions made by other teams. To facilitate this double-blind interaction, a moderator (Brad Boyce) employed a sharepoint website, which allowed permission-controlled access, as well as logging of submission date and submitter ID. The four modeling teams were given similar amounts of funding and similar time to complete the 'assignments'. All teams were given an opportunity to preview the assignments to verify that the problem did not possess intrinsic 'show-stoppers'. The teams were asked to not share their predictions or details of their methodology until all teams had submitted their predictions. An important exception was material property data, where the teams were asked to share all sources of material property data that they used to calibrate their models.

To facilitate an X-Prize style competition, it was necessary to identify several competing 'teams'. These teams were identified based on a key characteristic of the modeling paradigm that each team would employ: tearing parameters, localization elements, extended finite elements (XFEM), and peridynamics. Note that the 'tearing parameter' team name is associated with a specific physical model for crack initiation, whereas the other three team names were associated with various numerical implementation methods. These four teams were chosen to represent much of the breadth of modeling paradigms that are in use or under extensive development currently at Sandia. An overview of the modeling landscape applicable to solving ductile fracture problems is shown in Figure 1 and
Figure *2*. Other than the methodologies that the team titles imply, there was not other artificial stipulations placed on how each of the teams made their predictions. They were left to choose the modeling techniques that were most palatable. Moreover, each team was given the freedom to bound the uncertainty in their predictions with whatever bounding analysis they chose. In this way, the X-Prize was also an assessment on how well our analysts can bound the uncertainty in their predictions.

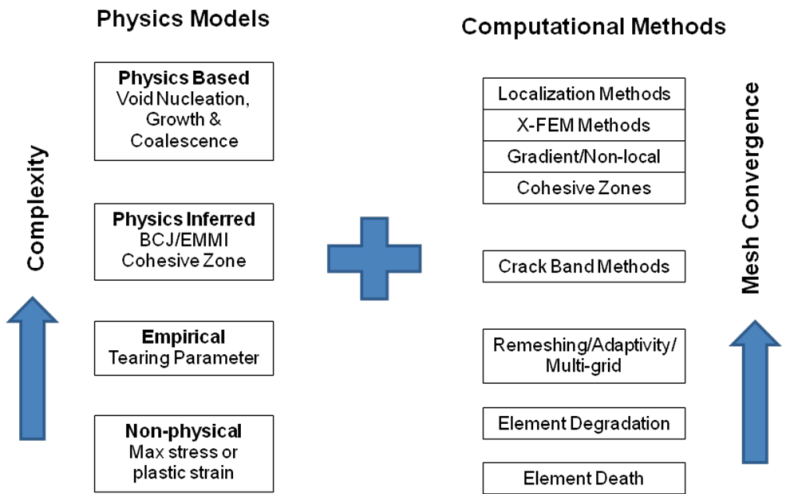

Figure 1. The 'landscape' of physical models that describe the conditions of crack nucleation and/or crack propagation, and computational methods for numerical implementation of the physical models.

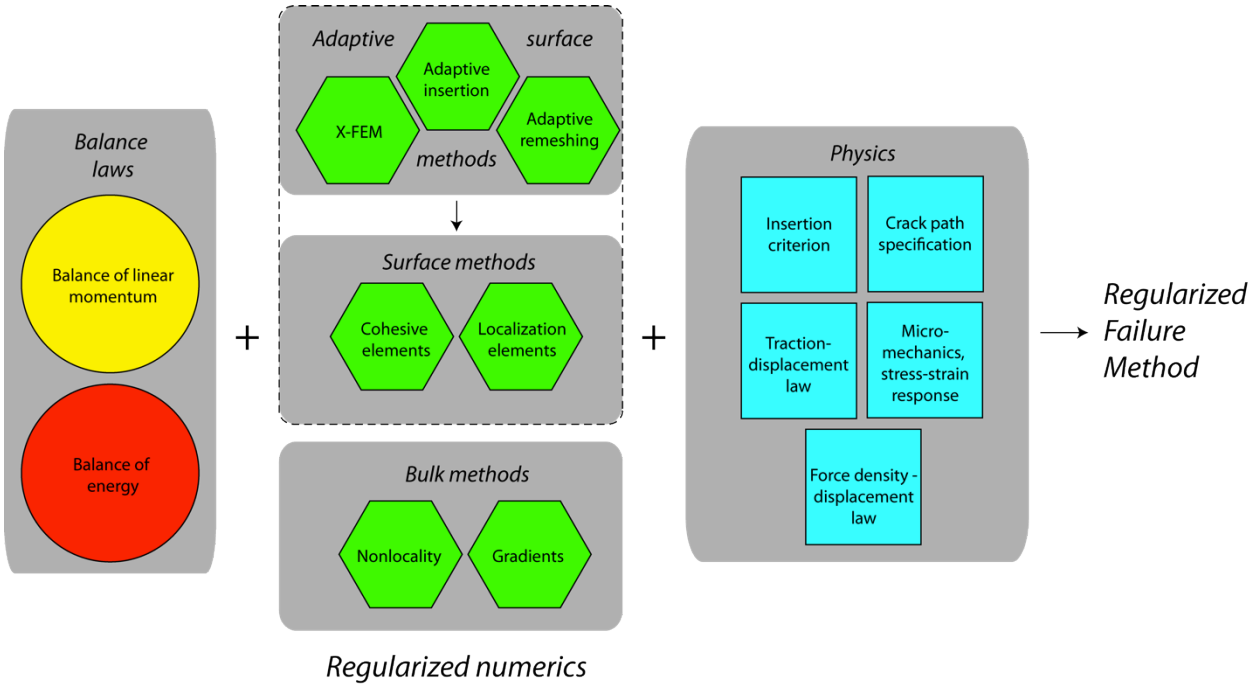

Figure 2. An alternative way to visualize the combinations of balance laws, numerical implementation, and physical models used to predict fracture scenarios.

The roadmap for this document is as follows: the three toy problems or challenge assignments are presented in Chapter 3, in much the same way as they were originally presented to each of the four prediction teams. Chapter 4 compares the blind predictions that were made to the experimental outcomes. The first four Appendices (A-D) describe in detail the modeling methodology, predictions, and error assessments for each of the four modeling paradigms. Finally, Appendix E provides additional quantitative details regarding the experimental outcomes of the three challenge problems.

3. CHALLENGE 'ASSIGNMENTS'

3.1 Challenge 1A: Crack Initiation from an Inclined Blunt Notch

Challenge 1A: *For a specimen as shown in Figure 3 (detailed drawings in Figure 4), with notch tip radius r = 0.0260", notch inclination length, L = 0.150", and inclination angle, α = 45°, what is the loadline displacement Δd, needed to induce crack initiation (in inches)? What is the peak force F applied to the sample prior to crack initiation (in pounds)?*

Some additional information was also provided:

- Material was precipitation hardened stainless steel alloy PH13-8Mo in the H950 heat treatment condition.
- Crack initiation was defined as the incurrence of a sharp flaw that was at least 100 μm in length.
- The sample was pin loaded in clevis grips, akin to a compact tension test described in ASTM E399.
- Load line displacement was measured via a knife-edge crack opening displacement gage.
- The test was conducted under displacement control, with a quasistatic displacement rate.

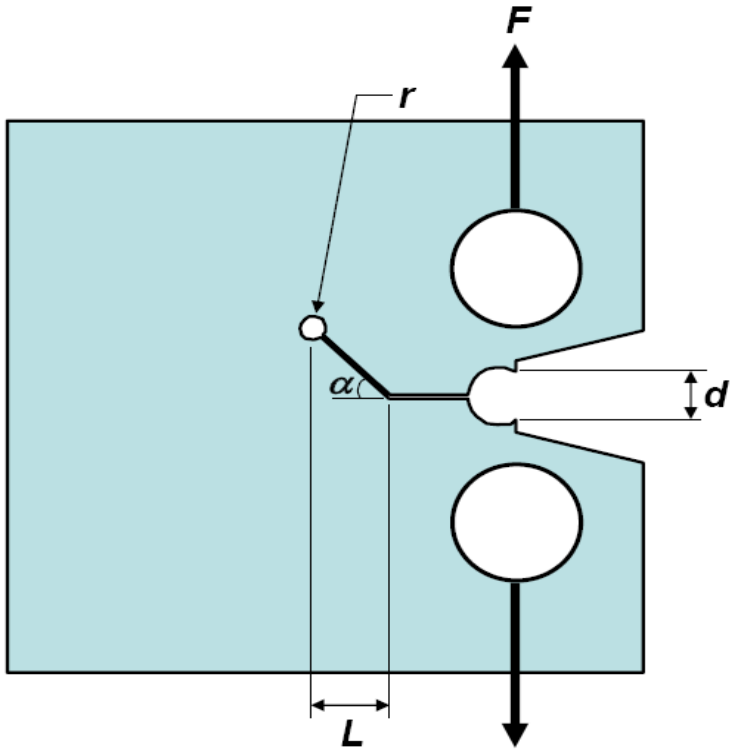

Figure 3. Schematic of the inclined blunt notch crack initiation problem for Challenge 1A. Detailed engineering drawings were also provided, as shown in Figure 4.

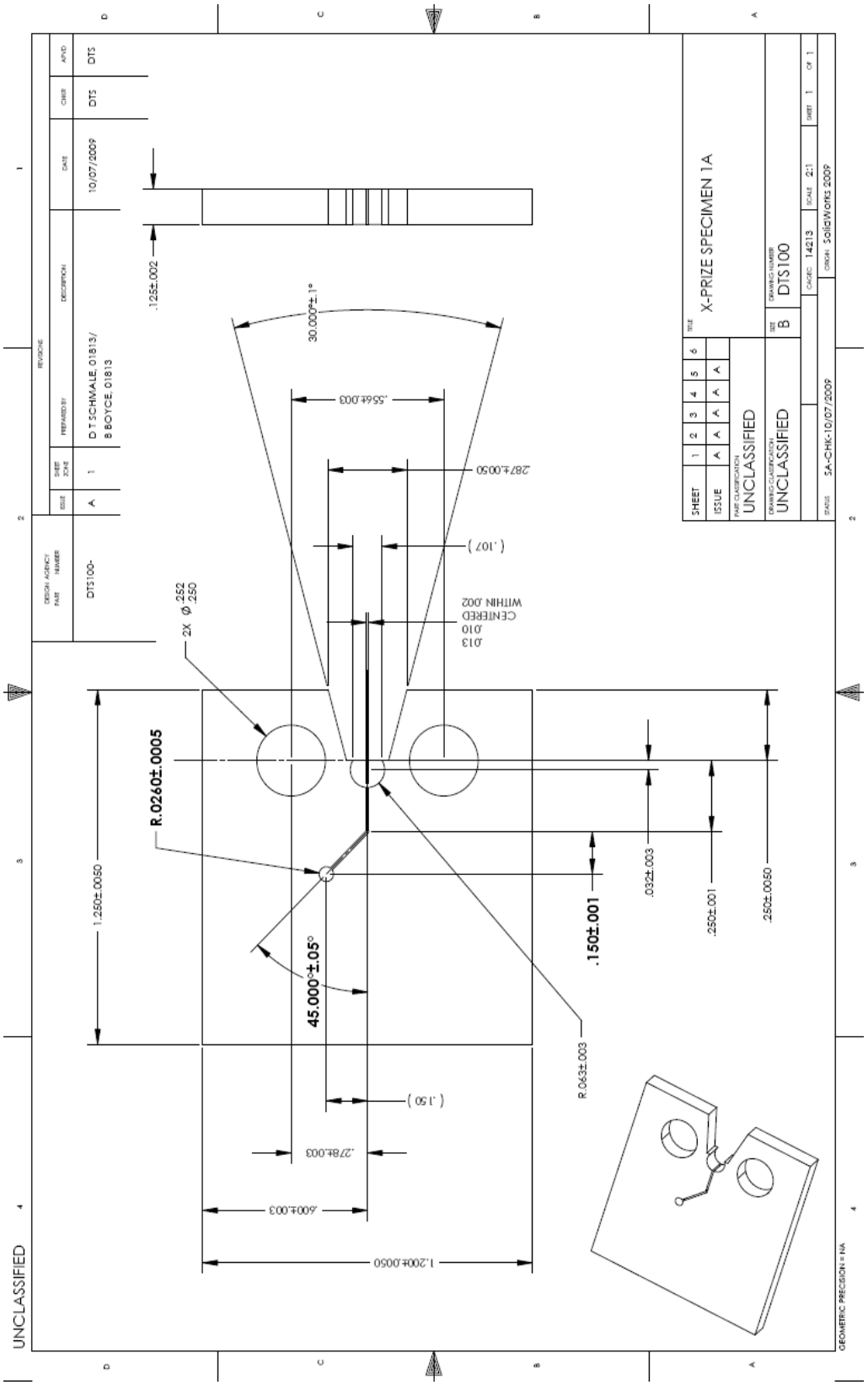

Figure 4. Detailed engineering drawings of the inclined blunt notch geometry. Dimensional tolerances represent the machining tolerances.

3.2 Challenge 1B: Propagation from an Inclined Blunt Notch

Challenge question 1B

1B.1 *For a specimen as shown in Figure 5, with geometry defined previously in Challenge 1A, what is the loadline displacement Δd needed to induce crack initiation (in inches) in aluminum alloy 2024-T3? What is the peak force prior to crack initiation?*

1B.2 *Six lines labeled A-G will be scribed prior to testing in the locations indicated. What is the order of crack propagation (e.g. A-B-D-C, etc.)?*

1B.3 *What is the force and displacement at which the crack reaches the 1st line?*

Please use the table below to report results. You can bound your answers if necessary.

Table 1. Format for prediction reporting for Challenge 1B.

		1B.1 Δd at crack initiation (mm)	1B.1 Peak force *prior* to crack initiation (kN)	1B.2 Crack path (e.g. D-E-F or D-A-E-B-F, etc.)	1B.3 Displacement Δd when crack reaches first line (mm)	1B.3 Force when crack reaches first line (kN)
2024-T3	Upper bound					
	BEST ESTIMATE					
	Lower bound					

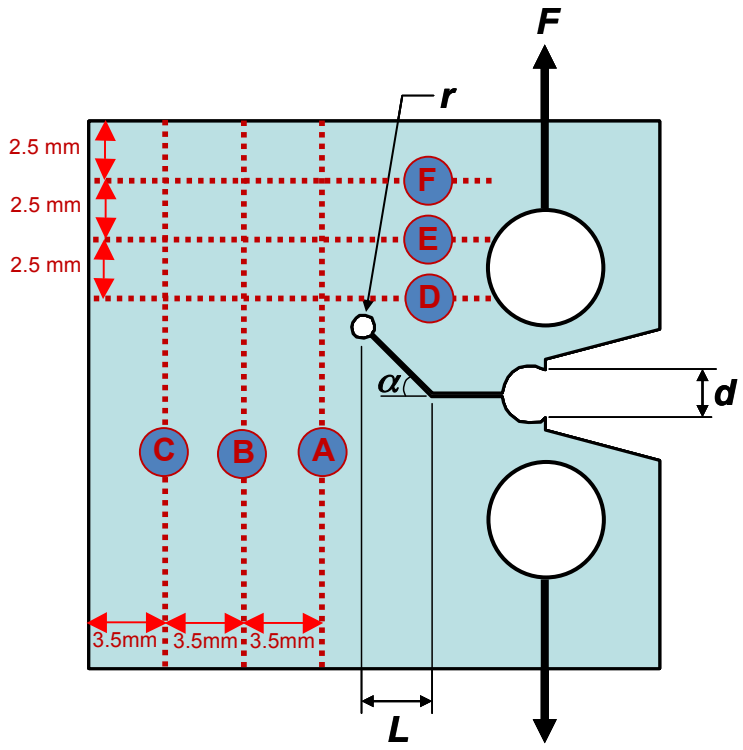

Figure 5. Schematic of the test geometry for Challenge 1B. Note that the geometry is identical to Challenge 1A. The only difference is the presence of fiduciary lines labeled A-F, with locations identified on this drawing.

3.3 Challenge 2A: Crack Propagation from a Sharp Mode-I Crack

The Challenge 2A geometry was manufactured from aluminum alloy 2024-T3. A detailed machining drawing is shown in Figure 6, including tolerances on all dimensions. It has the same outer dimensions as the previous X-Prize specimens (W=1.0”), but has a thickness of 0.25” (rather than the 0.125” thick specimens used in previous X-Prize studies). This specimen does not contain an inclined notch, but rather a straight pure mode-I notch to a length of a/W = 0.2, and a mode-I fatigue precrack has been grown to a/W = 0.3 per ASTM E399 standard load shedding techniques. To avoid shear lips on the surface of the specimen, 0.063” deep V-grooves have been machined into both sides along the Mode-I crack path.

For a displacement-controlled loading regimen, as shown in Figure 7 predict the unloading compliance (change of force over change in displacement), for unloads labeled A-D. What was the crack length at the peaks associated with A-D? Please report your compliance values in N/mm, and your crack length values in mm. You are welcome to bound your results as you see fit.

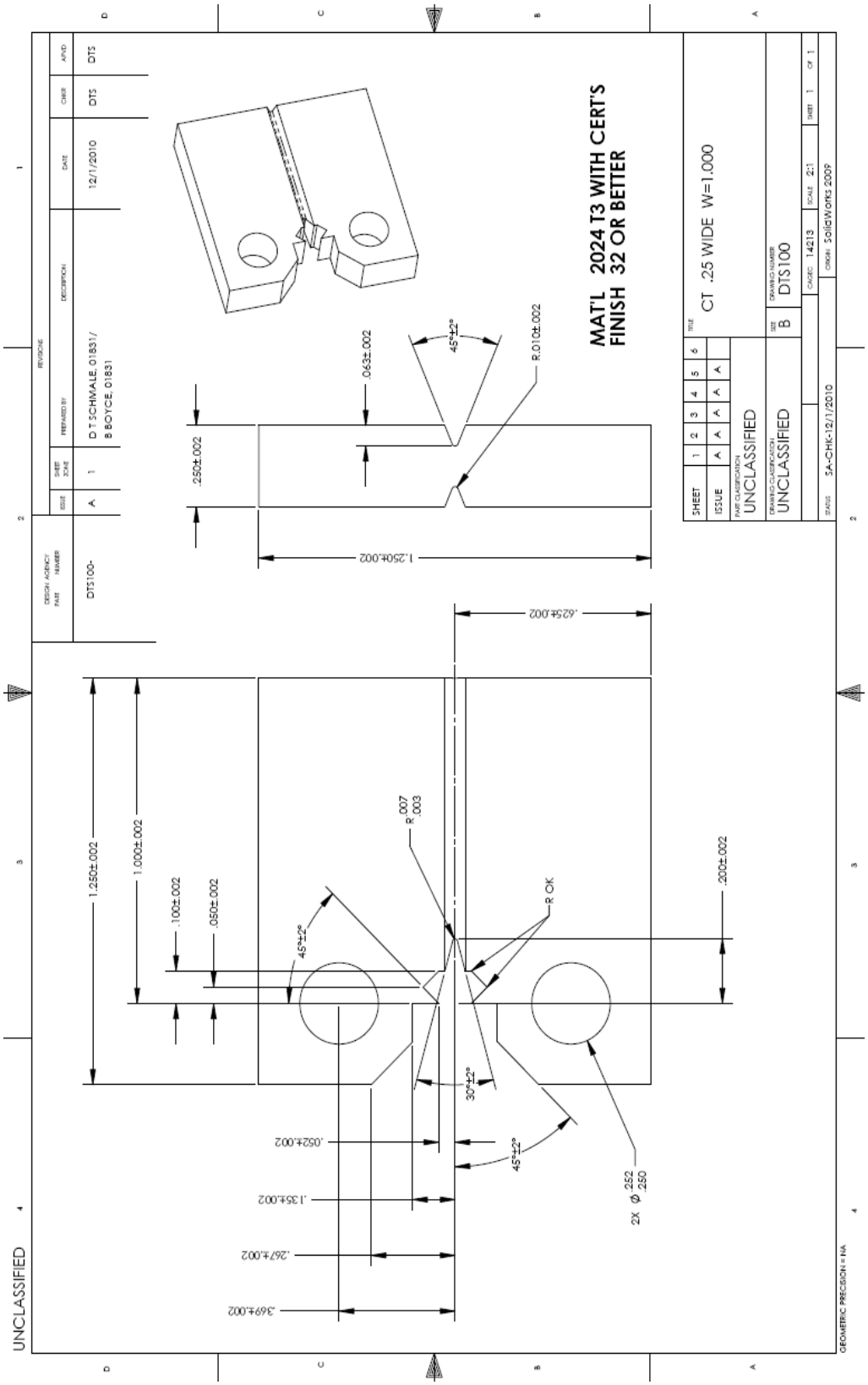

Figure 6. Engineering drawings for the Challenge 2A geometry

.

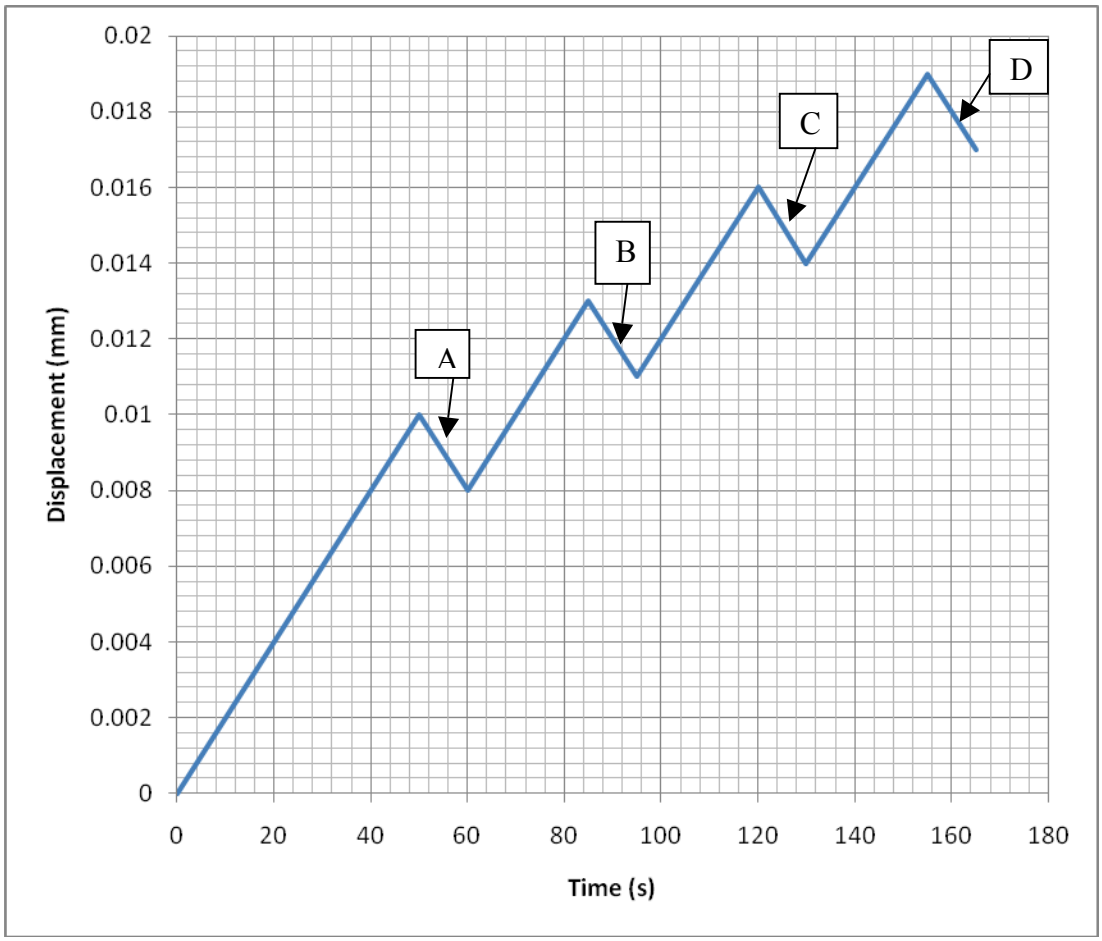

Figure 7. Loading profile for Challenge 2A

4. COMPARISON OF PREDICTIONS TO EXPERIMENTAL OBSERVATIONS

4.1 Challenge 1A: Crack Initiation from an Inclined Blunt Notch

In Challenge 1A, the modeling teams were asked to predict both the peak force prior to crack initiation and the loadline displacement at crack initiation. The details of how the predictions were made are described in Appendices A1, B1, C1, and D1. In addition, experiments were conducted to measure the actual forces and displacements, as described in Appendix E1. The resulting comparison between experimental results (red) and ***blind*** simulation predictions (black lines) is shown in Figure 8 and Figure 9. After this comparison had been made, each modeling team was given the opportunity to assess the sources of discrepancy if any. Those assessments can be found in Appendices A2, B2, C2, and D2.

It is worth noting that both the localization elements team and tearing parameter team had reported the force *at* crack initiation rather than the *peak force prior* to crack initiation. This can be viewed as misreporting of the results or misinterpretation of the question. Careful examination of their complete predictions revealed that the simulation itself had much more closely captured the experimental behavior than Figure 9 would imply. Nevertheless, this 'human' error is important to quantify, since it also can play a significant role in predictivity.

Once these 'human' reporting errors had been remedied, the resulting predictions compared much more favorably to the experimental outcome as shown in Figure 10. In fact, both the localization elements and tearing parameter teams appear to have produced results that coincide with the experimental outcome. However, these corrections were only made after the experimental results had been released, and in this way, they were no longer completely 'blind'. Both teams indicated that they had not made any adjustments to the code to report these new values, and indeed their blind force displacement curves were consistent with these reported values.

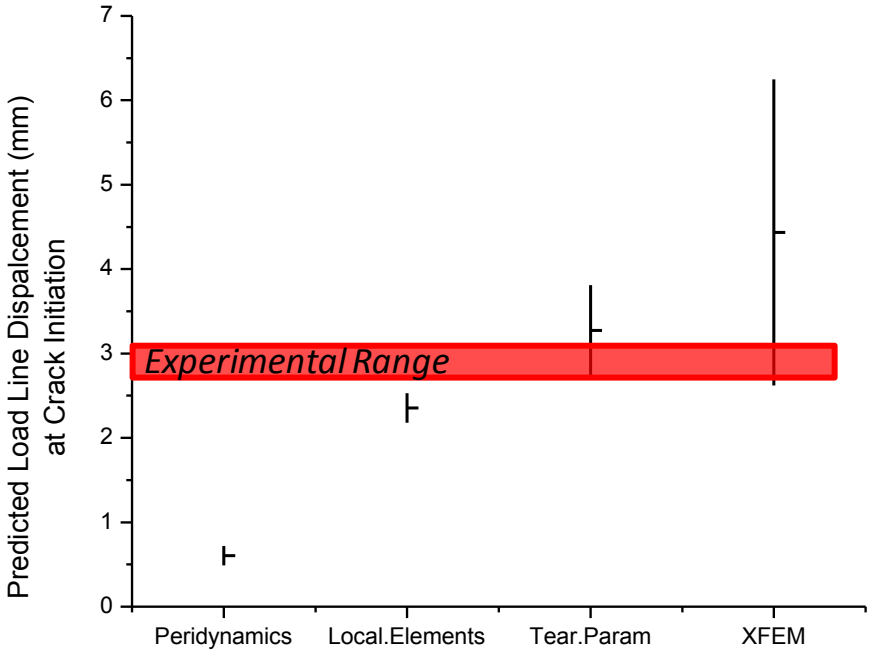

Figure 8. Comparison of blind predictions to experimental outcomes for Challenge 1A loadline displacement.

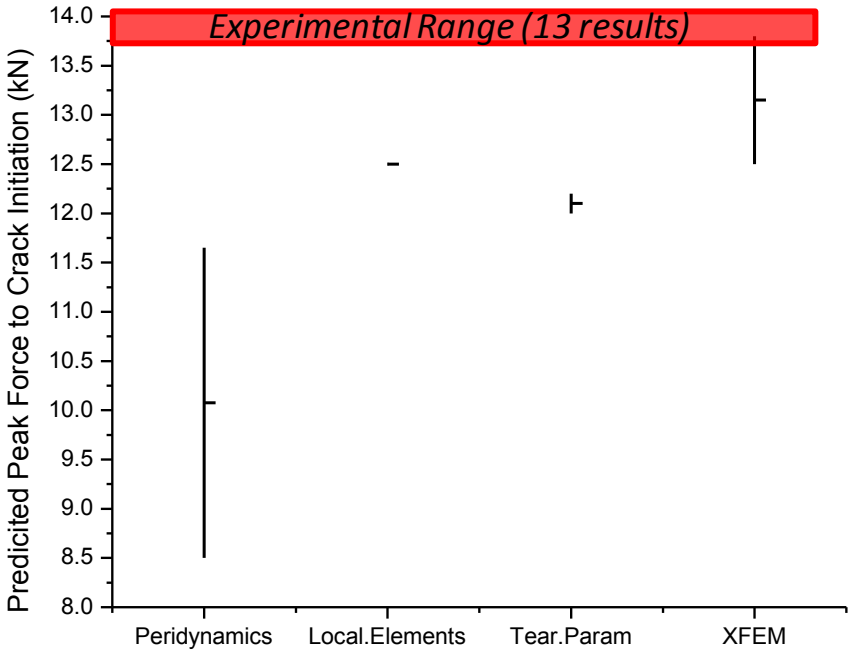

Figure 9. Comparison of blind predictions to experimental outcomes for Challenge 1A peak force prior to crack initiation.

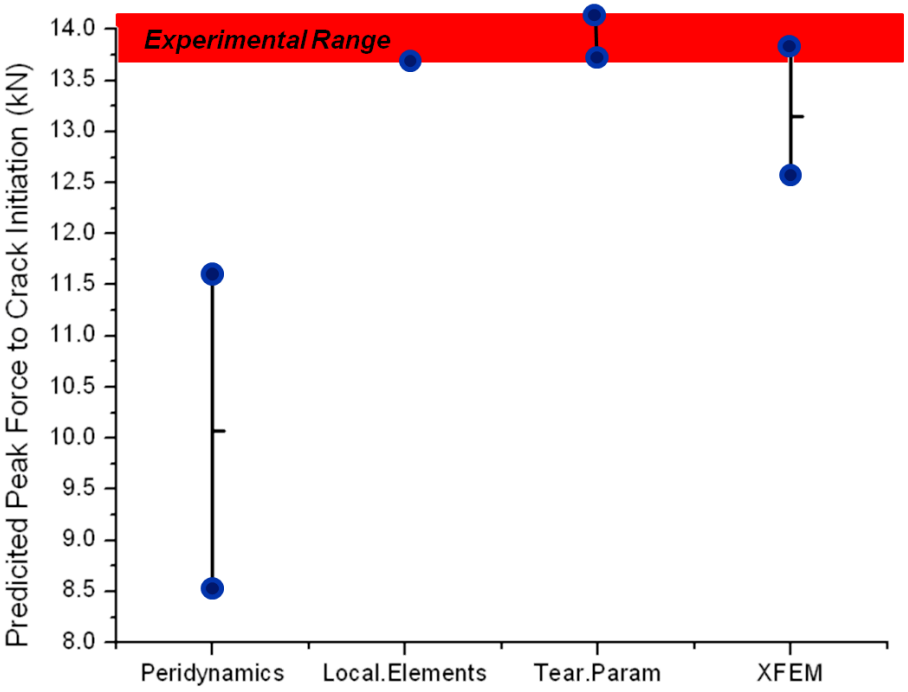

Figure 10. Comparison of predicted peak forces to experimental outcomes, after the localization elements and tearing parameter teams had remedied their reporting error. This graph better represents the predictivity of the codes than Figure 9.

4.2 Challenge 1B: Propagation from an Inclined Blunt Notch

In Challenge 1B, the teams were asked to predict a number of aspects of crack initiation and crack propagation. All teams (with the exception of an early implementation of XFEM in Sierra) were able to correctly predict the path of crack propagation within the fidelity demanded from the challenge. There was a more broad range of predictions regarding the point at which a propagating crack would reach line D, the first horizontal line, as shown in Figure 11. To examine the discrepancy between predictions and experimental results more closely, it is instructional to compare the complete load-displacement curves from predictions to experimental observations. This result is shown in Figure 12. It is clear from this figure that the Localization Elements and Tearing Parameter suffered the greatest errors due to poor prediction of the onset of cracking (initiation). On the other hand, both the XFEM and Peridynamics methods struggled to capture the softening behavior associated with crack propagation. Details of the experimental and computational methods as well as assessment of the sources of error are presented in the appendices.

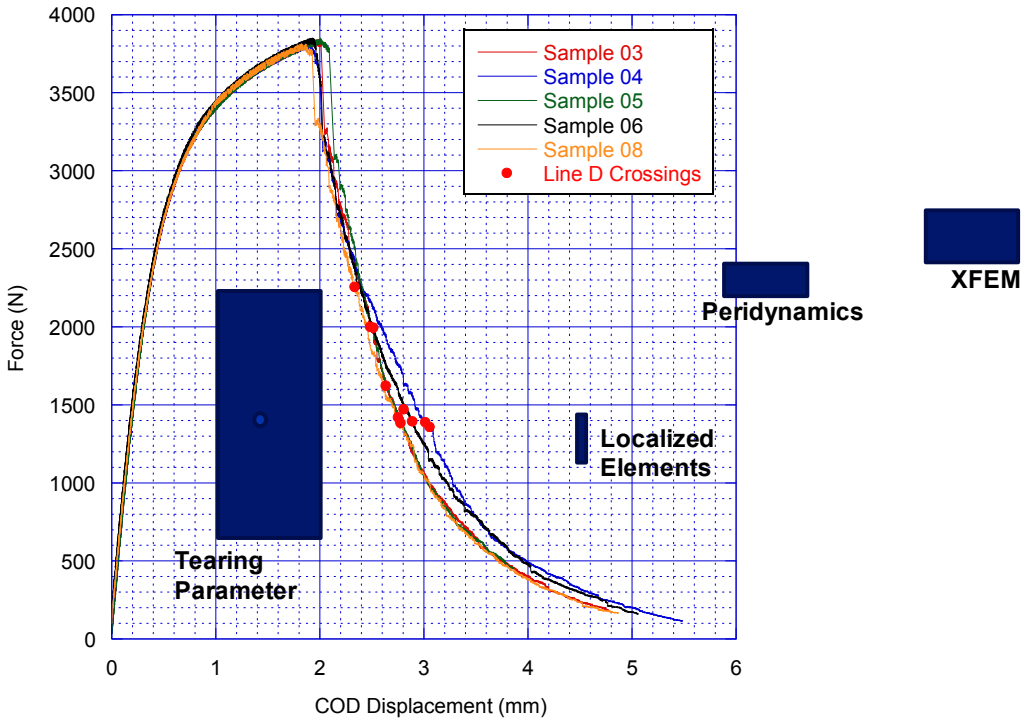

Figure 11. A comparison of the predicted ranges of Forces and Crack Opening Displacements (blue boxes) to the experimentally observed behavior (red dots) for the crack to reach the first horizontal line (line D). The five data curves represent the experimental force-displacement profile of five independent tests. Crack initiation occurred at the peak of this curve. The light blue dot in the tearing parameter box indicated the 'expected' mean behavior.

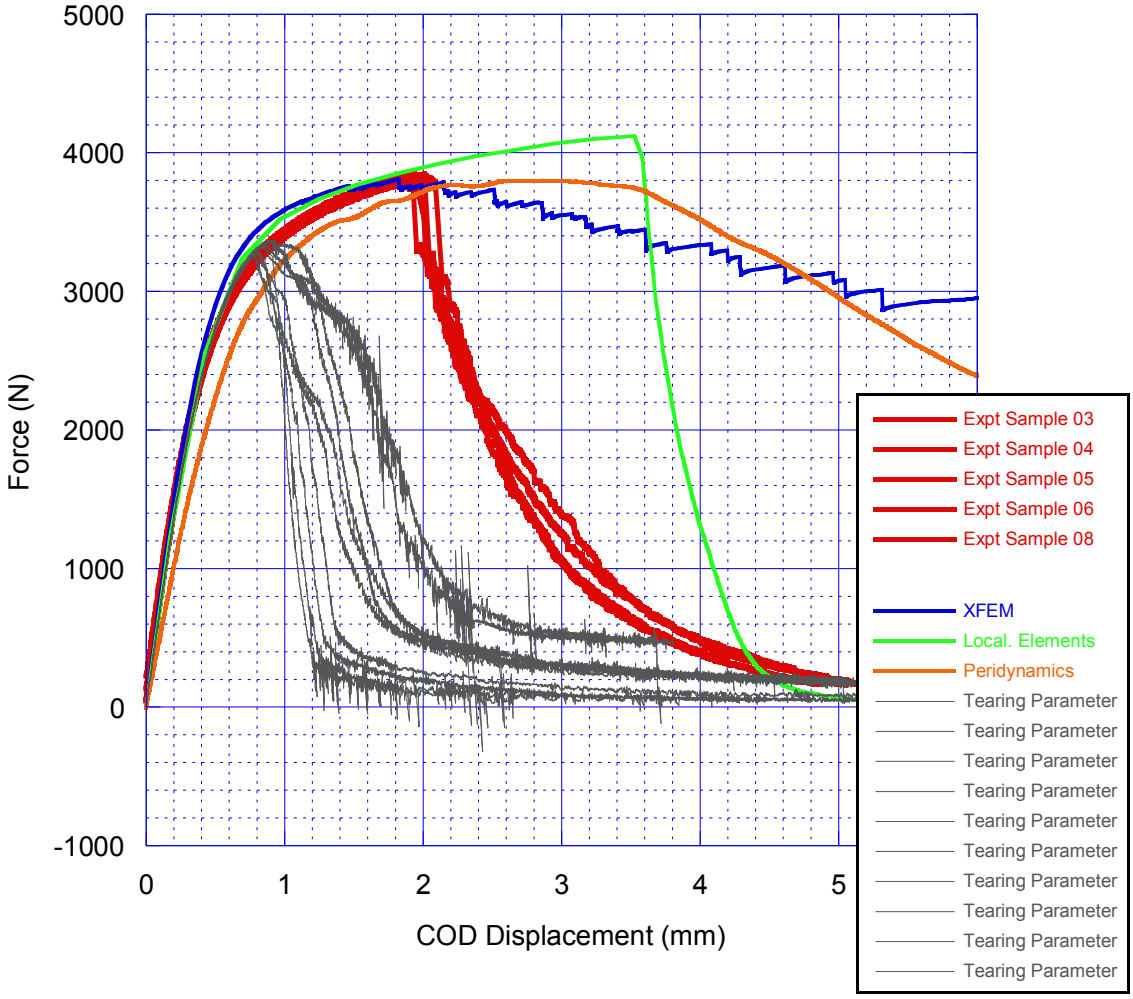

Figure 12. A comparison of the complete predicted load-displacement curves to experimental observation.

4.3 Challenge 2A: Crack Propagation from a Sharp Mode-I Crack

In Challenge 2A, the teams were asked to predict the normalized crack length (a/W) and remnant stiffness during crack propagation associated with a loading profile shown in Figure 7. The teams were asked to make such predictions at each of four unload peaks, labeled A-D in Figure 7. Two of those unload results are shown here in Figure 13 and Figure 14, respectively. In these figures, both the remnant stiffness and crack length are plotted for experiments (red dots) compared to the blind predictions (other data points). If one were to only compare predictions to experimental outcome in Figure 13 associated with Unload "A", one might come to the conclusion that the XFEM Abaqus method was the most predictive. However, Figure 14 associated with Unload "C" shows that the XFEM Abaqus method actually was underpredicting the degree of crack propagation and commensurate stiffness loss.

Another important 'human' error was present in these blind predictions. Here the tearing parameter group reported part of their results in units of total crack length (a/W), intermixed with results reported in relative crack length Δa/W. This intermixing without proper labeling led to the misinterpretation of the data, resulting in an offset of a/W of 0.3 on some of the data points. Note that 3 orange data points on Figure 13 and all 5 orange data points on Figure 14 should be shifted left 0.3 if the results had been properly reported. So, aside from this human error, the tearing parameter had much more realistic predictions, as can be seen in the corrected figures, Figure 14 and Figure 15.

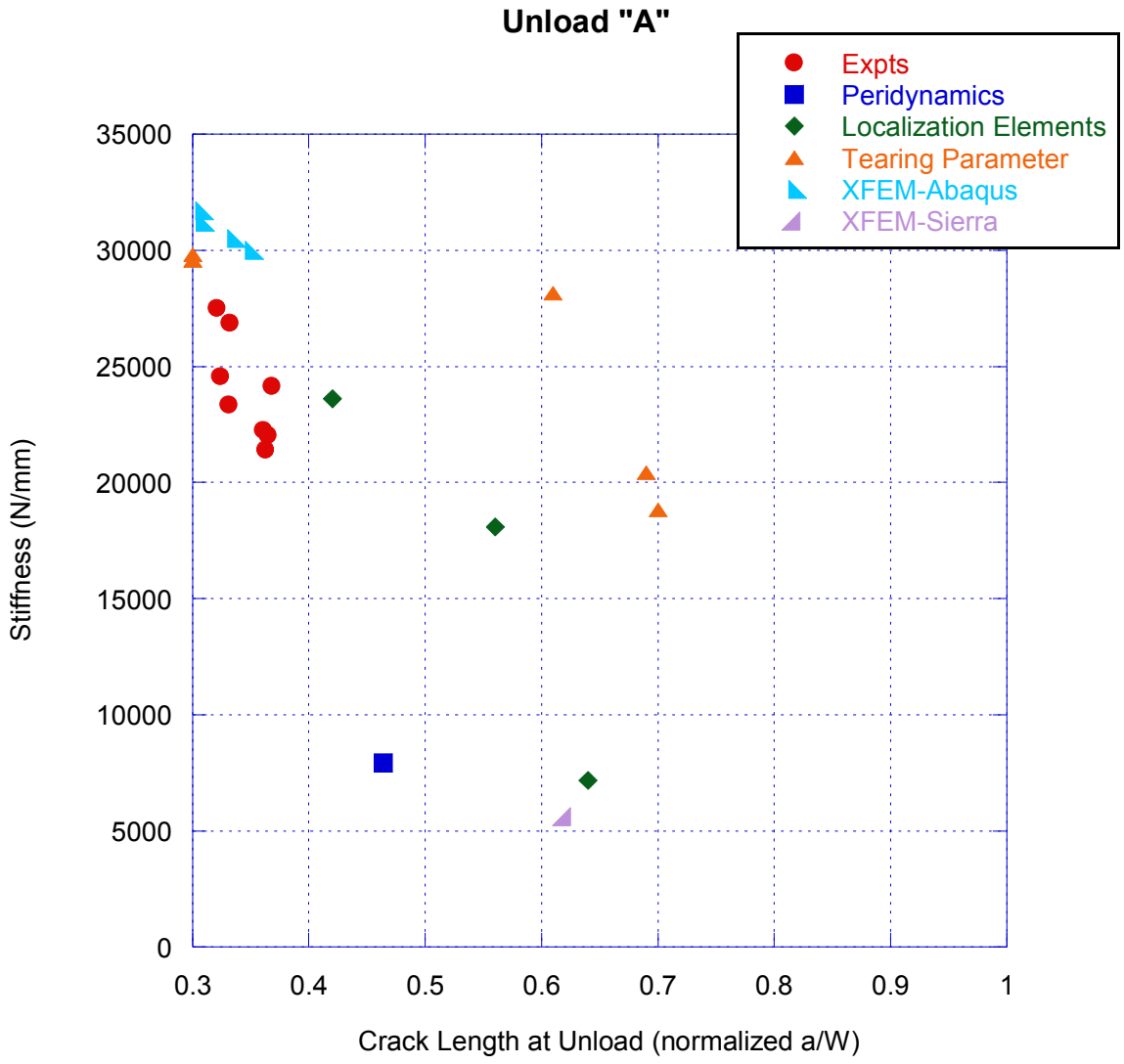

Figure 13. Comparison of experiments (red) to blind predictions for Unload A.

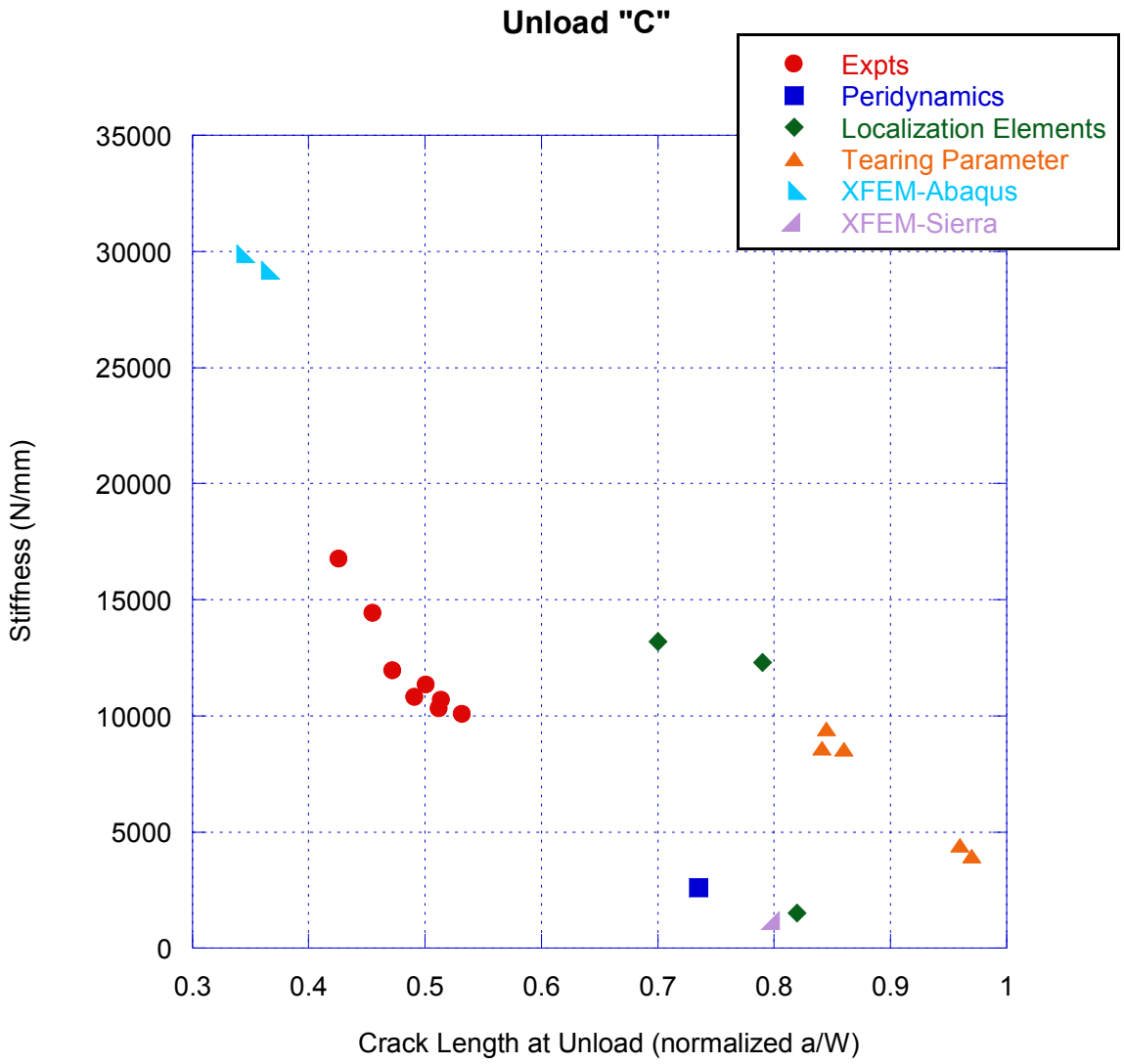

Figure 14. Comparison of experiments (red) to blind predictions for Unload C.

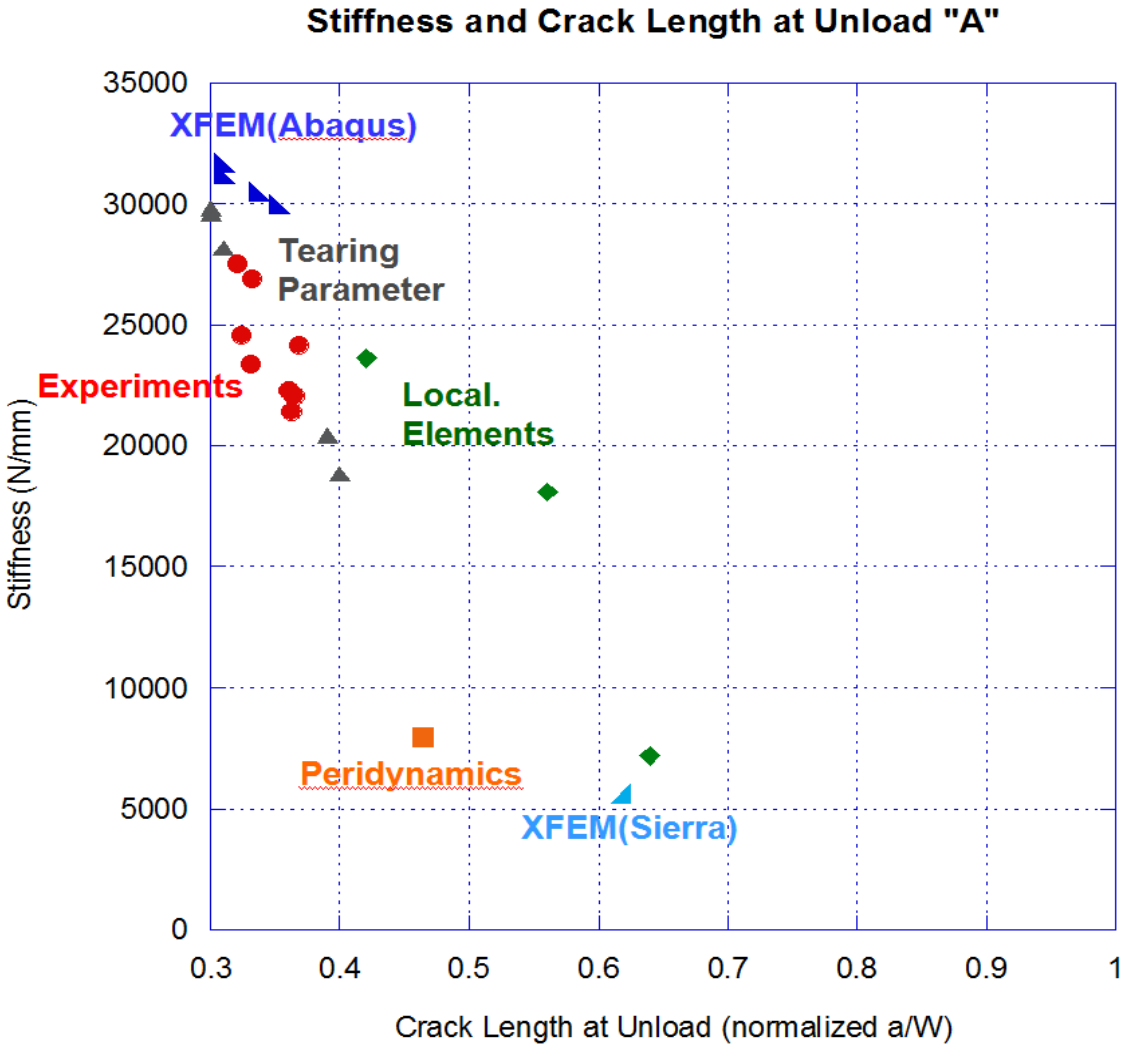

Figure 15. A comparison of the stiffness and crack length predictions to experimental values at unload "A" after the Tearing Parameter team had fixed the 0.3 a/W offset reporting error.

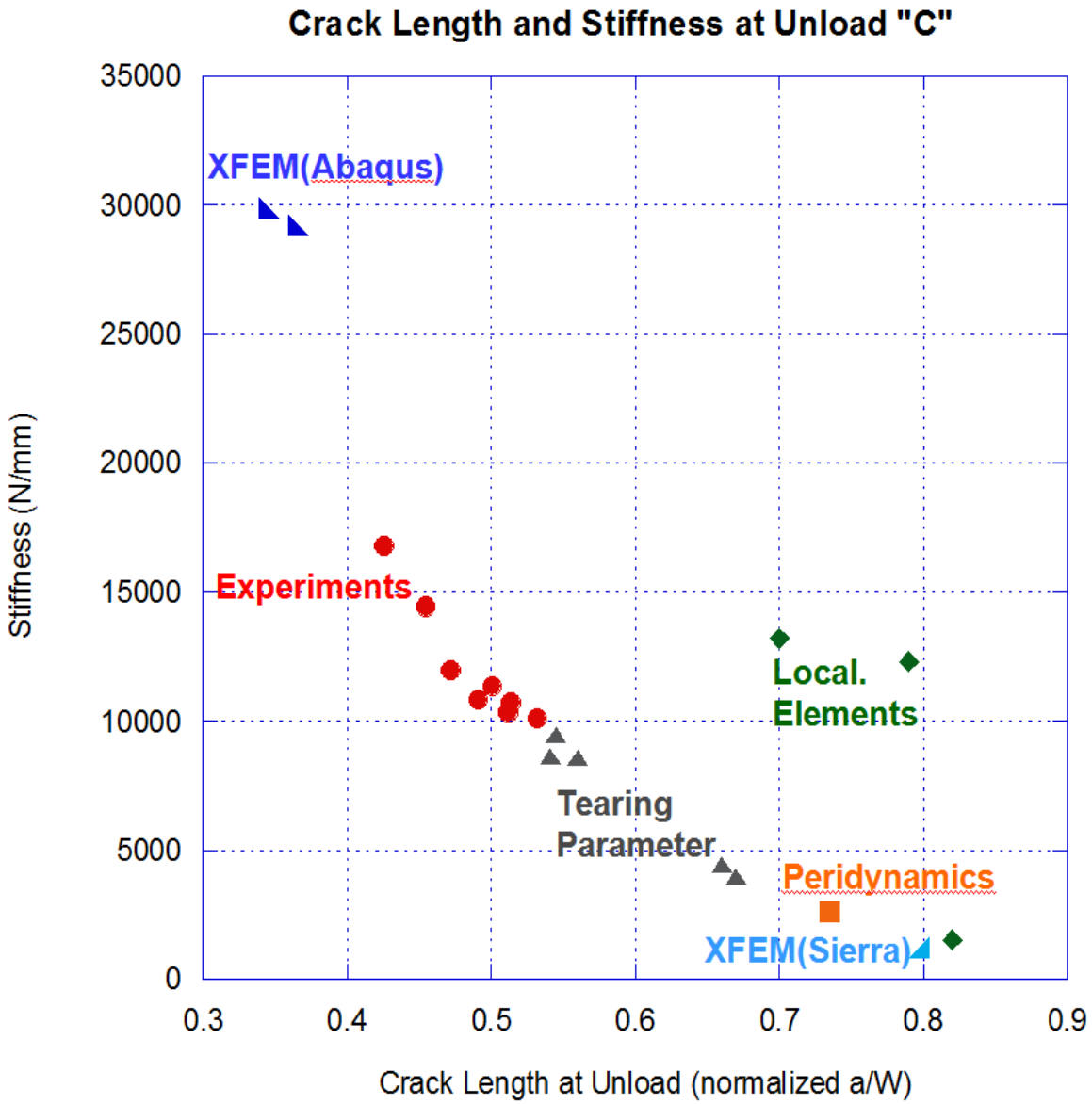

Figure 16. A comparison of the stiffness and crack length predictions to experimental values at unload "C" after the Tearing Parameter team had fixed the 0.3 a/W offset reporting error.

5. CONCLUSIONS AND SUMMARY

Each of the four modeling teams had substantial errors in their blind predictions. None of the teams were able to consistently predict quantitative force or displacement values to within the desired accuracy of ±10%, and in many instances the predictions were in error by a factor of 2X or more. The discussion of sources of error, included in the appendices, highlights the developmental nature of these methods.

The most mature technique was the tearing parameter technique, which has been in use at Sandia for over a decade. This technique has known shortcomings (mesh sensitivity issues, empirical form of the governing equation, etc.), but seemed to have the least dramatic errors in prediction, aside from cases of 'human' error. What is most troubling is that the tearing parameter severely underpredicted the onset of crack initiation in alloy 2024-T3, an error that was ascribed to the empirical exponent of 4 in the crack initiation constitutive equation. It was unclear from this study how the tearing parameter could be adjusted to be more robust against such an error, without extensive calibration data on the particular alloy of interest. The predictions reported by the Localization elements team clearly showed promise, with similar quantitative degrees of error to the tearing parameter. Yet, this method still had issues: a factor of 2 non-conservative overprediction of crack initiation displacements in Challenge 1B, and difficulties replicating unloading compliance in Challenge 2A. Both peridynamics and XFEM are clearly still in early phases of development and implementation. While these techniques may alleviate some of the concerns raised by tearing parameters in a conventional FEM framework, the early stage of their development may make it difficult to fairly assess the future potential of these methods at present time.

It is clear that this blind assessment effort has helped make each of the modeling teams more acutely aware of some of the weaknesses of their methods. Many of these weaknesses are discussed in detail in the Appendices, and as a result of the present effort, many of the teams are working to address these weaknesses. One surprising source of error that became apparent through an honest evaluation of the capabilities was 'operator' error, such as misinterpreting the desired prediction quantities, misreporting the results, or making dubious assumptions. It appears that these mistakes can overwhelm any predictivity (or numerical/physical error) that may be present in the models. Even issues with units can present real hurdles to making accurate predictions. These 'simple' mistakes are often quickly discounted after the fact. Yet they can have a quantitatively large effect on blind predictivity.

One common theme that appears to affect all of the modeling methods is the availability of calibration data on the particular alloy of interest. The current effort was restricted to readily available data, which typically includes tensile and K_{IC} data. All of the methods would benefit from more extensive calibration data beyond traditional material property tests. For example, a suite of test geometries spanning different degrees of stress concentrations, stress state, mode mixity, etc. could be useful to calibrate models prior to using them on an 'unknown' problem. There already appear to be early discussions regarding the development of such a test suite. Nevertheless, it is important to remember that reliance on such a test suite would mean that each alloy of interest would require extensive experimental evaluation prior to modeling.

APPENDIX A: TEARING PARAMETER APPROACH

Jerry Wellman, John Emery, and Kristin Dion

A1. Predictions For Challenge 1A

Executive Summary

There are a total of 12 finite element results report herein. For two element formulations there are three mesh densities and their appropriate energy dissipation terms. The Uniform Gradient 'UG' element formulation is the most reliable and stable. The Selective Deviatoric 'SD' element formulation requires further maturation. Predictions for crack nucleation should be taken from the intermediate or fine, uniform-gradient mesh results. The expected gage displacement range is 0.108 – 0.150 inch. The expected load range is 2740 – 2696 lbs.

A1.1 Introduction

The accurate modeling and prediction of ductile crack growth is of utmost importance to our mission at Sandia National Laboratories. Typically, void nucleation, growth and coalescence are the mechanisms attributed to ductile failure. Ductile crack nucleation and growth originating from smooth stress concentrators, *e.g.* bolt holes, are of particular interest and preclude traditional fracture mechanics approaches in the absence of a sharp crack. Further, models which account for the high stress triaxialities that force void growth are essential.

In the following report, the general approach used for ductile crack nucleation prediction is the multilinear elastic-plastic with tearing parameter failure (MLEPF) model. An overview of the approach is provided. Then, the details, as they relate to the x-Prize geometry and alloy, are described, the results of these analyses are reported and discussed. A, somewhat unsuccessful, attempt to use selectively reduced-integration elements to compare with standard under-integrated element formulation was conducted. The upside to the selectively reduced-integration is that they do not posses so-called zero-energy modes. This has been seen to be important in simulations using cohesive surface elements for sharp crack propagation. However, simulating failure with these elements is somewhat less mature than with single-point quadrature elements, as will be seen here, and requires further development. Nonetheless, for geometries with a smooth stress concentrator, as opposed to a sharp notch or crack, the single-point quadrature elements are proven to resolve the plasticity and provide accurate analysis results.

A1.2 General details of the multilinear elasto-plastic with tearing parameter failure approach

The MLEPF approach uses a multilinear elasto-plastic constitutive model with the standard von Mises yield criterion. In this report, the multilinear hardening curve was obtained by fitting experimental data from a round-bar tensile test. Further, the MLEPF approach uses a tearing parameter as a failure criterion, which was also obtained from the round-bar tensile test data. Crack propagation is modified by dissipating energy (critical crack

opening strain) during the element failure. The critical crack opening strain is a function of both material properties and element size. The following sections describe these processes in detail.

A1.2.1 Determining the multilinear elasto-plastic curve fit from round-bar tensile data

The multilinear hardening curve is obtained by using a finite element model of the round-bar tensile specimen to fit observed engineering stress versus engineering strain data. To do this, a 20-degree wedge of the round-bar specimen is modeled, using 3-planes of symmetry. Figure A17 shows a typical mesh. In order to force the localization and necking (geometric instability) to occur at the longitudinal mid-plane, the mesh uses a large-radius to slightly reduce the cross-sectional area at the longitudinal mid-plane.

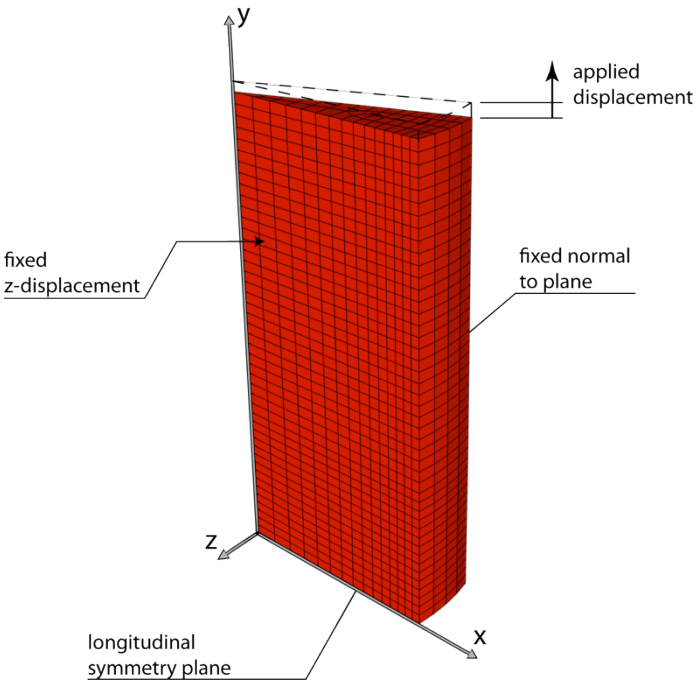

Figure A17. 20-degree wedge model for round-bar tensile test.

A1.2.2 Determining the critical tearing parameter

The tearing parameter accounts for the stress triaxiality at the crack tip by integrating a measure of triaxiality over the equivalent plastic strain. The tearing parameter is given by

$$T = \int_0^{\bar{\varepsilon}_f} \left\langle \frac{2\sigma_T}{3(\sigma_T - \sigma_m)} \right\rangle^4 d\bar{\varepsilon} \qquad (1)$$

where $\bar{\varepsilon}$ is the equivalent plastic strain, $\bar{\varepsilon}_f$ is the final equivalent plastic strain, σ_T is the maximum tensile stress, σ_m is the mean stress and the notation $\langle \bullet \rangle$ represents the standard Macaulay Bracket. One can note that for uniaxial loading, the term inside the Macaulay Brackets becomes unity and the tearing parameter is equivalent to using a limiting plastic strain for a crack growth criterion.

A critical value of the tearing parameter is chosen using the engineering stress versus strain curve from a standard round-bar tensile test.

A1.2.3 Determining the appropriate energy dissipation term

Ordinarily, the energy dissipation term, the critical crack opening strain, must be determined by a second physical test. A theoretical relationship can be established between element size and the value of critical crack opening strain to provide an element size independent simulation of crack extension. This relationship requires several assumptions of questionable accuracy. However, in the absence of data to establish an empirical relationship, this theoretical relationship was employed.

A1.3 Specific details of the approach for the x-Prize

For the x-Prize competition, the alloy chosen was PH13-8 H950. There were two sources of tensile data used, but neither came from a sample of material that will actually be used in the experimental component of this study. One source for tensile data came from Ref[1], section 2.6.6 of the Metallic Materials Properties Development and Standardization (MMPDS) handbook, referred to in the following as the "handbook" data. The other source of tensile data came from previous experimental work conducted at Sandia, referred to in the following as the "SNL test" data. There were a total of 3 tensile tests performed.

Two distinct element formulations were used in conjunction with the MLEPF model. First, a stand under-integrated, uniform-strain hexahedral element, the uniform-gradient (UG) element, with hour glass suppression was used. Second, a modified selectively-reduced-integration hexahedral element, the selective deviatoric (SD) element, was used. These element formulations necessarily give rise to different deformation behavior and, therefore, the extraction of Cauchy-stress, Logarithmic-strain hardening curves is somewhat dependent upon the element type selected. This is unavoidable given that the finite element analysis of the tensile test is an integral part of the curve fitting process.

In addition, there were multiple levels of mesh refinement studied with each element formulation. With the UG elements, three unstructured meshes were used with average element size of 0.01 inch, 0.005 inch, and 0.002 inch in the region of crack nucleation and propagation. With the SD elements, a structure mesh was used in an annular region near the stress concentrator. Here, the average element sizes were 0.0104 inch, 0.0044 inch, and 0.0024 inch. The following presents the material data used and the fits for both element formulations.

A1.3.1 Material data

Two sets of material stress-strain curves for PH13-8 H950 were used: the "handbook" and "SNL test". The handbook curve is the H950 curve from Ref[1] Figure A2.6.6.1.6(c): Typical tensile stress-strain curves (full range) at room temperature for various heat treated conditions of PH13-8Mo stainless steel bar. The dramatic difference between the handbook curve and the SNL test curves is attributed to differences in the gage length defined by differently sized extensometers. According to Ref [2], ASTM E 8 section 6.6.1,

the gage length shall be equal to four times the specimen diameter. For these specimens with diameter of 0.5 inch, the standard size clip gage is a 2-inch gage length. A 1-inch gage length gage was used in the SNL tests because ASTM E 8 section 5.4.1 states that "extensometers with gage lengths equal to or shorter than the nominal gage length of the specimen … may be used to determine the yield behavior." There is some risk that the shorter gage length did not span the entire necked region, producing some error in the curve between yield and failure. Use of the nominal 2 inch gage in future tensile tests may provide more accurate data between yield and failure. The engineering stress versus engineering strain curves for the tensile data are plotted in Figure A18.

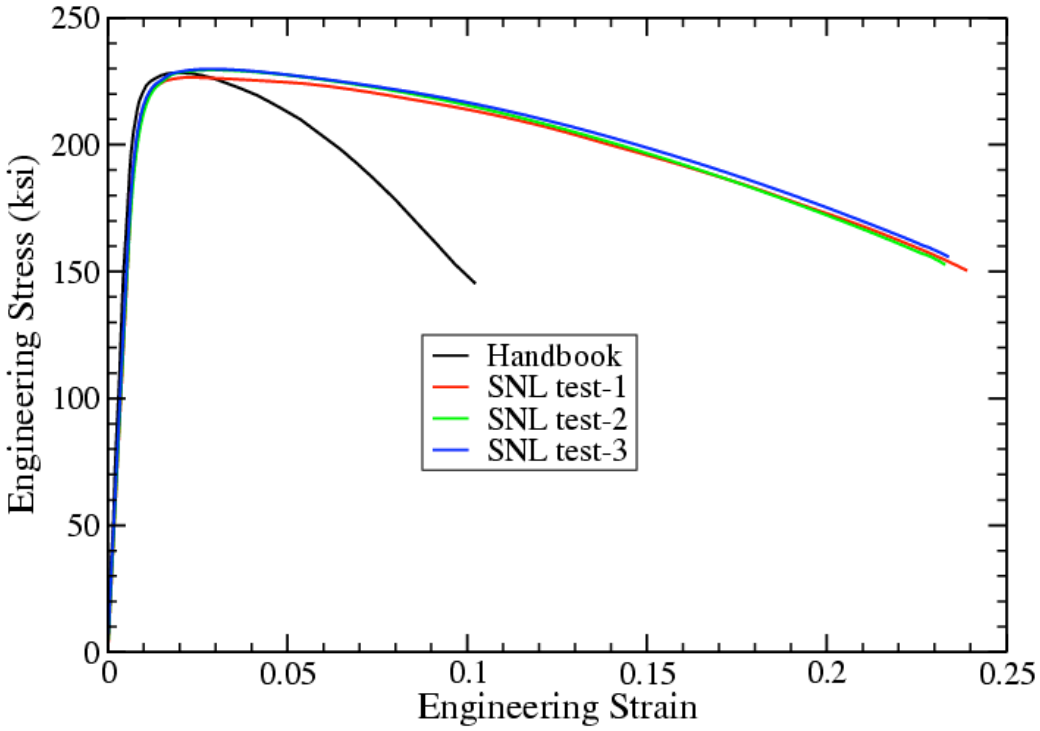

Figure A18. Engineering stress versus engineering strain curves for the tensile data.

A1.3.2 Material data fit for the uniform-gradient element formulation

The Cauchy-stress, Logarithmic-strain curves resulting from the fit using the uniform-gradient element are shown in Logarithmic Strain

Figure A19. The "handbook" and the "test-3" curves were selected to give an upper and lower bound (at least for strength) results for this data. The tearing parameters computed for these curve fits are also displayed on the figure.

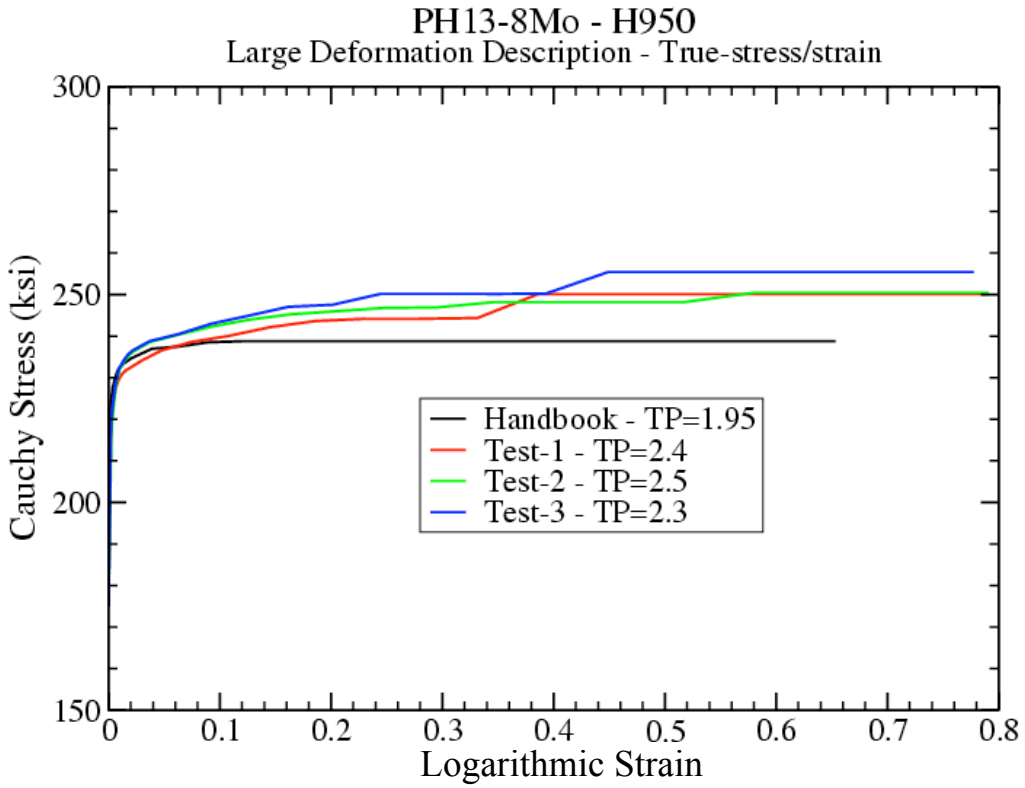

Figure A19. Hardening curves for the uniform-gradient element formulation.

In absence of data, two values of the critical crack opening strain (parameter defining the energy dissipation for crack extension) were chosen. A critical crack opening strain of 0.1 is expected to be a reasonable value for 0.01 inch element and the Ph13-8Mo material properties. A critical crack opening strain of 0.2 should be regarded as an upper bound for a 0.01 inch element. Using the theoretical relationship addressed above, the critical crack opening strains for the 0.005 inch elements around the keyhole are 0.19 and 0.38. Likewise, the critical crack opening strains for the 0.002 inch elements are 0.44 and 0.8.

A1.3.3 Material data fit for the selective deviatoric element formulation

The Cauchy-stress, Logarithmic-strain curves resulting from the fit using the uniform-gradient element are shown in Figure A20. Again, the "handbook" and the "test-3" curves were selected to give an upper and lower bound (at least for strength) results for this data. The tearing parameters computed for these curve fits are also indicated.

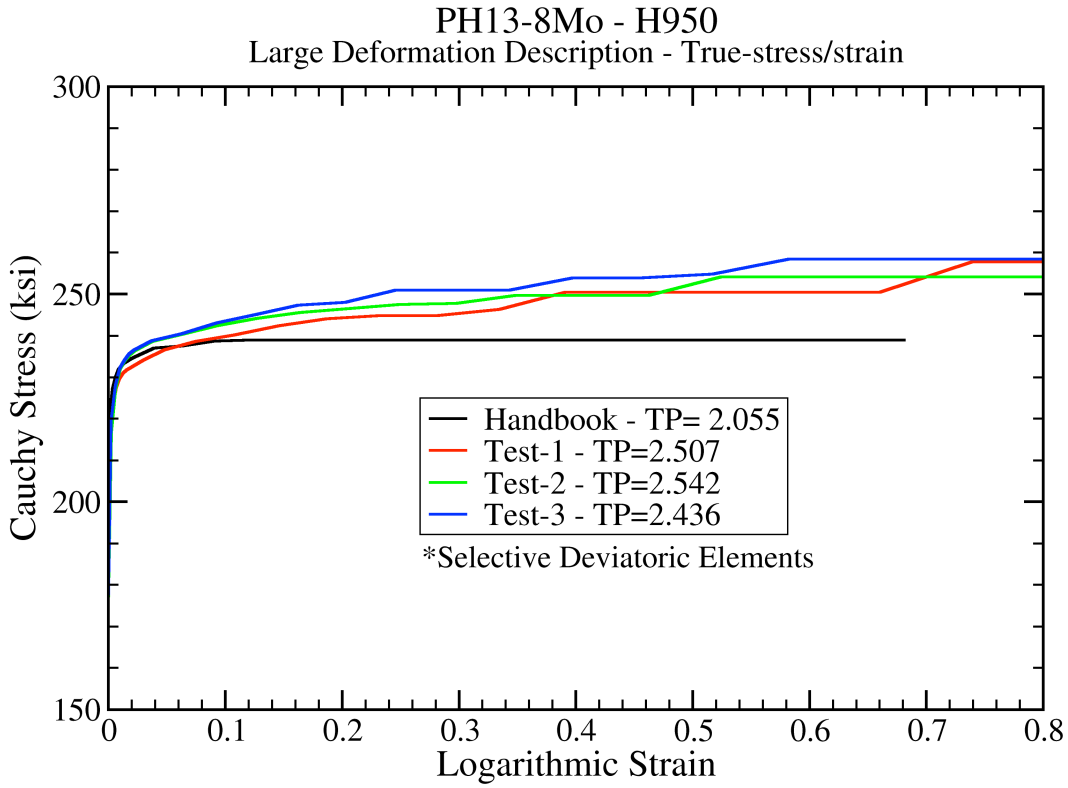

Figure A20. Hardening curves for the selective deviatoric element formulation.

In absence of data, two values of the critical crack opening strain (parameter defining the energy dissipation for crack extension) were chosen. A critical crack opening strain of 0.1 is expected to be a reasonable value for 0.0104 inch element and the Ph13-8Mo material properties. A critical crack opening strain of 0.22 should be regarded as an upper bound for a 0.0104 inch element. Using the theoretical relationship addressed above, the critical crack opening strains for the 0.0044 inch elements around the keyhole are 0.22 and 0.48. Likewise, the critical crack opening strains for the 0.0024 inch elements are 0.4 and 0.81.

A1.4 Results

There were two element formulations used in conjunction with the MLEPF model. The following describes the results of the simulations within the context of the two element formulations.

A1.4.1 MLEPF with uniform-gradient elements

Three unstructured meshes were prepared for the analysis of the X-Prize specimen 1a. All three meshes made use of a symmetry plane at the through-thickness center of the specimen. That is, the centerplane was constrained to provide no out-of-plane displacement while the outer surface was unconstrained appropriate to a free surface. The use of a plane-of-symmetry implies no out-of-plane displacement at the loading pins as well as no buckling of the specimen. The specimen is assumed to be thick enough that neither of these

deformation modes is possible. Half the loading pins are modeled as elastic material meshed equivalently with the bulk of the specimen. The specimen is loaded via imposed displacement (displacement control) at a single node in the elastic pin. Rotation about the load point is allowed but lateral translation is prevented. The coarsest of these meshes had near cubical elements near the keyhole of 0.01 inches. The total number of elements for the coarse mesh was 9,552. The intermediate mesh had keyhole elements of 0.005 inches for a total of 66,992 elements. The finest mesh had keyhole elements of 0.002 inches with a total element count of 433,584. The three meshes are shown in Figure A21.

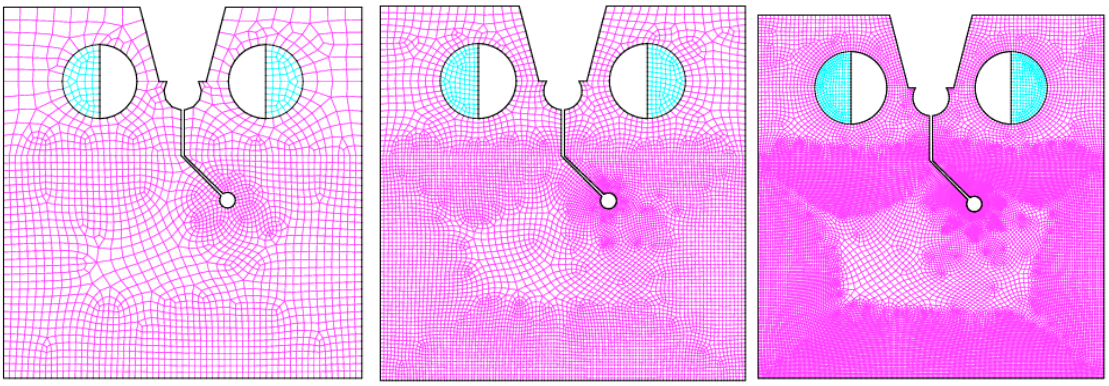

Figure A21. Coarse, intermediate and fine unstructured meshes - looking at the free surface.

Results are presented in Table A1 for the three meshes, the two material stress-strain curves, and the two energy dissipation terms. The start displacement and load refers to when the element first reaches the failure criterion (tearing parameter). The complete displacement and load refers to when the stress in the element has been decayed to zero. There is some ambiguity in the definition of failure between these two extremes. The failure location is approximated by hour on a clock face. The face of the specimen used is consistent with the machined slot at 10:30. The element number can be used to obtain a more accurate failure location when such a method has been defined. Results for the finest meshes are pending. Finite element solutions for these meshes are so computationally intensive as to be on the verge of being impractical.

Table A1. Surface tear predictions for the uniform-gradient elements.

Mesh	Material	CCOS	Start Displ. (inch)	Start Load (lb)	Comp. Displ. (inch)	Comp Load (lb)	Fail Elem. No.	Fail Loc
Coarse	Hdbk	0.1	0.0957	2983	0.0982	2904	308	5:00
Coarse	Hdbk	0.2	0.1118	2924	0.1195	2618	312	4:00
Coarse	Test-3	0.1	0.1115	3115	0.1180	3038	308	5:00
Coarse	Test-3	0.2	0.1318	3169	0.1485	3090	316	3:00
Inter	Hdbk	0.19	0.1084	2740	0.1111	2633	1288	4:30
Inter	Hdbk	0.38	0.1174	2803	0.1273	2641	1288	4:30
Inter	Test-3	0.19	0.1307	2853	0.1359	2696	1288	4:30
Inter	Test-3	0.38	0.1422	2877	>.1496	n.a.	1288	4:30

Fine	Hdbk	0.44	0.1118	2329	0.1134	2102		4:30
Fine	Hdbk	0.8	0.1235	2375	n.a.	n.a.		n.a.
Fine	Test-3	0.44	0.1343	2178	n.a.	n.a.		n.a.
Fine	Test-3	0.8	n.a.	n.a.	n.a.	n.a.		n.a.

The deformed shape and extent of the plastic zone for a typical result at failure is shown in Figure A6. Obviously, there is diffuse plasticity in the specimen by the time a visible crack has formed on the surface.

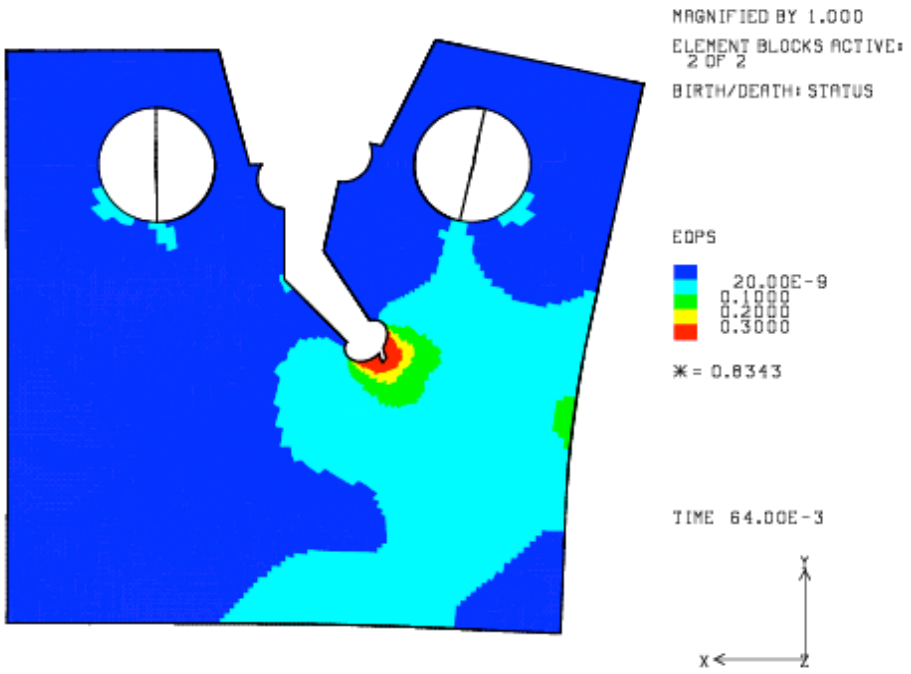

Figure A22. A typical deformed shape at failure showing the extent of the plastic straining.

The load versus gage-line displacement curves from the analyses are plotted in Figure A23. Figure A7 through Figure A26 shows the load versus displacement for all analyses that employed the Handbook material properties. Figure A24 shows the same results for the analyses that used the SNL test-3 material properties. To ease the comparison between the handbook properties and the SNL test-3 properties, a typical set of results is presented in Figure A25. The effect of energy dissipation is shown in Figure A26.

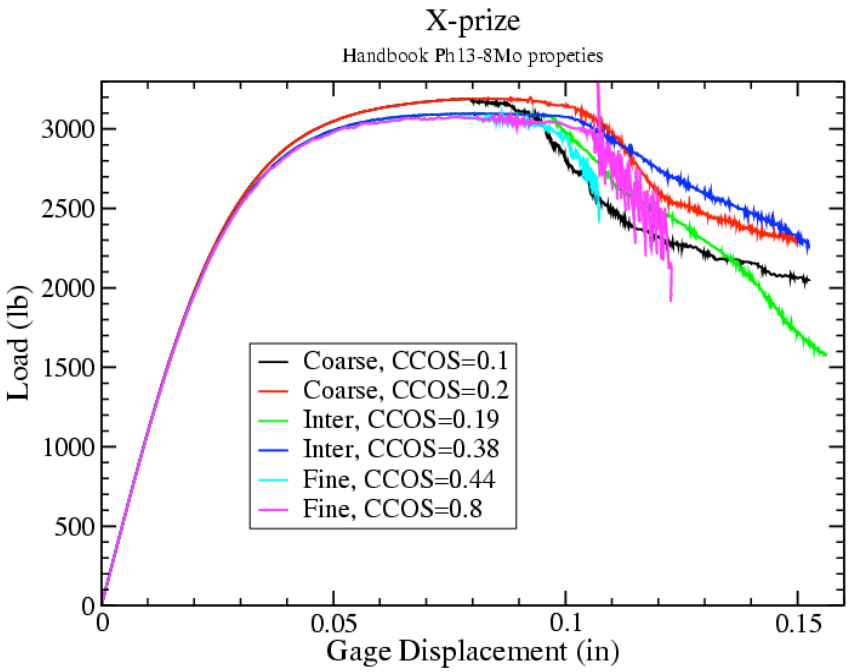

Figure A23. Load versus Displacement curves for the Handbook Ph13-8Mo.

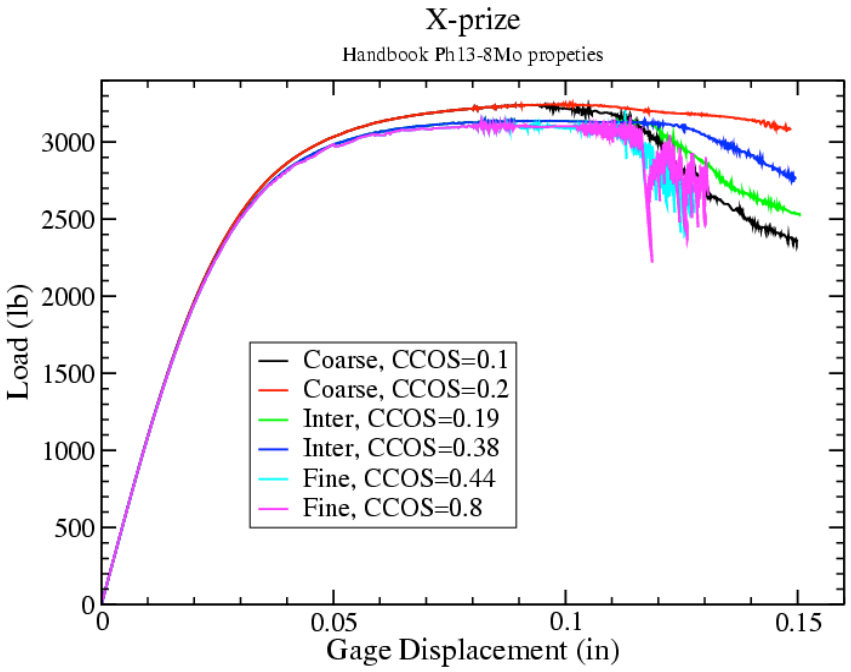

Figure A24. Load versus Displacement curves for Test-3 Ph13-8Mo.

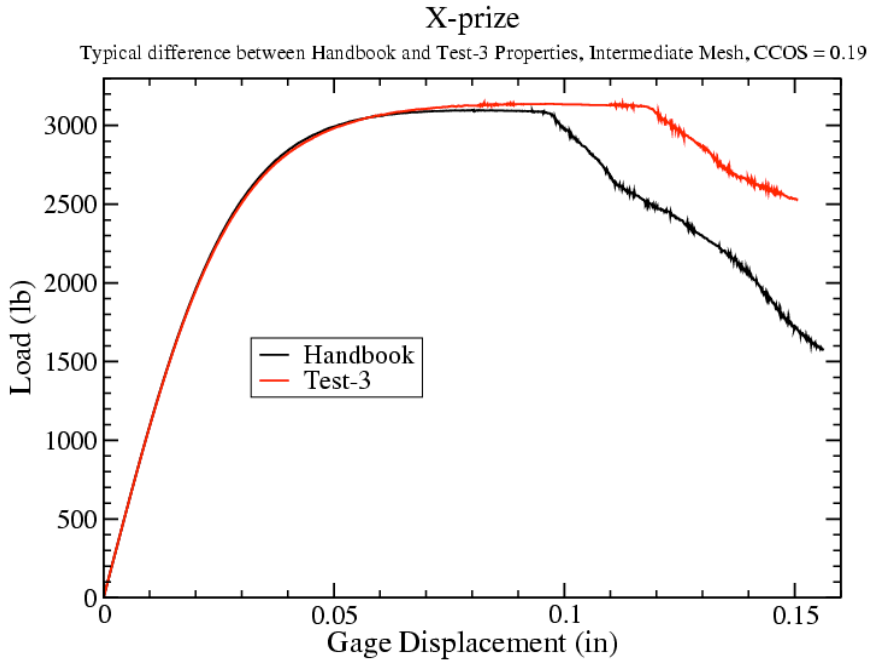

Figure A25. Typical difference between handbook and SNL test-3 results.

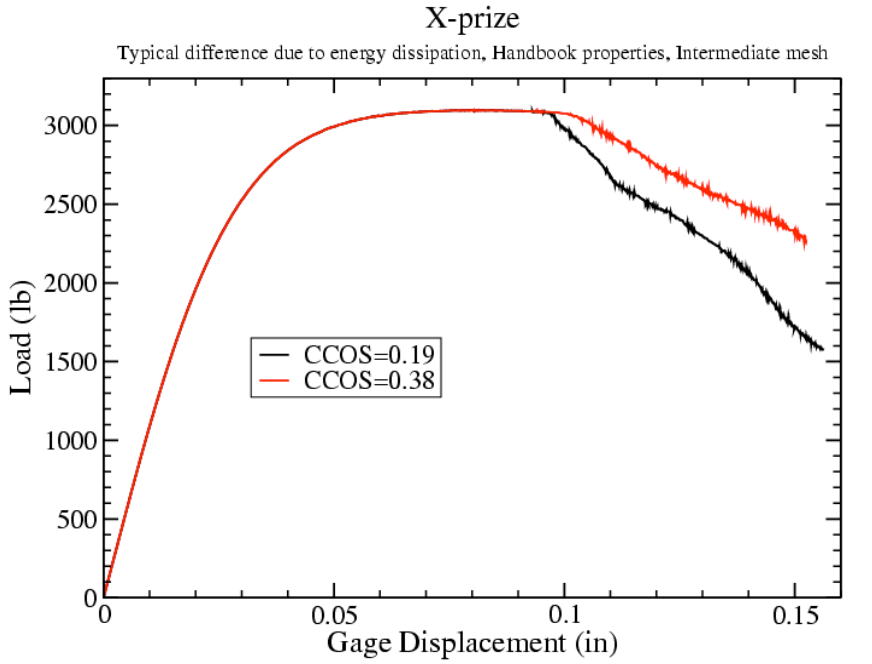

Figure A26. Typical difference resulting from varying the critical crack opening strain (energy dissipation) term.

A1.4.2 MLEPF with selective deviatoric elements

Three meshes were used with the selective deviatoric element formulation. The meshes were progressively refined and structured in an annular region near the stress concentrator. The finite element models using the SD elements used all the same symmetry and boundary conditions employed with the UG elements. For each mesh, the elements on the surface of the keyhole had aspect ratios of 1.0. The element size on the key hole was 0.0104 inch, 0.0044 inch, and 0.0024 inch for the coarse, medium and fine meshes, respectively. There were 3,392 elements, 23,112 elements, and 125,184 elements for the coarse, medium and fine meshes, respectively. The three meshes are shown in Figure A27.

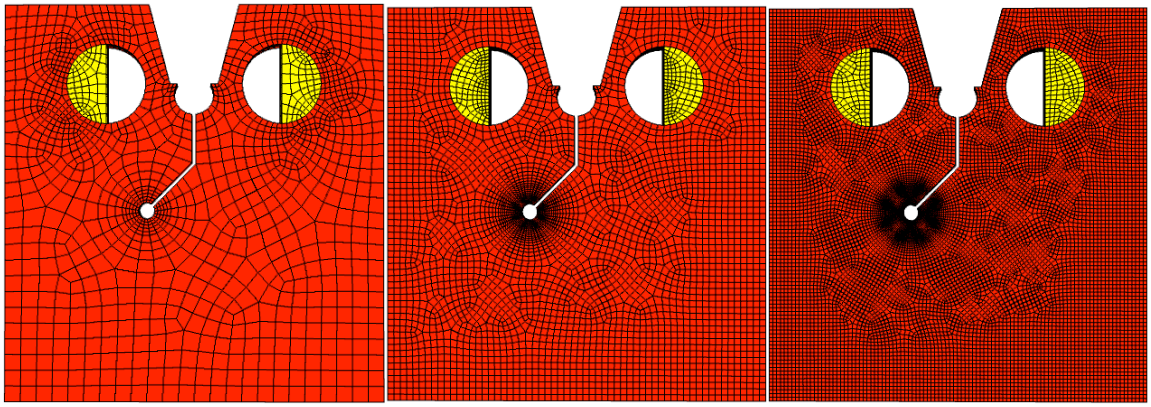

Figure A27. Three structured meshes used with selective deviatoric elements.

The SD element formulation uses full 8-point quadrature for the linear hexahedral elements. Consequently, meshes with SD elements are three to four times slower than with under-integrated UG elements. Further, the small element size in the medium and fine meshes in combination with the nature of the problem require very small load steps. As a result, the crack initiation results reported here, in Table A2, are for the coarsest mesh; results for the medium and fine mesh are pending successful completion of the analyses. However, the load versus clip gage curves reported do included results from the finer meshes and, by nature of their tending towards convergence, suggest that the coarsest mesh is inadequate.

Table A2. Surface tear predictions for the selective deviatoric elements.

Mesh	Material	CCOS	Start Displ. (inch)	Start Load (lb)	Comp. Displ. (inch)	Comp Load (lb)	Fail Elem. No.	Fail Loc
Coarse	Hdbk	0.1	0.1277	2546	0.1325	2440	2859	5:00
Coarse*	Hdbk	0.22	n.a.	n.a.	n.a.	n.a.	n.a.	n.a.
Coarse	Test-3	0.1	0.1616	2604	0.1690	2466	2860	5:00
Coarse	Test-3	0.22	0.1801	2590	0.1970	2404	2860	5:00

* result pending successful completion of analysis.

Figure A28 and Figure A29 plot the applied load versus clip gage displacement for the handbook and test-3 results, respectively. Clearly, the finer meshes are required for a converged solution. In general, the solution with the quasi-static solver is difficult to

obtain once the system begins to shed load. This is likely do to ill conditioning in the global tangent stiffness. The MLEPF model is applied per gauss point, which further complicates the analyses for elements with 8-quadrature points. Analyses with smaller time stepping could improve the capability to achieve a solution (and are queued on the capacity machines). Further exploration as to how to fail elements with multiple quadrature points is necessary.

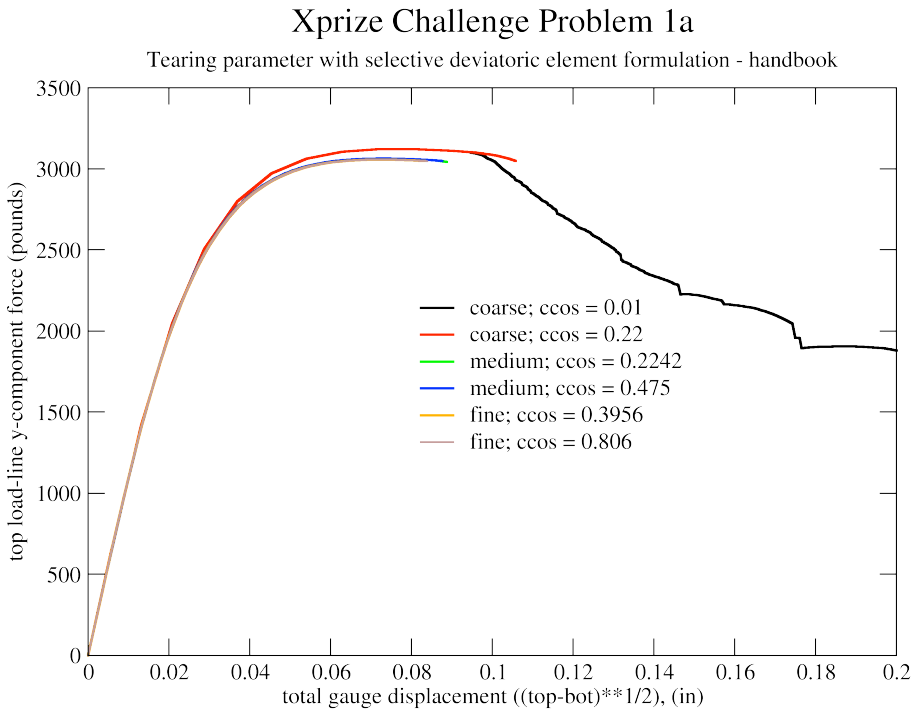

Figure A28. Load versus Displacement curves for the handbook data and selective deviatoric elements.

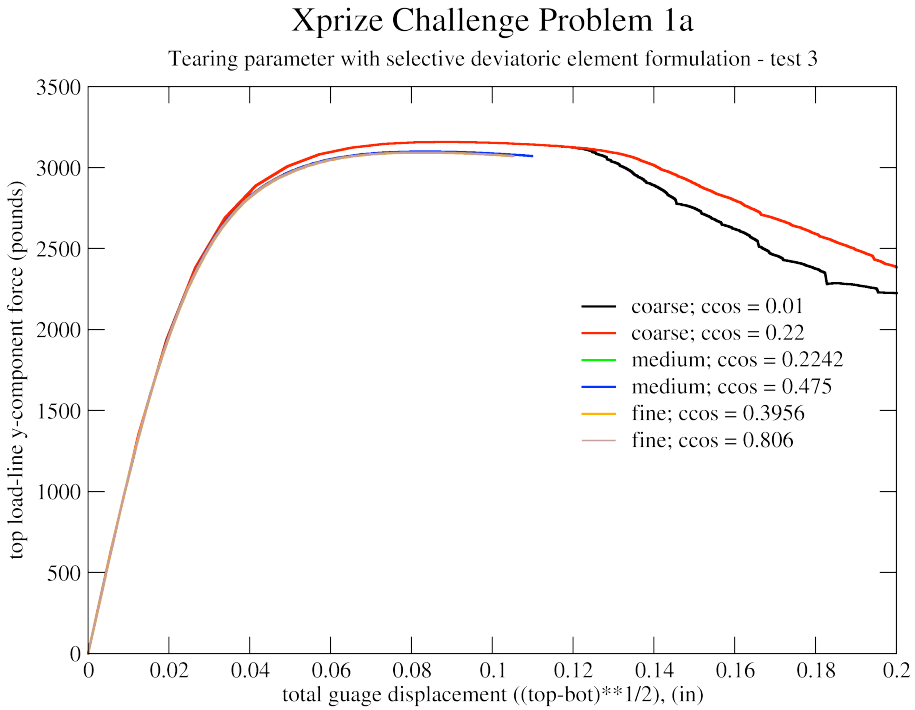

Figure A29. Load versus Displacement curves for the test-3 data and selective deviatoric elements.

Figure A30 compares the coarse mesh to the fine mesh and plots the extent of plasticity at an applied displacement of +/- 0.05 inch (*i.e.* prior to crack nucleation on the surface). Clearly, the fine mesh resolves the plasticity at the keyhole to a finer degree.

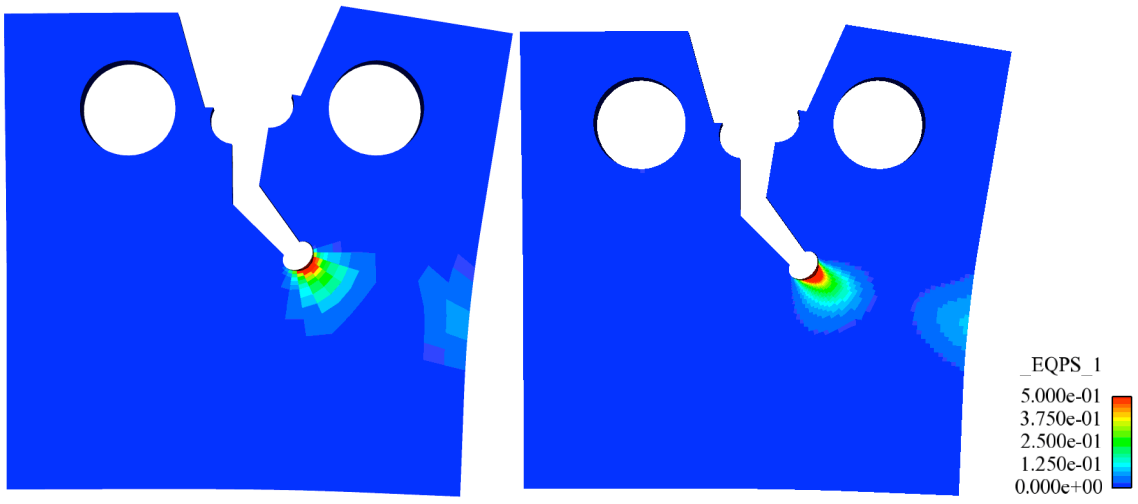

Figure A30. Plasticity in the specimen with coarse and fine meshes and selective deviatoric elements.

A1.5 Discussion

The results showed some interesting features. Failure of the first element on the free surface and thus all the loads reported in Table A1 and Table A2 occur post peak-load. This implies that the stiffness (energy stored) of the test machine, load train, etc. could be important to these results. In the case of load control, for quasistatics, only the peak load could be computed. There is no equilibrium position past peak load so no quasistatics code could converge on a solution. Of course, reality lies between load control and the displacement control assumed here.

For all cases with the UG elements the crack tunneled. That is, the crack initiated and extended at the center-plane prior to initiation at the free surface. The extent of tunneling appears to be primarily related to the energy dissipation term (CCOS). For the lower CCOS values, the extent of tunneling is about 0.02 inch (the extent of cracking is about 0.02 inch greater at the center-plane than at the surface). For the higher values of CCOS, the crack appears to tunnel about twice a much or about 0.04 inch. For the set of coarse mesh results with SD elements, the observations of crack tunneling are similar.

The failure does not start until a large, unconfined plastic zone has formed. Yielding occurs from the keyhole to free surfaces both to the nearest side and to the bottom of the specimen. Linear elastic fracture mechanics or even small scale yielding solutions are not appropriate to characterize failure in this specimen with this material. As is evident in Figure A22 and Figure A30, the displacements are also quite large, as expected for the extent of plastic deformation, with the keyhole noticeably deformed from its originally circular shape. The slot has opened extensively. However, of most importance, the notches for measuring the load line displacement show significant vertical displacement (not out-of-plane) along with the in-line displacement. Because the imposed displacement was only in-line (all lateral displacement was constrained) this vertical displacement of the measurement notches is entirely due to rotation of the specimen ears, primarily the ear above the keyhole and notch.

The predictions are made with a range of values for several obvious reasons. Primarily, there is a lack of experimental data to calibrate the energy dissipation variable in the computational model. Further, there is some ambiguity in the definition of crack nucleation due to the physical processes that are inherently lumped-into the tearing parameter and energy dissipation terms. In the absence of a sharp notch or starter crack, the tearing parameter and energy dissipation combine to account for gross plasticity, and void growth and coalescence. Thus, the experimental results are expected to lie somewhere between the starting displacement/load and the complete displacement/load, referring to Table A1 and Table A2. Further, the results for the SD elements are not robust enough at this point to make a reasonable comparison between element formulations.

A1.6 Summary and Conclusions

In conclusion, there were a total of 12 finite element results report herein. For two element formulations there were three mesh densities and their appropriate energy dissipation

terms. The UG element formulation is the most reliable and stable. The SD element formulation requires further maturation.

Predictions for crack nucleation should be taken from the intermediate or fine, uniform-gradient mesh results. The expected gage displacement range is 0.108 – 0.150 inch. The expected load range is 2740 – 2696 lbs.

A1.7 Appendix A.1 References

1. Battelle Memorial Laboratories, FAA William J. Hughes Technical Center, and U. S. Air Force Research Laboratory. *Metallic Materials Properties Development and Standardization (MMPDS)*. DOT/FAA/AR-MMPDS-01, January 2003.

2. ASTM International. *Standard Test Methods for Tension Testing of Metallic Materials.* ASTM E 8/E 8M-08, 2008.

A2. Follow-Up for Challenge 1A

1. Describe what material model you used for deformation (not crack initiation)? How did you calibrate that model against material properties? What parameters did you calibrate? Please specify what specific resources (datasets) you used to calibrate the parameters.

The multilinear elastic-plastic hardening model with the standard von-Mises yield criterion was used to represent the PH13-8Mo during deformation. This material model is documented in the Adagio 4.14 User's Guide section 4.2.7 and requires two elastic constants, a yield stress, and a hardening function to calculate the elastic and plastic deformation of the material.

The elastic constants and yield stress were obtained from the DOT/FAA/AR-MMPDS-01 handbook properties for PH13-8Mo. The Young's modulus used was 28,000 ksi, which is approximately equal to the handbook value of 28,300 ksi, and the Poisson's ratio used was 0.3, which is approximately equal to the handbook value of 0.28 reported in MMPDS Table 2.6.6.0(b). The yield stress of 175 ksi was obtained by visually inspecting the H950 curve from MMPDS Figure 2.6.6.1.6(c) to identify the proportional limit. These material properties were used for both element formulations and all mesh sizes and were not varied.

The hardening function was calibrated against four engineering stress-strain data sets, three from SNL experiments and one from the MMPDS-01 handbook. The handbook curve is the H950 curve from MMPDS-01 Figure 2.6.6.1.6(c): Typical tensile stress-strain curves (full range) at room temperature for various heat treated conditions of PH13-8Mo stainless steel bar. The dramatic difference between the handbook curve and the SNL test curves is due to the use of a smaller clip gage for the SNL data. According to ASTM E 8 section 6.6.1, the gage length shall be equal to four times the specimen diameter. For these specimens with diameter of 0.5 inch, the standard size clip gage is a 2-inch gage length. A 1-inch gage length gage was used in the SNL tests because ASTM E 8 section 5.4.1 states that "extensometers with gage lengths equal to or shorter than the nominal gage length of the specimen … may be used to determine the yield behavior." There is some risk that the shorter gage length did not span the entire necked region, producing some error in the curve between yield and failure. Use of the nominal 2 inch gage in future tensile tests may provide more accurate data between yield and failure. The engineering stress versus engineering strain curves for the tensile data are plotted in Figure A31.

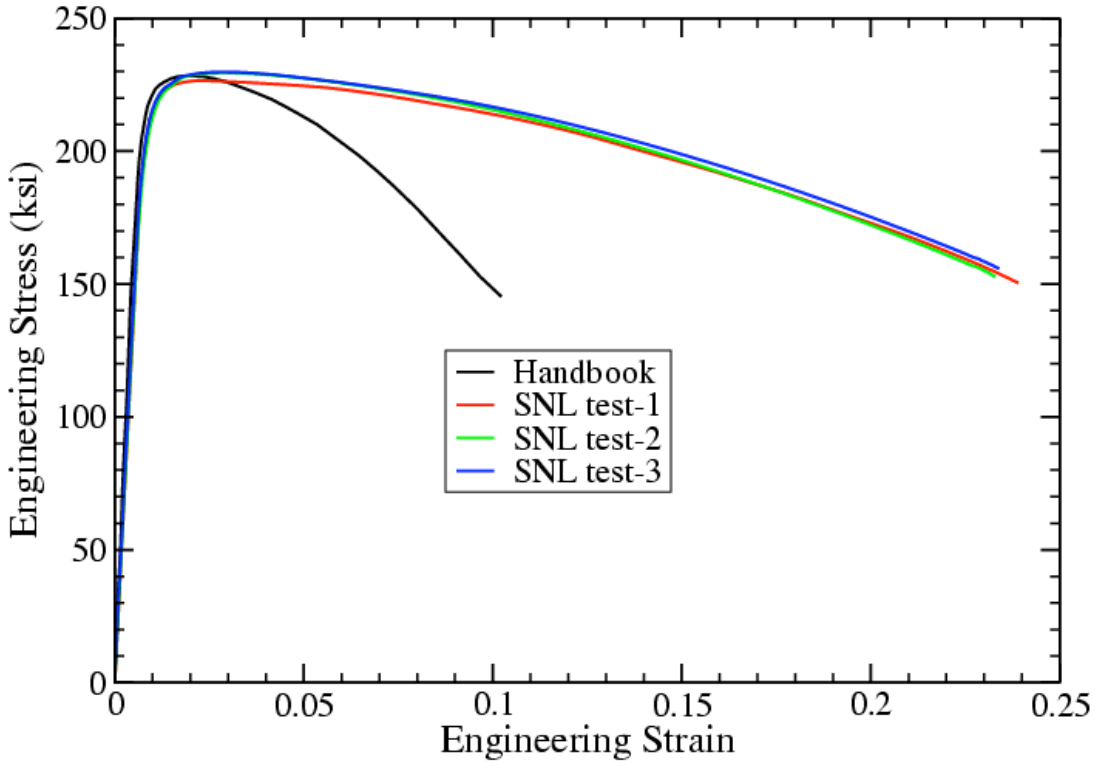

Figure A31. Engineering stress versus engineering strain curves for the tensile data.

The multilinear hardening curve is obtained by using a finite element model of the round-bar tensile specimen to fit observed engineering stress versus engineering strain data. To do this, a 20-degree wedge of the round-bar specimen is modeled, using 3-planes of symmetry.

Figure A32 shows a typical mesh. In order to force the localization and necking (geometric instability) to occur at the longitudinal mid-plane, the mesh uses a large-radius to slightly reduce the cross-sectional area at the longitudinal mid-plane. The mesh has a nominal element size of 0.012 inch and is biased so that element at the intersection of the axis and longitudinal mid-plane will have an aspect ratio of approximately 1:1 at failure. A finer mesh of the round bar tensile specimen was used to determine that the hardening curve and tearing parameter are insensitive to mesh refinement below the 0.012 mesh size.

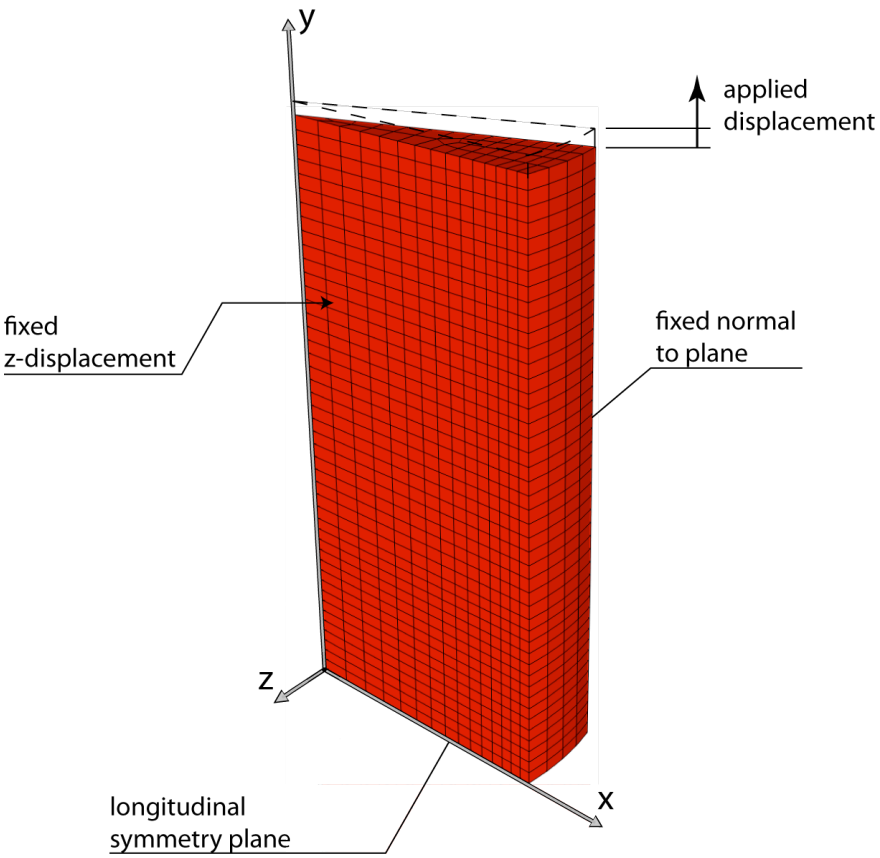

Figure A32. 20-degree wedge model for round-bar tensile test.

Two distinct element formulations were used in conjunction with the MLEPF model. First, a standard under-integrated, uniform-strain hexahedral element, the uniform-gradient (UG) element, with hour glass suppression was used. Second, a modified selectively-reduced-integration hexahedral element, the selective deviatoric (SD) element, was used. These element formulations necessarily give rise to different deformation behavior and, therefore, the extraction of Cauchy-stress, Logarithmic-strain hardening curves is somewhat dependent upon the element type selected.

The Cauchy-stress, Logarithmic-strain curves resulting from the fit using the uniform-gradient element are shown in Figure A33. The "handbook" and the "test-3" curves were selected for the analyses in this report to account for the upper and lower bound for Cauchy stress from these data. The tearing parameters computed for these curve fits are also displayed on the figure.

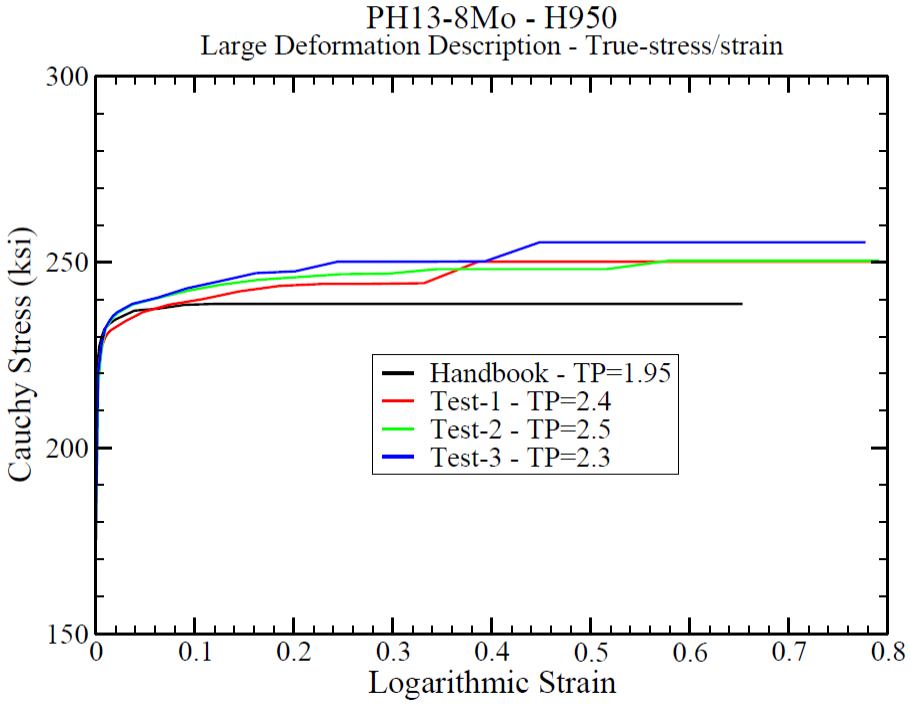

Figure A33. Hardening curves for the uniform-gradient element formulation.

The Cauchy-stress, Logarithmic-strain curves resulting from the fit using the selective deviatoric element are shown in Figure A34. Again, the "handbook" and the "test-3" curves were selected as representative of the upper and lower bound of Cauchy stress results for these data. The tearing parameters computed for these curve fits are also shown.

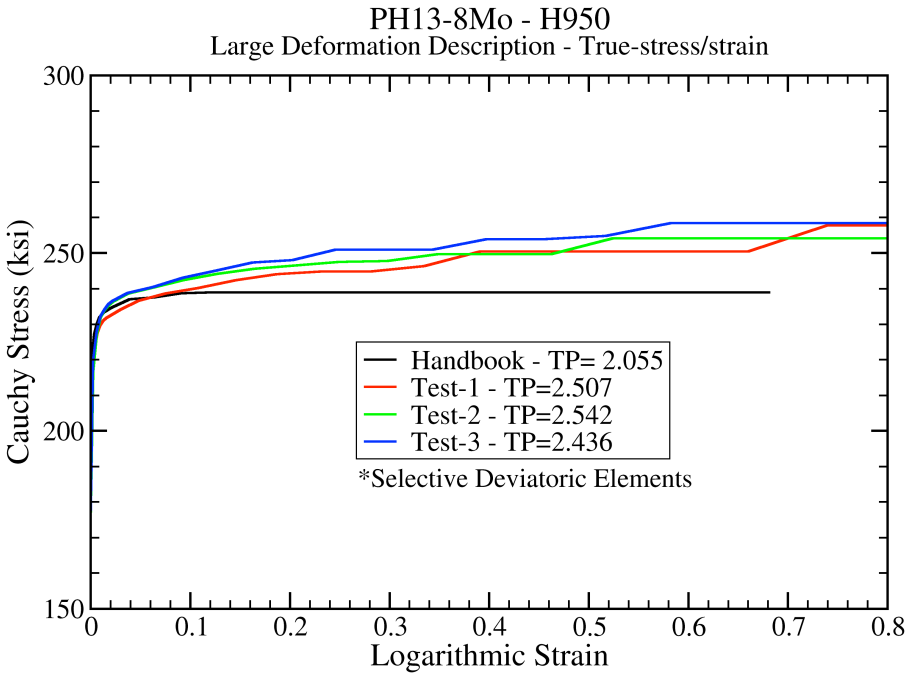

Figure A34. Hardening curves for the selective deviatoric element formulation.

2. Describe what material model you used for crack initiation? How did you calibrate that model against material properties? What parameters did you calibrate? Please specify what specific resources (datasets) you used to calibrate the parameters.

The multilinear elastic-plastic hardening model with failure (mlep-fail) was used to predict crack initiation. This material model is documented in the Adagio 4.14 User's Guide section 4.2.7 and requires a critical tearing parameter and critical crack opening strain to calculate crack initiation and propagation.

The tearing parameter accounts for the stress triaxiality at the crack tip by integrating a measure of triaxiality over the equivalent plastic strain. The tearing parameter is given by

$$T = \int_0^{\bar{\varepsilon}_f} \left\langle \frac{2\sigma_T}{3(\sigma_T - \sigma_m)} \right\rangle^4 d\bar{\varepsilon} \qquad \textit{(1)}$$

where $\bar{\varepsilon}$ is the equivalent plastic strain, $\bar{\varepsilon}_f$ is the final equivalent plastic strain, σ_T is the maximum tensile stress, σ_m is the mean stress and the notation $\langle \bullet \rangle$ represents the standard Macaulay Bracket. One can note that for uniaxial tensile loading, the term inside the Macaulay Brackets becomes unity and the tearing parameter is equivalent to using a limiting plastic strain for a crack growth criterion.

The finite element analyses of the round bar tension specimen were post processed with Algebra to calculate the tearing parameter. The critical tearing parameter is chosen as the maximum value of tearing parameter in the analysis at the end of the engineering stress versus engineering strain curve. Each analysis of a tension specimen produces a hardening curve and critical tearing parameter which should be used together. The critical tearing parameters for all tension specimen analyses are shown in Figure A33 and Figure A34 above. The contour plot of tearing parameter for the analysis of SNL Test 3 is shown in Figure A35 as a typical result.

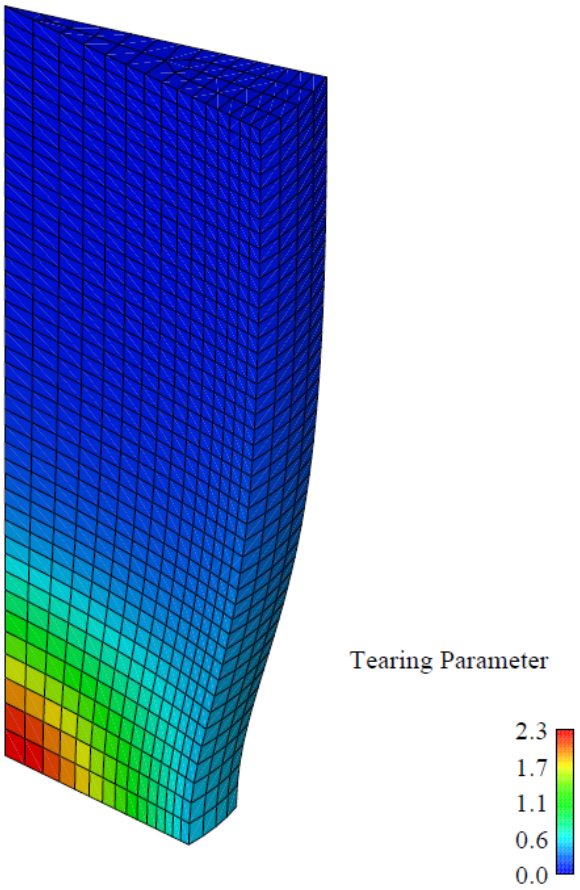

Figure A35. Analysis of tension test fit to SNL Test 3 data using uniform-gradient element formulation.

After the critical tearing parameter has been reached at a material point, the stress at that point is uniformly decayed to zero over a user-specified amount of strain in the mode one direction. This energy dissipation term is referred to as the critical crack opening strain. The critical crack opening strain is a function of both material properties and element size. Ordinarily, the critical crack opening strain must be determined by a second physical test. This second test has not yet been specified, but it should ideally be one in which significant stable crack propagation exists.

Due to an absence of test data for PH13-8Mo, the critical crack opening strain could not be determined for this material. Consequently, two values of the critical crack opening strain were chosen for each element size. These two values were chosen based on previous experience with other precipitation hardened steels and were representative of an average value and an upper bound.

For uniaxial straining, the work of separation can be analytically computed for a given out-of-plane element dimension and critical crack opening strain. Using this relationship, the critical crack opening strain to maintain a constant work of separation for a different element size can be calculated as

$$e_2 = \frac{-3\,h_1/h_2 + \sqrt{h_1/h_2}\sqrt{12e_1 + 4e_1^2 + 9\,h_1/h_2}}{2\,h_1/h_2} \qquad (2)$$

where e_1 and e_2 are the critical crack opening strains corresponding to out-of-plane element heights h_1 and h_2, respectively. Equation 2 assumes a constant, element-size-independent traction at crack initiation which may not be realized numerically. Preliminary evidence suggests a functional dependence on in-plane element dimension as well as the out-of-plane dimension in equation 2. However, in the absence of data to establish an empirical relationship, this theoretical relationship was employed.

A2.1 Crack opening strain for uniform-gradient element

A critical crack opening strain of 0.1 is expected to be a reasonable value for 0.01 inch element and the Ph13-8Mo material properties. This value was chosen to be approximately equal to the critical crack opening strain of 0.07 calculated for 17-4PH with a 0.01 inch element. Based on the characterization of many metallic materials, a critical crack opening strain of 0.2 should be regarded as an upper bound for a 0.01 inch element.

Using the theoretical relationship addressed above, the critical crack opening strains for the 0.005 inch elements around the keyhole are 0.19 and 0.38. Likewise, the critical crack opening strains for the 0.002 inch elements are 0.44 and 0.8.

A2.2 Crack opening strain for selective deviatoric element

A critical crack opening strain of 0.1 is expected to be a reasonable value for 0.0104 inch element and the Ph13-8Mo material properties. A critical crack opening strain of 0.22 should be regarded as an upper bound for a 0.0104 inch element. Using the theoretical relationship addressed above, the critical crack opening strains for the 0.0044 inch elements around the keyhole are 0.22 and 0.48. Likewise, the critical crack opening strains for the 0.0024 inch elements are 0.4 and 0.81.

3. How was uncertainty captured in your simulation: (a) material variability, (b) uncertainty in the failure criterion?

Uncertainty due to material variability was addressed by selecting hardening curves and associated tearing parameters that provide an upper and lower bound for maximum Cauchy stress developed in the material. Further uncertainty in the failure criterion was addressed by selecting a typical value and an upper bound value for the critical crack opening strain which governs energy dissipation during crack development.

4. Please summarize your examination (if any) of mesh dependency of your result.

Mesh dependency was examined as a function of element formulation and of mesh size. There were two element formulations used in conjunction with the MLEPF model. For each element formulation, a coarse, medium and fine mesh were used to investigate the effect of mesh size on the result. The use of selective deviatoric elements with element death is an active area of development that may provide more accurate answers in problems involving large deformations. However, the analyses using selective deviatoric elements are not robust enough at this point in time to compare to the analyses using uniform gradient elements. The results for the medium and fine meshes with uniform gradient elements are similar, so these results are considered to be a converged answer for this analysis approach.

A2.3 MLEPF with uniform-gradient elements

Three unstructured meshes were prepared for the analysis of the X-Prize specimen 1a. All three meshes made use of a plane-of-symmetry mid way through the thickness of the specimen. Thus, the hidden face of the meshes of Figure A36 were constrained to no displacement normal to that face. The faces shown were constraint and traction free. The coarsest of these meshes had near cubical elements near the keyhole of 0.01 inches. The total number of elements for the coarse mesh was 9,552. The intermediate mesh had keyhole elements of 0.005 inches for a total of 66,992 elements. The finest mesh had keyhole elements of 0.002 inches with a total element count of 433,584. The three meshes are shown in Figure A36.

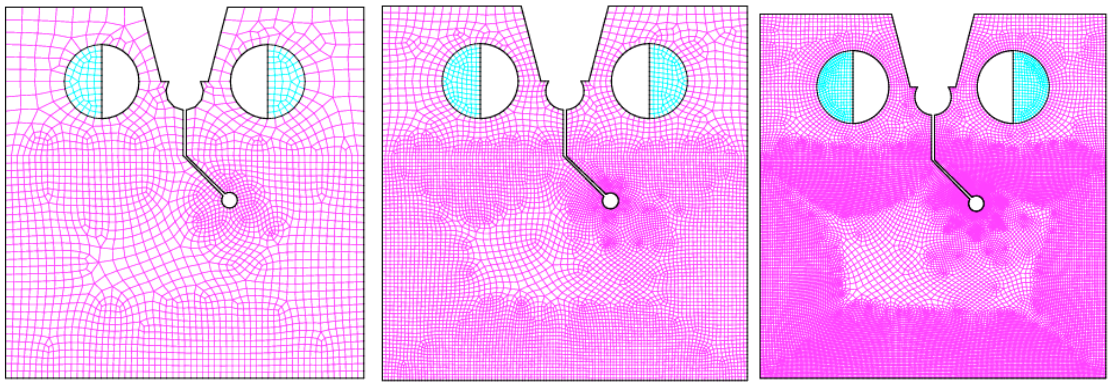

Figure A36. Coarse, intermediate and fine unstructured meshes - looking at the free surface.

Results are presented in Table A3 for the three meshes, the two material stress-strain curves, and the two energy dissipation terms. The start displacement and load refers to when the first element on the free surface at the key-hole reaches the failure criterion (tearing parameter). The complete displacement and load refers to when the stress in that element has been decayed to zero. There is some ambiguity in the definition of failure between these two extremes. The failure location is approximated by hour on a clock face. The face of the specimen used is consistent with the machined slot at 10:30. The element number can be used to obtain a more accurate failure location when such a method has been defined. Some results for the finest meshes are pending. Finite element solutions for

these meshes are so computationally intensive as to be on the verge of being impractical. Note: for all meshes, the crack tunnels. That is, cracking occurs earlier and extends further at he center-plane than at the free surface. For the finest mesh, the first element to fail was a small distance from the edge of the key-hole. The failure then propagated back to the key-hole surface.

Table A3. Surface tear predictions for the uniform-gradient elements.

Mesh	Material	CCOS	Start Displ. (inch)	Start Load (lb)	Comp. Displ. (inch)	Comp Load (lb)	Fail Elem. No.	Fail Loc
Coarse	Hdbk	0.1	0.0957	2983	0.0982	2904	308	5:00
Coarse	Hdbk	0.2	0.1118	2924	0.1195	2618	312	4:00
Coarse	Test-3	0.1	0.1115	3115	0.1180	3038	308	5:00
Coarse	Test-3	0.2	0.1318	3169	0.1485	3090	316	3:00
Inter	Hdbk	0.19	0.1084	2740	0.1111	2633	1288	4:30
Inter	Hdbk	0.38	0.1174	2803	0.1273	2641	1288	4:30
Inter	Test-3	0.19	0.1307	2853	0.1359	2696	1288	4:30
Inter	Test-3	0.38	0.1422	2877	>.1496	n.a.	1288	4:30
Fine	Hdbk	0.44	0.1118	2331	0.1169	2004	4448	4:30
Fine	Hdbk	0.8	0.1213	2354	0.1362	2175	4448	4:30
Fine	Test-3	0.44	0.1343	2285	0.1430	2156	4448	4:30
Fine	Test-3	0.8	0.1430	2536	0.1612	2155	4448	4:30

The deformed shape and extent of the plastic zone for a typical result at failure is shown in Figure A37. Obviously, there is diffuse plasticity in the specimen by the time a visible crack has formed on the surface.

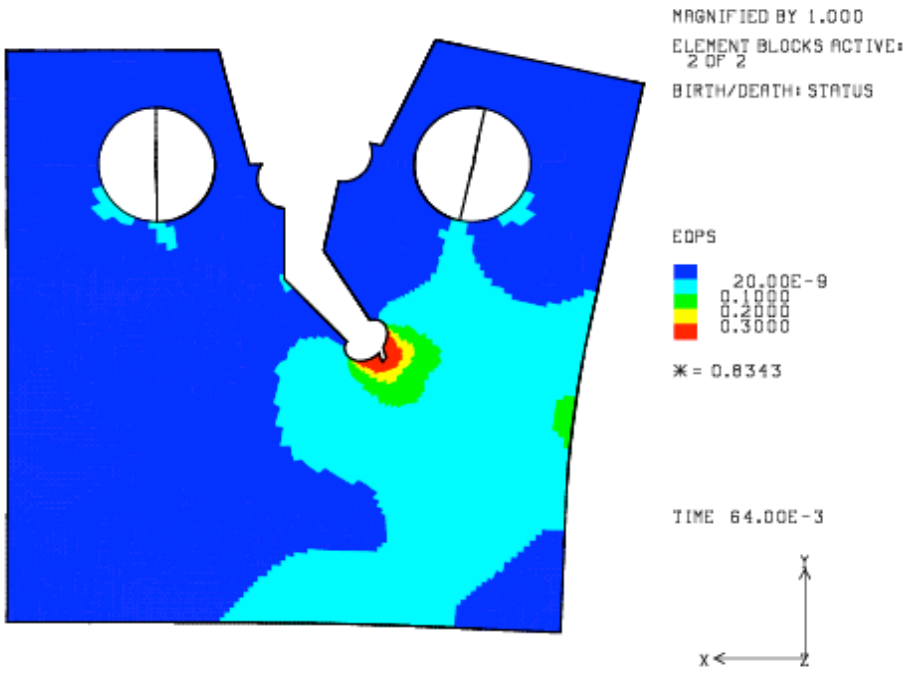

Figure A37. A typical deformed shape at failure showing the extent of the plastic straining.

The load versus gage displacement curves from the analyses are plotted in Figure A38 through Figure A41. Figure A38 shows the load versus displacement for all analyses that employed the Handbook material properties. Figure A39 shows the same results for the analyses that used the SNL test-3 material properties. To ease the comparison between the handbook properties and the SNL test-3 properties, a typical set of results is presented in Figure A40. The effect of energy dissipation is shown in Figure A41.

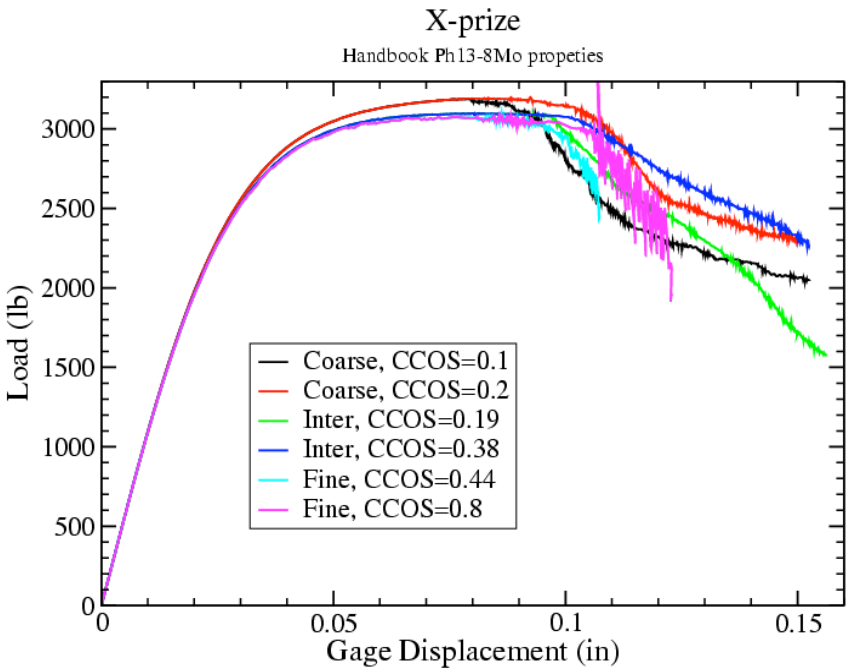

Figure A38. Load versus Displacement curves for the Handbook Ph13-8Mo.

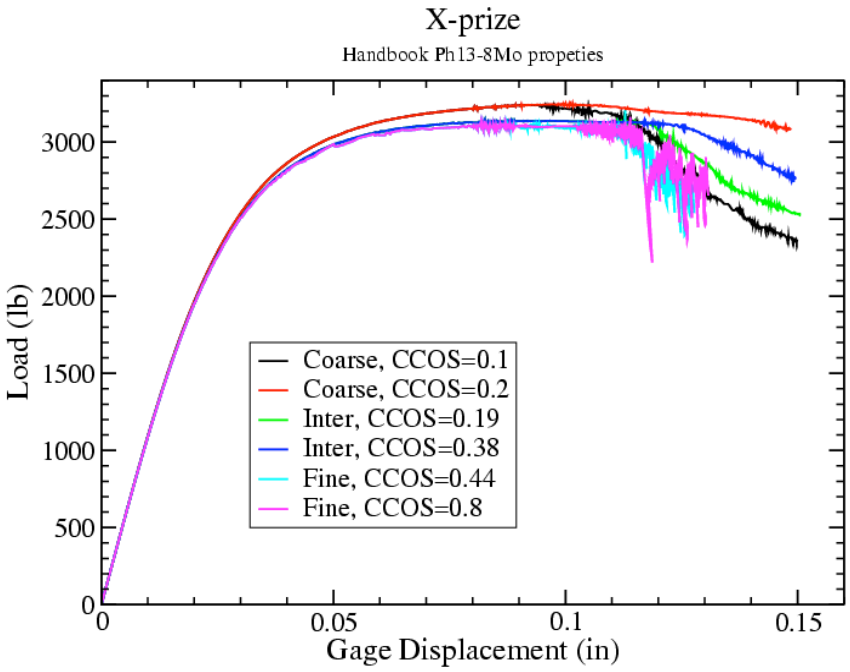

Figure A39. Load versus Displacement curves for Test-3 Ph13-8Mo.

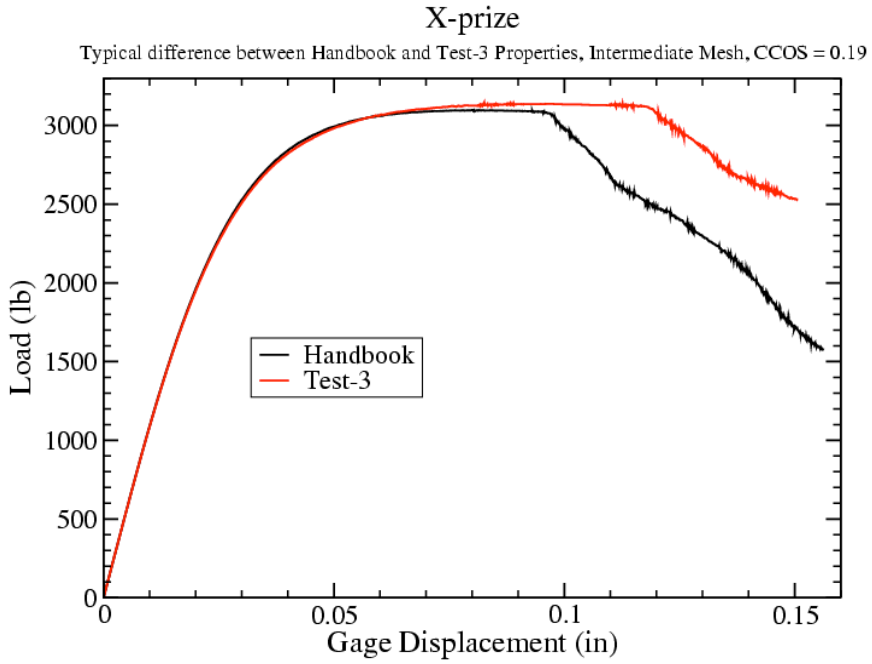

Figure A40. Typical difference between handbook and SNL test-3 results.

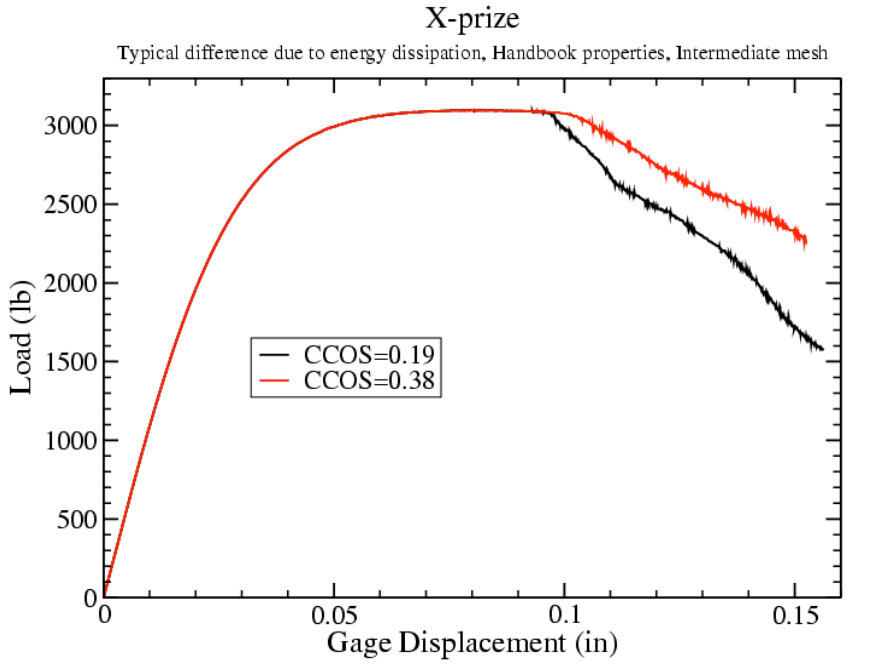

Figure A41. Typical difference resulting from varying the critical crack opening strain (energy dissipation) term.

A2.4 MLEPF with selective deviatoric elements

Three meshes were used with the selective deviatoric element formulation. The meshes were progressively refined and structured in an annular region near the stress concentrator. The finite element models using the SD elements used all the same symmetry and boundary conditions employed with the UG elements. For each mesh, the elements on the surface of the keyhole had aspect ratios of 1.0. The element size on the key hole was 0.0104 inch, 0.0044 inch, and 0.0024 inch for the coarse, medium and fine meshes, respectively. There were 3,392 elements, 23,112 elements, and 125,184 elements for the coarse, medium and fine meshes, respectively. The three meshes are shown in Figure A42.

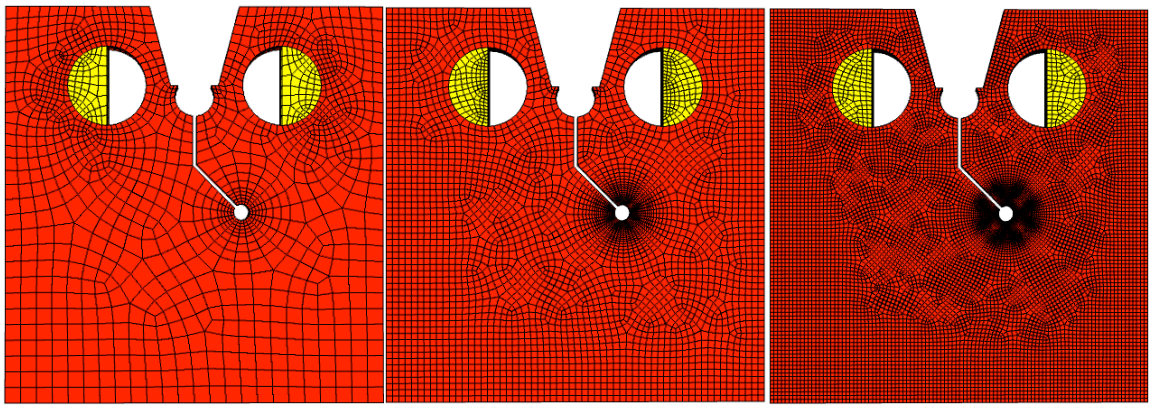

Figure A42. Three structured meshes used with selective deviatoric elements.

The SD element formulation uses full 8-point quadrature for the linear hexahedral elements. Consequently, meshes with SD elements are three to four times slower than with under-integrated UG elements. Further, the small element size in the medium and fine meshes in combination with the nature of the problem require very small load steps. As a result, the crack initiation results reported here, in Table A4, are for the coarsest mesh; results for the medium and fine mesh are pending successful completion of the analyses. However, the load versus clip gage curves reported do included results from the finer meshes and, by nature of their tending towards convergence, suggest that the coarsest mesh is inadequate.

Table A4. Surface tear predictions for the selective deviatoric elements.

Mesh	Material	CCOS	Start Displ. (inch)	Start Load (lb)	Comp. Displ. (inch)	Comp Load (lb)	Fail Elem. No.	Fail Loc
Coarse	Hdbk	0.1	0.1277	2546	0.1325	2440	2859	5:00
Coarse*	Hdbk	0.22	n.a.	n.a.	n.a.	n.a.	n.a.	n.a.
Coarse	Test-3	0.1	0.1616	2604	0.1690	2466	2860	5:00
Coarse	Test-3	0.22	0.1801	2590	0.1970	2404	2860	5:00

* unable to obtain a converged result.

Figure A43 and Figure A44 plot the applied load versus clip gage displacement for the handbook and test-3 results, respectively. Clearly, the finer meshes are required for a converged solution. In general, the solution with the quasi-static solver is difficult to obtain once the system begins to shed load. This is likely do to ill conditioning in the global tangent stiffness. The MLEPF model is applied per gauss point, which further complicates the analyses for elements with 8-quadrature points. Analyses with smaller time stepping were unable to obtain convergence. Further exploration as to how to fail elements with multiple quadrature points is necessary.

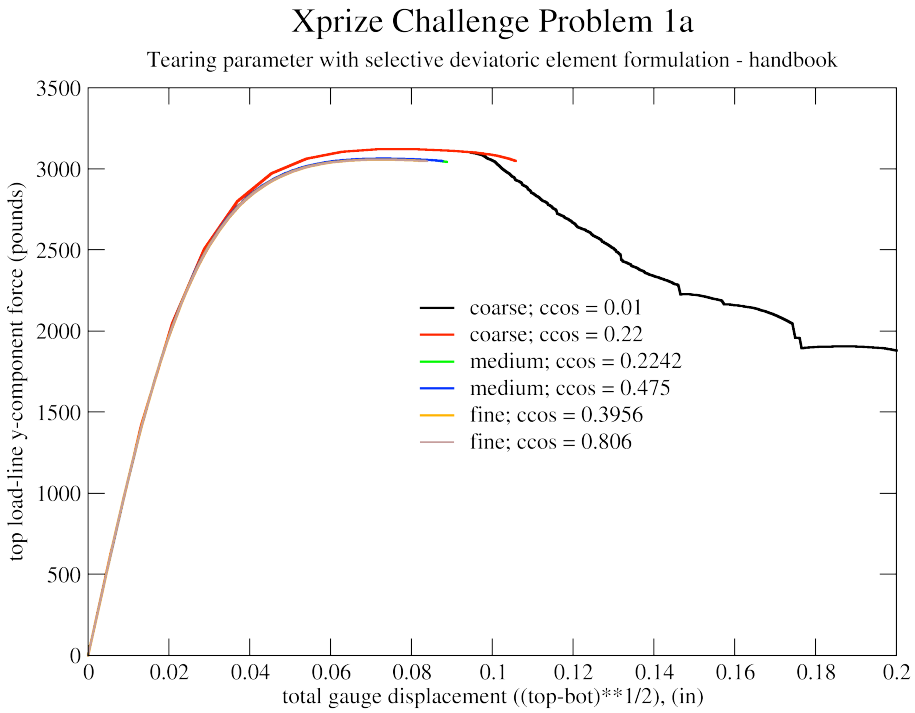

Figure A43. Load versus Displacement curves for the handbook data and selective deviatoric elements.

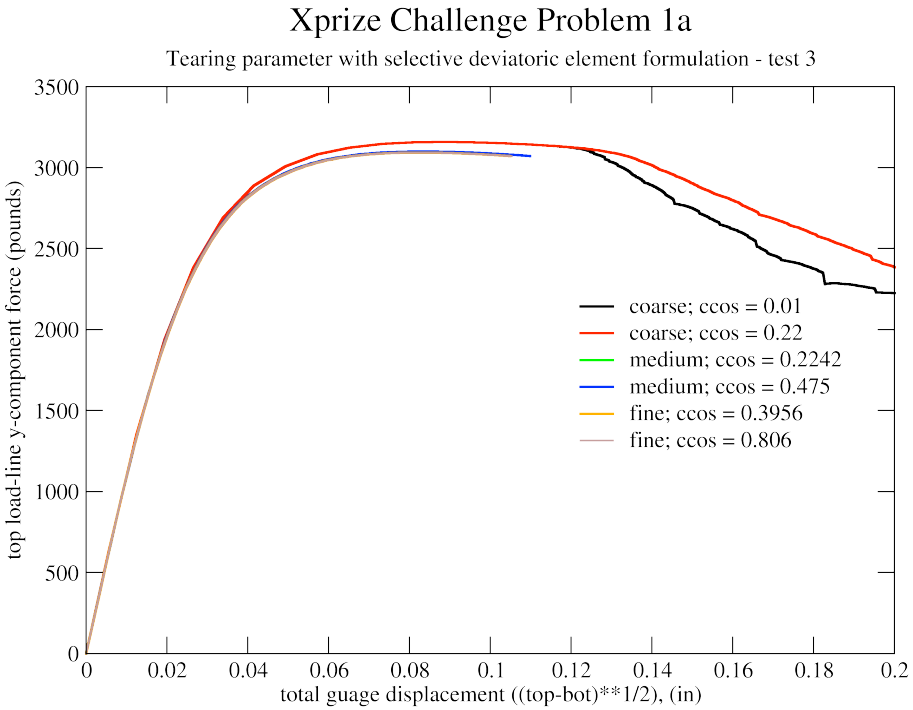

Figure A44. Load versus Displacement curves for the test-3 data and selective deviatoric elements.

Figure A45 compares the coarse mesh to the fine mesh and plots the extent of plasticity at an applied displacement of +/- 0.05 inch (*i.e.* prior to crack nucleation on the surface). Clearly, the fine mesh provides higher resolution of the plasticity at the keyhole.

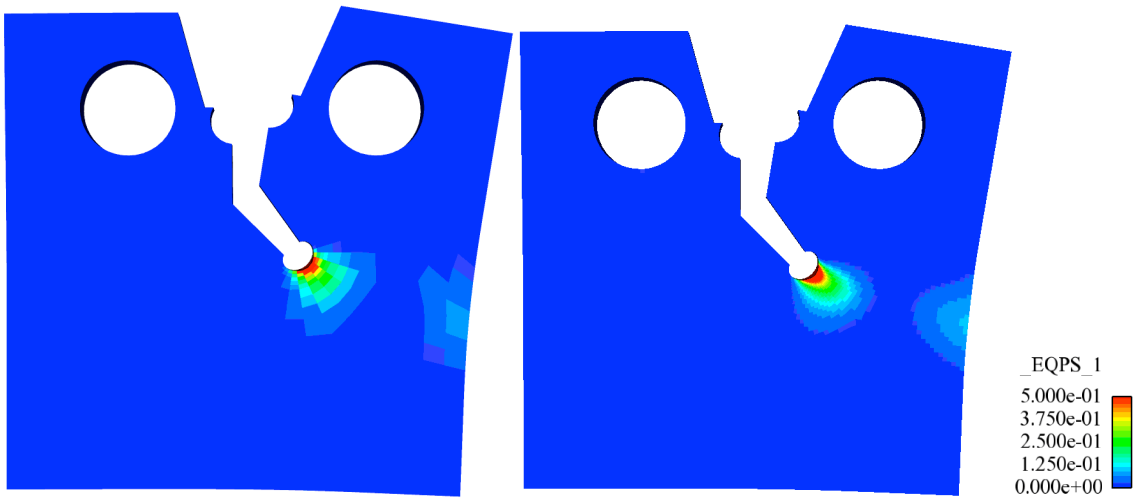

Figure A45. Plasticity in the specimen with coarse and fine meshes and selective deviatoric elements.

5. Computational Efficiency. Estimate the node-hours and processor speed used to run one solution to the problem. Report a range if necessary, for example if you used different mesh sizes, report the time for each of the mesh sizes.

Table A5 presents the data regarding computational efficiency. The time is not reported for the analyses using the selective deviatoric element formulation with the medium and fine meshes because no converged solution was achieved after peak loading.

Table A5. Computational Efficiency on TLCC Glory.

Element formulation	Mesh	# of elems	# of procs	Wall Time (hr)	Node-hours
UG	Coarse	9,552	16	13-20	208-320
UG	Medium	66,992	16	67-77	1072-1232
UG	Fine	433,584	64	192	12288
SD*	Coarse	3,392	2	0.63	1.27

* run on the standard Linux desktop (4 cores @ 3.0GHz, 4GB RAM),

6. What force (or range of forces) is predicted at a load line displacement of 0.01 in? 0.02 in? 0.03 in? 0.04 in?

Force and gage opening pairs are tabulated for the requested openings in Table A6 and Table A7 for the calculations with the uniform-gradient formulation and the selective deviatoric formulation, respectively. For clarity, Figure A46 provides an illustration of the gage displacement reported. In the figure, the locations where gage displacements are measured are indicated as "gage attachments". In the undeformed, as-manufactured configuration, the gage opening measures "h", see figure inset. As deformation is applied, the gage attachment points will deform with an x- and y-component, indicated as "dx" and "dy" in the figure. Table A6 and Table A7 report the total displacement as

$$\delta = \sqrt{dx^2 + dy^2} \ . \qquad (3)$$

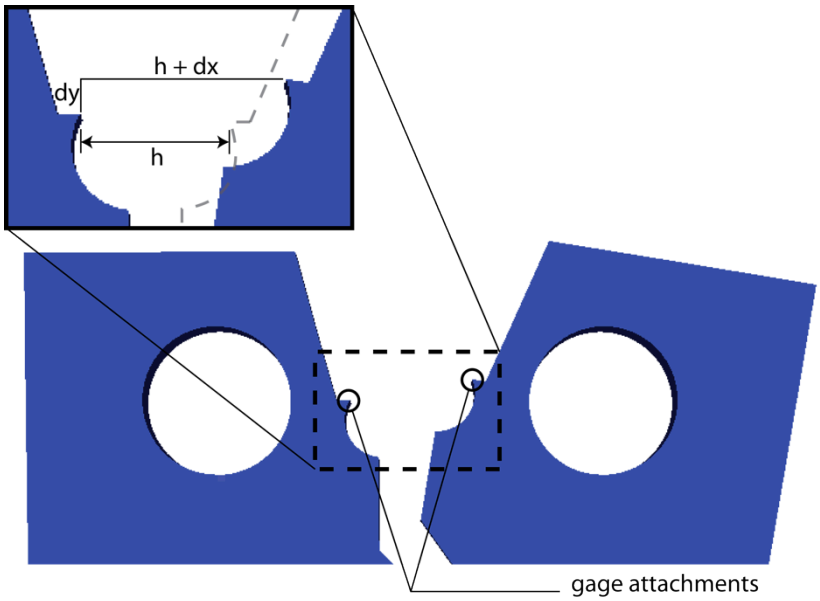

Figure A46. Illustration of gage displacement calculation.

Table A6. Force (lb) versus gage displacement (in.) with uniform-gradient formulation.

Element	Mesh	Material	Force (lb) at gage displacement δ (in.)			
			δ = 0.01	δ = 0.02	δ = 0.03	δ = 0.04
Uniform Gradient	Medium	Handbook	1090	1961	2528	2841
Uniform Gradient	Medium	Test 3	1087	1951	2509	2822
Uniform Gradient	Fine	Handbook	1089	1956	2523	2829
Uniform Gradient	Fine	Test 3	1087	1950	2508	2816
Minimum			1087	1950	2508	2816
Maximum			1090	1961	2528	2841
Mean			1088	1955	2517	2827

For the calculations with the selective deviatoric element formulation, the force corresponding to a given gage displacement for the medium versus the fine mesh was virtually indistinguishable. Consequently, Table 5 reports only one set of forces for each material data set.

Table A7. Force (lb) versus gage displacement (in.) with selective deviatoric formulation.

Element	Material	Force (lb) at gage displacement δ (in.)			
		δ = 0.01	δ = 0.02	δ = 0.03	δ = 0.04
Selective Deviatoric	Handbook	1096	1966	2527	2833
Selective Deviatoric	Test 3	1092	1954	2511	2818

7. Describe the strengths and weaknesses of your approach.

A major strength of this approach is that the analyst does not need to guess the crack direction to build the model. Meshing techniques typically used for nonlinear analyses may be employed.

A strength of this analysis approach is that a modest number of parameters are required. Five scalar parameters and one function are required to characterize the material. All materials properties, except the critical crack opening strain, are available from a simple tension test.

A weakness is mesh line dependencies exist with this approach because a crack path is constrained to follow a series of adjacent hex elements. Different mesh topologies will produce different crack paths. This effect is reduced but never eliminated by mesh refinement.

A weakness in the use of uniform gradient elements is the presence of zero energy, or hourglass, modes of deformation. Hourglass control forces are used to resist the zero energy modes of deformation and stabilize the results. These hourglass forces also resist localized deformations and have been shown to negatively affect the ability to characterize ductile materials in the structural softening regime.

A weakness in the use of selective deviatoric elements is that the implementation of element death in an element with eight integration points is not well understood. An additional parameter, "kill when _ integration points remain", is required. For these calculations the element was killed when six integration points remain.

A weakness is that an analyst will often not have enough data to calculate the correct critical crack opening strain for a given material and mesh size. A topic of active research is to improve the method of determining the critical crack opening strain for various materials and mesh sizes. Uncertainty in critical crack opening strain will create some error in the analyses of this challenge assignment and is expected to generate larger error in problems with more significant crack propagation.

Another limitation is that it is difficult to predict when the crack becomes visible on the surface of the specimen. The method assumes that no significant voids or cracks are present in a hex element before the critical tearing parameter is reached, and that the element can carry no load after the critical crack opening strain is reached. The crack is assumed to be visible on the surface after the surface element reaches critical tearing parameter and before the element reaches the critical crack opening strain. The challenge assignment is to predict when the crack is between 0.00394 in. (0.1 mm) and 0.0197 in. (0.5 mm) in length on the free surface of the specimen. Based on the uniform gradient meshes, this range of lengths is 39% to 197% of the coarse mesh size, 79% to 394% of the medium mesh size, and 197% to 985% of the fine mesh size. The results reported in Table A3 and Table A4 bound the point at which the crack emerges in the first surface element. Further post-processing of analysis results would be required to determine the load and displacement at the specified surface crack lengths of 0.00394 inch and 0.0197 inch.

A2.5 Wrap-Up Questions

Q1. What was the % difference of your predictions to the experimental values (max force prior to crack initiation and COD displacement at crack initiation)?

The predictions of maximum force prior to crack initiation and crack opening displacement at crack initiation from the Uniform Gradient element are shown in Table A8. Three mesh sizes, two material property sets, and two values of critical crack opening strain were used in twelve analyses. The start crack opening displacement (COD) is measured at the time at which an element on the specimen free surface first reaches the failure criterion (tearing parameter). The complete crack opening displacement is measured at the time at which the stress in that element has been decayed to zero. There is some ambiguity in the definition of failure between these two points in time, so both the start and the complete COD are reported.

Table A8. Analysis Results Using Uniform Gradient Elements

Mesh	Material	CCOS	Max. Load (kN)	Start COD (mm)	Complete COD (mm)
Coarse	Hdbk	0.1	14.18	2.431	2.494
Coarse	Hdbk	0.2	14.2	2.840	3.035
Coarse	Test-3	0.1	14.41	2.832	2.997
Coarse	Test-3	0.2	14.43	3.348	3.772
Inter	Hdbk	0.19	13.77	2.753	2.822
Inter	Hdbk	0.38	13.77	2.982	3.233
Inter	Test-3	0.19	13.95	3.320	3.452
Inter	Test-3	0.38	13.95	3.612	3.800
Fine	Hdbk	0.44	13.67	2.771	2.969
Fine	Hdbk	0.8	13.7	3.015	3.459
Fine	Test-3	0.44	13.8	3.294	3.449
Fine	Test-3	0.8	13.8	3.498	3.990

Table A9 shows the comparison of the results from the twelve uniform gradient element analyses to the results from the experiments from both laboratories.

Table A9. Comparison between Analysis Results Using Uniform Gradient Elements and Experimental Results

		Analysis	Experiment	% Difference
Max. Load (kN)	Mean	13.969	13.955	0.10
	Std Dev	0.270	0.161	
COD (mm)	Mean	3.174	2.960	7.22
	Std Dev	0.411	0.091	

The results of the analyses using the selective deviatoric element integration are summarized in Table A10. As has been previously discussed, the unstable nature of this crack geometry gave rise to significant numerical difficulty when the crack began to propagate. Hence, the gage openings at crack initiation are not captured for all mesh densities. Table A11 presents the statistics of the maximum load prediction. Unlike Table A9, the gage opening is not included in Table A11 because there are too few results to provide meaningful statistics.

Table A10. Summary of results from analyses using selective deviatoric element integration

Mesh	Material	CCOS	Max. Load (kN)	Start COD (mm)	Complete COD (mm)
Coarse	Hdbk	0.1	13.88	3.244	3.366
Coarse	Hdbk	0.22	13.88	2.619	n.a.*
Coarse	Test-3	0.1	14.05	4.105	4.293
Coarse	Test-3	0.22	14.05	4.575	5.004
Intermediate	Hdbk	0.22	13.63	n.a.	n.a.
Intermediate	Hdbk	0.48	13.63	n.a.	n.a.
Intermediate	Test-3	0.22	13.78	n.a.	n.a.
Inter	Test-3	0.48	13.78	n.a.	n.a.
Fine	Hdbk	0.4	13.59	n.a.	n.a.
Fine	Hdbk	0.81	13.59	n.a.	n.a.
Fine	Test-3	0.4	13.75	n.a.	n.a.
Fine	Test-3	0.81	13.75	n.a.	n.a.

*n.a. = not available

Table A11. Statistics of results from analyses using selective deviatoric element integration

		Analysis	Experiment	% Difference
Max. Load (kN)	Mean	13.78	13.955	1.25
	Std Dev	0.16	0.161	

Q2. If you (or your team) submitted revised predictions, either after the initial due date, or after the comparison between modeling results, did your revisions bring the prediction closer to the experimental values?

The team made an error in reports prior to April 15th, 2010 and mistakenly reported the force at crack initiation rather than the maximum force prior to crack initiation. For the intermediate and fine mesh sizes, the force at crack initiation on the surface is between 12% and 30% smaller than the maximum force. Reporting the correct quantity reduced our error from over 20% to less than 1%.

Q3. Describe the source(s) of discrepancy (if any) between your prediction and the experimental result. Where possible, provide quantitative estimates of how much your prediction might have improved if these sources were incorporated into the prediction. Discuss the ease or difficulty in incorporating such improvements in future work.

Figure A47– Figure A49 show that the analyses results are close to the experimental values on average and have a larger variation. The spread in the analyses results was due to three factors: 1) variation in the strain hardening behavior of the material from multiple tests; 2) the definition of crack nucleation; and, 3) limited data from which to appropriately choose the energy dissipation term (the critical crack opening strain). As discussed in previous reports, there were several sets of stress/strain data available. The results reported here summarize the findings using upper and lower bounds from the available material data. For the xPrize Challenge Problem 1a, crack nucleation was specifically defined as a visible surface crack between 100 and 500 microns in length. Crack initiation in our model is defined and reported for both the onset of stress decay at the free surface and for when the stress has been fully decayed to zero at the free surface. Finally, determining the appropriate value for the energy dissipation term *independent of element size* is an area of ongoing research. Data from a stable crack growth experiment can, and has successfully been, used to determine the energy dissipation term for a set element size; however, no such data was available for this PH13-8Mo H950. Thus, best-guess estimates for the parameter, as well as its variation for element size, were used for this project.

Figure A50– Figure A52 show selected results from the analyses using the selective deviatoric element integration formulation. The predictions for maximum load prior to cracking are very accurate. The results for gage opening displacement are less conclusive due to the lack of data for the medium and fine meshes.

A sample of this material was tested according to ASTM E8 by Modern Industries, Inc. in April 2010, and the results indicate that this material is approximated fairly well by the handbook test data. The external lab data measured a tensile strength of 225.85 ksi. The handbook data, which was used as the lower bound for stress, had a tensile strength of 228.30, which is 1.1% higher. SNL-Test 3, which was used as the upper bound for stress, had a tensile strength of 229.81 ksi, which is 1.75% higher. The handbook data gives predictions which are closer to the X-Prize results. This external lab did not record the full range engineering stress-engineering strain data, so a Cauchy stress-logarithmic strain curve could not be determined. Since the handbook properties seem to work well, further testing is not required.

Comparison of the analyses to the X-Prize results indicates that the most accurate analyses were run on intermediate and fine meshes with the handbook material properties. The estimated nominal value of critical crack opening strain bounds the experimental minimum crack opening displacement while the estimated maximum value of critical crack opening strain bounds the experimental maximum. These four analyses are compared to the experimental data in Table A12.

The handbook data is the only material property data generated using the recommended 2 inch long extensometer on a 0.5 inch diameter round bar specimen. The SNL tests used a 1 inch extensometer and there is some risk that this did not capture the entire necked region

of the tension specimen and introduced some error in the Cauchy stress-logarithmic strain curve.

Table A12. Comparison between Experimental Results and Analysis Results Using Uniform Gradient Elements with only Handbook Properties on Intermediate and Fine Meshes

		Analysis	Experiment	% Difference
Max. Load (kN)	Mean	13.728	13.955	-1.63
	Std Dev	0.051	0.161	
COD (mm)	Mean	3.001	2.960	1.38
	Std Dev	0.243	0.091	

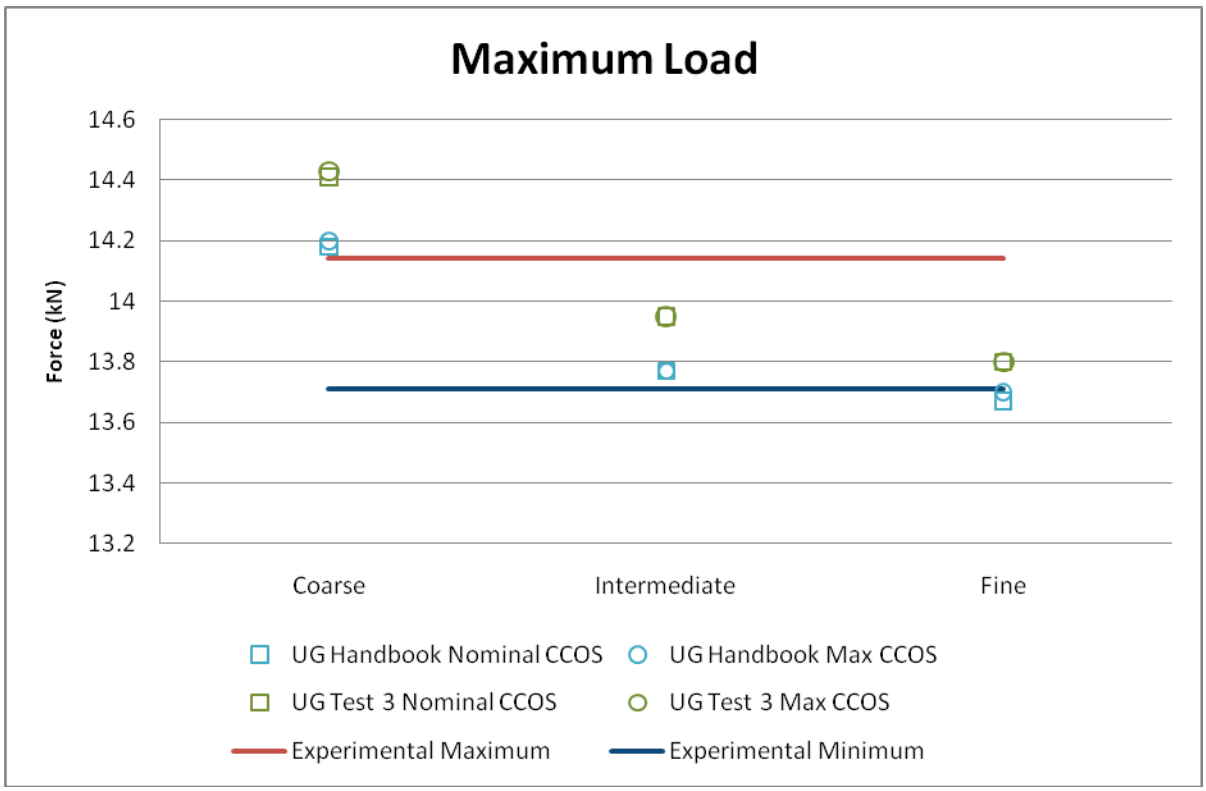

Figure A47. Maximum Load Prior to Crack

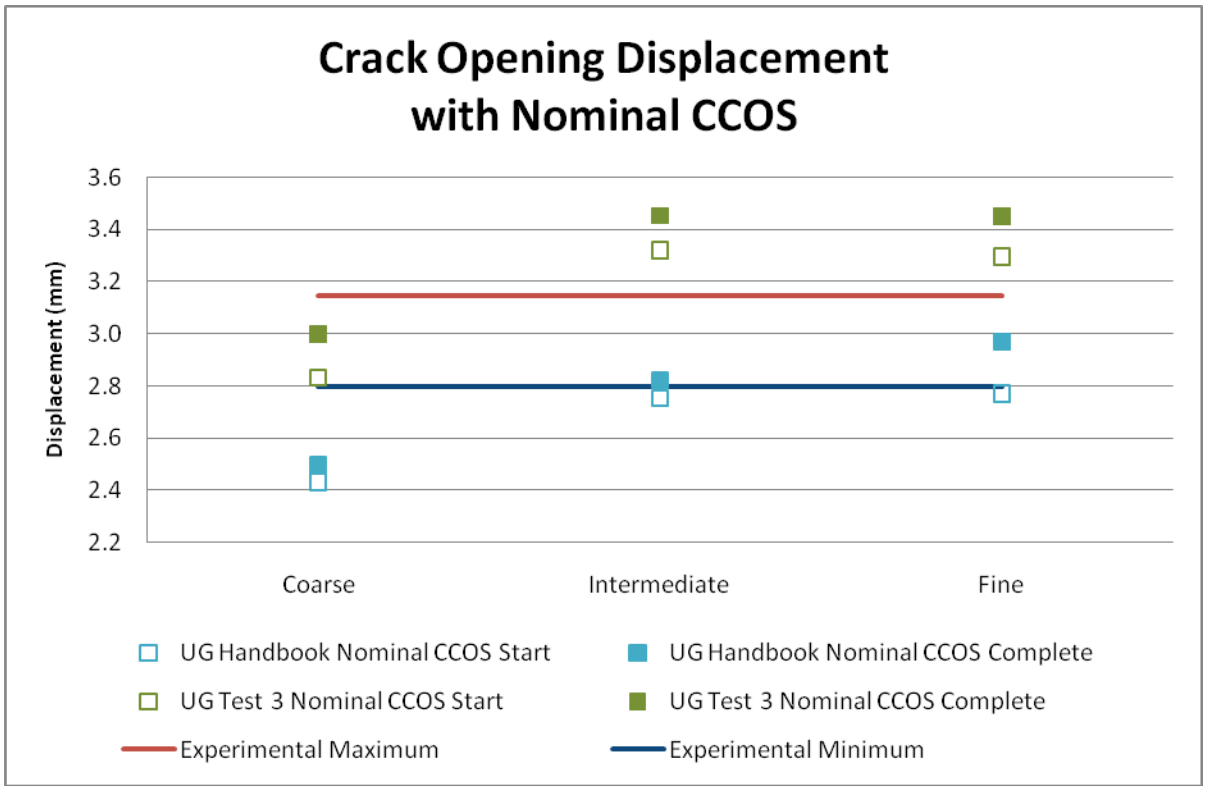

Figure A48. Crack Opening Displacement at Crack Initiation Using Uniform Gradient Elements with a Nominal Value of Critical Crack Opening Strain

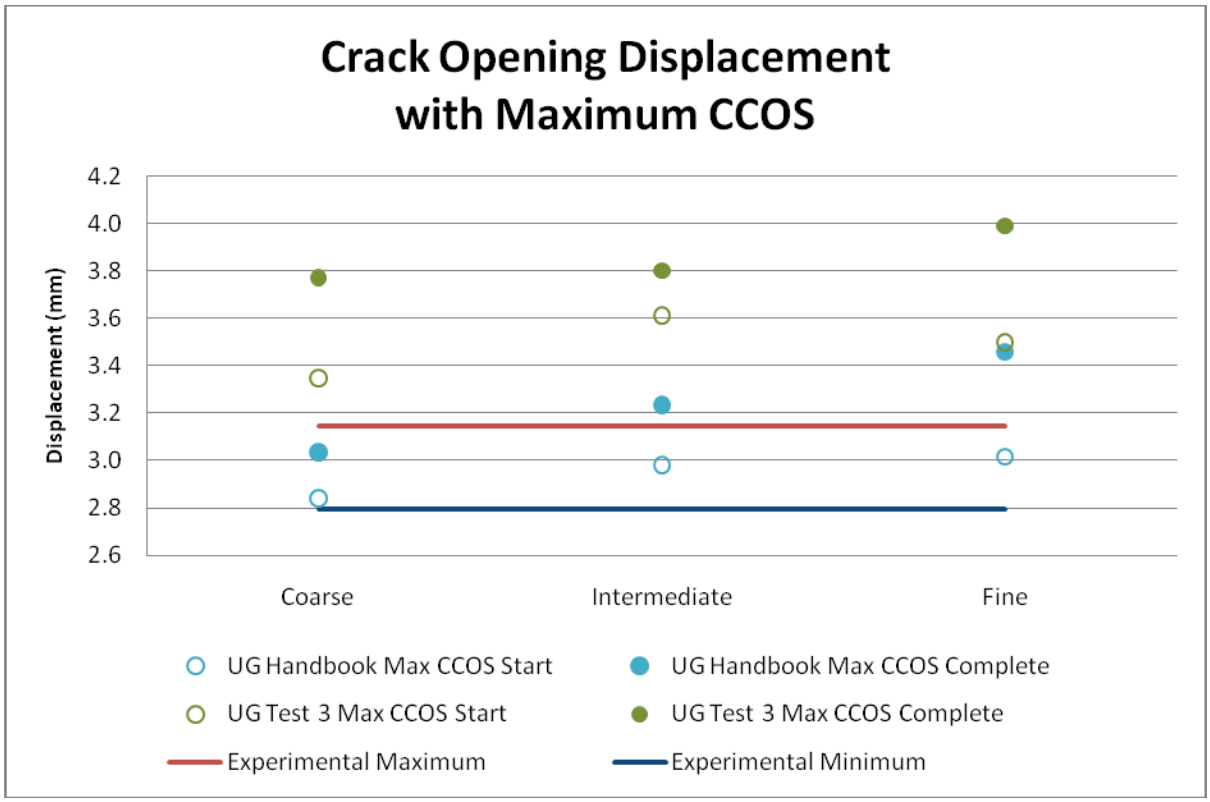

Figure A49. Crack Opening Displacement at Crack Initiation Using Uniform Gradient Elements with a Maximum Value of Critical Crack Opening Strain

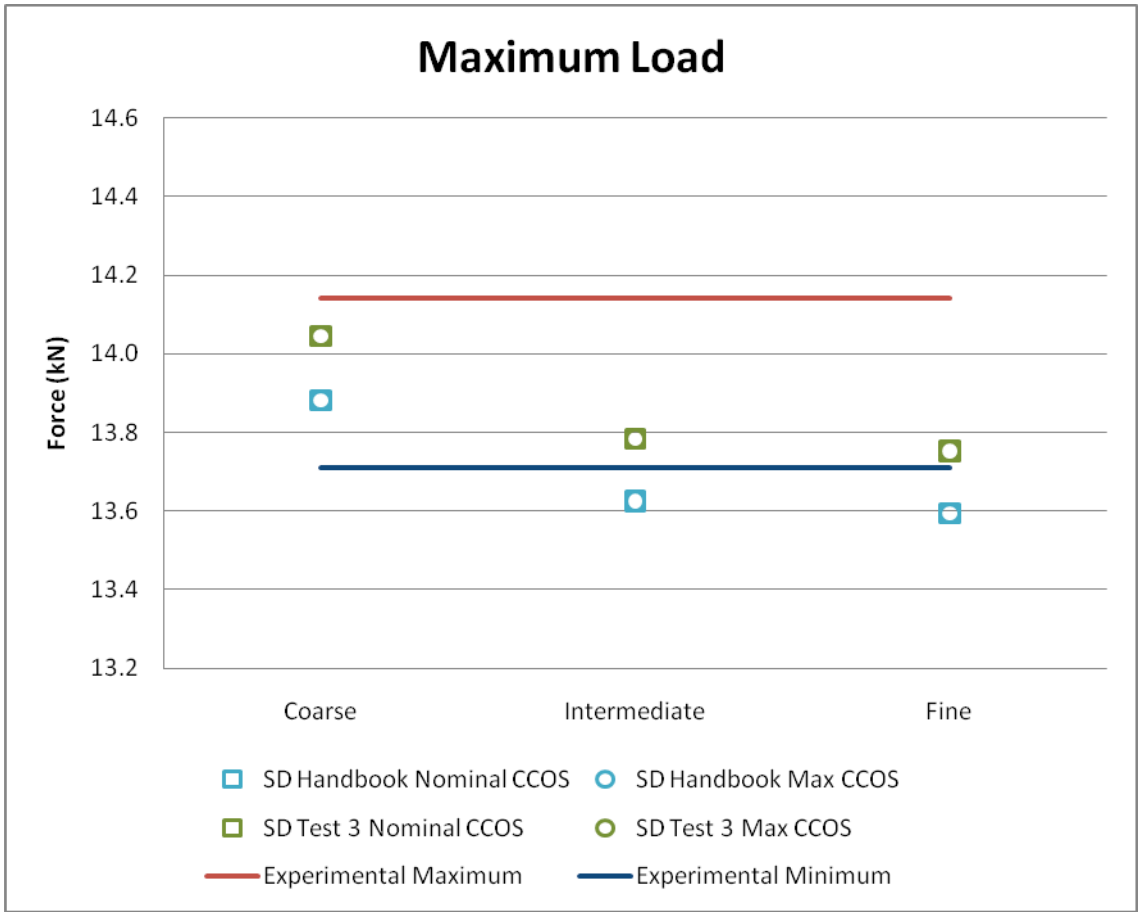

Figure A50. Predicted maximum load from analyses using selective deviatoric element integration.

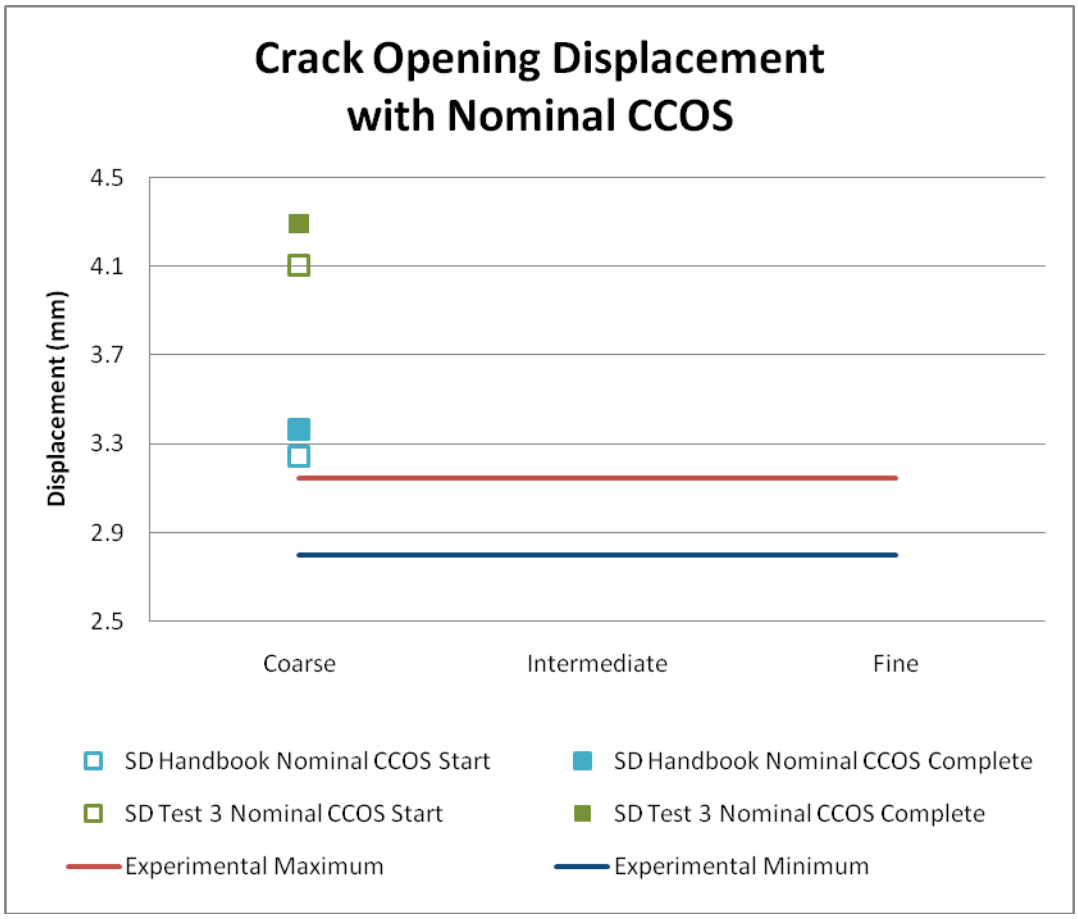

Figure A51. Predicted gage opening displacement from analyses using selective deviatoric element integration with nominal energy dissipation.

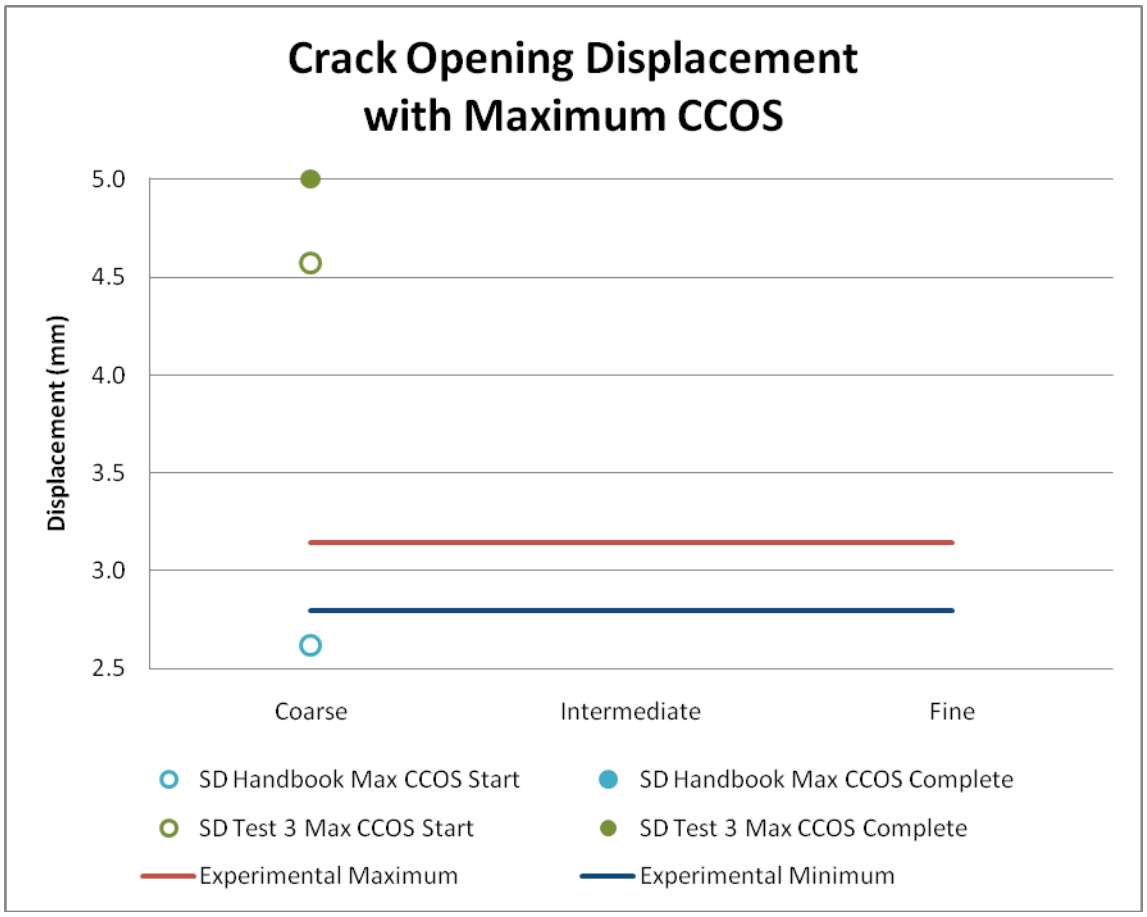

Figure A52. Predicted gage opening displacement from analyses using selective deviatoric element integration with maximum energy dissipation.

Q4. Was this effort helpful for the development and evaluation of your modeling paradigm? How might we improve the challenges in the future?

This effort provided an excellent source of validation data. For the "tearing parameter" approach, crack propagation is the area most in need of further development. The lack of slow stable crack propagation in the current geometry, material system did not provide data of use to the investigation of slow stable crack propagation. For optimum use in development of the "tearing parameter" approach, a more ductile material and/or test geometry would provide a greater development value.

A3. Predictions For Challenge 1B

Executive Summary

There are a total of 10 finite element results report herein. There are three mesh densities, two material properties descriptions (primary difference is the strain hardening), and two approaches to the energy dissipation to try to achieve element size independence. Because the intent of challenge 1-b was investigate crack propagation, the selective deviatoric (SD) element formulation was not included. The SD element requires further development for stability in a material softening regime such as that produced during stress decay utilized with the tearing parameter approach to ductile failure. The uniform gradient (UG) element formulation was used exclusively here. For initiation, the expected gage displacement range is 0.754 – 1.212 mm. The expected maximum load range prior to cracking is 3.268 – 3.371 kN. The first scribe line intersected is line D. Intersection of line D by the crack occurs between 1.003 – 1.422 mm. displacement at a load between 0.65 – 2.45 kN.

A3.1 Introduction

The ductile failure X-Prize is a project to assess the maturity of failure modeling approaches as well as their accuracy and potential. In the following report, the general approach used to predict ductile failure initiation and propagation is the multilinear elastic-plastic with tearing parameter failure (MLEPF) model. An overview of the approach is provided. Then, the details, as they relate to the x-Prize geometry and alloy, are described, the results of these analyses are reported and discussed. In an earlier challenge, an attempt to use SD elements was conducted. The advantage of the SD elements is the lack of zero-energy modes thus eliminating the need for suppression of such modes. This has been shown to be valuable in simulations using cohesive surface elements for sharp crack propagation. However, simulating failure with SD elements is somewhat less mature than with single-point quadrature UG elements, and requires further development. For geometries with a low gradient, smooth stress concentrator, as opposed to a sharp notch or crack, the single-point quadrature UG elements were proven in challenge 1-A to resolve the plasticity and provide sufficiently accurate analysis results. At present, it is an assumption that UG elements are adequate for the stress and strain gradients associated with crack propagation.

A3.2 General details of the multilinear elasto-plastic with tearing parameter failure approach

The MLEPF approach uses a multilinear elasto-plastic constitutive model with the standard von Mises yield criterion. In this report, the multilinear hardening curve was obtained by fitting experimental data from a round-bar tensile test. Further, the MLEPF approach uses a tearing parameter as a failure criterion, which was also obtained from the round-bar tensile test data. Crack propagation is accompanied by dissipating energy (critical crack opening strain) during the element failure. The critical crack opening strain is a function of both material properties and element size. Element size independent crack propagation can be achieved by appropriately varying the critical crack opening strain with element size. The following sections describe these processes in detail.

A3.2.1 Determining the multilinear elasto-plastic curve fit from round-bar tensile data

Prediction of ductile failure is inherently a large strain, large deformation process. The Cauchy-stress, logarithmic-strain conjugates are used in the finite deformation codes at SNL. The strain hardening defined in terms of Cauchy-stress and logarithmic-strain is obtained by using a finite element model of the tensile specimen to perform the inverse problem. That is, the Cauchy-stress versus logarithmic-strain curve that gives the experimental engineering-stress versus engineering-curve as the solution to a finite element analysis of the tensile specimen is extracted. Here, the gage section of a flat tensile specimen is used. Figure A53 shows the finite element mesh. There are 3-planes of symmetry, the back, left hand side and the bottom. There are imposed displacements on the top of the specimen. The front and right hand side of the specimen are traction free. In order to force the localization and necking (geometric instability) to occur at the longitudinal mid-plane (plane of symmetry), the mesh uses a large-radius to slightly reduce (less than 0.1 per cent) the cross-sectional area at the longitudinal mid-plane. The engineering-stress versus engineering-strain result is derived from the load and displacement of finite element model and compared to the experimental results.

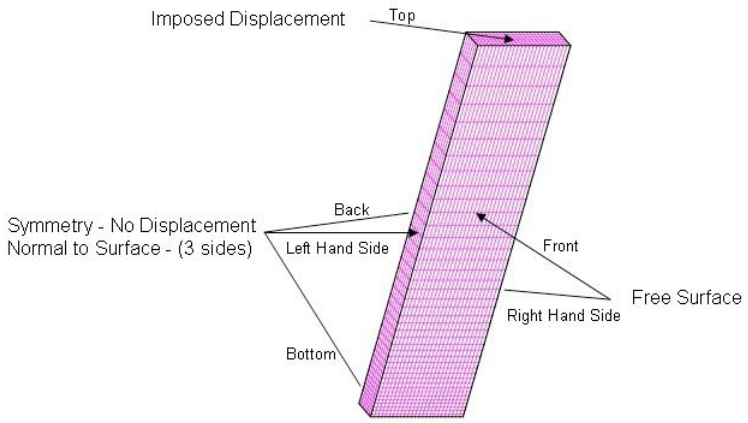

Figure A53. Model for flat specimen tensile test.

A3.2.2 Determining the critical tearing parameter

The tearing parameter accounts for the stress triaxiality at the crack tip by integrating a measure of triaxiality over the equivalent plastic strain. The tearing parameter is given by

$$T = \int_0^{\bar{\varepsilon}_f} \left\langle \frac{2\sigma_T}{3(\sigma_T - \sigma_m)} \right\rangle^4 d\bar{\varepsilon} \qquad (1)$$

where $\bar{\varepsilon}$ is the equivalent plastic strain, $\overline{\varepsilon_f}$ is the final equivalent plastic strain, σ_T is the maximum tensile stress, σ_m is the mean stress and the notation $\langle \bullet \rangle$ represents the standard Macaulay Bracket. One can note that for uniaxial loading, the term inside the Macaulay Brackets becomes unity and the tearing parameter is equivalent to using a limiting plastic strain for a crack growth criterion.

A critical value of the tearing parameter is chosen by integrating equation (1) for all elements of the tensile test simulation and picking the maximum value of the tearing parameter at the maximum displacement (maximum engineering strain) achieved in the actual tensile test.

There are mesh sensitivities, particularly for coarse meshes, in this entire material property fitting process. It is assumed that these mesh sensitivities are minimized for sufficient geometric resolution to adequately capture the size and shape of the necked region. For highly ductile materials, such resolution probably requires insight into the initial aspect ratio of the elements that will be in the necked region or remeshing. In the model used here (shown above), the elements at the bottom corners of the specimen were roughly 0.01 inch with aspect ratios close to 1 to 1 to 1. This was deemed adequate for the low ductility of 2024-T3 aluminum which exhibits minimal necking behavior.

A3.2.3 Determining the appropriate energy dissipation term

In theory, the energy dissipation term, the critical crack opening strain, can be determined from a second physical test. The optimum form of this second test is open to discussion. The critical crack opening strain is expected to be a function of material properties as well as specimen size. A theoretical relationship can be established between element size and the value of critical crack opening strain to provide an element size independent simulation of crack extension. However, this relationship does not address the material properties effects. This relationship also requires several assumptions of questionable accuracy. Both this relationship and an empirical relationship based on a series of solutions to one form of a second test are used here. The starting point (the critical crack opening strain for the coarsest mesh) was based on this empirical relationship.

A3.3 Specific details of the approach for challenge 1-B

For challenge 1-B, a heat treatable aluminum alloy, 2024-T3, was chosen. The details of the material description are discussed below. Because the intent of challenge 1-B was crack propagation, prior experience dictated the use of the single-point-integrated, uniform-strain, 8-noded hexahedral element, uniform-gradient (UG) element, with hour glass suppression. The tearing parameter approach is more mature using this element than with available higher order elements

In addition, there were multiple levels of mesh refinement studied with each element formulation. With the UG elements, three unstructured meshes were used with average element size of 0.01 inch, 0.005 inch, and 0.002 inch in the region of crack nucleation and propagation. The following presents the material data used and the fits for both element formulations.

A3.3.1 Material data

There were little full stress-strain data available for this alloy in a suitable product form. The primary source of data selected was clad sheet material [1]. The cladding was quite thin (2.5% of the total thickness) and not expected to contribute significantly to the strain hardening behavior of the specimen. Yield, ultimate and elongation values from tensile testing on this particular plate of material (not the full stress-strain curve, were available. These values were used to adjust the stress-strain curve from the clad material. The stress-strain curve for the clad material was shifted upward by 3.5 ksi and extended horizontally by 0.07 in/in to match these reported values. Later in the challenge, full stress-strain tensile data for this material became available [2]. This curve had numerous local increases in stress (curve was lumpy). Prior to use the curve was smoothed. The engineering stress versus engineering strain curves for both sets of tensile data (modified for set 1 and smoothed for set 2) are plotted in Figure A54.

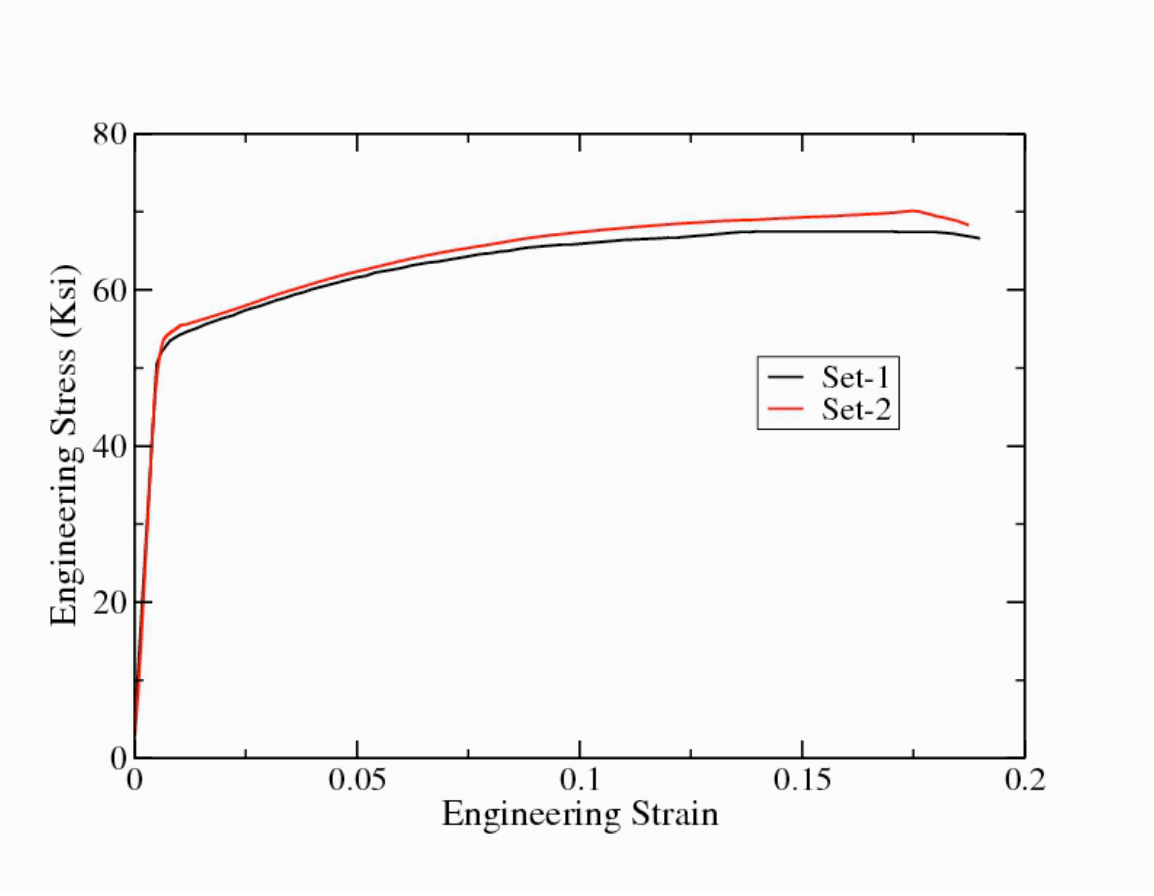

Figure A54. Engineering stress versus engineering strain curves for the 2024-T3 tensile data.

A3.3.2 Material data fit for the uniform-gradient element formulation

The Cauchy-stress, Logarithmic-strain curves resulting from the fit using the uniform-gradient element are shown in Figure A55. In order to not "run off the end of the curve" for differing stress states where the ductility could be greater then for the tensile specimen, the data has been extrapolated based on a straight line through the last two data points from the fitting process. The tearing parameters computed for these materials, 0.32 for set-1 data and 0.28 for set-2 data, are also displayed on the figure.

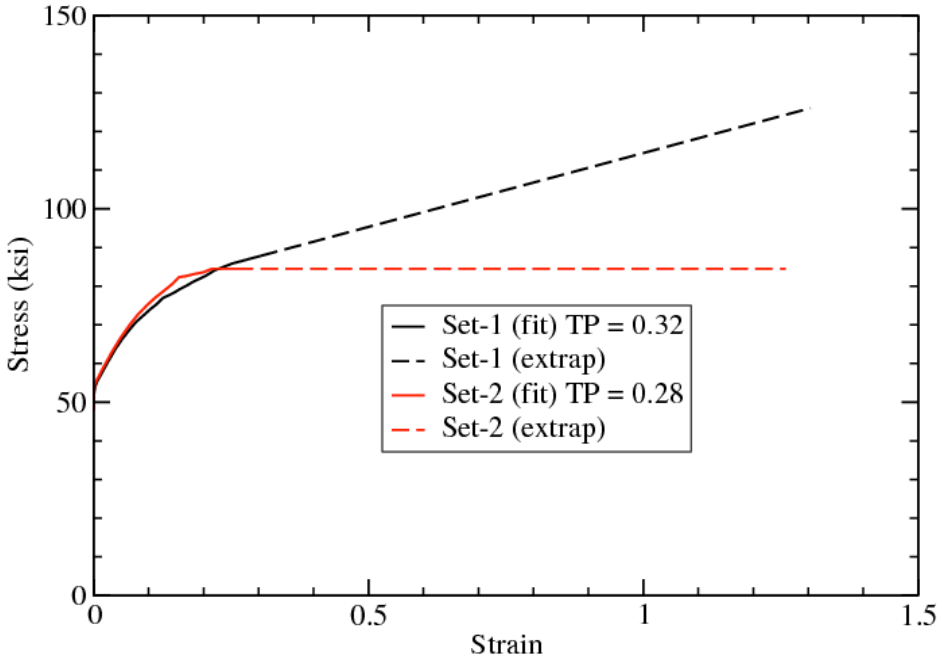

Figure A55. Hardening curves for the uniform-gradient element formulation for B024-T3 Aluminum.

A3.3.3 Critical crack opening strain (energy dissipation)

The empirical estimation scheme for the critical crack opening strain yielded a value of 0.14 for an element size of 0.01 inch for both sets of material descriptions. This same scheme results in critical crack opening strains of 0.17 for 0.005 inch element and 0.19 for 0.0025 inch elements for both material descriptions. The constant energy dissipation assumption results in critical crack opening strains of 0.26 for material set 1 and 0.27 for material set 2 for an element size of 0.005 inch. Likewise, the constant energy dissipation results in a critical crack opening strain of 0.048 for set 1 and 0.050 for set 2 for an element size of 0.0025 inch.

A3.3.4 Finite element mesh

Three semi-unstructured meshes were prepared for the analysis of the X-Prize specimen for challenge 1-B. All three meshes made use of a symmetry plane at the through-thickness center of the specimen. That is, the centerplane was constrained to provide no out-of-plane displacement while the outer surface was unconstrained appropriate to a free surface. The use of a plane-of-symmetry implies no out-of-plane displacement at the loading pins as well as no buckling of the specimen. The specimen is assumed to be thick enough that neither of these deformation modes is possible. Half the loading pins are modeled as elastic material meshed contiguously with the bulk of the specimen. The specimen is loaded via imposed displacement (displacement control) at a single node in the elastic pin. Rotation about the load point is allowed but lateral translation is prevented. The challenge 1-B specimen had grid lines scribed so that crack propagation could be described unambiguously (at least within a tolerance). Grid lines "A", "B", "C", were horizontal while grid lines "D", "E", "F", were vertical. These lines were reproduced in the finite element mesh through the use of element set boundaries. The material properties were identical across these element set boundaries. Thus the boundaries were a post-processing aid and had no effect upon the solution beyond the imposition of a set of straight line element edges. The coarsest of these meshes had near cubical elements near the keyhole of 0.01 inches. The total number of elements for the coarse mesh was 14,844. The intermediate mesh had keyhole elements of 0.005 inches for a total of 69,920 elements. The finest mesh had keyhole elements of 0.0025 inches with a total element count of 470,496. The three meshes are shown in Figure A56.

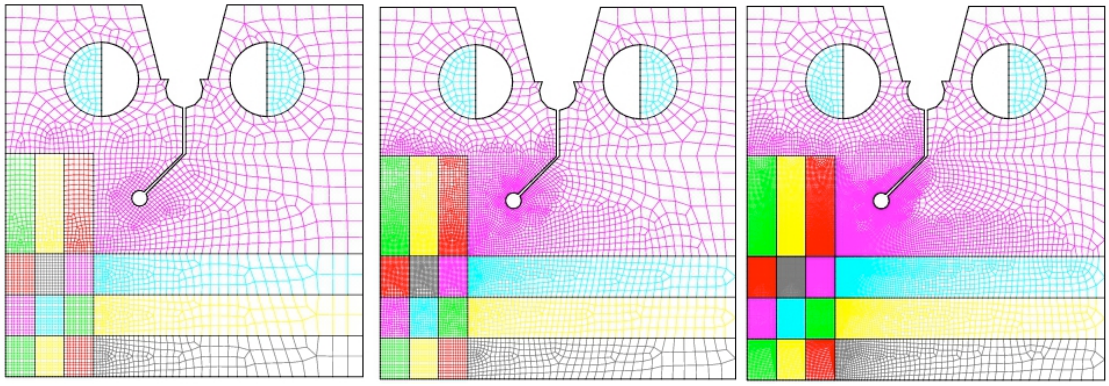

Figure A56. Coarse, intermediate and fine unstructured meshes - looking at the centerplane.

A3.4 Results

Results are presented in Table A13 for the three meshes, the two material stress-strain curves, and the two energy dissipation terms. The key for the specimen is material set #, followed by mesh #, followed by the critical crack opening strain. For example, S1-M1-P14 refers to material property set 1, Mesh-1 (the coarsest), critical crack opening displacement equal to 0.14. Peak load is the maximum load achieved during the analysis. Typically, peak load occurs prior the initiation of the failure. Displ @ initiation is the load line displacement when the failure has occurred in the first element on the surface of the specimen. Crack path refers to the intersection of the crack with the grid lines on the

specimen described in section 3.4 above. Displ or Load @ 1st intersect refers to the displacement or the load at which the crack intersects the first of the scribe lines, in all cases for these analyses, line "D" (the vertical boundary between the magenta and the red element blocks shown above). Finally, Displ or Load @ "E" refers to the displacement or load at which the crack intersects grid line "E". Here that intersection takes place along the uppermost vertical red and yellow element block boundary. There is some ambiguity in the definition of failure. The top value in Table A13 references the achievement of the tearing parameter. The lower value references the point at which the stress in the element has decayed to zero. The difference between these two values is the energy dissipation controlled by the critical crack opening strain. Note: the number of output steps (quasi-temporal discretization) also contributes to this ambiguity.

Table A13. Analysis results for Challenge 1-B

Specimen	Peak Load (kN)	Displ @ Initiation (mm)	Crack path	Displ @ 1st Intersect (mm)	Load @ 1st Intersect (kN)	Displ @ "E" (mm)	Load @ "E" (kN)
S1-M1-P14	3.307	0.800 0.925	D-E-F-?	1.435 1.514	1.49 1.19	1.656 1.727	0.93 0.78
S2-M1-P14	3.319	0.805 0.859	D-E-F-?	1.300 1.387	1.82 1.29	1.542 1.615	0.87 0.76
S1-M2-P17	3.281	0.808 0.866	D-E-F-?	1.171 1.265	2.06 1.25	1.265 1.379	1.25 0.53
S1-M2-P26	3.337	0.864 0.919	D-E-F-?	1.521 1.603	1.73 1.33	1.763 1.834	0.79 0.65
S2-M2-P17	3.274	0.754 0.813	D-E-F-?	1.130 1.252	1.68 0.69	1.252 1.336	0.69 0.41
S2-M2-P27	3.340	0.864 0.919	D-E-F-?	1.402 1.560	1.87 1.16	1.646 1.720	0.79 0.65
S1-M3-P19	3.287	0.815 0.935	D-E-F-?	1.003 1.107	2.45 1.25	1.107 1.217	1.25 0.54
S1-M3-P48	3.371	1.095 1.212	D-E-F-?	1.928 2.002	1.33 1.17	2.002 2.210	1.17 0.86
S2-M3-P19	3.268	0.876 0.937	D-E-F-?	1.029 1.146	1.67 0.65	1.029 1.146	1.67 0.65
S2-M3-P50	3.364	1.039 1.099	D-E-F-?	1.803 1.882	1.47 1.19	1.882 2.090	1.19 0.82

The results in Table A13, are reformatted in terms of best estimate along with upper and lower bounds in Table A14. This provides an easier view of average results and variances.

Table A14. Average and variation in results for Challenge 1-B

	Peak Load (kN)	Displ @ Initiation (mm)	Crack path	Displ @ 1st Intersect (mm)	Load @ 1st Intersect (kN)	Displ @ "E" (mm)	Load @ "E" (kN)

Upper Bound	1.212	3.371		2.002	2.45	2.002	1.67
Best Estimate	0.910	3.315	D-E-F-?	1.422	1.437	1.571	0.86
Lower Bound	0.754	3.268		1.003	0.66	1.029	0.41

A typical deformed shape of the challenge-1B specimen at nearly complete crack propagation is shown in Figure A57.

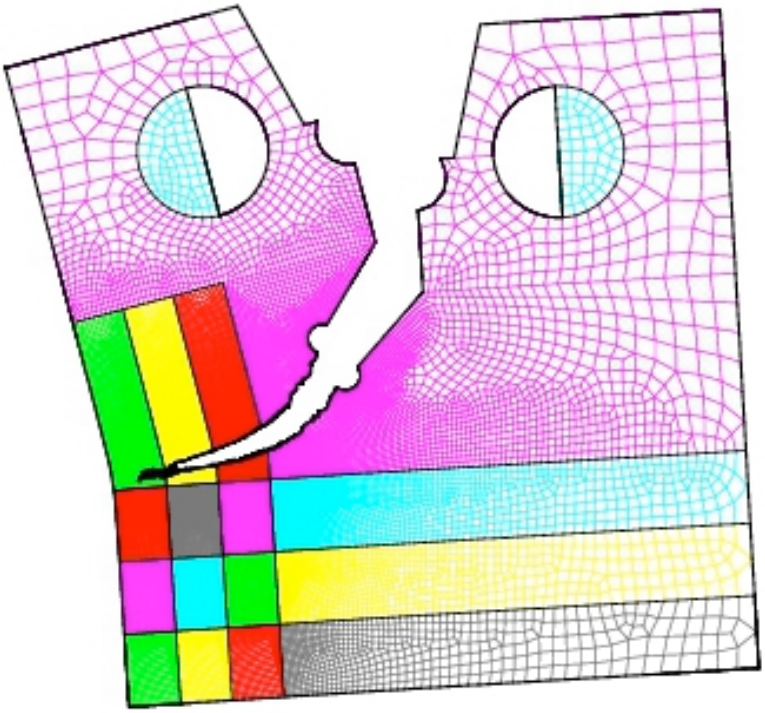

Figure A57. Deformed shape showing crack propagation.

The load versus gage-line displacement curves from the analyses are plotted in Figure A58 through Figure A61. Figure A58 shows the load versus displacement for all analyses that employed the set-1 material properties. Figure A59 shows the same results for the analyses that used the set-2 material properties. To ease the comparison between the set-1 properties and the set-2 properties, typical (intermediate mesh, critical crack opening strain = 0.17) of results are presented in Figure A60. The typical effect of the critical crack opening displacement (energy dissipation term) (set-1 material properties, intermediate mesh) is shown in Figure A61.

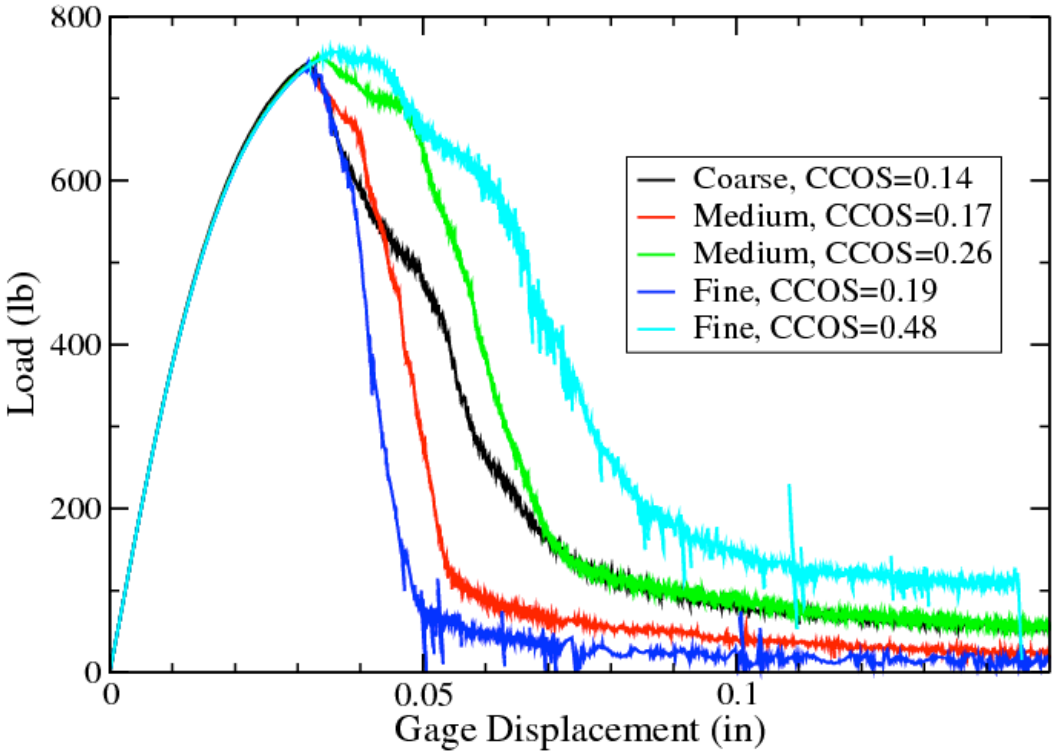

Figure A58. Load versus Displacement curves for set-1 material properties of 2024-T3Aluminum.

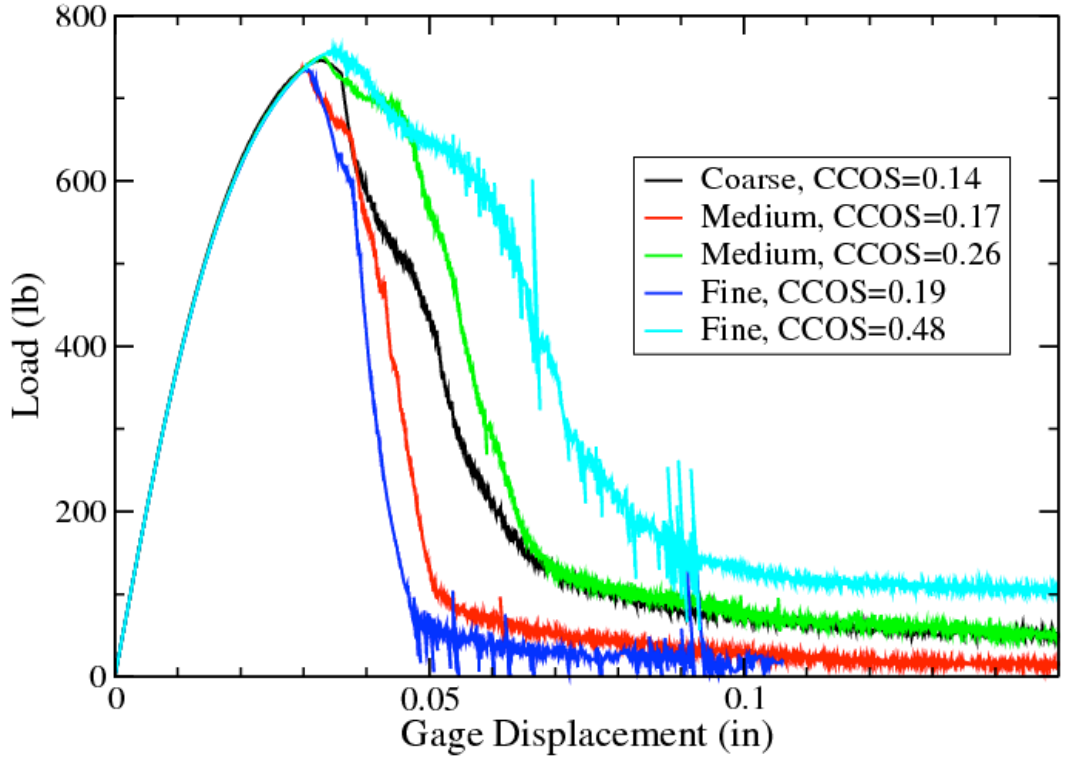

Figure A59. Load versus Displacement curves for set-2 material properties for 2024-T3 Aluminum.

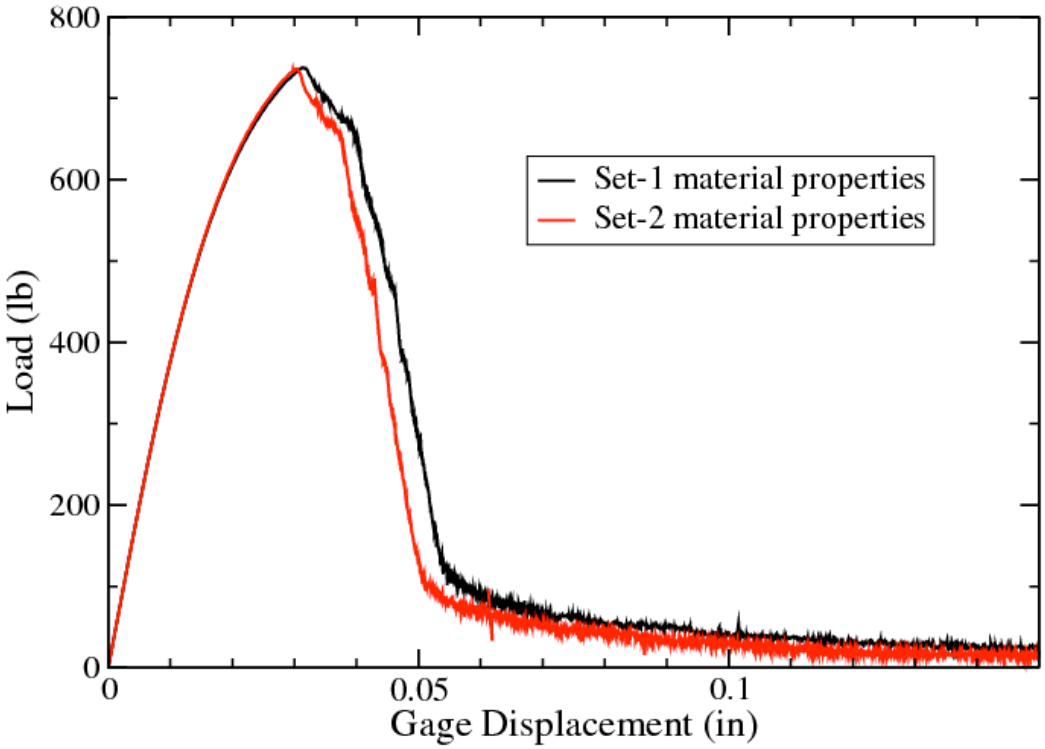

Figure A60. Typical difference between handbook and SNL test-3 results.

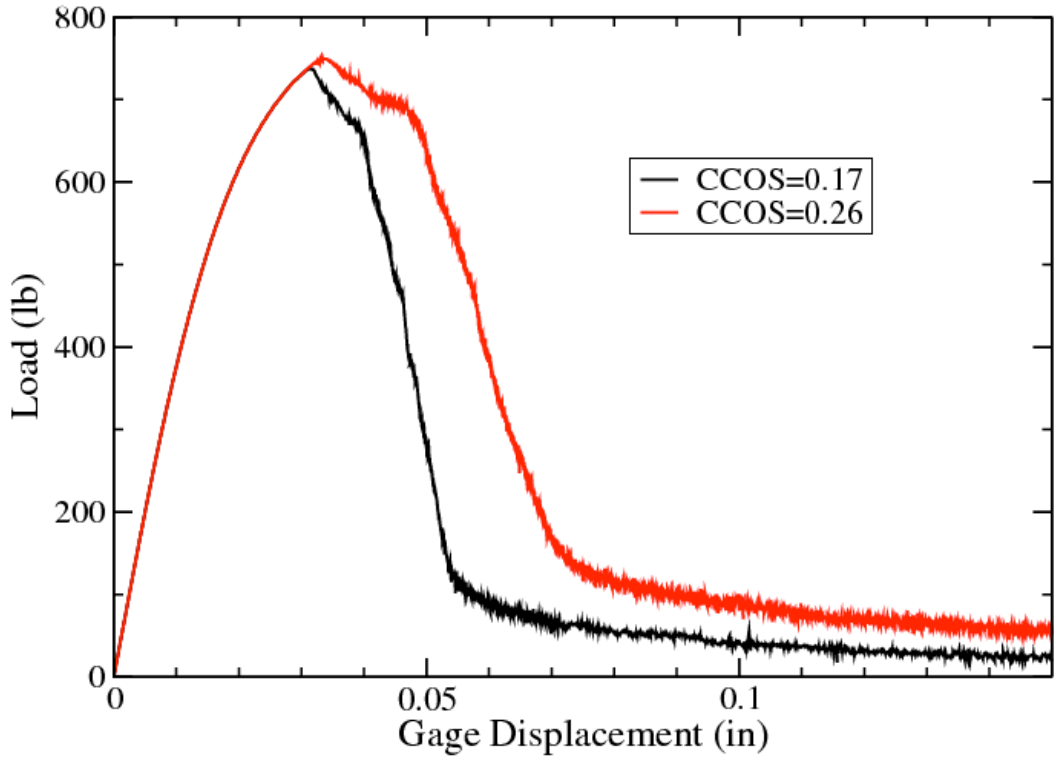

Figure A61. Typical difference resulting from varying the critical crack opening strain (energy dissipation) term.

A3.5 Discussion

In an attempt to define which parameters led to the most variation, the average values for all results with one parameter setting were subtracted from the average values for the alternate parameter setting. Table A15 shows these results.

Table A15. Variation based on a specific parameter for Challenge 1-B

	displ@ initiation (mm)	Peak Force (kN)	Displ @ 1st intersect (mm)	Load @ 1st intersect (kN)	Displ @ "E" (mm)	Load @ "E" (kN)
Step size & failure ambiguity	0.114	0	0.15	0.96	0.113	0.295
Material properties	0.027	0.0036	0.066	0.176	0.090	0.025
CCOS mesh-2	0.081	0.061	0.317	0.103	0.433	0.
CCOS mesh-3	0.221	0.090	0.832	0.215	0.921	0.0175

Row 1 shows the effect of the ambiguity in failure definition coupled with the variation caused by the load step size (quasistatic temporal discretization). This effect is quite large, easily the second largest effect seen. This variation could be mitigated by somewhat by increasing the frequency of the results output. However, increasing the quasi-temporal frequency output can lead to extremely large files and subsequent post-processing difficulties. Row 2 shows the difference caused by the two sets of materials properties. Both sets of material properties are quite similar and this is reflected in the small variation caused by this parameter. Rows 3 and 4 explore the effects of the energy dissipation term. Note: the constant energy dissipation scheme does not allow setting the energy dissipation, it just provides a scheme to adjust the value as a function of element size. The initial energy dissipation for mesh 1 was set using the empirical estimate. Therefore, there is no energy dissipation variation associated with mesh 1. The variation between the empirical estimate for critical crack opening strain and the assumption of constant strain energy dissipation is large. The values for mesh-3 are larger than those for mesh-2 because the element size difference from mesh-1 is larger for mesh-3 than for mesh-2. Neither scheme gives an element size independent result. The empirical estimate dissipates too little energy with decreasing element size while the constant energy scheme dissipates too much. This is an area of active research.

As was the case for challenge 1-A, challenge 1-B results implies that the stiffness (energy stored) of the test machine, load train, etc. could be important. This was investigated by adding elastic bars (acts like a spring) to the load application points. The mesh used is shown in Figure A62 with the imposed displacement boundary condition changed from the center of the elastic half plugs to the ends of the thin bars attached to these original loading locations.

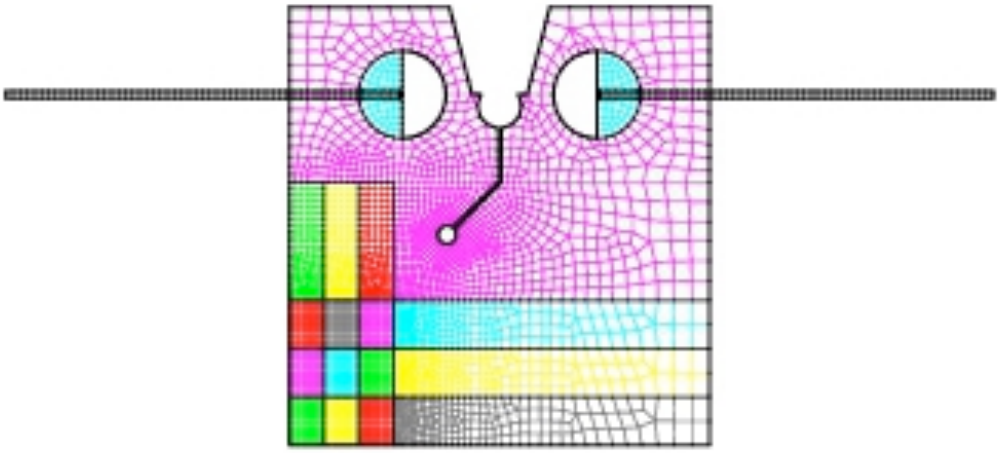

Figure A62. Finite element model for challenge 1-B with added compliance.

Several different spring rates were achieved by varying the elastic modulus of the loading bars. The spring rate will be increased until a similar result to the infinite stiffness quasistatics result is achieved. To date, the spring rate has been varied from 1100 lb./in to 1.1E12 lb./in. Even at the highest spring rate tried thus far, the quasistatics result was not achieved. At a spring rate of 1.1E12, the difference in horizontal displacement between the end of the bar and the original loading point (center of the cyan region above) was 0.7e-9 inch. It was surprising that this level of stored energy is still important. The primary difference between the infinite stiffness results and the compliant results was the stability of the crack and the crack direction. Up to reaching crack instability, the results were virtually identical. When the crack went unstable (defined here as more than 100 elements failing in one load step) the crack path changed from horizontal (cutting grid lines D-E-F) to vertical (cutting grid lines A-B-C). This is shown in the left hand side of Figure A63. If the solution procedure is switched from quasistatics to transient dynamics at the time of crack instability, the original crack path is recovered. This is shown in the right hand side of Figure A63. These preliminary results show a great deal of sensitivity to stored and dissipated energy. The switch from quasistatics to transient dynamics produces a reduction in the load step of several orders of magnitude and also introduces inertia. Both these changes can have profound effects on the energy balance in the simulation.

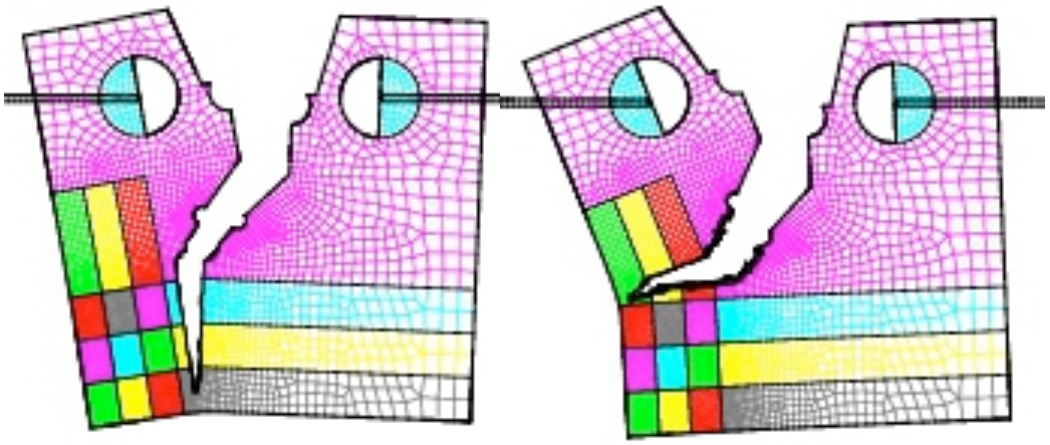

Figure A63. Challenge 1-B simulation with added compliance, left hand side shows the quasistatic crack path, right hand side shows the crack path with the hand-off to transient dynamics at start of unstable crack propagation.

Finally, similar to challenge-1, crack tunneling was observed. That is, the crack initiated and extended at the center-plane prior to initiation at the free surface. Crack tunneling developed early in the simulation after which propagation appeared occur with a constant amount of tunneling (self-similar crack growth). The magnitude of the tunneling was nearly element size independent.

A3.6 Summary and Conclusions

In conclusion, two material property sets, three mesh densities with two energy dissipation terms for two of the meshes. A total of ten simulations were run for challenge 1-B. Simulations were relatively trouble free until the remaining ligament approached 2% of the specimen thickness. At this point, not surprisingly, convergence was difficult to attain. Energy dissipation can be used to achieve an element size independent solution, however, more work is needed to predict the magnitude of this term. The critical crack opening strain (energy dissipation) parameter leads to the greatest source of variability in the simulation of crack propagation using the "tearing parameter" approach.

Energy storage in the specimen, the load train, and the loading machine are important in the simulation. It would be interesting to determine if these predictions could be validated experimentally. The transfer from a quasistatic to a transient dynamic framework to handle crack propagations instabilities has been demonstrated.

A3.7 References

1. Military Handbook – Metallic Materials and Elements for Aerospace Vehicle Structures, MIL-HDBK-5E, Vol 1, Pg 3-97. June, 1987.
2. Modern Industries, Inc., Materials Research Division, Certificate of Analysis Sample S-162606, EXCEL spreadsheet, Eire, Pennsylvania, July, 2010.

A4. Follow-Up for Challenge 1B

Introduction

In keeping with the fundamental premise of the X-Prize challenge, the various techniques used to model ductile failure were completed prior to the availability of the experimental results. As expected there were differences between the experiment and the analysis. Also, in keeping with the intent of the X-Prize, the analysis teams were asked to investigate the differences between pre-test predictions and the experiment and apply knowledge gained during review of the experimental results in an effort reduce these differences. Specifically, each team was asked to answer the following question and engage in the proposed discussion.

1. *What do you believe were the most significant sources of error that produced discrepancy between your model and experimental results? Where possible, provide quantitative estimates of how much your prediction might have improved if these sources were incorporated into the prediction. Discuss the ease or difficulty in incorporating such improvements in future work.*

This memo documents such post-test evaluations for the Tearing Parameter approach to modeling ductile failure.

A4.1 Differences between experimental results and Tearing Parameter Predictions

As can be seen in Figure A64, the Tearing Parameter approach under predicts failure initiation for the Challenge 1-B specimen.

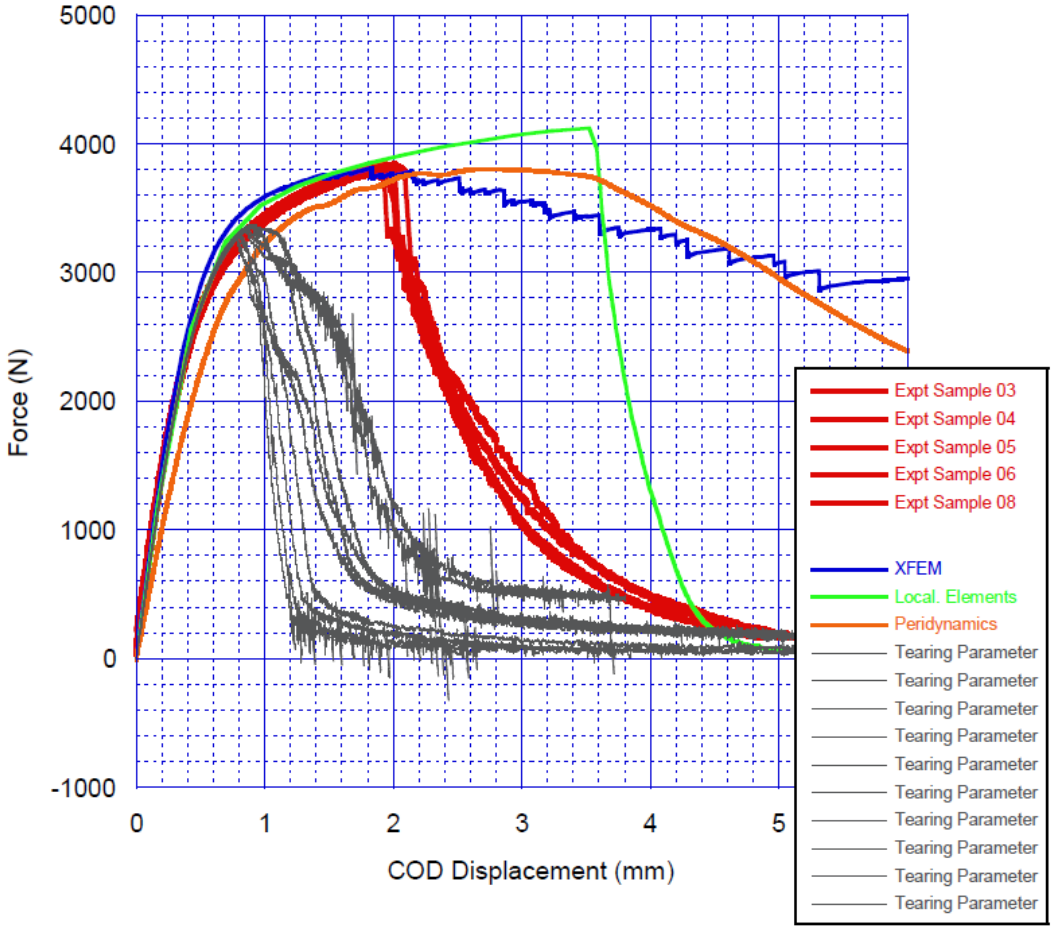

Figure A64. Predictions versus experiment for challenge 1-b.

The Tearing Parameter approach has only one parameter that is not completely fixed by the material properties generated in a tensile test. This parameter is the "critical crack opening strain" which is used to define the energy dissipated in propagating the crack. The "critical crack opening strain" defines the magnitude of the strain component perpendicular to the crack flanks over which the stresses in the element are decayed to zero. As such, this parameter is primarily used to adjust the crack propagation behavior. This parameter only affects the "apparent" initiation behavior in that it slows the stress decay and can thus affect the global peak load marginally. The effect of a change in "critical crack opening strain (CCOS)" is shown in Figure A65.

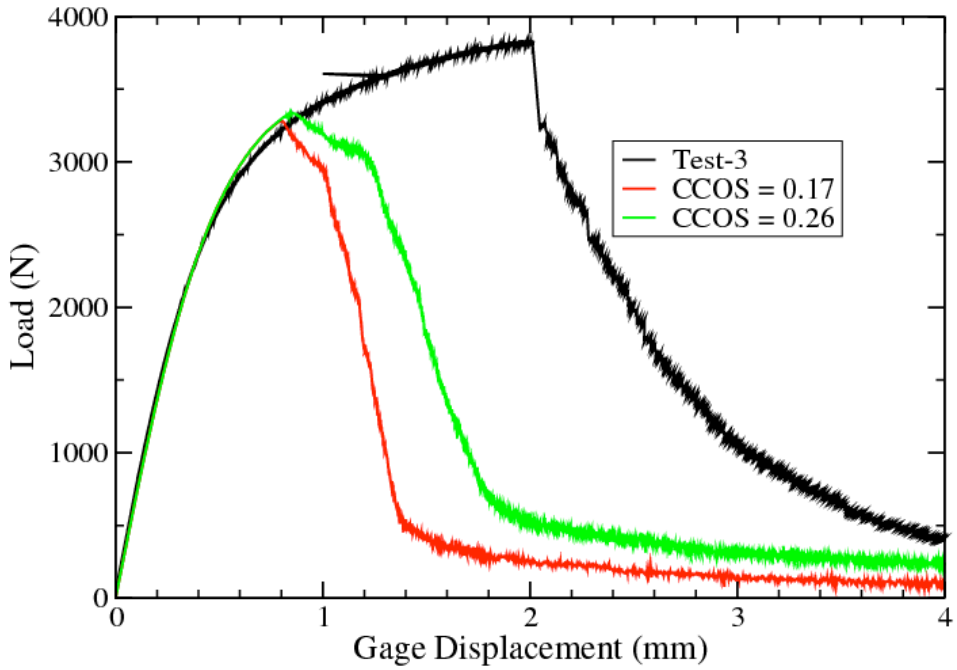

Figure A65. Effect of the critical crack opening strain (energy dissipation) parameter (red and green curves) compared to one experimental result (black curve).

As can be seen in Figure A65, the "critical crack opening strain" parameter has a small effect on the failure initiation load and displacement. The "correct" value for critical crack opening strain was chosen for the coarsest mesh used in the previous study. The value of 0.17 was chosen for the element size in this mesh (the intermediate mesh from the prior study) based on an empirical fit to achieve element size independence. The value of 0.26 was based on a computation by Jay Foulk that assumed element size independence would be achieved by making the energy dissipation per unit crack flank area constant. In this case, 0.17 was slightly too small while 0.26 was too large. The intent here is to show that increasing "critical crack opening strain" is not a reasonable approach to making the simulation match the experiment. Should the critical crack opening strain parameter be increased enough to match the load drop in the experiment, the propagation regime of this problem would be modeled entirely incorrectly (the load decay would be virtually flat).

A second approach to attempting to match the experimental result was based on reformulating the tearing parameter itself. Recall that the tearing parameter as currently employed has the stress state term has an exponent of 4.

$$TP = \int \left\langle \frac{2\sigma_T}{3(\sigma_T - \sigma_m)} \right\rangle^4 d\varepsilon_p$$

This exponent was chosen rather arbitrarily to match a series of notched tension tests on materials rather more ductile than the 2024-T3 aluminum used here. Perhaps modification of the exponent is appropriate for less ductile materials. Figure A66 shows the effect of varying the exponent between 0 and 4.

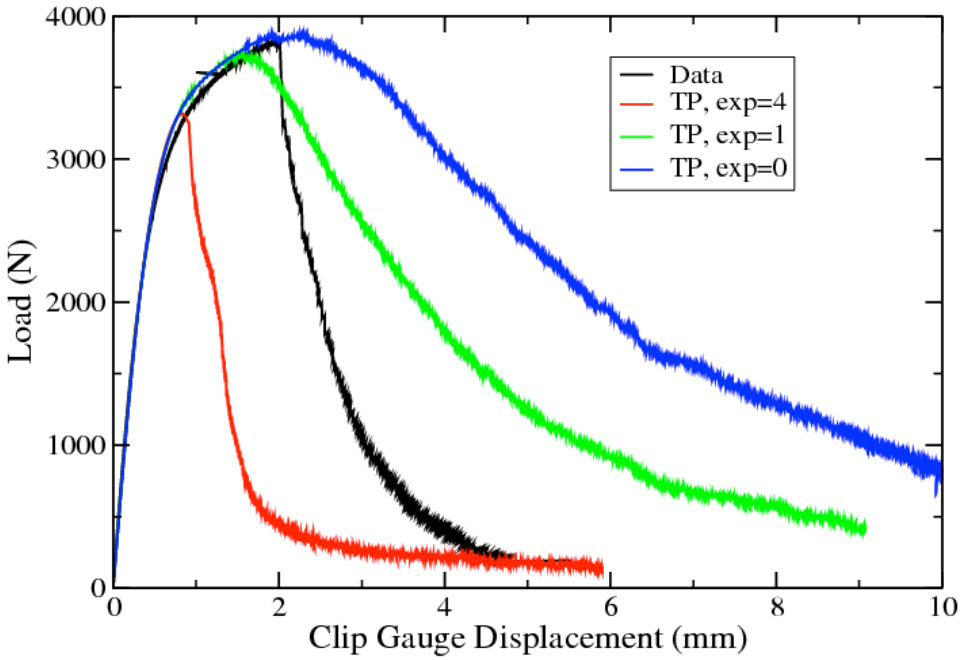

Figure A66. Effect of the varying the exponent in the tearing parameter definition.

From Figure A66 it can be seen that the analytical failure initiation appears to be a reasonable match to the experiment for an exponent of zero. Note: a tearing parameter exponent of zero is equivalent to using a failure criterion of the effective plastic strain. Using the effective plastic strain as a failure criterion implies that there is no effect of stress triaxiality on the failure. That is, in the limit of pure triaxial tension, there would be no failure for this material; clearly an untenable position. In addition, the failure propagation is too slow using this modification of the tearing parameter. Decreasing the critical crack opening strain to zero has only a minor effect on the analytical propagation curve which still lies significantly above the propagation curve for the modified tearing parameter with an exponent of one. Modification of the tearing parameter is not an effective way to make the simulation match the experiment.

The final option to match simulation to experiment involved using both the tearing parameter and the critical crack opening strain as free parameters. If the tearing parameter is set to a value of 1.3 and the critical crack opening strain is set to a value of 0.05, the simulation curve in Figure A67 results.

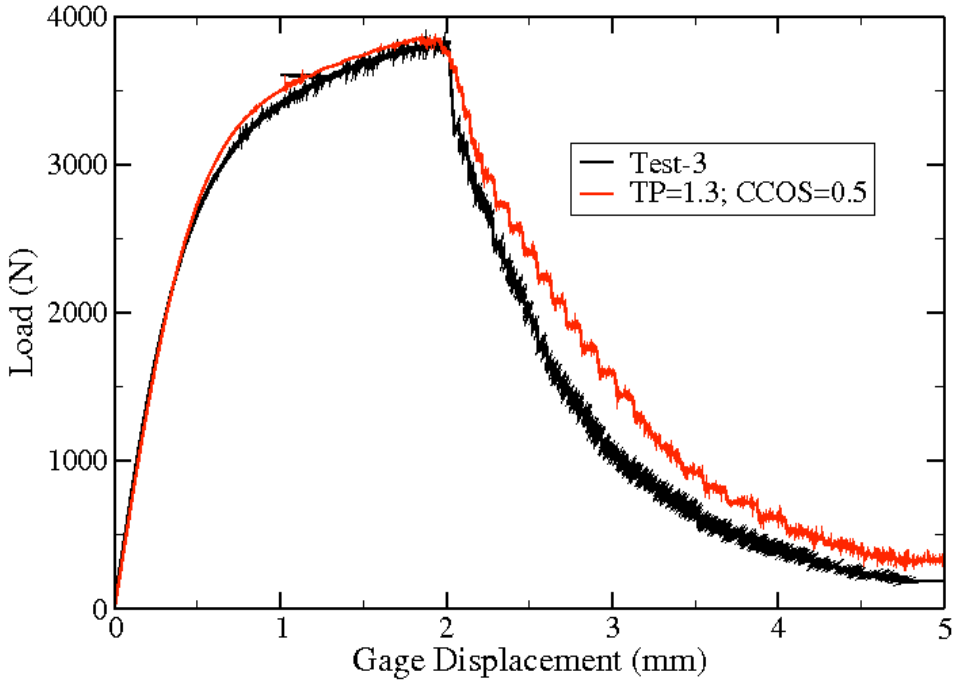

Figure A67. Best match obtainable – all failure parameters tunable

This is quite a good match to the experiment. However, such manipulations render the entire concept of simulation worthless. There is no longer any hint of predictability. This is simply an exercise in "tuning" a model to match an experiment with the full expectation that such "tuning" is inherently problem dependent. That is, there is an expectation that a different set of parameters would be required for each problem modeled. The only thing Figure A67 shows is that if an experimental result already exists, the simulation tool can reproduce it if the user is willing to manipulate the input parameters using non-physical, non-supportable values.

A4.2 Conclusion

There are no easy fixes to the early prediction of failure for the X-Prize challenge 1-b using the tearing parameter approach. The tearing parameter approach has been successful for other problems, so it becomes important to identify the differences that exist between successful use and the overly conservative prediction here. The most obvious difference is the material properties of 2024-T3 aluminum compared to all other materials tried so far. The 2024-T3 aluminum is very much less ductile than any other material for which the tearing parameter has been used. In terms of true-strain to failure, the 2024-T3 has a value of about 0.26 while all other materials tried have had a value greater than 1. In terms of reduction-in-area, the 2024-T3 has a value of about 0.25 while all other materials have had values in excess of 0.5. Finally, all other materials used have shown appreciable necking seen as a pre-failure load drop in a tension test. The 2024-T3 shows no such necking. The simplest conclusion is that for materials exhibiting insufficient ductility (where insufficient ductility is thus far poorly defined), the tearing parameter approach can be expected to give conservative (early prediction of failure) results.

A5. Predictions for Challenge 2A

Executive Summary

The X-Prize challenge 2-A is a sharp notched compact tension specimen with side grooves designed to primarily measure crack propagation. An unloading compliance technique with 4 unload steps was employed. The experimental displacement versus time loading was approximated in the analysis. The stiffness (unloading compliance) of the analysis during the unload steps was determined along with the crack length at the start of the unload step. These are the primary results that will be reported.

A5.1 Introduction

The ductile failure X-Prize is a project to assess the maturity of failure modeling approaches as well as their accuracy and potential. In the following report, the general approach used to predict ductile failure initiation and propagation is the multilinear elastic-plastic with tearing parameter failure (MLEPF) model. There are a total of 5 finite element results reported herein. There are two mesh densities, two material properties descriptions (primary difference is the strain hardening). In one additional analysis the energy dissipation was adjusted to achieve the same maximum load as the coarse meshes (near element size independence). Because the intent of challenge 2-A was investigate crack propagation, the selective-deviatoric (SD) element formulation was not included. The SD element requires further development for stability in a material softening regime such as that produced during stress decay utilized with the tearing parameter approach to ductile failure. The uniform gradient (UG) element formulation was used exclusively here. An overview of the approach is provided. Then, the details, as they relate to the x-Prize challenge 2-A geometry and alloy, are described.

A5.2 General details of the multilinear elastic-plastic with tearing parameter failure approach

The MLEPF approach uses a multilinear elastic-plastic constitutive model with the standard von Mises yield criterion. In this report, the multilinear hardening curve was obtained by fitting experimental data from a round-bar tensile test. Further, the MLEPF approach uses a tearing parameter as a failure criterion, which was also obtained from the round-bar tensile test data. Crack propagation is accompanied by dissipating energy (critical crack opening strain) during the element failure. The critical crack opening strain is a function of both material properties and element size. Element size independent crack propagation can be achieved by appropriately varying the critical crack opening strain with element size. The following sections describe these processes in detail.

A5.2.1 Determining the multilinear elastic-plastic curve fit from round-bar tensile data

Prediction of ductile failure is inherently a large strain, large deformation process. The Cauchy-stress, logarithmic-strain conjugates are used in the finite deformation codes at SNL. The strain hardening defined in terms of Cauchy-stress and logarithmic-strain is obtained by using a finite element model of the tensile specimen to perform the inverse problem. That is, the Cauchy-stress versus logarithmic-strain curve that gives the

experimental engineering stress versus engineering curve as the solution to a finite element analysis of the tensile specimen is extracted. Here, the gage section of a flat tensile specimen is used. Figure A68 shows the finite element mesh. There are 3-planes of symmetry, the back, the left hand side and the bottom. There are imposed displacements on the top of the specimen. The front and right hand side of the specimen are traction free. In order to force the localization and necking (geometric instability) to occur at the longitudinal mid-plane (plane of symmetry), the mesh uses a large-radius to slightly reduce (less than 0.1 per cent) the cross-sectional area at the longitudinal mid-plane. The engineering stress versus engineering strain result is derived from the load and displacement of finite element model and compared to the experimental results.

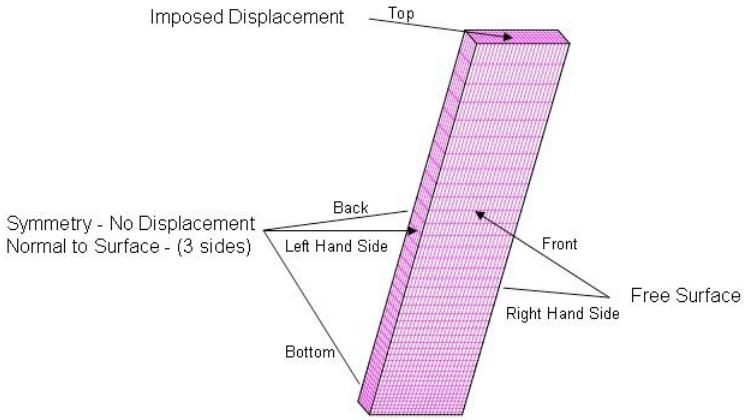

Figure A68. Model for flat specimen tensile test.

A5.2.2 Determining the critical tearing parameter

The tearing parameter accounts for the stress triaxiality at the crack tip by integrating a measure of triaxiality over the equivalent plastic strain. The tearing parameter is given by

$$T = \int_0^{\bar{\varepsilon}_f} \left\langle \frac{2\sigma_T}{3(\sigma_T - \sigma_m)} \right\rangle^4 d\bar{\varepsilon} \qquad (1)$$

where $\bar{\varepsilon}$ is the equivalent plastic strain, $\bar{\varepsilon}_f$ is the final equivalent plastic strain, σ_T is the maximum tensile stress, σ_m is the mean stress and the notation $\langle \bullet \rangle$ represents the standard Macaulay Bracket. One can note that for uniaxial loading, the term inside the Macaulay Brackets becomes unity and the tearing parameter is equivalent to using a limiting plastic strain for a crack growth criterion.

A critical value of the tearing parameter is chosen by integrating equation (1) for all elements of the tensile test simulation and picking the maximum value of the tearing

parameter at the maximum displacement (maximum engineering strain) achieved in the actual tensile test.

There are mesh sensitivities, particularly for coarse meshes, in this entire material property fitting process. It is assumed that these mesh sensitivities are minimized for sufficient geometric resolution to adequately capture the size and shape of the necked region. For highly ductile materials, such resolution probably requires insight into the initial aspect ratio of the elements that will be in the necked region or remeshing. In the model used here (shown above), the elements at the bottom corners of the specimen were roughly 0.01 inch with aspect ratios close to 1 to 1 to 1. This was deemed adequate for the low ductility of 2024-T3 aluminum which exhibits minimal necking behavior.

A5.2.3 Determining the appropriate energy dissipation term

In theory, the energy dissipation term, the critical crack opening strain, can be determined from a second physical test. The optimum form of this second test is open to discussion. The critical crack opening strain is expected to be a function of material properties as well as element size. A theoretical relationship can be established between element size and the value of critical crack opening strain to provide an element size independent simulation of crack extension. However, this relationship does not address the material properties effects. This relationship also requires several assumptions of questionable accuracy. Both this relationship and an empirical relationship based on a series of solutions to one form of a second test are used here. The starting point (the critical crack opening strain for the coarsest mesh) was based on this empirical relationship.

A5.3 Specific details of the approach for challenge 2-A

For challenge 2-A, a heat treatable aluminum alloy, 2024-T3, was chosen. The details of the material description are discussed below. Because the intent of challenge 2-A was crack propagation, prior experience dictated the use of the single-point-integrated, uniform-strain, 8-noded hexahedral element, uniform-gradient (UG) element, with hour glass suppression. The tearing parameter approach is more mature using this element than with available higher order elements

In addition, there were multiple levels of mesh refinement studied with each element formulation. With the UG elements, three unstructured meshes were used with average element size of 0.01 inch and 0.005 inch in the region of crack nucleation and propagation. The following presents the material data used and the fits for both element formulations.

A5.3.1 Material data

There were little full stress-strain data available for this alloy in a suitable product form. The primary source of data selected was clad sheet material [1]. The cladding was quite thin (2.5% of the total thickness) and not expected to contribute significantly to the strain hardening behavior of the specimen. Yield, ultimate and elongation values from tensile testing on this particular plate of material were available, but not the full stress-strain curve. These values were used to adjust the stress-strain curve from the clad material. The stress-strain curve for the clad material was shifted upward by 3.5 ksi and extended

horizontally by 0.07 in/in to match these reported values. Later in challenge 1-B, full stress-strain tensile data for this material became available [2]. This curve had numerous local increases in stress (curve was lumpy). Prior to use the curve was smoothed. The engineering stress versus engineering strain curves for both sets of tensile data (modified for set 1 and smoothed for set 2) are plotted in Figure A53.

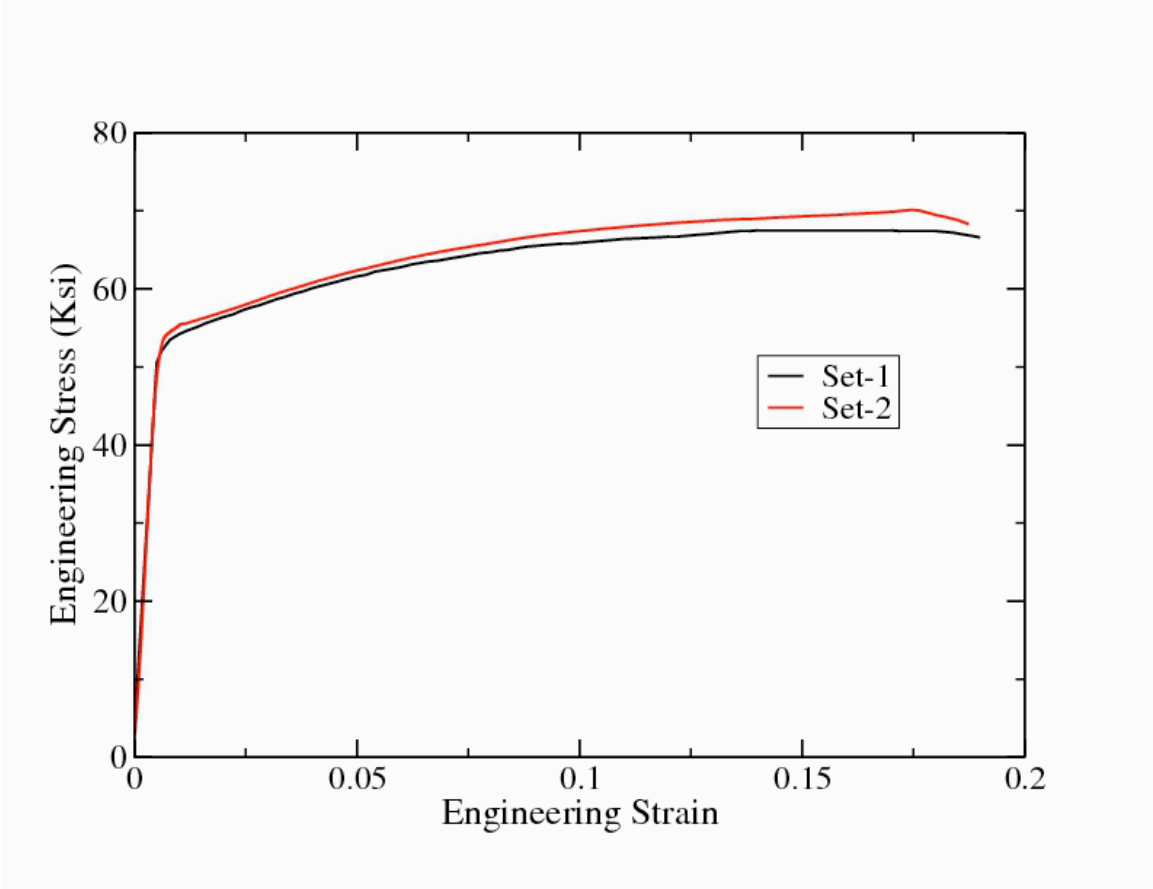

Figure A69. Engineering stress versus engineering strain curves for the 2024-T3 tensile data.

A5.3.2 Material data fit for the uniform-gradient element formulation

The Cauchy-stress, Logarithmic-strain curves resulting from the fit using the uniform-gradient element are shown in Figure A70. In order to not "run off the end of the curve" for differing stress states where the ductility could be greater then for the tensile specimen, the data has been extrapolated based on a straight line through the last two data points from the fitting process. The tearing parameters computed for these materials, 0.32 for set-1 data and 0.28 for set-2 data, are also displayed on the figure.

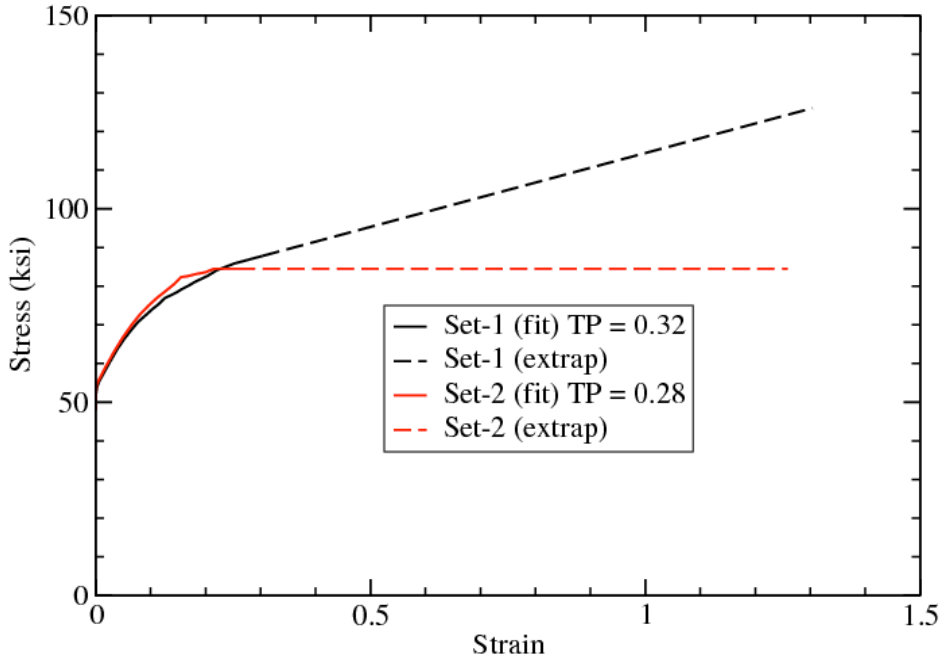

Figure A70. Hardening curves for the uniform-gradient element formulation for B024-T3 Aluminum.

A5.3.3 Critical crack opening strain (energy dissipation)

The empirical estimation scheme for the critical crack opening strain yielded a value of 0.17 for an element size of 0.01 inch for both sets of material descriptions. This same scheme results in critical crack opening strains of 0.20 for 0.005 inch elements for both material descriptions. A trial and error approach showed that a critical crack opening strain of 0.25 for the smaller element gave a similar peak load as the coarse element with a critical crack opening strain of 0.17. The results for this critical crack opening strain are also shown.

A5.3.4 Finite element mesh

Two semi-unstructured meshes were prepared for the analysis of the X-Prize specimen for challenge 2-A. Both meshes made use of a symmetry plane at the through-thickness center of the specimen. That is, the center-plane was constrained to provide no out-of-plane displacement while the outer surface was unconstrained appropriate to a free surface. The use of a plane-of-symmetry implies no out-of-plane displacement at the loading pins as well as no buckling of the specimen. The specimen is assumed to be thick enough that neither of these deformation modes is possible. Half the loading pins are modeled as elastic material meshed contiguously with the bulk of the specimen. The specimen is loaded via imposed displacement (displacement control) at a line of nodes along the central axis of the

elastic pin. Rotation about the load point is allowed but lateral translation is prevented. The fatigue crack is represented by removal of a single layer of elements. Thus the fatigue crack has a square crack root of 0.01 inch for the coarse mesh and 0.005 for the finer mesh. The total number of elements for the coarse mesh was 15,114. The finer mesh had a total element count of 112,219. The two meshes are shown in Figure A71.

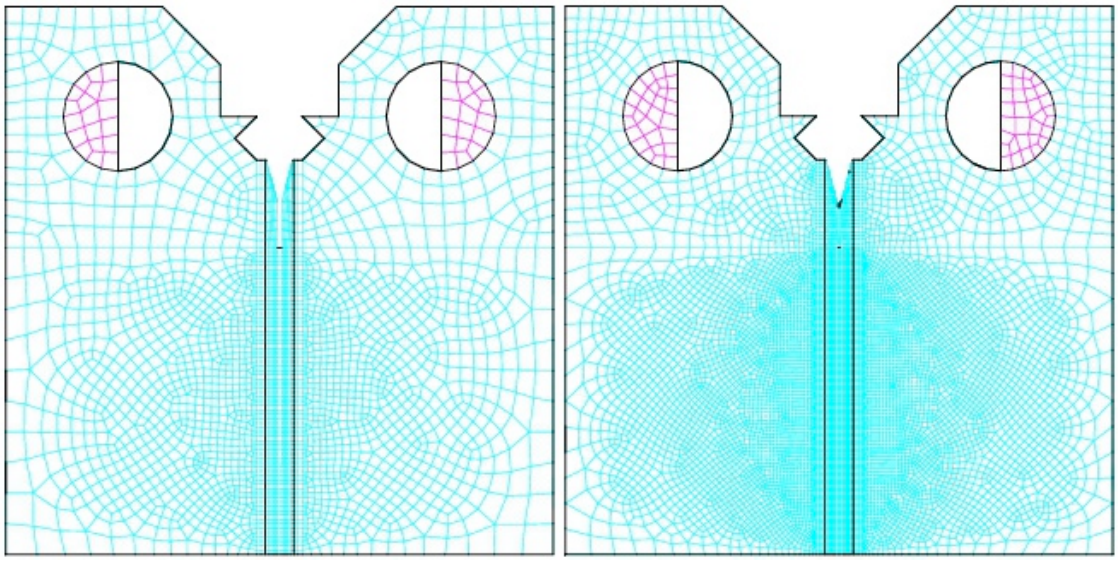

Figure A71. Coarse and fine unstructured meshes - looking at the center-plane.

A5.4 Results

The accuracy of the displacement loading in the analysis is shown in Figure A72. The error is due to the lack of feedback in the analysis between the applied loading point and the displacement measuring location. In the experiment, the displacement is controlled by the clip gage. In the analysis, the loading had to be specified a priori.

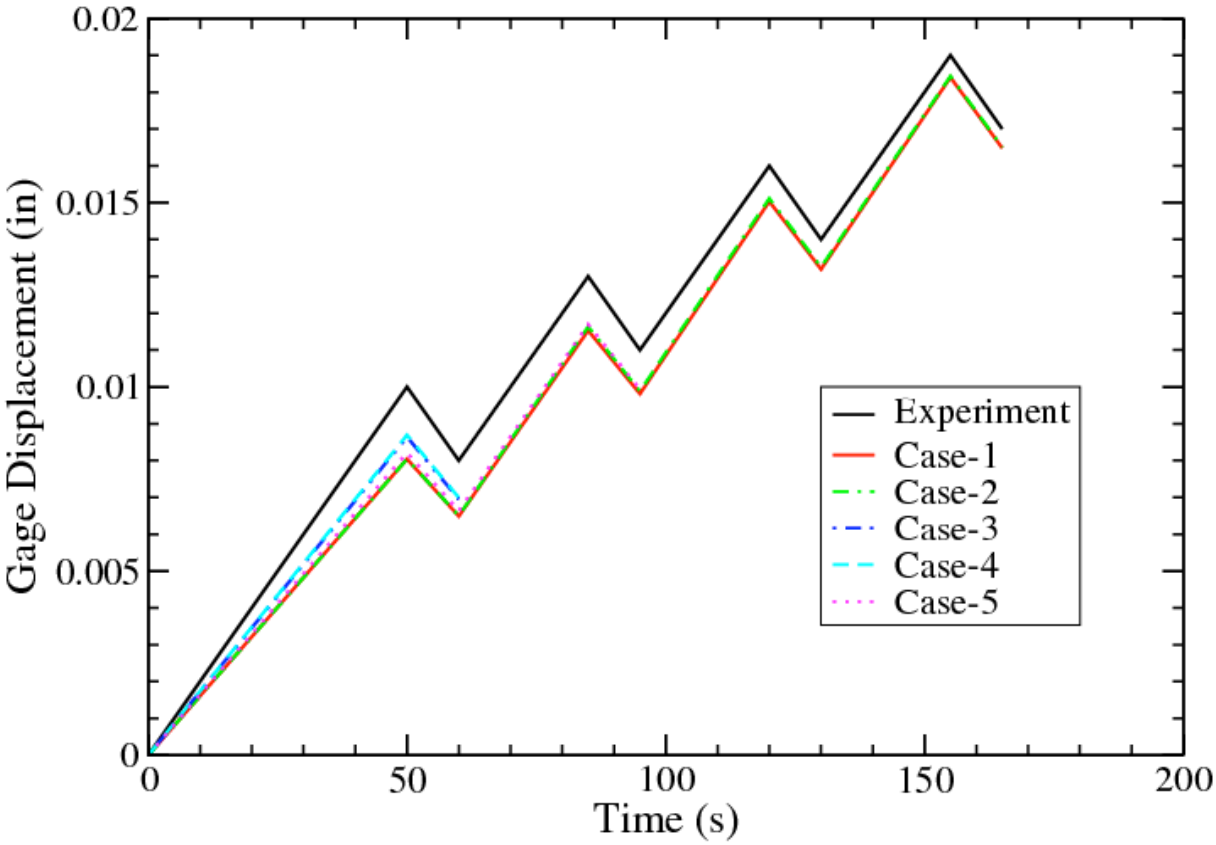

Figure A72. Comparison of Experimental Displacement versus Time with Analysis

Table A16 shows the critical parameters for each of the five analyses. This can be used as a key to the results in Table A17 and Table A18. The tearing parameter is based on the mechanical properties and the fit to the strain hardening curve for the two descriptions of the 2024-T3 aluminum. The critical crack opening strain was based on the current estimation scheme under development except for case-5. The critical crack opening strain for case-5 was based on achieving the same peak load using the smaller elements as the peak load for the larger elements. The crack length at the start of the four (A-D) unloading steps is shown in Table A17. Note: this is crack length – the initial slot and fatigue crack has been added to the crack extension in the value reported here. Both the minimum extension (at the center plane-of-symmetry) and the maximum extension (at the root of the side-notch) are reported. The difference in crack length between these locations looks like uncertainty. However, it is just an extreme example of crack front curvature. An effective crack length, akin to that used in fracture testing, could be defined but this has not yet been done. The unloading compliance for the four unloading steps is shown in Table A18.

Table A16. Description of the 5 analyses

	Element Size	Tearing Parameter	Critical Crack Opening Strain
Case-1	0.01 in	0.317	0.17
Case-2	0.01 in	0.277	0.17
Case-3	0.005 in	0.317	0.20
Case-4	0.005 in	0.277	0.20

Case-5	0.005 in	0.317	0.25

Table A17. Crack length at start of unload steps A-D

	Crack length @ A	Crack length @ B	Crack length @ C	Crack length @ D
Case-1	0 mm	10.4-10.9 mm	13.5-14.2 mm	15.7-16.3 mm
Case-2	0 mm	10.4-10.9 mm	13.5-14.0 mm	15.7-16.3 mm
Case-3	9.4–10.3 mm	13.2–14.1 mm	16.3-17.1 mm	18.3-18.9 mm
Case-4	9.8-10.7 mm	13.6-14.4 mm	16.6-17.3 mm	18.7-18.9 mm
Case-5	7.7-8.5 mm	10.7-11.8 mm	14.0-14.6 mm	15.9-16.7 mm

Table A18. Unloading Compliance (stiffness) during unload steps A-D

	A	B	C	D
Case-1	29,569 N/mm	17,605 N/mm	9,423 N/mm	5,163 N/mm
Case-2	29,795 N/mm	16,383 N/mm	8,615 N/mm	4,935 N/mm
Case-3	20,413 N/mm	9,314 N/mm	4,422 N/mm	2,323 N/mm
Case-4	18,823 N/mm	8,771 N/mm	3,959 N/mm	2,092 N/mm
Case-5	28,145 N/mm	15,558 N/mm	8,571 N/mm	4,854 N/mm

The load versus displacement curves for the analyses are shown in Figure A73.

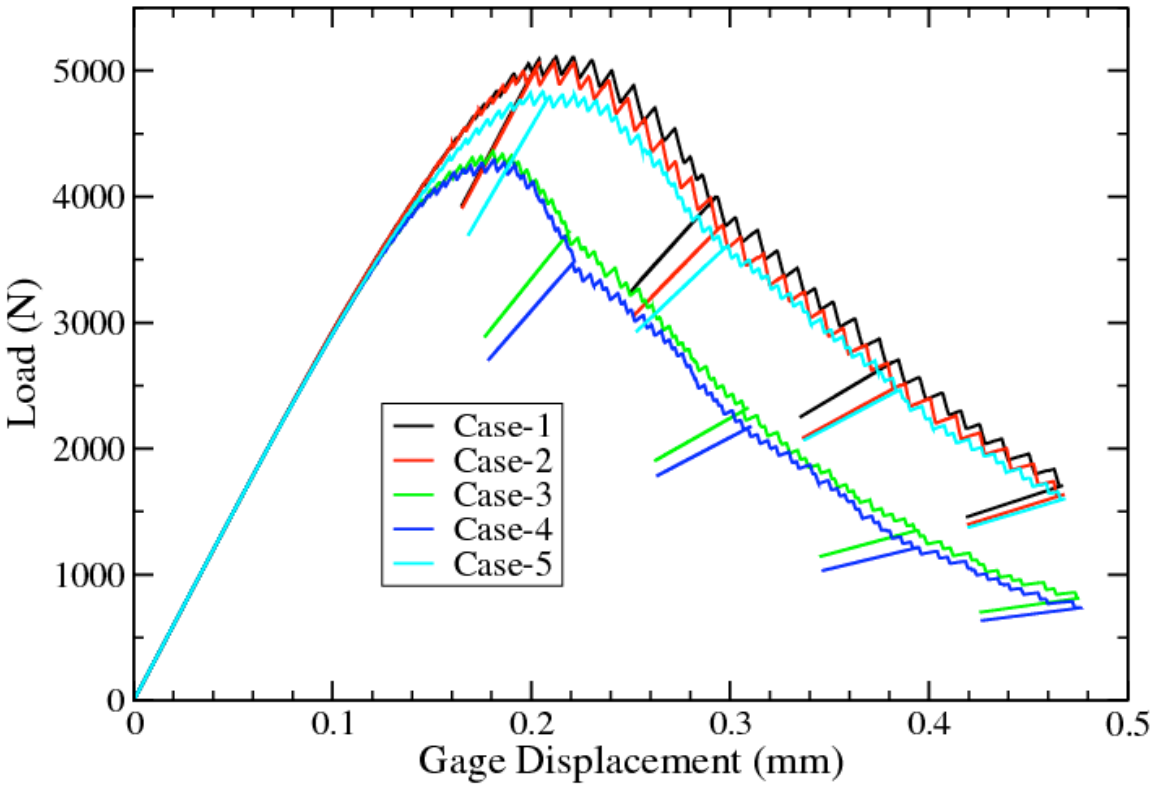

Figure A73. Load versus Displacement (Unloading Compliance) from Analysis

A5.5 Discussion

Given the results of challenge 1-B the crack growth is expected to be over-predicted here. Some additional sources of error in the analyses are, as discussed above, the difference in application of the displacements. The experiment uses a feedback loop from the clip gage to drive the cross-head displacement. In the analysis, the load roller displacements are input without any feedback from the displacements at clip gage location. For challenge 2-A, the analytically predicted crack extension is challenging. The analysis predicts much more extensive cracking at the root of the side groove than at any other part of the specimen. This is even more pronounced for the finer mesh. This leads to the extremely large uncertainty of the crack length for the finer mesh results in Table A17. Finally, the results shown here show the need for further research on predicting the "correct" value to use for the energy dissipation (critical crack opening strain) term. The two material properties sets are very similar. Thus, the analysis results do not show much variation with material property. The results are more sensitive to element size largely due to the uncertainty in adjusting the energy dissipation term (critical crack opening strain) to achieve mesh size independence. The appropriate value of the energy dissipation term is an area of active research.

A5.6 Summary and Conclusions

In conclusion, two material property sets, two mesh densities, and with two energy dissipation terms for a total of 5 simulations were run for challenge 2-A. Simulations were more difficult than for the earlier challenges, with poor convergence occasionally occurring during periods where many elements were decaying stress during a load step. The use of an hourglass viscosity value of 0.001 stabilized the solution sufficiently to allow the problem to run to completion. Finite element "predictions" for the challenge 2-A geometry and loading were presented.

A5.7 References

1. Military Handbook – Metallic Materials and Elements for Aerospace Vehicle Structures, MIL-HDBK-5E, Vol 1, Pg 3-97. June, 1987.
2. Modern Industries, Inc., Materials Research Division, Certificate of Analysis Sample S-162606, EXCEL spreadsheet, Eire, Pennsylvania, July, 2010.

A6. Follow-Up For Challenge 2A

Introduction

In keeping with the fundamental premise of the X-Prize challenge, the various techniques used to model ductile failure were completed prior to the availability of the experimental results. As expected there were differences between the experiment and the analysis. Also, in keeping with the intent of the X-Prize, the analysis teams were asked to investigate the differences between pre-test predictions and the experiment and apply knowledge gained during review of the experimental results in an effort reduce these differences. This discussion will follow the same format as was used for prior challenges.

1. *What do you believe were the most significant sources of error that produced discrepancy between your model and experimental results? Where possible, provide quantitative estimates of how much your prediction might have improved if these sources were incorporated into the prediction. Discuss the ease or difficulty in incorporating such improvements in future work.*

This memo documents such post-test evaluations for the Tearing Parameter approach to modeling ductile failure.

A6.1 Differences between experimental results and pre-test Tearing Parameter Predictions

The major error between the experimental results and the predictions of the Tearing Parameter team were due to errors in transmission of the data. The analysis results match the experimental results much more closely than the initial X-Prize post-test figure indicates. The Tearing Parameter team mistakenly included the notch and the initial fatigue crack in the reported crack lengths, with the exception of the crack lengths at A for the two coarsest meshes. Thus, in the initial X-Prize post-test figure, normalized crack lengths are 0.3 too large except for these two cases. These two coarsest mesh cases were reported as zero crack length in error. The Tearing Parameter team modeled the problem in pounds and inches so the results needed to be converted to report crack lengths in millimeters. The 0.3 inches of notch and fatigue crack was added to the crack length prior to converting from inches to mm. Unfortunately, for the two cases of zero crack extension, it was recognized that unit conversion was not needed, and the addition of the initial crack length during the conversion process was forgotten. The table below contain the correct results of normalized crack length versus stiffness for the tearing parameter technique from the pre-test simulations.

Table A19. Corrected crack length predictions for 0.3 a/W offset.
CASE-1

Load Point	A	B	C	D
Normalized Crack Length (a/W)	0.3	0.41-0.44	0.53-0.56	0.62-0.64
Stiffness	29567	17605	9423	5163

(N/mm)				

CASE-2

Load Point	A	B	C	D
Normalized Crack Length (a/W)	0.3	0.41-0.44	0.53-0.55	0.62-0.64
Stiffness (N/mm)	29795	16383	8615	4935

CASE-3

Load Point	A	B	C	D
Normalized Crack Length (a/W)	0.37-0.405	0.52-0.555	0.64-0.675	0.72-0.745
Stiffness (N/mm)	20413	9314	4422	2323

CASE-4

Load Point	A	B	C	D
Normalized Crack Length (a/W)	0.385-0.42	0.535-0.565	0.655-0.68	0.735-0.745
Stiffness (N/mm)	18823	8771	3959	2092

CASE-5

Load Point	A	B	C	D
Normalized Crack Length (a/W)	0.305-0.335	0.42-0.465	0.53-0.575	0.625-0.66
Stiffness (N/mm)	28145	15558	8571	4854

A plot (Figure A74) of the experimentally measured and analytically predicted (pre-test) load displacement curves shows the comparison quite well.

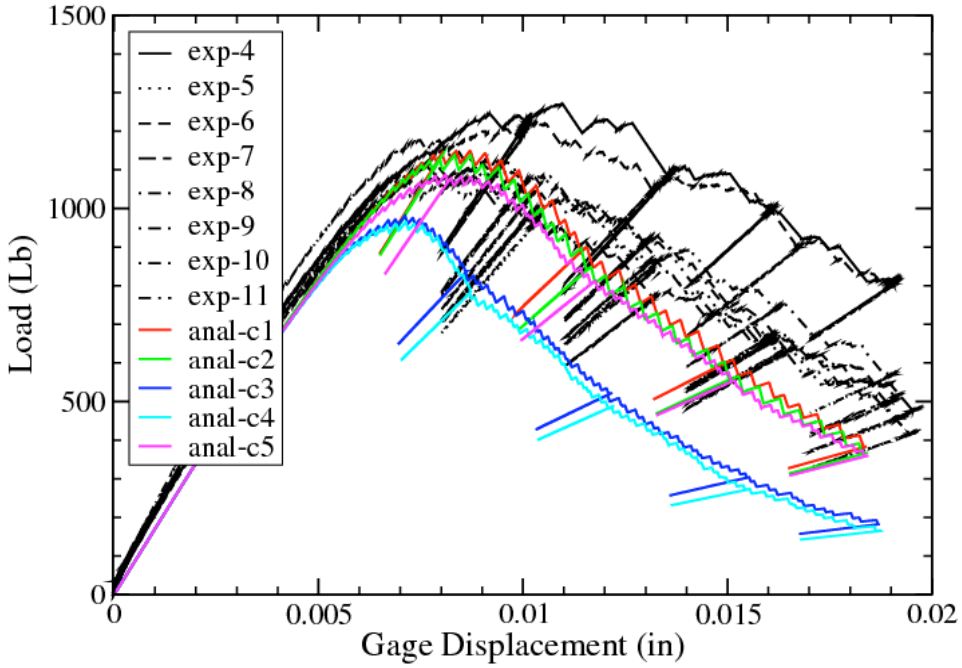

Figure A74. Comparison of Experiment and Pre-test Analysis Load versus Displacement Curves.

Table A20. Pre-Test Analysis Parameters

	Element Size	Tearing Parameter	Critical Crack Opening Strain
Case-1	0.01 in	0.317	0.17
Case-2	0.01 in	0.277	0.17
Case-3	0.005 in	0.317	0.20
Case-4	0.005 in	0.277	0.20
Case-5	0.005 in	0.317	0.25

Figure A74 includes seven experimental load and five pre-test simulation load versus displacement curves. The five pre-test simulations included two coarse meshes (model parameters from two tensile tests) and two finer mesh (same two model parameter sets) simulations performed with the current "critical crack opening strain" estimation scheme. As can be seen from Figure A58, the differences in the material properties from the two tensile tests were insignificant. The fifth analysis curve was performed by adjusting the "critical crack opening strain" to a value that resulted in element size independent results. That is, the fine mesh simulation produced a very similar result to the coarse mesh result. The " critical crack opening strain" is a modeling parameter that controls the energy dissipation during crack growth. Establishing the value of this parameter is the focus of current research. The current estimation scheme is an attempt to set this parameter to a reasonable value "a priori". As can be seen from Figure A74, the estimation scheme for the "critical crack opening strain" yielded a value that over-predicted the crack growth.

A6.2 Post-test Tearing Parameter Analysis

With the availability of the experimental results, it was clear that the analyses of the Tearing Parameter team were over-predicting the crack growth. The "critical crack opening strain" is the model parameter that controls the energy dissipated during crack growth and thus crack growth rate. The "critical crack opening strain" parameter was increased until the analytical load versus displacement curves matched the experimental results. Because of minimal differences between the two material properties sets, only the first set of materials properties were used here. These results are shown in Figure A59.

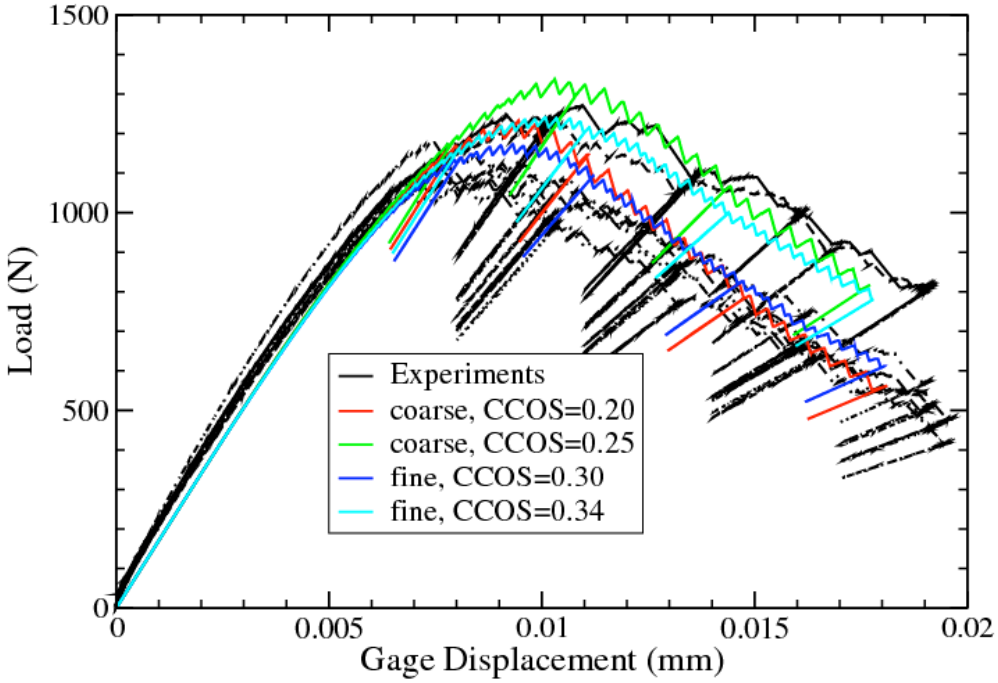

Figure A75. Comparison of Experiment and Post-test Analysis Load versus Displacement Curves.

Table A21. Post-Test Analysis Parameters

	Element Size	Tearing Parameter	Critical Crack Opening Strain
Case-1a	0.01 in	0.317	0.20
Case-1b	0.01 in	0.317	0.25
Case-3a	0.005 in	0.317	0.30
Case-3b	0.005 in	0.317	0.34

As shown in Figure A59, the new values of "critical crack opening strain" provide a better match for the peak loads and the displacement at peak load. The total "gage length" is less for the analyses. The unloading compliance slopes appear to match the experiment quite well. The post-test analyses are post-processed to obtain normalized crack length and

unloading compliance as was done for the original pre-test analyses. These results are shown below.

Table A22. Post-test analyses.

Case-1a, Coarse mesh, CCOS = 0.2

Load Point	A	B	C	D
Normalized Crack Length (a/W)	0.3 to 0.38	0.36 to 0.47	0.48 to 0.58	0.57 to 0.67
Stiffness (N/mm)	29906	23820	13168	7914

Case-1b, Coarse mesh, CCOS = 0.25

Load Point	A	B	C	D
Normalized Crack Length (a/W)	0.3 to 0.38	0.33 to 0.44	0.43 to 0.54	0.51 to 0.62
Stiffness (N/mm)	29968	28477	18951	12328

Case-3a, Fine mesh, CCOS = 0.3

Load Point	A	B	C	D
Normalized Crack Length (a/W)	0.325 to 0.425	0.405 to 0.515	0.51 to 0.615	0.59 to 0.69
Stiffness (N/mm)	29320	21793	13264	8515

Case-3b, Fine mesh, CCOS = 0.34

Load Point	A	B	C	D
Normalized Crack Length (a/W)	0.31 to 0.42	0.38 to 0.5	0.465 to 0.585	0.545 to 0.66
Stiffness (N/mm)	29841	24836	16857	11355

A6.3 Conclusion

Setting the optimal value for the "critical crack opening strain" (the measure of energy dissipation with crack growth) is still a focus of active research. The lack of well controlled crack growth experimental results (along with well characterized material properties for the same material) presents some difficulty in establishing the technique for setting this model parameter. The data from the X-Prize challenges, challenge 2-A included, will be used to enhance this technique.

For challenge 2-A, the analysis results are insensitive to the value of "tearing parameter" and sensitive to the value of "critical crack opening strain". The differences in Figure A74 and Figure A75 are due to changes in critical crack opening strain. For the coarse mesh, Figure A74 shows our best pre-test estimate of the value of "critical crack opening strain"

was 0.17, and Figure A75 shows that values of 0.2 and 0.25 match the experimental results very closely. For the fine mesh, Figure A74 shows that our best pre-test estimate of the value of "critical crack opening strain" was 0.2 while Figure A75 shows values of 0.3 and 0.34 match the experiment very closely.

It is possible that our use of a uniform gradient element formulation is contributing to the difficulty in setting the critical crack opening strain parameter a priori to achieve accurate mesh size independent analysis results. A potentially more accurate element formulation is a selective deviatoric (SD) hex, but currently element death is not a robust capability with the SD element. A potential path forward includes improvements to element death in SD hexes. Current research into integrating the element size into the stress decay to implement a constant energy dissipation per unit crack area are underway in the Sierra Mechanics framework.

APPENDIX B: PERIDYNAMICS APPROACH

John T. Foster and Stewart A. Silling

B1. Predictions for Challenge 1A

Abstract

The Ductile Failure X-Prize project is funded by Advanced Simulation and Computing (ASC) and coordinated at Sandia National Laboratories. The intent is to challenge different groups of computational solution techniques in conducting blind simulations of increasing complexity in modeling the nucleation, initiation, and propagation of ductile failure in engineering materials. The simulations are to be conducted in a blind fashion without any analyst knowledge of the experimental results nor the results of the other computational teams. This paper documents the results of the peridynamics team for assignment 1A, a compact-tension-like specimen that has been uniquely featured and loaded to failure. Peridynamics is a reformulation of classical continuum theory that replaces the partial differential equations of motion with a set of integral-differential equations, and has the unique ability to model discontinuous displacement fields in a mathematically consistent fashion, where the spatial derivatives in the classical theory would be undefined. This allows for straightforward modeling of crack nucleation, coalescence, and propagation without the need for special numerical techniques or external crack growth laws. Discussion of the modeling methods utilized along with the results of the simulations are shown.

B1.1 Introduction

The peridynamic model [references B1-B4] is a continuum reformulation of the classical partial differential equation of motion (conservation of momentum). It has been most notably used to model the deformation of bodies in which discontinuities (e.g., cracks) occur spontaneously. The basic equations are applicable even when singularities appear in the deformation field. These discontinuous deformations would lead to an inability to evaluate spatial derivatives in the classical formulation and special techniques would be required to analyze the problem. Recalling from classical continuum theory the conservation of momentum equation shown in Equation 1[1]

$$\rho\ddot{\mathbf{u}}[\mathbf{x},t] = \nabla\cdot\boldsymbol{\sigma}[\mathbf{x},t] + \mathbf{b}[\mathbf{x},t] \qquad (1)$$

where, ρ, u, b are statistically defined quantities representing continuum notions of mass density, vector valued displacement, and body force density, respectively. σ is a second order tensor which satisfies the equation, typically called the first Piola-Kirchhoff stress tensor. The independent variables x and *t* are defined as a position vector in the reference configuration and time, respectively.

[1] Notation convention: Throughout this paper tensor quantities will be denoted by boldface type. First order tensors may be referred to in the text as vectors. States are denoted by uppercase bold letters with an underscore.

In the peridynamic model, the second term on the right hand side of Equation 1, called the divergence of the stress tensor, is replaced with an integral functional. The functional relates forces or "bonds" between material particles in a continuum and is valid over any body without restriction on displacements (e.g., continuity, differentiability). The word "bond" appears in quotation here because there isn't necessarily any notion of connectivity, such as a spring like force, between material points; there is simply some force potential between them. The peridynamic equation of motion is given in Equation 2

$$\rho\ddot{\mathbf{u}}[\mathbf{x},t] = \int_{\mathcal{H}} \{\underline{\mathbf{T}}[\mathbf{x},t]\langle\mathbf{x}'-\mathbf{x}\rangle - \underline{\mathbf{T}}[\mathbf{x}',t]\langle\mathbf{x}-\mathbf{x}'\rangle\} dV_{\mathbf{x}'} + \mathbf{b}[\mathbf{x},t] \qquad (2)$$

where, x' is the position vector of some neighboring material point with respect to x and $dV_{x'}$ is the differential volume of x'. $\mathcal{H}$ describes the family of continuum points x' with respect to x. $\mathcal{H}$ is typically defined by a sphere of radius δ with center at x. Figure B76a shows an illustration of a peridynamic continuum body, $\mathcal{B}$.

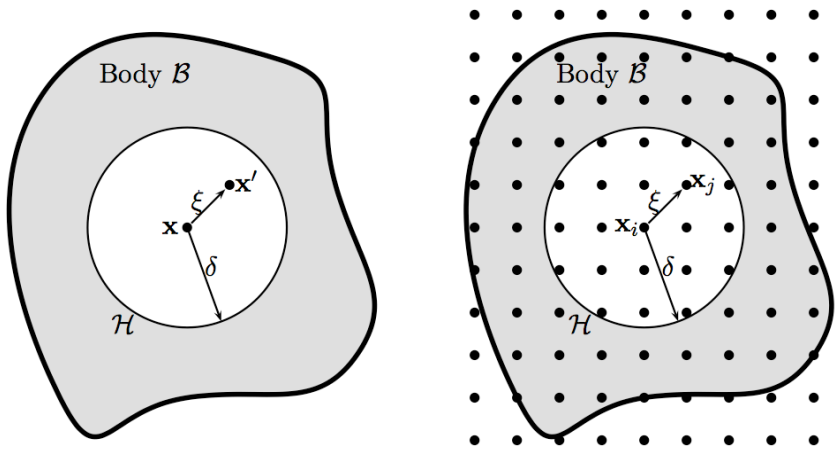

(A) Continuum. (B) Discrete.

Figure B76. Schematic of peridynamic representations.

$\underline{\mathbf{T}}$ is defined as the peridynamic force-vector state. The concept of vector states is similar to that of a second order tensor in that they both map vectors into vectors, but vector states do not have to be linear or continuous functions. The angle brackets, ⟨⟩, in Equation 2 indicate the vector on which the state operates. $\underline{\mathbf{T}}$ maps a deformation-vector state into a force-vector state for each material point within $\mathcal{H}$. All of the material constitutive response is contained in the force-vector states which are dependent on the totality of deformations of all material points within the family $\mathcal{H}$, not just on the deformation of x and x'(i.e., they are *not* pairwise forces).

It has been shown that if the analyst is only interested in the bulk response of the material then the choice of δ is essentially arbitrary [B1]. However, if length scale is important, δ can be chosen appropriately, for example, to account for van der Waals forces in molecular dynamics modeling. Equation 2 has been shown to reduce to Equation 1 in the limit as $\delta \rightarrow 0$, assuming a certain smoothness of the displacement field as required for the existence of the partial derivatives [B5].

In order to solve general problems in solid mechanics Equation 2 is discretized and the integral is replaced with a finite sum. The resulting formula is shown in Equation 3

$$\rho\ddot{\mathbf{u}}[\mathbf{x}_i,t] = \sum_{j=1}^{k}\{\underline{\mathbf{T}}[\mathbf{x}_i,t]\langle\mathbf{x}_j-\mathbf{x}_i\rangle-\underline{\mathbf{T}}[\mathbf{x}_j,t]\langle\mathbf{x}_i-\mathbf{x}_j\rangle\}V_j+\mathbf{b}[\mathbf{x}_i,t]\ \forall\ i=1,2,\ldots,\mathcal{N} \tag{3}$$

where $\mathbf{x}_i$ represents a discrete material particle, or node, and $\mathbf{x}_j$ represents a single node within the horizon, $\mathcal{H}$. k represents the total number of nodes within $\mathcal{H}$, and $\mathcal{N}$ represents the total number of nodes within the peridynamic body of interest. V_j is the volume of the $\mathbf{x}_j$ node. Figure B76b shows an illustration of a discretized peridynamic body $\mathcal{B}$. Figure B76b is shown with a structured grid of material points, however this is just for illustrative purposes as the grid could be unstructured. This process is described in detail in Silling et al.[B6], and results in a mesh free method of solving complex mechanics problems. An explicit time integration scheme is used to solve these equations for dynamic problems in the Sandia National Laboratories code, Emu. Emu discretizes a continuum body into nodes, each with a known volume in the reference configuration; this results in a meshfree method in the sense that there are no elements or geometric connectivities between the nodes. Emu has been used to solve many problems of interest for engineering communities who deal with projectile penetration and perforation, fragmentation, etc.

In this paper, we will use the peridynamic method along with a novel failure model, implemented in Emu, to conduct blind simulations of Ductile Failure X-Prize specimen 1A, in order to determine the load-line displacement and loading force at which a crack will nucleate.

B1.2 Constitutive Modeling

While it is possible to define material response purely in terms of force-vector states, most constitutive modeling to date has been done in terms of classical notions of stress and strain. Within the peridynamic framework we can take advantage of the existing database of constitutive models and experimental data with the process described in the following sections.

The first step in implementing a traditional (formulated in terms of stress and strain) constitutive model into the peridynamic framework is finding an approximation to the local deformation gradient, **F**, for each node. Recall from classical continuum mechanics that the deformation gradient is a defined by Equation 4[2]

$$\mathbf{F} = \mathbf{I} + \mathbf{u}\nabla_{\mathbf{x}} \tag{4}$$

where, **I** is the identity tensor and $\nabla_{\mathbf{x}}$ is the gradient operator with respect to **x** in the reference configuration. In order for **F** to be defined, all of the partial derivatives contained in **u** $\nabla_{\mathbf{x}}$ must exist. This requires the displacement field to be continuously differentiable. In other forms of computational mechanics (e.g., Finite Element Method) these partial derivatives must only be defined in a weak sense in order for **F** to exist;

[2] $F_{ij} = \delta_{ij} + \frac{\partial u_i}{\partial x_j}$ using indicial notation.

however, we will not make this restriction in the peridynamic formulation [B7]. We will use the true deformation, defined by a deformation-vector state $\underline{\mathbf{Y}}\langle\boldsymbol{\xi}\rangle$(Equation 5), to approximate **F**

$$\underline{\mathbf{Y}}[\mathbf{x},t]\langle\boldsymbol{\xi}\rangle = \boldsymbol{\xi} + \boldsymbol{\eta} \tag{5}$$

where, $\boldsymbol{\xi}$ is the relative position between two material points,

$$\boldsymbol{\xi} = \mathbf{x}' - \mathbf{x} \tag{6}$$

and $\boldsymbol{\eta}$ is the relative displacement,

$$\boldsymbol{\eta} = \mathbf{u}[\mathbf{x}',t] - \mathbf{u}[\mathbf{x},t] \tag{7}$$

$\underline{\mathbf{Y}}\langle\boldsymbol{\xi}\rangle$ is a vector function that associates any bond $\boldsymbol{\xi}$ with the deformed image of the bond. Because $\mathbf{F}$ is a second order tensor it is only capable of mapping a sphere into an ellipsoid, whereas, $\underline{\mathbf{Y}}$ is capable of mapping more complex kinematics.

To approximate the deformation gradient from the true deformation via the deformation vector-state we start by defining a non-local *shape tensor* with the following integral:

$$\mathbf{K}[\mathbf{x},t] = \int_{\mathcal{H}} \omega\left(|\boldsymbol{\xi}|\right)\left(\boldsymbol{\xi}\otimes\boldsymbol{\xi}\right) dV_{\mathbf{x}'} \tag{8}$$

where $\otimes$ is the dyadic product operator, and ω is defined as an *influence function*, which is scalar valued and dependent on $|\boldsymbol{\xi}|$. In this implementation, ω is always either 0 or 1, which corresponds to whether the bond is "broken" or not. Broken bonds are the method in which material failure is introduced in the peridynamic theory, and while this is one of the primary advantages of the theory its discussion will be postponed until the next section. ω could also be used as a distributable influence function where certain material neighbors have more influence than others. The integral in Equation 8 results in a positive definite tensor when evaluated; therefore, **K** will always be invertible.

Knowing the shape tensor, the approximated deformation gradient, **F**, at a material point **x** is given by Equation 9.

$$\hat{\mathbf{F}}[\mathbf{x},t] = \left[\int_{\mathcal{H}} \omega\left(|\boldsymbol{\xi}|\right)\left(\underline{\mathbf{Y}}\langle\boldsymbol{\xi}\rangle\otimes\boldsymbol{\xi}\right) dV_{\mathbf{x}'}\right]\mathbf{K}^{-1} \tag{9}$$

The deformation gradient can be shown to be exact for a homogenous deformation. This is always true irrespective of the location of a material point within a body, even along boundaries or near discontinuities. If we assume a constant deformation-vector state, $\underline{Y}_i = F_{ip}\,\xi_p$, then the proof follows:

$$\begin{aligned}
\hat{F}_{ij} &= \left[\int_{\mathcal{H}} \omega\left(\xi\right) F_{ip}\xi_p\xi_k dV_{\mathbf{x}'}\right] K^{-1}_{kj} \\
&= F_{ip}\left[\int_{\mathcal{H}} \omega\left(\xi\right) \xi_p\xi_k dV_{\mathbf{x}'}\right] K^{-1}_{kj} \\
&= F_{ip}K_{pk}K^{-1}_{kj} \\
&= F_{ip}\delta_{pj} \\
&= F_{ij}
\end{aligned}$$

With the deformation gradient in hand, the rest of the kinematics follow the standard definitions laid out in many texts. If we assume a hyperelastic material (in the sense of classical elasticity theory) which has a strain energy density function, $\Omega(\mathbf{F})$ in the classical description of $\mathbf{F}$, as well as a strain energy density function, $W(\underline{\mathbf{Y}})$, in the peridynamic description of $\underline{\mathbf{Y}}$ then through the correspondence of the two descriptions, the following relationship can be verified [4]:

$$\underline{\mathbf{T}}\langle\boldsymbol{\xi}\rangle = \omega\left(|\boldsymbol{\xi}|\right)\boldsymbol{\sigma}\mathbf{K}^{-1}\boldsymbol{\xi} \tag{10}$$

where, $\boldsymbol{\sigma}$ is the first Piola-Kirchhoff stress defined by the following tensor gradient:

$$\boldsymbol{\sigma} = \frac{\partial\Omega\left(\mathbf{F}\right)}{\partial\mathbf{F}} \tag{11}$$

For the Ductile Failure X-Prize Assignment 1A specimen[3], which is made of the steel alloy Ph13-8Mo with the H950 heat treatment, an elastic-perfectly plastic constitutive response was chosen to represent the material. The Cauchy stress, $\boldsymbol{\tau}$, is provided using von Mises plasticity theory and then converted to the first Piola-Kirchhoff stress using the relationship shown in Equation 12,

$$\boldsymbol{\sigma} = \det\left(\hat{\mathbf{F}}\right)\boldsymbol{\tau}\hat{\mathbf{F}}^{-T} \tag{12}$$

which is then substituted into Equation 10 in order to resolve the force-vector states acting on the "bonds."

A model fit of the constitutive response is shown in Figure B77. The data was collected in a quasi-static test apparatus manufactured by MTS, and conducted by technicians in Sandia National Laboratories Structural Mechanics Lab on July 1, 2008. The data was provided in raw (force as a function of displacement) form to the participants of the Ductile Failure X-Prize project by Dr. Jerry Wellman. The data was then converted to measures of true stress and Lagrangian strain for comparison to an Emu simulation of a representative specimen in uniaxial tension. It is believed that the apparent "softening" of the material at approximately 10% strain is due to necking of the material at which time the data is not representative of the actual stress state, but becomes a structural test. For this reason, the "softening" is ignored and the material treated as perfectly plastic. The model fit results in an elastic (Young's) modulus of 198 GPa with a flow stress of 1630 MPa; a Poisson ratio of 0.278 was taken from the Aerospace Structural Metals Handbook [B8].

[3] A detailed drawing of the specimen is included in the appendix of this document.

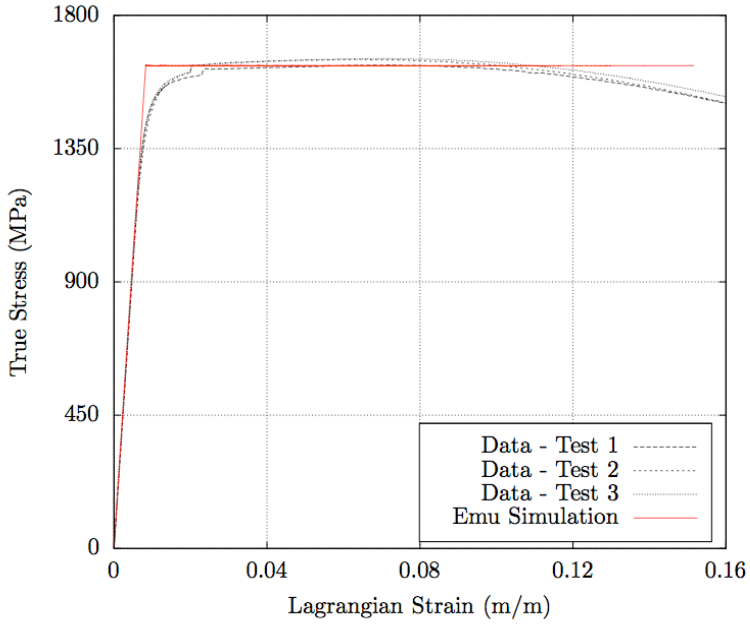

Figure B77. Constitutive model fit.

B1.3 Failure Models

The method of damage (failure, cracks, etc.) nucleation, coalescence, and propagation within the peridynamic model is through the permanent breaking of 'bonds'. Recall that within the state-based peridynamic framework, the state-forces could potentially act in any conceivable direction, Figure B78 shows a notional illustration of this relationship,

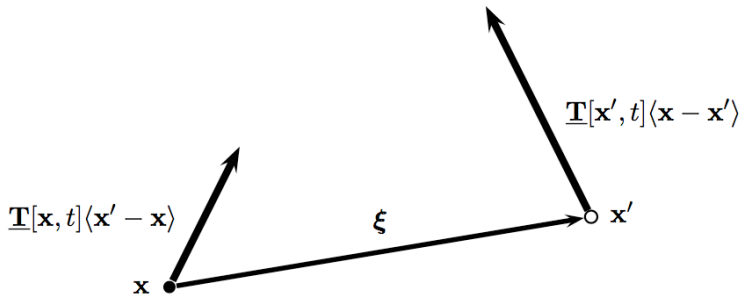

Figure B78. Notional illustration of relationship between state-forces and "bond

In the numerical simulation of fracture many methods have been utilized to characterize when a material might fail. A few examples are the plastic strain to failure, stress triaxiality, lode angle dependence, etc. Most of these methods have some dependence on either the stress or strain histories. Since peridynamics is cast in a form that does not require the notion of stress (although we use stress as a convenience for material modeling in the previous section), we wish to develop a failure criterion derived not from any stress or strain criterion, but instead using thermodynamic notions of work or energy. We can calculate the amount of work (energy) density performed on a "bond", w_t , projecting the force vector-states onto the relative displacement vector. The calculation is performed by Equation 13.

$$w_\xi = \int_0^{\eta(t_{final})} \{\underline{\mathbf{T}}[\mathbf{x}, t]\langle \mathbf{x}' - \mathbf{x}\rangle - \underline{\mathbf{T}}[\mathbf{x}', t]\langle \mathbf{x} - \mathbf{x}'\rangle\} \cdot d\boldsymbol{\eta} \qquad (13)$$

where the integrand of Equation 13 is known as the *dual force density*. Equation 13 defines w_ξ as having units of energy per unit volume squared. It represents an amount of work density done on a bond due to displacing the two material points **x** and **x'** relative to one another from zero to some final scalar value of displacement, $\eta(t_{final})$, which is a function of time. This projection neglects any work done on the points due to rigid body translation.

We will assume that the energy density contained in a bond is fully recoverable[4] by reversing the deformation, unless it exceeds some critical energy density, w_c. Let us attempt to define w_c in terms of material property that can be experimentally determined. Referring to Figure B79,

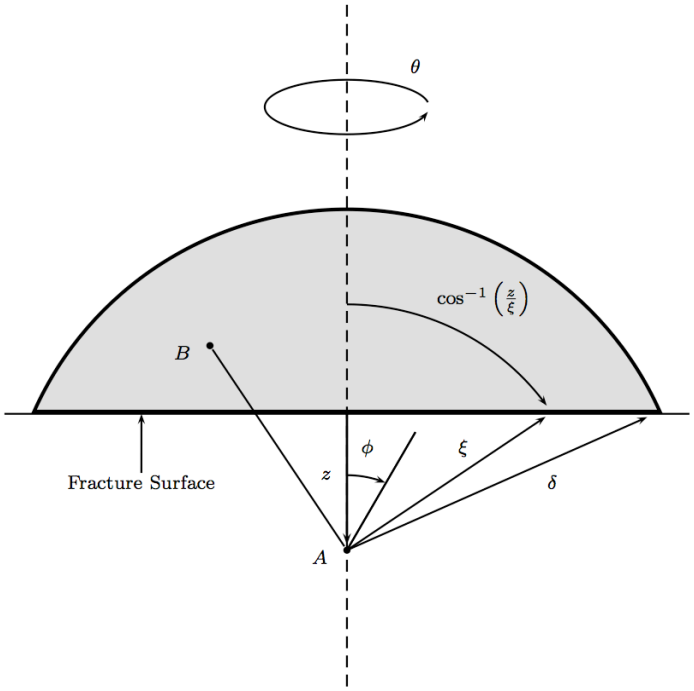

Figure B79. Schematic of fracture surface.

let us consider all points *A* along the dashed line, $0 < z < \delta$, connected to all points *B* across a fracture plane of unit area and within a spherical cap of radius δ with respect to *A* (the shaded area in Figure B79). If we assume there is a critical energy density, w_c, associated with moving each point *A* relative to each point *B*, that when exceeded will cause the removal of any potential between the two points (irreversible bond breakage), then we can sum up all of these energy densities through integration and equate the result with the energy release rate, *G*. That is, the energy required to open a new fracture surface of unit area. This equation is as follows:

[4] The bond energy density will only be fully recoverable if we assume a classically hyperelastic material model, if we assume a dissipative material model then some of the work done on the bond may be permanent.

$$G = \int_0^{\delta} \int_0^{2\pi} \int_z^{\delta} \int_0^{\cos^{-1} z/\xi} w_c \xi^2 \sin\phi \, d\phi d\xi d\theta dz \tag{14}$$

When evaluated and solved for w_c, Equation 15 reduces to:

$$w_c = \frac{4G}{\pi \delta^4} \tag{15}$$

Now we have a critical value of energy density that is based solely on material properties. We can compare this critical energy density to the individual bond energy densities calculated via Equation 13 to determine when the bonds will individually fail. Cracks will nucleate and grow when a number of bond failures coalescence into a surface and propagate. This phenomenon will emerge naturally without the need to specify when and where the cracks will appear through some external criterion. Another advantage to the peridynamic model and allowing the bonds to break in this fashion is that it leads to an unambiguous notion of damage, ψ. The percentage of material damage a continuum point has undergone is simply the volume fraction of broken bonds. For example, if one material point interacts with one hundred others and one bond is broken, the material point is considered 1% damaged.

To numerically implement this failure criterion with the constitutive model described in the previous section, we will activate bond breakage through the use of the influence function contained in the deformation gradient and shape tensors. The term ω(|**ξ**|) was defined as an influence function. It can be used to assign a weight to the amount of influence each bond within the horizon exerts on the point **x**. We can use it to implement damage by setting the influence to zero for the bonds that are broken. Therefore, the failure criterion expressed mathematically is as follows:

$$\omega\left(|\boldsymbol{\xi}|\right) = \begin{cases} 0 & w_{\boldsymbol{\xi}} > w_c \\ 1 & \text{otherwise} \end{cases} \tag{16}$$

When numerically implemented into the explicit dynamics code Emu, we calculate $w_{\boldsymbol{\xi}}$ for every bond at each time step in the simulation and compare it to w_c. If $w_{\boldsymbol{\xi}}$ exceeds w_c, then the influence function is set to zero for that bond, and the bond is effectively left out of the calculation of the deformation gradient at the next time step. The force that was exerted on the point **x** by the broken "bond" will now have to be assumed by the remaining intact "bonds". This additional load on the intact "bonds" may cause them to subsequently break thereby mimicking damage propagation throughout the structure; however, if we are using the method of relating classical stress-strain relationships back into force vector-states as described in the last section we can also employ the classical damage mechanics technique of lowering the yield surface by some percentage of damage allowing the material to effectively soften. This is illustrated mathematically in Equation 17.

$$Y_d = Y\left(1 - \psi\right) \tag{17}$$

where, Y_d, is the scalar value of the damaged yield surface and Y is the original flow stress

The method described above is one advanced way to model damage evolution within peridynamics. A simpler method of breaking "bonds" would be to define a critical stretch,

s_c, at which a "bond" will irreversibly break. The critical stretch is then compared to the actual "bond" stretch shown in Equation 18.

$$s_\xi = \frac{|\boldsymbol{\xi} + \boldsymbol{\eta}| - |\boldsymbol{\xi}|}{|\boldsymbol{\xi}|} \tag{18}$$

The damage is then activated in a analogous fashion to that described previously through the influence function. The critical stretch criterion allows for a simple and effective way to allow damage to propagate within peridynamics, but is not readily determined from convention material properties testing; therefore, it must be estimated using the analysts engineering intuition or by first "fitting" to one set of fracture experiments.

Both the critical work (energy) density criterion and the critical stretch criterion will be used to explore the crack nucleation on the Ductile Failure X-Prize specimen 1A in the following section.

B1.4 Grid Generation

The objective of Ductile Failure X-Prize Assignment 1A was to numerically simulate the quasi-static loading of a uniquely featured specimen made from Ph13-8Mo steel with the H950 heat treatment, and attempt to predict the load line displacement, loading force, and geometric location at which a crack will nucleate.

The first challenge undertaken in the predictive simulations was to generate a discrete grid of peridynamic nodes that efficiently represent the specimen. Initially, a rectangular lattice of nodes was generated that filled the volume of the sample and then the individual features were removed to provide the final geometry. The initial grid spacing was set to 2.54×10^{-4} m, the resulting grid is shown in Figure B80a. This grid resulted in 159780 total nodes with 16 nodes around the circumference of the small hole at the end of the notch.

An artifact of the rectangular lattice configuration is that the small hole is not resolved exactly. This can cause crack nucleation artifacts because of stress concentrators along the hole edges. By using a smaller grid spacing the resolution of the small hole improves, but the number of total nodes increases dramatically. Because Emu is an explicit dynamics code and we are trying to use it to model quasi-static events we must apply the load very slowly to make any dynamic effects negligible, this results in very long run times even with moderate grid spacings.

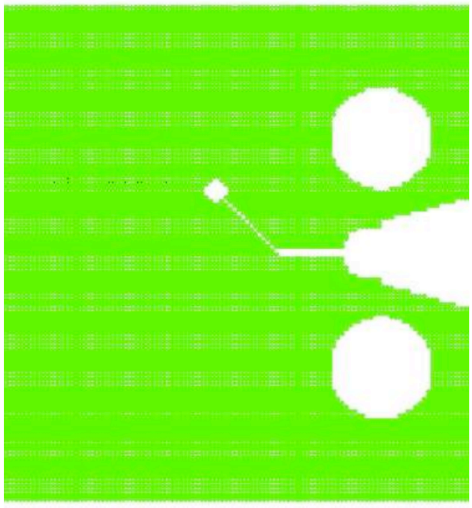

(A) Rectangular lattice grid.

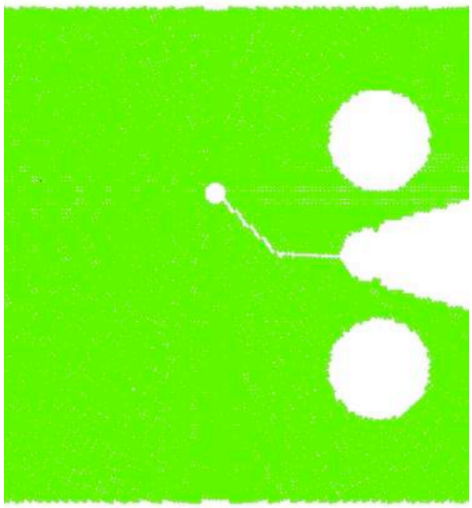

(B) Concentric circular grid.

Figure B80. Comparison of grid configurations

If the grid spacing is decreased too much the time step must be lowered for stability of the numerical simulation and the total run time becomes prohibitively long. Therefore, another grid arrangement was utilized where concentric circles of nodes radiate out from the small hole with a distance between the concentric circles of 2.54×10^{-4} m with a target dimension of the circumferential grid spacing of the same value. Of course, if we divide the circumference of each circle by 2.54×10^{-4} m we would rarely get an integer value and if the nodes were placed along the circumference with this spacing the circle would not complete itself and strange grid artifacts would occur. Therefore, the circumferential grid spacing is only a target distance and allowed to change by a small amount for each concentric circle so that when the circumference is divided by this target distance ± some small perturbation, the result is an integer number of nodes. This results in each circle appearing to be complete, and is a nice luxury of a meshless numerical technique. This

technique resulted in 159864 total nodes and 18 nodes around the circumference of the small hole, the resulting grid is shown in Figure B80b.

The maximum perturbation from the target grid spacing resulted in a circumferential grid spacing of 2.60 x 10^{-4} m and the minimum result was 2.51 x 10^{-4} m. Because the perturbations where small, we used the assumption that the individual node volumes are identical, but the internal volume calculator in Emu may not result in the exact node volumes, therefore, a CAD program was used to find the exact volume of the entire specimen and this volume was divided by the total number of nodes which resulted in an individual node volume manually supplied to the code of 1.703 x 10^{-11} m^3. When the other features are removed from this radial mesh, the features and the outer edges of the sample appear to be somewhat "ragged" this is acceptable because it was assumed, and later shown, that the crack does in fact nucleate from the small hole and therefore the exact resolution of the other features is not as important as the exact resolution of the small hole. Magnified images of the hole resolution are shown in Figure B81.

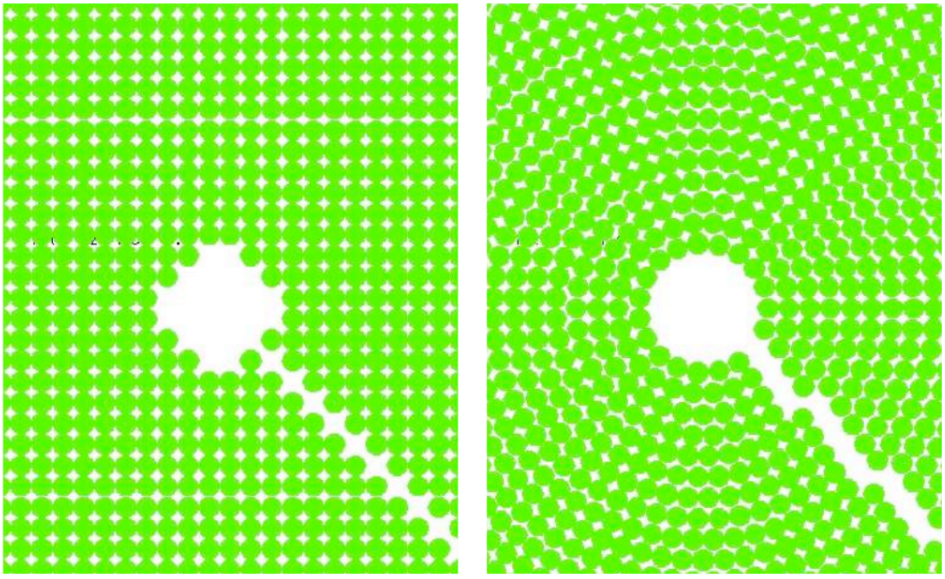

(A) Rectangular lattice grid. (B) Concentric circular grid.

Figure B81. Comparison of magnified hole.

Simulations were run using both grid descriptions above and an identical failure criterion. The results of crack tip position in the x_1 (positive to the right, in Figure B80 and Figure B81) as a function of load line displacement from these simulations is shown in Figure B82. A discussion of how the load is applied and how the actual nucleation point is determined will be discussed in the following sections; Figure B82 is only intended to show the solution differences that result because of irregularities around the small hole. The hatched region in Figure B82 is the x_1 coordinate region where the hole lies. The x_1 crack tip position lines that are within this hatched region are meaningless and occur because the search algorithm that looks for crack nucleation begins its search from the center of the hole. Δ in Figure B82 refers to the driving dimension for grid spacing.

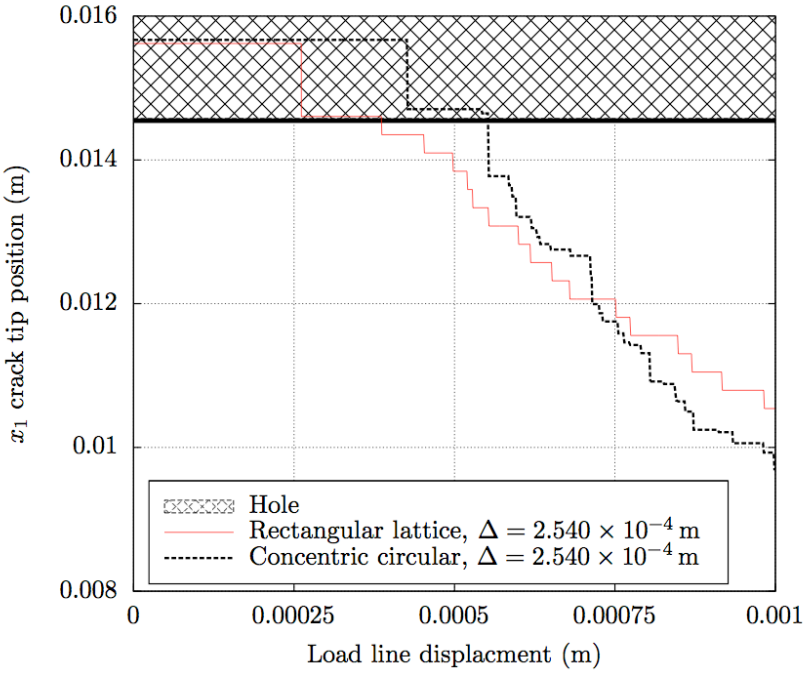

Figure B82. x_1 crack tip position as a function of load line displacement.

B1.5 Numerical Simulations – Energy Failure Criterion

There is not an implicit solver within the numerical peridynamics code Emu; therefore, in order to simulate quasi-static experiments we have to apply a velocity boundary condition with a small magnitude; this, combined with a very small time step creates long run simulation times even when running in on parallel processors. Unfortunately, the energy failure criterion described earlier has not been programmed to run in parallel, therefore, the number of simulations and discretization level of the grid was somewhat limited for this failure criterion. These simulations took approximately 4 days on a single processor.

The velocity boundary condition was applied through a special contact boundary condition at the edges of the two large holes in a fashion that allowed displacement in the x_2 direction (positive up in Figure B80 and Figure B81) without restriction on motion in any other direction (i.e., there are no artificial moments at the "contact points" around the large holes). The load line displacement was tracked through time by monitoring two "tracer" nodes along the load line at locations near where a clip-gage would be used in experiments to monitor load line displacement. The "quasi-static" loading conditions were considered valid by monitoring the load line displacement for oscillations. A velocity was chosen that was small enough that the oscillations were minimal and nearly gone completely by the crack nucleation time.

The energy failure model described earlier uses an input of energy release rate, G. Energy release rate is not a commonly collected experimental measurement; however, we can convert from fracture toughness to energy release rate for plane stress loading with the following equation:

$$G = \frac{K_{Ic}^2}{E} \tag{19}$$

where, E, is the elastic modulus and K_{Ic} is the materials fracture toughness. Of course, these relationships are derived from the assumptions (e.g., small scale yielding) of linear elastic fracture mechanics (LEFM) and if the material has a large plastic response at the crack initiation point and these assumptions are not valid, then K_{Ic} is not a meaningful experimentally determined measurement. Nevertheless, a fracture toughness value for Ph13-8Mo was reported to be 70 MPa-m$^{1/2}$ from [B9], and was used as in input to the code. Although not reported in [B9], there is usually some experimental spread on values for fracture toughness; therefore, simulations were also ran at ± 10% of the reported value. The relationship in Equation 14 is, in fact, more general and not restricted to LEFM assumptions, therefore G could equally be replaced with a J-Integral type failure parameter, J_{Ic}, for elastic-plastic failure if such a measurement was available. Another possibility would be to experimentally determine a J-Integral like measurement around a blunt notch (this would be more representative of a hole, rather than a sharp crack) and use it an input to this failure model. These other suggested measurements may provide more accurate results for a ductile failure.

Because of the way cracks nucleate and growth in an unguided fashion within Emu and the fact that there is not connectivity between the node locations it is somewhat difficult to determine exactly when a very small crack will nucleate. An algorithm was used to search for the maximum x_1 location where a threshold amount of bond failure was reached and this is assumed to be the crack tip position. The search begins from the center of the small hole in the specimen. To determine the actual load line displacement we will assume the crack growth rate is constant right after the nucleation and fit a line to this increment of crack growth. The place where this line intersects the boundary of the small hole will be the crack nucleation point. This fit is done on a plot of x_1 crack tip position as a function of load line displacement and is shown in Figure B83.

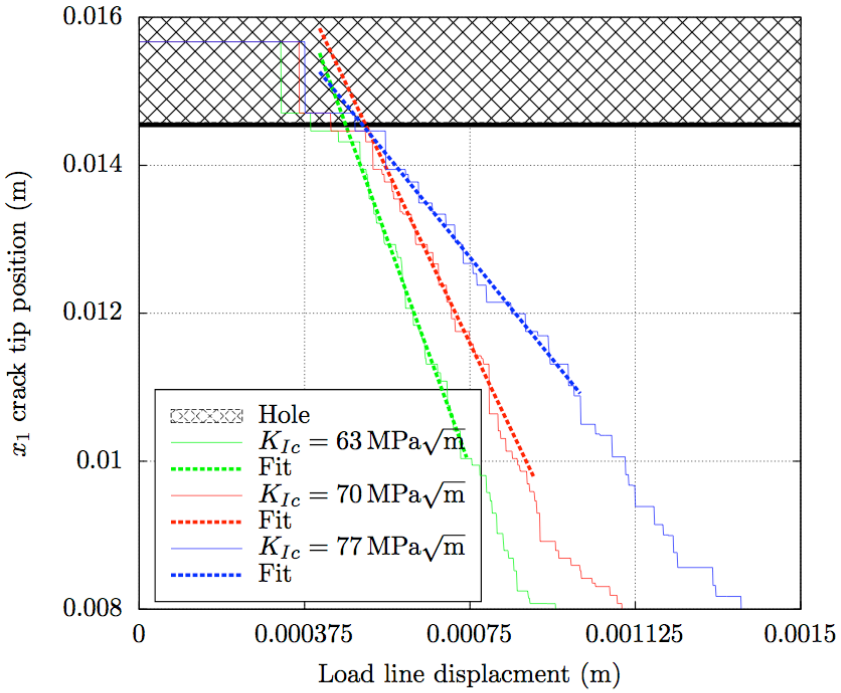

Figure B83. x_1 crack tip position as a function of load line displacement – energy failure criterion.

The fit results in the following equation:

$$x_1 = -12.4888 u_{ll} + 0.0210 \qquad (20)$$

where, x_1 is the crack tip position and u_{ll} is the load line displacement. If we substitute the x_1 position for the edge of the small hole into Equation 20 and solve for u_{ll} we can estimate the load line displacement at which a crack will nucleate. This assumes that the crack nucleates at the maximum x_1 position of the hole which may not be exact, but should give a very close approximation. Using this procedure the load line displacement at which a crack will nucleate is 0.00051 m. The ± 10% simulations are also shown in Figure B83. There appears to be very little effect of changing the K_{Ic} by 10% on the load line displacement at crack nucleation, but there is definite effect on the propagation.

If we take any plane normal to the x_2 direction in the specimen we can easily sum all the peridynamic forces acting on the nodes to get a total force, if the sample is assumed to be in equilibrium then this total force should be equal to the applied load on the specimen. Because these are explicit dynamics simulations there are some (while minimal) transient dynamic effects which cause "noise" in the total load; therefore, the total load was filtered at 10000 Hz to eliminate some of he higher frequency "noise." This filtered load was then plotted as a function of load line displacement along with a reference to the crack nucleation point that was solved previously. The result is shown in Figure B84. The result is a load of approximately 8.5 kN at the crack nucleation point.

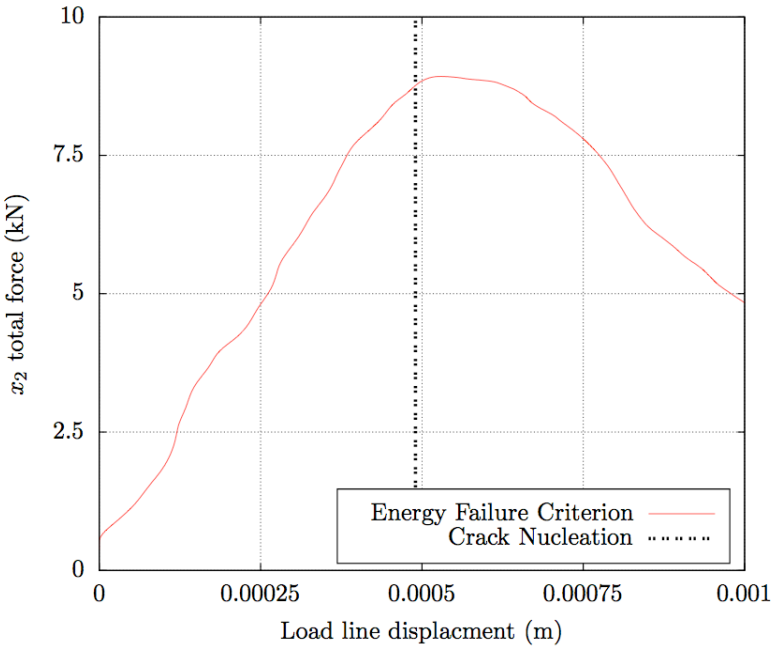

Figure B84. x_2 total force as a function of load line displacement – energy failure criterion.

While propagation was not part of this assignment it was necessary to run the simulation out some time past nucleation in order to back fit the nucleation time. Since the results were available they are shown in for qualitative purposes.

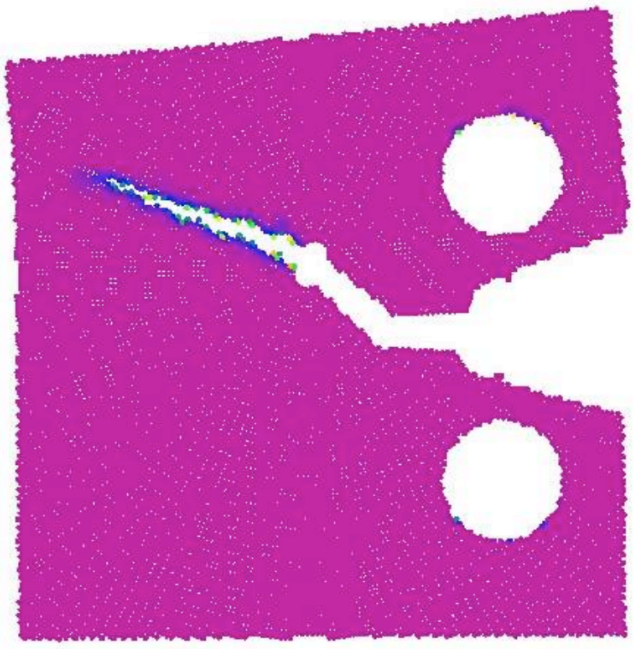

Figure B85. Simulation results showing crack initiation and propagation – energy failure criterion.

B1.6 Numerical Simulations – Critical Stretch Criterion

The critical stretch energy criterion is a much simpler method to model material failure in peridynamics and has been shown to give representative results for many materials. In fact, for a state-based material model in which the force vector-state directions are colinear with the "bond" vector, $\boldsymbol{\xi}$, which we call an *ordinary state based material*, the critical stretch criterion represents a failure criterion where the "bonds" fail at a constant energy release rate. However, it is somewhat difficult to determine experimentally what the correct critical stretch, s_c, should be for a given material. The results shown here are for a critical stretch of s_c=0.12, this number was based on engineering intuition gained from observing the elongation in the uniaxial tension tests and the total elongation reported in [B8]. Ideally, if one where to have the experimental results from one set of fracture experiments, the analyst could "fit" the critical stretch criterion and proceed with blind simulations of other fracture experiments.

Another advantage of the critical stretch criterion as implemented within Emu is that is runs efficiently in parallel; therefore, providing greatly reduced run times and the opportunity to utilize a smaller grid spacing. The grid used in these simulations was similar to the concentric circular grid described earlier except used a driving dimension of Δ=2.03 x 10^4 m, resulting in 312000. This simulation took approximately 10 hours on 16 processors. The results for the crack nucleation as a function of load line displacement is shown in Figure B86.

The resulting equation from the curve fit is shown in Equation 21.

$$x_1 = -8.00931 u_{ll} + 0.0203661 \tag{21}$$

Substituting the x_1 position of the hole into Equation 21 and solving for u_{ll} gives a load line displacement at the time of fracture of 0.00072 m.

The x_2 total force as a function of load line displacement is shown in Figure B86. The maximum load at crack nucleation is 11.65 kN.

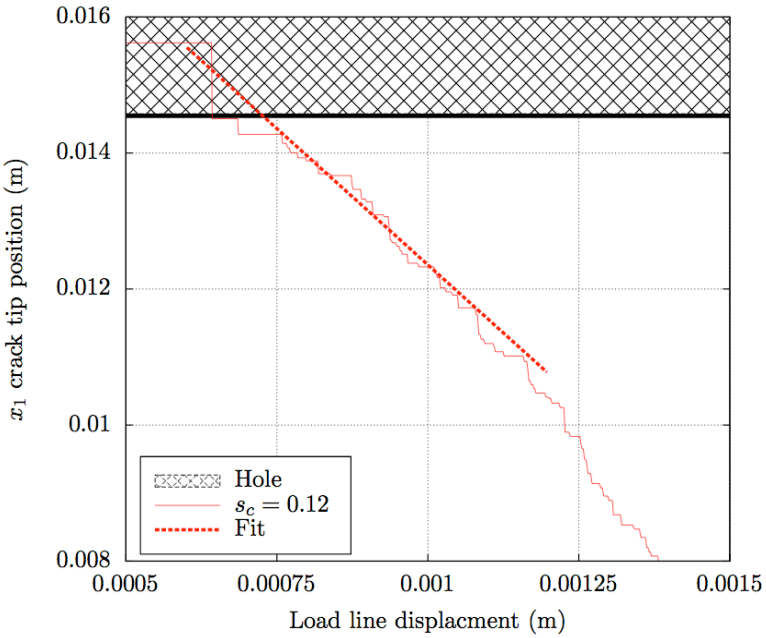

Figure B86. x_1 crack tip position as a function of load line displacement – critical stretch criterion.

For a qualitative look at the crack nucleation and propagation, a simulation for the critical stretch criterion loading condition is shown in Figure B87.

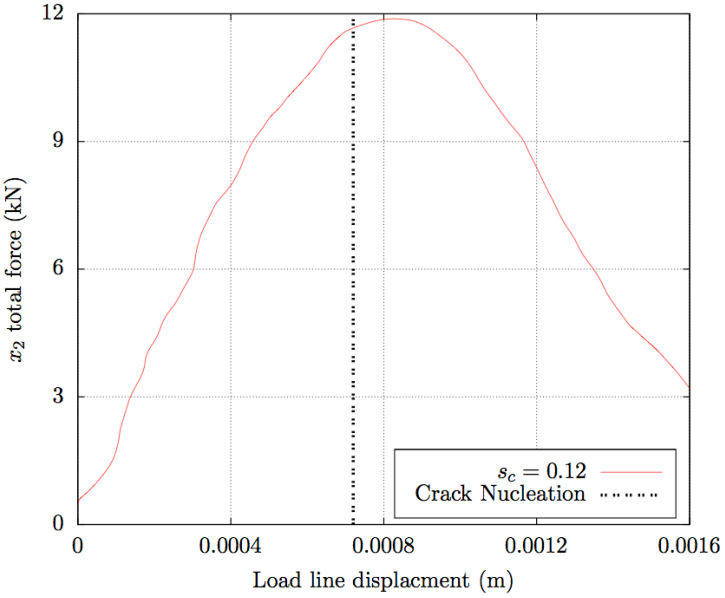

Figure B87. x_2 total force as a function of load line displacement – critical stretch criterion.

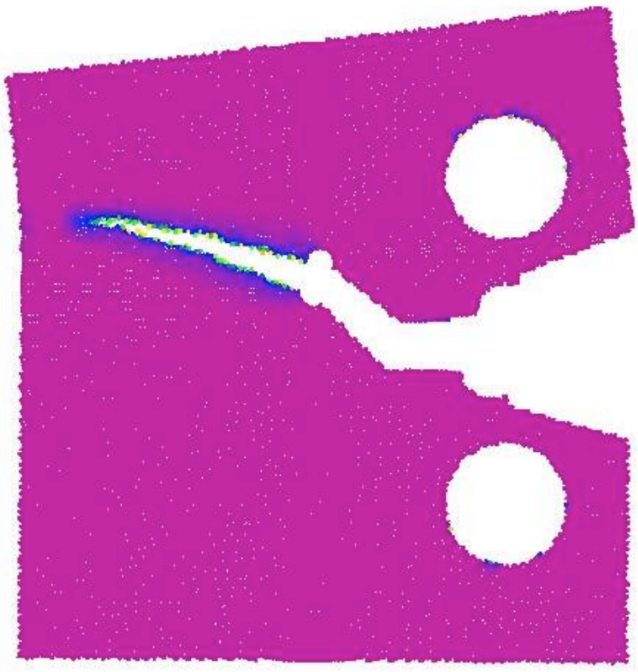

Figure B88. Simulation results showing crack initiation and propagation – critical stretch criterion.

B1.7 Summary of Results

The results from the two failure criterion simulations are summarized in Table B1:

Table B1. Summary of results from simulations.

	Load line displacement @ nucleation		Applied Load @ nucleation	
Units	SI	English	SI	English
Energy Failure	5.1×10^{-4} m	0.020 in	8.5 kN	1911 lbf
Critical Stretch	7.2×10^{-4} m	0.028 in	11.65 kN	2619 lbf

B1.8 Appendix B1 References

[B1] S.A. Silling. Reformulation of elasticity theory for discontinuities and long-range forces. *Journal of the Mechanics and Physics of Solids*, 48(1):175–209, 2000.

[B2] S.A. Silling. Dynamic fracture modeling with a meshfree peridynamic code. In KJ Bathe, editor, *Computational Fluid and Solid Mechanics*, pages 641–644, Amsterdam, 2003. Elsevier.

[B3] S.A. Silling, M. Zimmermann, and R. Abeyaratne. Deformation of a peridynamic bar. *Journal of Elasticity*, 73(1):173–190, 2003.

[B4] S.A. Silling, M. Epton, O. Weckner, J. Xu, and E. Askari. Peridynamic states and constitutive modeling. *Journal of Elasticity*, 88:151–184, 2007.

[B5] S.A. Silling and R.B. Lehoucq. Convergence of peridynamics to classical elasticity theory. *Journal of Elasticity*, (93):13–37, 2008.

[B6] S.A. Silling and E. Askari. A meshfree method based on the peridynamic model of solid mechanics. *Computers and Structures*, 83(17-18):1526–1535, 2005.

[B7] E. Askari, F. Bobaru, R.B. Lehoucq, M.L. Parks, S.A. Silling, and O. Weckner. Peridynamics for multiscale materials modeling. In Journal of Physics: Conference Series, volume 125, page 012078. Institute of Physics Publishing, 2008.

[B8] WD Klopp. Ferrous alloys. *Aerospace Structural Metals Handbook*, Code 1510:1-8, 1988.

[B9] J.E. Campbell. Application of fracture mechanics for selection of metallic structural materials. J. E. Campbel l,(ED.) et al., Metals Park, OH, American Society for Metals, 1982, 384, page 72, 1982.

B2. Follow-Up for Challenge 1A

1. *What was the % difference of your predictions to the experimental values (max force prior to crack initiation and COD displacement at crack initiation)?*

	Load Line Displacement	Peak Force
Critical Stretch Criterion	72.4%	15.16%
Critical Energy Criterion	76.5%	38.62%

2. *If you (or your team) submitted revised predictions, either after the initial due date, or after the comparison between modeling results, did your revisions bring the prediction closer to the experimental values?*

Additional predictions are summarized below:

After the results from the experiments were released additional simulations were ran, by changing the critical stretch "bond" breakage criterion, which for the perfectly plastic material model used here corresponds to a constant energy release rate at the crack tip. Using a much larger critical stretch criterion than was used in the blind simulations, the Emu codes was able to simulate the force as a function of load line displacement curve quite well. This is shown in the Figure B89.

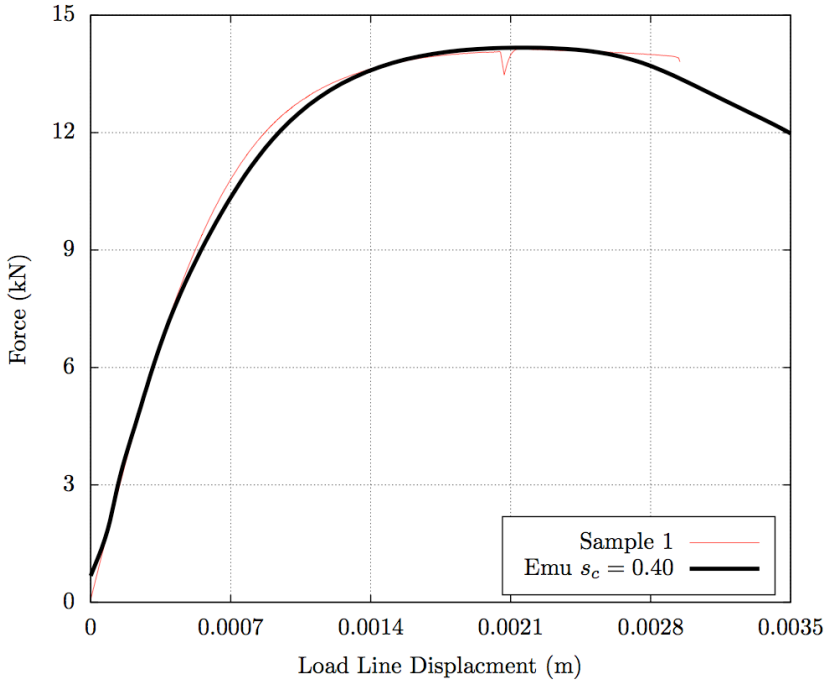

Figure B89. Predicted force-displacement response compared to experimental 'Sample 1'.

The value of critical stretch used here was 40% whereas the value used in the initial experiments was 12%. By simply changing the critical stretch criterion (effectively

increasing the materials ductility) and nothing else, the initial direction of crack propagation was also captured well, even though this was not part of the objectives of this assignment, it is shown in Figure B90 below for illustration.

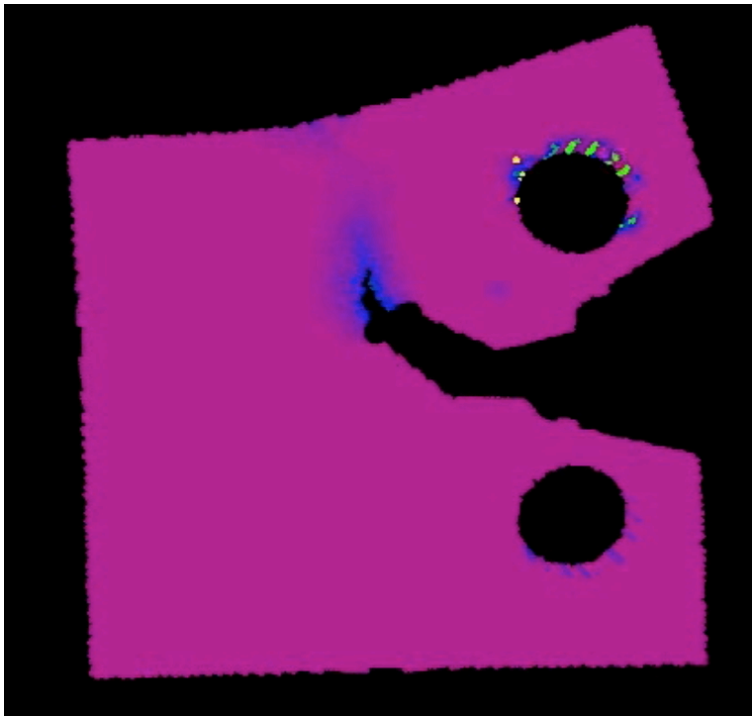

Figure B90. Crack propagation trajectory as predicted by Peridynamics.

The results of the revised simulations are shown in the following table. The energy failure criterion was abandoned for these simulations because for a perfectly plastic material model, both criterions correspond to a constant energy release rate, and the appropriate information to populate the energy criterion model is not available.

Table B2. Revised simulation results.

	Load Line Displacement	Peak Force
Critical Stretch Criterion	10.3%	1.3%

More simulations to really hone in on the exact value of critical stretch could possibly bring the simulations and results even closer.

3. *Describe the source(s) of discrepancy (if any) between your prediction and the experimental result. Where possible, provide quantitative estimates of how much your prediction might have improved if these sources were incorporated into the prediction. Discuss the ease or difficulty in incorporating such improvements in future work.*

The biggest source of discrepancy as illustrated above was the incorrect failure criterion value. As demonstrated with a better value for the critical stretch criterion we have greatly improved the accuracy of the simulation. In future work, if there is available data of actual crack initiation/propagation tests for a material we should be able to get a better fit for this value. As stated in the original report the values for the failure criterion used in the initial

predictions were based on fracture toughness type tests that assume an existing flaw. These were not adequate values for initiating a new crack from a blunt notch.

4. *Was this effort helpful for the development and evaluation of your modeling paradigm? How might we improve the challenges in the future?*

Yes, this was a helpful effort, it showed highlighted the deficiencies in using fracture mechanics type initiation physics for ductile failure problems. I believe the direction the program is taking moving into crack propagation problems is the correct course.

B3. Predictions for Challenge 1B

Peridynamics was applied to predict crack initiation and propagation for the Challenge 1B specimen. The peridynamic analysis utilized state-based peridynamics as implemented in the solid mechanics code Sierra/SM. Material behavior was modeled with an elastic-plastic constitutive law with piecewise linear hardening, and material failure was captured with a critical stretch bond breaking law. Calibration of material properties was achieved via a simulated a tensile test and a simulated compact tension test.

Table B3. Predictions for Challenge 1B.

		1B.1 Δd at crack initiation (mm)	1B.1 Peak force prior to crack initiation (kN)	1B.2 Crack path (e.g. D-E-F or D-A-E-B-F, etc.)	1B.3 Displacement Δd when crack reaches first line (mm)	1B.3 Force when crack reaches first line (kN)	1B.4 Displacement Δd when crack reaches line E (mm)	1B.5 Force when crack reaches line E (kN)
2024-T3	Upper bound	3.4	3.8	D-E-F-A	6.7	2.4	10.5	1.3
	BEST ESTIMATE	2.8	3.8	D-E-F-A	6.3	2.3	9.9	1.3
	Lower bound	2.2	3.7	D-E-A-F	5.9	2.2	9.5	1.0

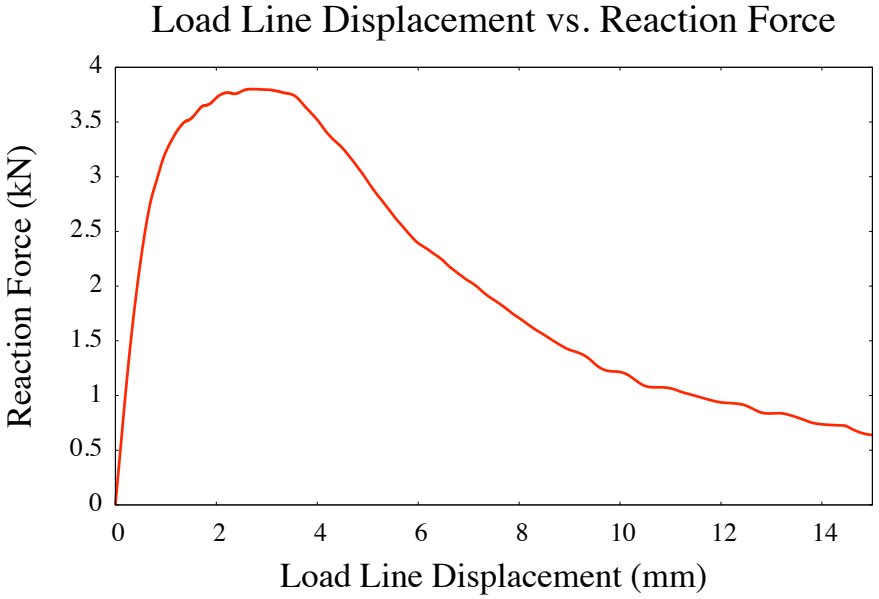

Figure B91 . Reaction force vs. load line displacement (filtering applied to remove high-frequency noise).

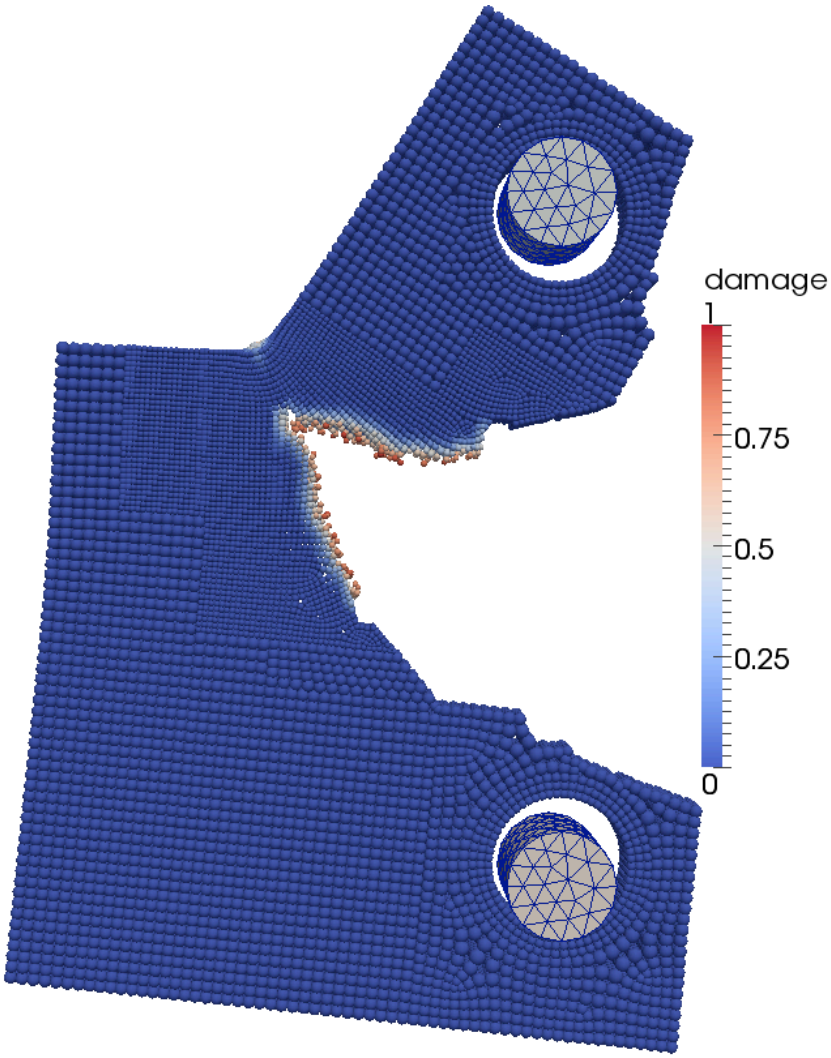

Figure B92. Damage (percentage of broken bonds) during crack propagation.

B4. Follow-Up for Challenge 1B

What do you believe were the most significant sources of error that produced discrepancy between your model and experimental results? Where possible, provide quantitative estimates of how much your prediction might have improved if these sources were incorporated into the prediction. Discuss the ease or difficulty in incorporating such improvements in future work.

The largest discrepancy in the load displacement history seen in our work was the rate at which the force was shed after crack initiation. Factors contributing to this discrepancy may include the choice of bond failure criterion, an error in the hourglass control algorithm[5] utilized in the simulation, and the loading rate applied in the explicit dynamics simulation.

A possible source of error is the bond failure criterion. We use a critical stretch criterion that corresponds to a constant energy release rate. It is observed in experimental data that a constant energy release rate is valid for brittle materials, but that is most likely not the case for these ductile materials. Improvements will likely need to be made here. It is believed that by averaging nodal state variables over a bond it may be possible to implement more classical failure models into this implementation of peridynamics, this has not been thoroughly explored yet.

During the course of this work, it came to light that the hourglass control algorithm within the peridynamics implementation of Sierra Mechanics had an error in which rigid body motion was penalized, this could have been one source that caused the load shedding inaccuracy. This algorithm has been fixed and is undergoing evaluation to see if any improvements are seen in the simulation of this problem.

Finally, we know that having to run these simulations using an explicit time-stepping scheme causes unwanted dynamic effects to enter the simulation. Usually this shows up as oscillations in the force-displacement curves, but it is possible that we are loading the sample at a rate faster than the finite crack growth velocity and therefore not getting the desired outcome. This is speculation at this point and needs to be investigated further.

[5] Hourglass control is needed in this peridynamics implementation that utilizes an approximate deformation gradient in order to map the kinematics back to a classical model that utilizes a stress tensor to describe the material constitutive properties. This is done as a convenience in order to hook into Sierra's Lame material library, but is not really part of "standard" state-based peridynamics.

B5. Predictions for Challenge 2A

Abstract

The Ductile Failure X-Prize project is funded by DOE Advanced Simulation and Computing (ASC) and coordinated at Sandia National Laboratories. The intent is to challenge different groups of computational solution techniques in conducting blind simulations of increasing complexity in modeling the nucleation, initiation, and propagation of ductile failure in engineering materials. The simulations are to be conducted in a blind fashion without any analyst knowledge of the experimental results nor the results of the other computational teams. This paper summarizes the results of the peridynamics team for Challenge 2A, a compact-tension specimen with side grooves that was loaded and unloaded via a prescribed displacement control measured at the crack mouth opening. Peridynamics is a reformulation of classical continuum theory that replaces the partial differential equations of motion with a set of integral-differential equations, and has the unique ability to model discontinuous displacement fields in a mathematically consistent fashion, where the spatial derivatives in the classical theory would be undefined. This allows for straightforward modeling of crack nucleation, coalescence, and propagation without the need for special numerical techniques or external crack growth laws. A reproduction of the problem statement and summary of results for simulations of Challenge 2A using peridynamics is provided.

B5.1 Problem statement

The Challenge 2A geometry has been prepared from aluminum alloy 2024- T3. A detailed machining drawing is included as a pdf (in Appendix A), including tolerances on all dimensions. It has the same outer dimensions as the previous X-Prize specimens (W=1.0), but has a thickness of 0.25 (rather than the 0.125 thick specimens used in previous X-Prize studies). This specimen does not contain an inclined notch, but rather a straight pure mode-I notch to a length of a/W = 0.2, and a mode-I fatigue precrack has been grown to a/W = 0.3 per ASTM E399 standard load shedding techniques. To avoid shear lips on the surface of the specimen, 0.063 deep V-grooves have been machined into both sides along the Mode-I crack path. For a displacement-controlled loading regimen, as shown below (reproduced in Figure B93 with time scaling), predict the unloading compliance (change of force over change in displacement), for unloads labeled A-D. What was the crack length at the peaks associated with A-D? Please report your compliance values in N/mm, and your crack length values in mm. You are welcome to bound your results as you see fit, but recognize that overly broad bounds suggest a lack of predicitivity.

B5.2 Predictions

An aspect of Challenge 2A that proved challenging to the analyst was the prescribed displacement loading/unloading. In the experiment, a clip gage that measured displacement was attached to the knife edges at the crack mouth and this measurement was fed into the standard test frame as a reference signal which in turn controlled the pin displacement. Without considerable effort, given the tools available to the analyst,

controlling the pin displacement based on measurements taken at the knife edge is not possible to do using the peridynamics implementation in the SIERRA/Solid Mechanics transient dynamics code. Therefore, a trail-and-error effort was undertaken to match the experimental displacements. This trial-and-error approach was further complicated by the fact that the knife edge load line displacement changes considerably with crack initiation and advancement. What this means is that any changes to the simulation material or failure model which influences crack initiation and propagation requires a new trail- and-error calibration of the loading/unloading. The "best-fit" prescribed displacement results compared to the experimental displacements is shown in Figure B93. Note that the simulation displacements are much "smoother" than the experimental displacements. This was done intentionally by fitting trigonometric functions through the experimental data. The purpose of this "smoothing" was to reduce any dynamic effects that may result from abrupt transitions in displacement in an explicit dynamics calculation. In addition, the total time in which the simulation was conducted is several orders of magnitude faster than the total time of the experiment. For this reason, the experimental displacement curve shown in Figure B93 is time scaled to match the total simulation time. It is unknown, at this point, how much affect either the "smoothing" of the prescribed displacement or running the computation very fast as required by the explicit integration scheme will have on the reported results.

Many simulations were conducted over the course of this challenge. Figure B94 represents the analyst team's best prediction for pin reaction force as a function of load line displacement measured at the knife edges. Straight lines were fit to each of the four unload regions to infer the unloading compliance of the sample. The slope of these lines (represented as m in the legend of Figure B94) are respective unloading compliances. In addition, the crack length was estimated at the beginning of each of these unloads, referred to as A, B, C, and D in the problem statement. The reason for describing the crack length as an estimation, stems from the nature of how cracks are formed in a peridynamics simulation. In peridynamics, cracks are formed when many broken "bonds" coalesce to a surface; therefore, precisely defining the resulting surface is difficult. Table B4 summarizes the compliances during the unloads that occur after the peaks labeled A, B, C, and D in the problem statement and the crack length (measured from the knife edge) as best estimated at these peaks.

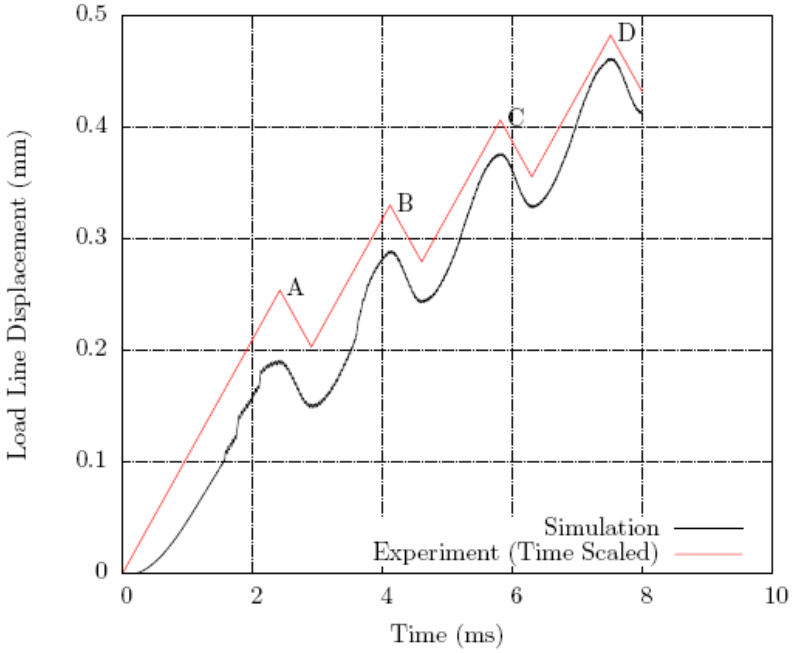

Figure B93. Load line displacement as a function of time

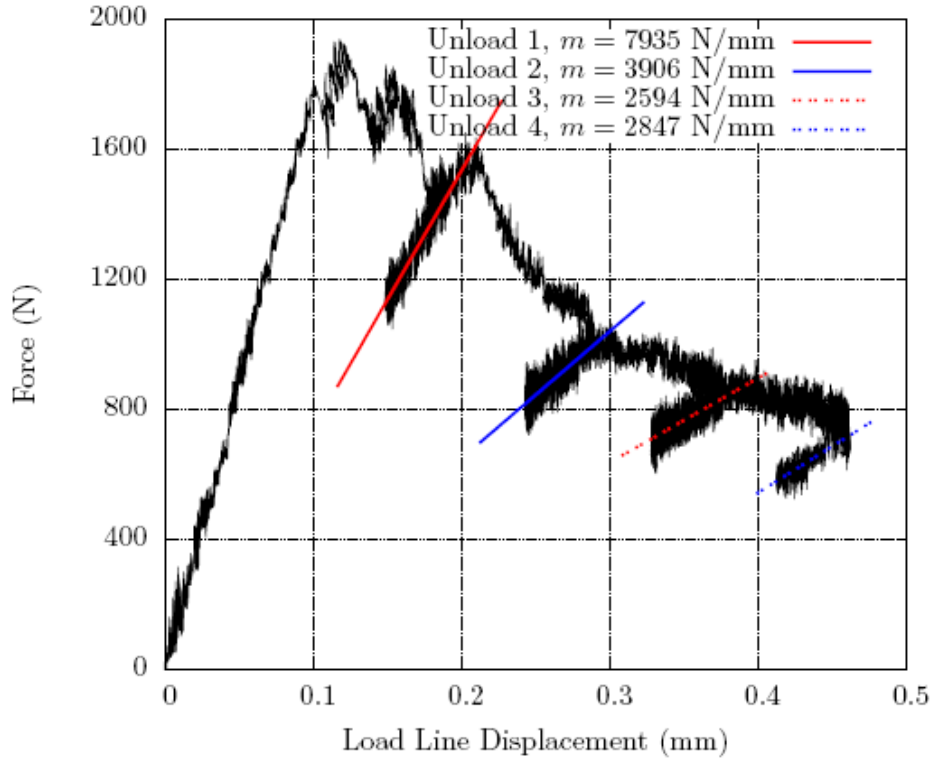

Figure B94. Pin reaction force as a function of load line displacement

Table B4. Summary of results from simulation

Peak Label	Unloading	Total Crack Length, a
A	7935 N mm−1	11.78 mm
B	3906 N mm−1	16.67 mm
C	2594 N mm−1	18.66 mm
D	2847 N mm−1	19.81 mm

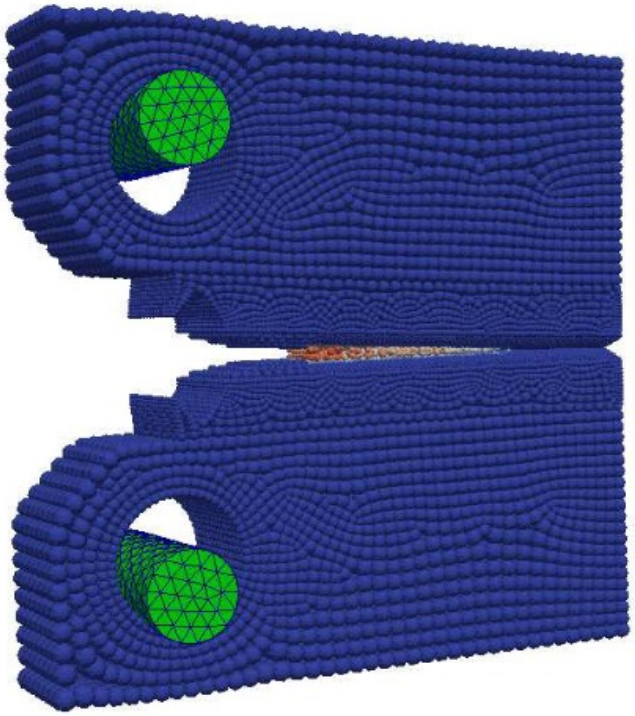

Figure B95. Snapshot of simulation animation

Figure B95 shows an animation of the load/unload simulation showing the crack advancement in color contours of damage. Displacements are exaggerated by a scale factor of two to aide in the visualization.

B5.3 Final Remarks

In preparation for this challenge a tremendous amount of time was spent by the analysts calibrating the peridynamic bond failure models based on the results of Challenge 1B. The recent simulations of Challenge 1B show a marked improvement over the blind simulations that where turned in originally. Additional physics where added to the bond failure models which resulted in these improvements. When the parameters that gave the "best results" for Challenge 1B where used in the blind simulations for Challenge 2A, the result was that the precrack never advanced. There is a considerable amount of difference in the two Challenges,1B having a very blunt defect and 2A having a sharp precrack, and it is not completely a surprise that our calibration parameters did

not work as it is observed in experiments to collect Fracture Toughness and Notch Toughness values in metals that the energy release rates are much larger when the defect is blunt. Since our calibrations from 1B resulted in zero crack growth in the 2A simulations, and it was assumed that we were not being asked to predict a "fracture experiment" without fracture, an extrapolation technique was used to de- termine what the bond failure should be using information from 1B after the crack initiated from the blunt defect. The crack behavior is quite strongly sensitive to the bond failure model and for this reason we chose to turn in our single "best estimate" as opposed to submitting many answers resulting in large error bounds.

One extremely positive take-away from this exercise was that all of the analysis effort concentrated on investigations into the physics and choice of the bond failure model, as well as the time spent attempting to achieve the proper displacements through the load/unloading cycles. Peridynamics was successful in providing a framework for modeling three-dimensional crack growth, no numerical difficulties were encountered in modeling crack propagation, arrest, and further propagation.

B6. Follow-Up for Challenge 2A

The presentation of the experimental results revealed that our simulations under predicted the unloading stiffness and over predicted the crack length at the unloads. The over prediction of crack length is explained by the fact that the crack initiated too soon, or at too small a peak load. A possible explanation is that our failure model was calibrated using data from Challenge 1B, in which the crack initiated after a considerable amount of plastic flow had taken place around the inclined notch. This plastic flow created a complex stress state in the vicinity of the crack initiation site, possibly including a high degree of ``triaxiality'' or ``confinement'' that aided in the crack initiation. Since our bond failure model did not include an explicit dependence on triaxiality, but rather used a heuristic fit to the Challenge 1B data, and because it is very unlikely that the current Challenge included anything but a pure Mode I stress state with little plasticity at the crack tip, it is speculated that the crack initiated too soon due to an artificial effect of triaxiality that implicitly appeared in the bond failure model but was not occurring in the experiments. This could be improved by utilizing a bond failure model that had an explicit dependence on triaxiality. This feature was discussed during the lead up to submission of the predictions for this Challenge, but was not implemented in time to turn in results. Since the unloading stiffness is related to the crack ligament in the sample, it only follows that we under predicted the stiffness as a result of over predicting the crack length. The crack length reported in our prediction for Unload A roughly corresponds to the crack length reported at Unload C in the experiments. Taking this into consideration, it is encouraging that the unloading stiffness reported in our prediction for Unload A is roughly comparable to the unloading stiffness reported at Unload C in the experiments.

In summary, had our bond failure model not severely under predicted the load at which the crack initiated, it is believed that our crack length and unloading stiffness predictions would have been in closer agreement with the experiments.

APPENDIX C: LOCALIZATION ELEMENTS

Jay Foulk, Alejandro Mota, Jake Ostein, Arthur Brown, and John Emery, Alex Lindblad

C1. Predictions for Challenge 1A

Abstract

The simulation of fracture and failure in a production environment with limited experimental data is a daunting task. In this work, we examine fracture/failure in the context of a local damage model regularized by localization elements. We demonstrate that not only is the method convergent but also explore the applicability of the methodology in the context of both academic and non-standard fracture geometries. We illustrate how one with limited data might populate the models and then how to apply them with rigor. In short, we attempt to demonstrate that the implementation is sufficiently verified and validated for a production environment and can be employed for implicit quasi-statics as well as explicit transient dynamics.

Key words: localization elements ductile fracture damage mechanics Finite elements

C1.1 Introduction

Ductile crack nucleation and growth is a complex phenomenon that plays a key role in component structural reliability. Thus, computational models that accurately predict such phenomenon are of utmost importance to structural analysts and designers. Void nucleation, growth and coalescence are the mechanisms typically associated with ductile failure. Ductile crack nucleation and growth originating from smooth stress concentrators, e.g. bolt holes, are of particular interest and, in the absence of a sharp crack, preclude traditional fracture mechanics approaches. The stress field in the vicinity of such geometrical stress concentrators is often complex having a high stress triaxiality, the ratio between the mean stress and the effective stress. This triaxial stress state exacerbates the mechanisms. Hence, predictive models frequently include the triaxiality.

C1.2 Framework for Prediction

We seek to develop a class of methods for solution to the balance of linear momentum for quasi-statics, implicit-dynamics, and explicit-dynamics. In this document, we will focus on quasi-statics. However, we will include a the conditions for a stable time step for explicit calculations. Because many applications involving ductile fracture evolve over ms, explicit transient dynamics can be employed. However, discretization issues and longer time scales favor implicit dynamics. Implicit dynamics can also be favorable to quasi-statics regarding issues of crack stability.

C1.2.1 Material

In this work we will focus on structural metals. Specifically, the alloy selected for analysis is PH13-8 H950 martensitic stainless steel. The H950 condition was selected because it is the most commonly employed heat treatment and contains both high strength and relatively high

toughness. Data sheets provided the elastic properties and the hardness. A series of tensile tests were also given. It is evident that the yield strength of the alloy (no matter the metric) is substantial. Those series of tests are noted in Figure C96. We note that without information regarding neck formation, one might assume the material necks after relatively small strains (~0.02 mm/mm). An inverse problem must them be employed to examine the extend of hardening within the neck. Without information regarding the evolution of the neck, that inverse problem might be problematic. In addition to an inhomogeneity in the strain field, one must also deal with inhomogeneities in strain rates. In addition to providing information regarding deformation, each tests also fails. Fortunately the tests are closely grouped so that we will not worry (initially) about specimen to specimen variations.

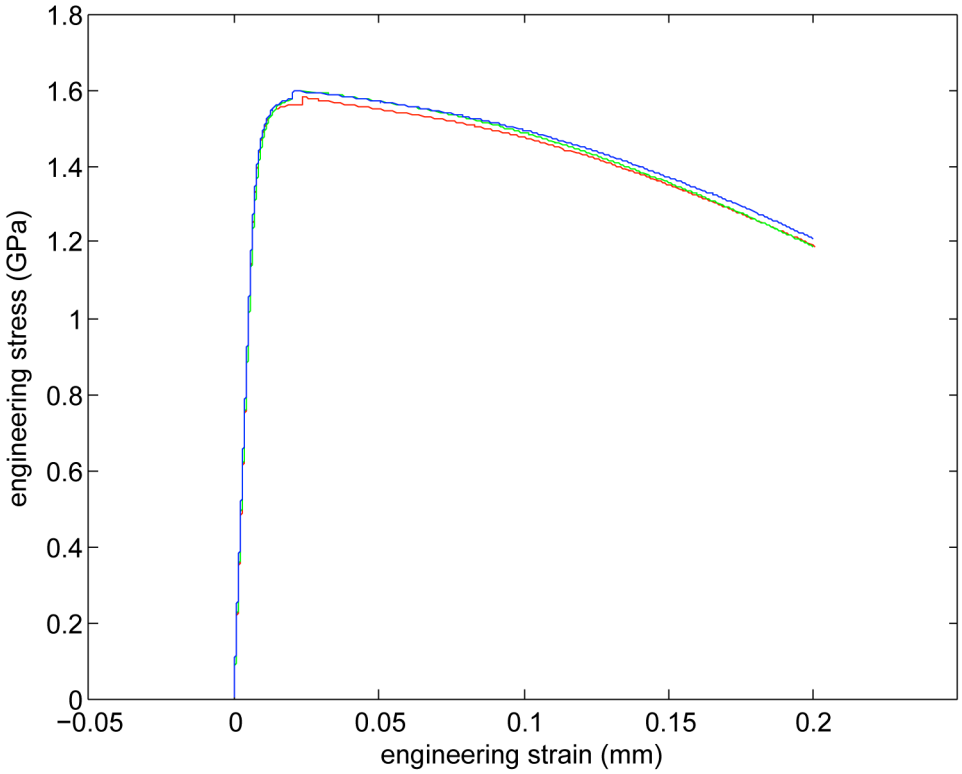

Figure C96. Three tensile tests performed on PH13-8 H950 stainless steel. After relatively little deformation, necking might have occurred. Geometric information with regard to the shape and evolution of the neck was not available. Note that the yield stress is nearly 1.6 GPa.

After looking through the literature, we could only supplement a tensile test with the plane strain fracture toughness. Given in [C3] , the plane strain fracture toughness K_{Ic} is 70 $MPa\sqrt{m}$. The alloy was employed on the B-1B bomber and the values are quoted as valid fracture toughness tests performed for that program.

C1.2.2 Failure modes

Out the outset, we assume that the alloy will fail through the micromechanics of void nucleation, growth, and coalescence. The evolution of these processes is influenced the geometry, product form, and loading. Specifically, we will be predicting fracture initiation for a particular thickness. Given the plane-strain fracture toughness, we cannot easily predict the variation of toughness with thickness (without tests that explore that transition). Decreasing thickness results

in lower triaxialities and reduced void growth. In addition, increased plasticity aids resistance curve (R-curve) behavior. In general, the fracture mode will change from flat-fracture (mode I) to mixed-mode fracture (mode I-III) with decreased thickness. Without experimental data, one will have difficulty being predictive. However, we can explore simple models tuned to limited data to determine both the applicability of the model and need for future testing.

C1.2.3 Constitutive model

Because we are employing a single quasi-static test to characterize the deformation of the alloy, we limit elastic-plastic response to independent of both rate and temperature. In this work, we employ a viscoplasticity model (Brown 2010) and essentially turn off rate dependence and temperature dependence. The flow rule is given as

$$\dot{\varepsilon}_p = f\{\sinh[\frac{\bar{\sigma}}{(1-\phi)(\kappa+Y)} - 1]\}^n \quad (1)$$

where ε_p is the equivalent plastic strain, $\bar{\sigma}$ is the effective stress, f and n govern rate dependence, ϕ is the scalar damage parameter concentrating the stress, and Y and κ and represent the initiate yield stress and isotropic hardening variable, respectively. For our studies, we consider f to be large such that the response is effectively rate independent and also independent of n. The yield stress Y was taken to be 1.6 GPa. The isotropic hardening variable κ evolves through an evolution equation that incorporates hardening H and recovery R_d.

$$\dot{\kappa} = [H - R_d\kappa]\dot{\varepsilon}_p \quad (2)$$

We note that if H is constant and R_d is effectively zero, we obtain linear hardening. For this study, we have chosen H to be 492 MPa and R_d to be 0.001. The hardening modulus was based on data obtained from [C4] for PH13-8 H977. Bridgman correction factors were employed to yield a final true stress and true strain (effective) of 1.75 GPa and 0.308, respectively.

In addition to a model for plastic flow, the model also incorporates scale damage (or porosity). By scalar, we assume that the damage evolution to be isotropic and described by [C5]

$$\dot{\phi} = \{\frac{1}{(1-\phi)^m} - (1-\phi)\}\sinh[\frac{2(2m-1)}{2m+1}\frac{\langle\sigma_h\rangle}{\bar{\sigma}}]\dot{\varepsilon}_p \quad (3)$$

where the evolution of the damage ϕ is governed by the hydrostatic stress $\sigma_h = \frac{1}{3}\mathrm{tr}[\sigma]$, effective stress $\bar{\sigma}$, power-law creep exponent m, and the equivalent plastic strain ε_p. For power law creep, $\dot{\varepsilon}_{ss} = \dot{\varepsilon}_0(\bar{\sigma}/\sigma_0)^m$ and ε_0, σ_0, and m are material properties. Note that, in practice, we do not conduct a creep test to obtain material properties. Rather, we use the aforementioned functional form and fit m to experimental data (or handbook values). If we are able to span many triaxialities $\langle\sigma_h\rangle/\bar{\sigma}$ for a single m, we might consider that the approximation of dilute void growth in a power-law medium is justified. However, without experimental data spanning triaxility, we cannot adequately evaluate the applicability of the functional form.

Because of the lack of experimental data, we attempted to bound m through extremes in the triaxiality. Given that Figure C96 does provide the displacement at failure, we can model the evolution of the neck and predict the displacement at failure. We consider this to be a lower bound on the triaxility but it is possible that thin sheet (a product form not addressed in this study) may exhibit lower constraint. The other experimental quantity we can employ is the plane-strain fracture toughness K_{Ic}. Through the application of a far-field displacement field

derived from linear elastic fracture mechanics (LEFM), we can effectively simulate a plane-strain fracture toughness test. One still needs to contend with the issue determining the crack length for initiation, but at least we can explore an upper bound on the triaxiality. The details of these studies and the bounds they yield will be discussed in Section C1.3.

C1.2.4 Regularization

Because we have chosen to employ a local damage model that includes softening, we need employ a method for regularization. If we choose to plow ahead with a local model, the system will bifurcation and corrupt the partial differential equation. In short, we will be solving an ill-posed problem. The corruption of the equation we are attempting to solve, the balance of linear momentum, is revealed to the analyst as a mesh-dependent solution. Because common methods of regularization add a length scale to the system that is independent of the mesh size, we often refer to regularization as mesh-independent methodologies. In general, the methods of regularization can be grouped into surface and bulk approaches. Surface methodologies relegate the failure process to surface separation. Laws that govern surface separation are often referred to as cohesive laws. A length scale governing gap separation yields a process zone size. A cohesive surface element contains both the upper and lower surfaces and integrates the response through a mid-plane. Alternate bulk methodologies include nonlocal and gradient methods. Nonlocal methods typically employ the same local model with nonlocality in the variables that load to bifurcation. The classical implementation is a nonlocal ball with a gaussian weight function. Gradient methods may mirror nonlocal methods or introduce additional physics. Partial differential equations are introduced to regularize local ordinary differential equations. In each case, one must resolve the introduced length scale. Many elements should span the process zone size, nonlocal ball, or damage front.

Another methodology recently introduced by [C12] is localization elements. Localization elements still seek to lump the failure process to a surface. However, rather than pose an additional model for surface separation, localization elements employ the same local model and introduce a novel, multiplicative deformation gradient to evolve the failure process. The deformation gradient stems from a multiplicative decomposition of in-plane F^{P} and an out-of-plane $F^{\perp}$ deformation gradients where $F = F^{\mathsf{P}}F^{\perp}$. The in-plane or membrane deformation is constrained by $F^{\mathsf{P}}N = N$ and the out-of-plane deformation is

$$F^{\perp} = I + \frac{\Delta}{h} \otimes N. \qquad (4)$$

The length scale is imparted through h and it typically referred to as the band thickness. We must note that this thickness is a material property but the length scale introduced into the simulation (via a process zone size) is an outcome of h, the material model, and the mode of loading. Figure C97 illustrates the displacement jump Δ, input length scale h, and the mid-plane with normal N and traction T.

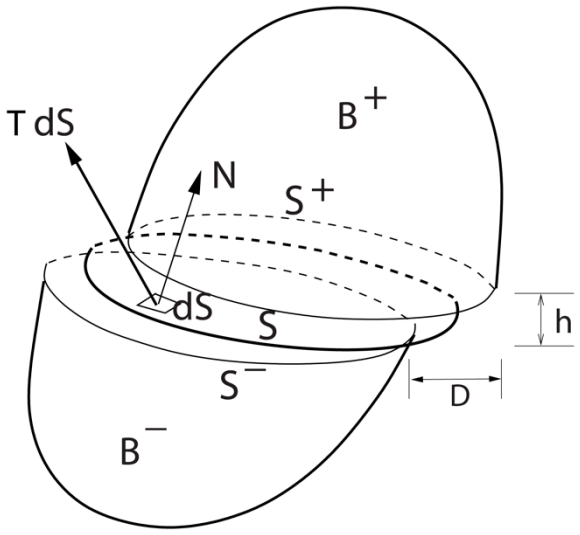

Figure C97. The deformation gradient results from a multiplicative decomposition of the deformation gradient of in-plane and out-of-plane deformations. The perpendicular displacement gradient $F^{\perp}$ results from the displacement jump Δ, input length scale h, and mid-plane normal N.

We again note that this approach contrasts other surface methods which employ both a bulk model and a surface (typically cohesive) model. The two model approach does have applicability but it also suffers from a few notable issues when applied to ductile fracture. One issue revolves around the cohesive strength. If the cohesive strength is over 5 times the yield stress, J_2 with hardening cannot guarantee that local fields will satisfy the required cohesive strength. Consequently, the crack will blunt and not propagate. Although one can invoke other phenomenological approaches to plasticity (strain-gradient plasticity, crystal plasticity, etc.), this argument stems from the fact that the analyst has chosen a cohesive approach to fracture and not that J_2 is necessarily inadequate.

Other issues that can complicate cohesive formulations stem from the fact that the micromechanics might convolute the cohesive approach. For example, in many structural alloys, void nucleation, growth, and coalescence dominate the failure process. Void growth have been shown to be heavily dependent on the triaxiality, $\langle\sigma_H\rangle/\bar{\sigma}$ where σ_H is the hydrostatic stress and $\bar{\sigma}$ is the effective stress. Put simply, the traction on a surface is independent of the in-plane stresses. Consequently, it is difficult to incorporate features such as the triaxiality into cohesive approaches to fracture. One must employ data structures to sample or project (and average) the triaxility from adjacent bulk elements. The kinematics of localization elements (with F^{P}) simplifies the implementation and naturally yields quantities $\langle\sigma_H\rangle/\bar{\sigma}$ relevant to void growth.

For the work presented herein, we will limit our work to predefined planes. This is obviously a disadvantage and we are working on adaptive methods for generalized fracture. Adaptive insertion, adaptive remeshing, and X-FEM are being considered. We still believe that we can still learn a great deal from a seeded path. Verification and addressing challenging problems is necessary to make improvements and modifications to the methodology.

C1.2.4.1 Addressing volumetric locking

Initial simulations revealed that fully-integrated localization elements, like four-noded quadrilateral elements, lock during isochoric deformations. To remedy this issue, we implemented a constant pressure formulation (Nagtegaal 1974, Hughes 1980). Rather than form an averaging operator ($\overline{\mathrm{B}}$), we instead elect to volume average (or in this specific case, area average) the pertinent kinematic quantities such that a mean pressure will result for each integration point. For hypoelasticity, the stress in the "unrotated" configuration can be written as

$$T = \lambda \mathrm{tr}[d] I + 2\mu d \tag{5}$$

where T and d are the stress and the rate of deformation tensor in the unrotated configuration ($T = R^T \sigma R$, $d = R^T D R$). Because the pressure is only a function of the $\mathrm{tr}[d]$, we can find

$$\hat{d} = \frac{1}{\int_{S_e} dA} \int_{S_e} \mathrm{tr}[d] dA \tag{6}$$

and use the area averaged quantity $\hat{d}$ to redefine the unrotated rate of deformation tensor

$$d = d + \frac{1}{3}(\hat{d} - \mathrm{tr}[d]) I \tag{7}$$

at each integration point in the element spanning S_e. We did verify that this construction does yield a constant pressure and did remedy locking. For hyperelastic models, the methodology is very similar. Provided the stored energy function is uncoupled, the pressure is a function of J where $J = \det[F]$. We define $\hat{J}$ to be the area averaged quantity

$$\hat{J} = \frac{1}{\int_{S_e} dA} \int_{S_e} \det[V] dA \tag{8}$$

where V is the left stretch tensor and $\det[V] = \det[F]$. Note that we use V because it is handy and the material model interface does not pass F. We can then redefine the left stretch

$$V = \hat{J}^{\frac{1}{3}} I (J^{-\frac{1}{3}} V) \tag{9}$$

at each integration point in the element spanning S_e. We still need to verify the methodology for uncoupled stored energy functions.

C1.3 Populating the resistance

Given little information, we are challenged to populate a damage model. As noted in Section C1.2, we will attempt to employ simulations of vastly different triaxialities to bound the material behavior. Because we expect the failure process zone to be on the order of hundreds of microns, we select a normal length scale h to be roughly an order of magnitude smaller than the process zone size. For this specific case, we selected $h = 30\ \mu m$. It is our hope that for the boundary value problem of interest, the selected h will generate a process zone size that is representative of the failure mode. Because we do have K_{Ic} toughness, we will employ a K-field boundary condition and simulate the plane-strain fracture toughness. In addition we will also consider necking in the smooth tension. The ability to use the bounds from the K-field simulation to simulate failure in a necked sample will provide insight with regard to the damage model and determine if the model for void growth is applicable over a range of triaxialities.

C1.3.1 K-field simulations

The K-field boundary condition is employed through the analytical solution for a crack in an infinite domain. That solution yields the stresses, strains, and displacements at some radius r and angle θ. Therefore, given a crack location in the body, one can always establish a local, polar coordinate system to yield the displacement field (u_1, u_2) for any (X_1, X_2). We stress that the linear elastic fracture mechanics solution is not appropriate for near-tip fields but it is quite appropriate for the far-field. Provided that the crack-tip nonlinearities are in a small region compared to the region of the body (small-scale yielding) one can apply a far-field LEFM displacement field and accurately assess the predicted fracture toughness. We should also add that because the fields at the far-field are reflective infinitesimal deformations, we have a nice representation of the driving force. The coarsest K-field mesh is illustrated in Figure C98. Elements at the crack tip are 60 μm. In this case the element size is twice the value of h. Future refinements, $s = 30$ μm and $s = 15$ μm, are employed to investigate mesh convergence. Because we only have the plane-strain fracture toughness K_{Ic} = 70 $MPa\sqrt{m}$, we are not quite sure the crack length about which K_{Ic} was recorded. Consequently, we will sample the applied K_{app} for increasing crack lengths and make judgements regarding initiation and resistance-curve behavior.

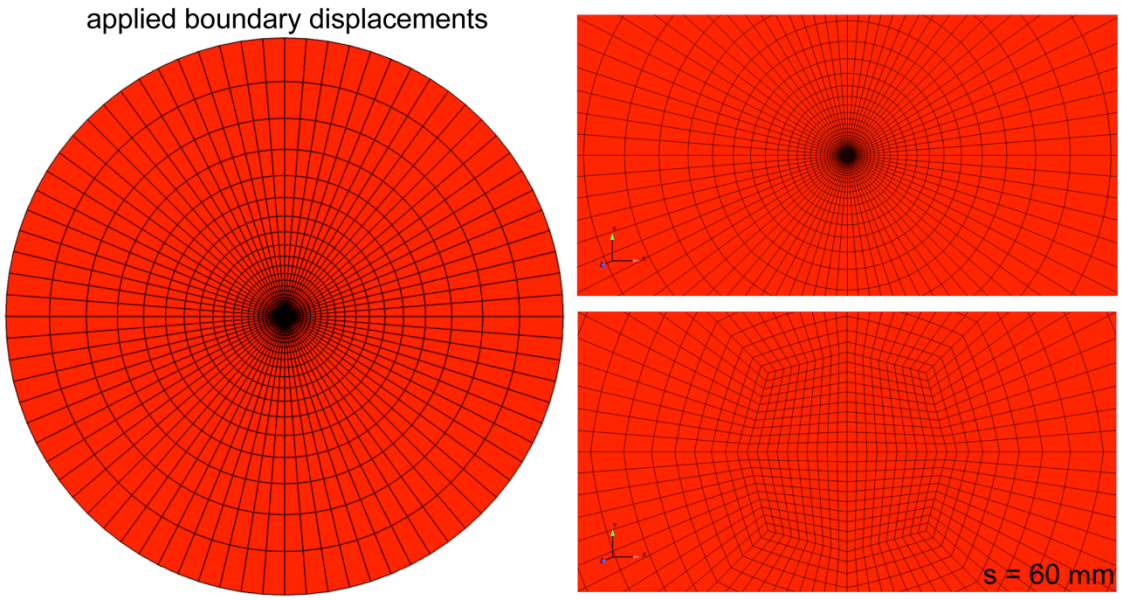

Figure C98. Discretization of the K-field geometry. For a given applied stress intensity factor, $K_{I,app}$, a displacement field is derived from LEFM and applied to the outer boundary via a node set. Elements are the crack tip are on the order of 60 μm.

To illustrate the concept of varying m and recording the K_{app} at two elements of crack growth, we include Figure C99. The element size is 30 μm and we are recording the toughness K_c at an increment of crack growth $\Delta a = 60$ μm. As expected, the toughness varies with m. For the selected bulk model, it appears that m = 5 is near the plane-strain toughness and that the value is bounded by m = 4 and m = 6. In Figure C99, the plastic zone (red) is shown through ε_p > 0.001. Again, as expected, the plastic zone size scales with the toughness. Less obvious is the shape of the plastic zone. For values of m = 4 and m = 5, the plastic zone appears to be "physical" or aligned with what one might obtain if they just simulated crack-tip blunting

without damage evolution. Large values of m clearly distort the plastic zone size. For m = 8, the plastic zone appears almost circular.

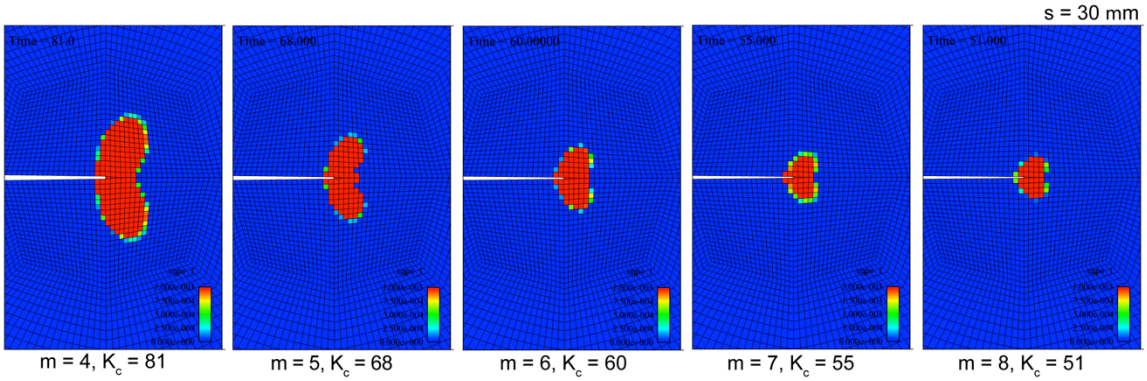

Figure C99. The plastic zone size for varying damage parameter m after 60 μm of propagation (Δa). The mesh size s at the crack tip is 30 μm. The plane-strain fracture toughness for PH13-8 H950 is 70 $MPa\sqrt{m}$.

After numerous simulations, one can construct a table to differentiate the element size s and the material parameter m, Table . Increases in toughness with crack length do indicate resistance curve (R-curve) behavior. Although we do expect that finer meshes to yield increased R-curve behavior, there is a definite transition between the predicted toughness for s = 60 μm and s = 30 μm. This transition stems from the fact that larger mesh sizes do not enable the crack to blunt. The material has an extremely high yield stress and small plastic zone size. For larger meshes, both the peak triaxility and the equivalent plastic strain reside in the same element (at the crack tip). In contrast, for finer elements, blunting occurs and the peak triaxility moves into the body. Now, the peak triaxility and the peak equivalent plastic strain reside at different locations and the evolution of damage is mitigated thus yielding an increased toughness. The lack of convergence between $s = 15$ μm and $s = 30$ μm is cause for alarm. For $s = 15$ μm, the element size is half of h. Thus the membrane forces might play a role in this process. While consistent with the derivation of a "band" of thickness h, localization elements have zero-thickness in the reference configuration. Future work will focus on the role membrane forces and how they affect crack tip fields and the resulting toughness when s is on the order of h. Based on these findings, we align the bounds for m with simulations for s = 30 μm. We will consider $4 < m < 6$.

Table C1. The predicted toughness under variance in the damage parameter m and the mesh size s.

m	mesh size	$\Delta a = 30$ μm	$\Delta a = 60$ μm	$\Delta a = 120$ μm	$\Delta a = 240$ μm
3*4	15	>100	>100	>100	>100
	30	60	81	>100	>100
	60			65	66
3*5	15	>100	>100	>100	>100
	30	52	68	82	87
	60			59	59
3*6	15	87	87	?	?

	30	47	60	70	77
	60			51	52
3*7	15	74	77	78	79
	30	44	55	62	65
	60			50	50
3*8	15	67	70	70	71
	30	42	51	57	58
	60			47	49

C1.3.2 Smooth tension

Given bounds for m from the K-field simulations, we can now revisit the smooth tension specimen and determine the applicability of the bounds for lower triaxialities. The discretizations used to simulate smooth tension are illustrated in Figure C100. Because the necking process is not localized, our meshes are relatively coarse ($s = 318 \ \mu m$, $635 \ \mu m$) compared to those employed in the K-field simulations. Consequently, the results are not valid beyond crack initiation because we are not capturing the process zone size. That said, the process appears to be over-driven so we do not, in this particular case, need to resolve crack propagation. Note that although the simulations do exhibit this behavior, we derive our notions of crack stability from the experiment and not the simulations (they are not resolved).

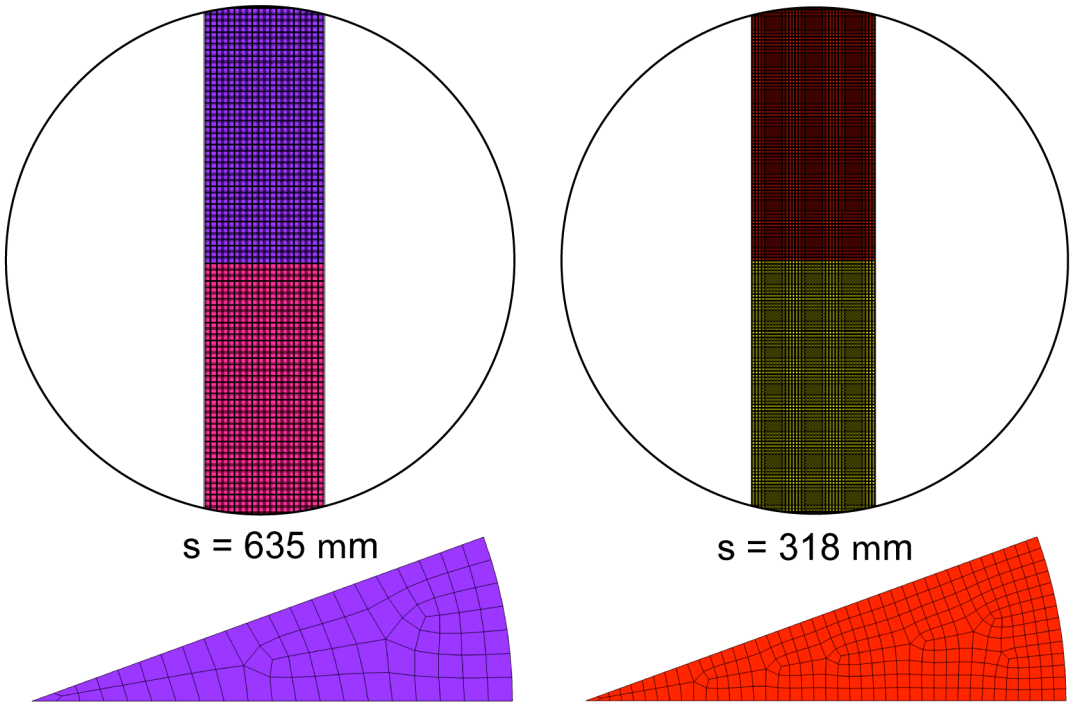

Figure C100. Discretization of the tension geometry. The bar radius is 12.7 mm and length is 50.8 mm. Within a gauge section of 25.4 mm, the specimen is tapered by 2.54 μm over 12.7 mm to control the location of the neck.

The simulated specimen is 50.8 mm long with a radius of 12.7 mm. We taper the bar by 2.54 μm over 12.7 mm within the 25.4 mm gauge section to control the location of the neck. Because we only have access to three-dimensional formulations, we approximate axisymmetry with a 30^o wedge. Results from the smooth tension simulations are given in Figure C101. We note that linear hardening is clearly only an approximation to the material behavior. We might interpret through the experimental results that more hardening at lower strains and less hardening at higher strains. However, it is difficult to quantify without knowledge of neck geometry. Rather than fit to the curve without knowledge of the neck, we have accepted the current approximation which does effectively illustrate that the material is hardening in the necking region. Simulations that did not include hardening yielded a slope tremendously different than the experimental finding.

Examining the smooth tension results, we might choose to select $m = 6$. Although this does seem logical, we remind the reader that we would be tuning our material properties to relatively low triaxiality. For this geometry, the peak triaxility $\langle \sigma_h \rangle / \bar{\sigma}$ is 0.66. In contrast, triaxialities reach 2.44 in the K-field simulations. Without experimental data at numerous $\langle \sigma_h \rangle / \bar{\sigma}$, we cannot validate our current model parameters (which include a fixed h) or even if the model is adequate to span $0.66 < \langle \sigma_h \rangle / \bar{\sigma} < 2.44$. We do not hold [C5] sacred. It is only a dilute model for void growth. Without data spanning the triaxialities of interest, one might consider simulating the range of m and then examining the fields of triaxiality for the body of interest. If the fields are similar to the fields employed to tune the model one may have more confidence in the solution (similitude). However, there is no substitute for more experimental data that may or may not exhibit a change in the mode of failure.

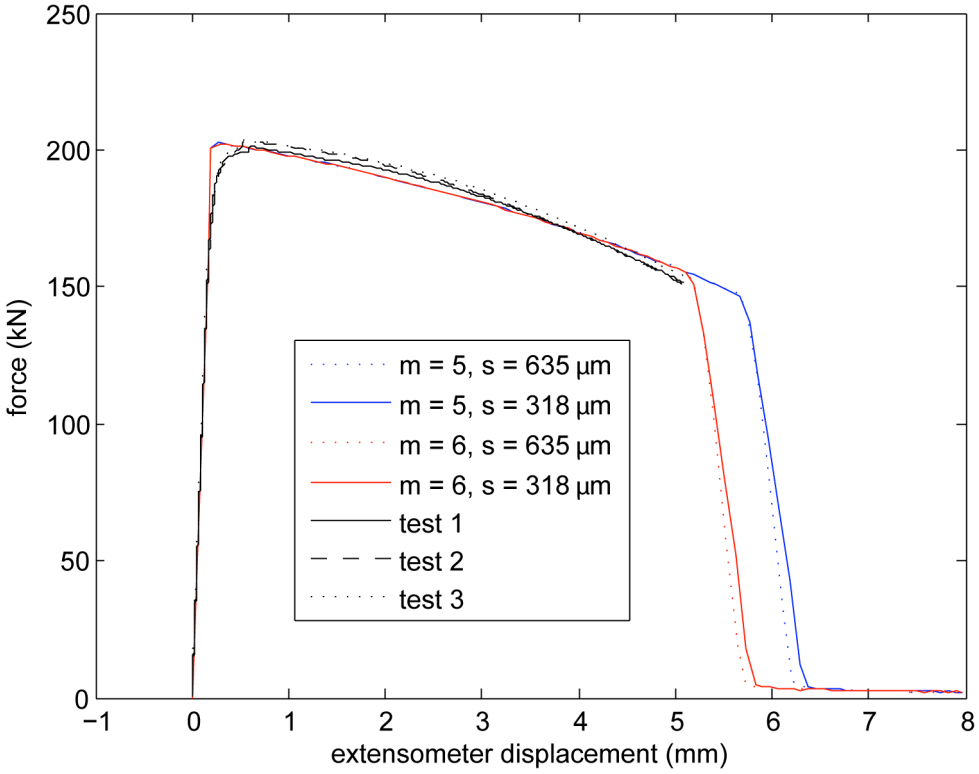

Figure C101. Simulated necking for a smooth bar with geometric imperfection. While linear hardening is a tremendous approximation, it does yield an unloading slope that reflects the

necking process. Note that the unloading slope is not a function of damage and is controlled through continued hardening in the necking region.

C1.4 Prediction mixed-mode initiation and propagation

For the purposes of validating the method, a unique specimen was designed, fabricated and tested. In this section, the problem is described and the results are presented.

C1.4.1 Specimen geometry and the model

Figure C102 shows the geometry for the X-prize competition. The specimen was modeled after the well known compact tension specimen geometry. At of the notch opening, there were attachment points for the extensometer to measure notch opening as a function of applied displacement. The notch lead straight away from these attachment points for approximately 6.3 mm, perpendicular to the axis of loading. The straight section of the notch was followed with a section of approximately 7.25 mm inclined at 45. At the terminal end of the notch, a 0.66 mm radius keyhole was drilled to provide a smooth stress concentration. The geometry was not fatigue pre-cracked and the resulting stress triaxiality at mid-thickness was 0.93. For comparison purposes, the predictions for crack nucleation were to be compared with an experimentally visible surface crack 100-500 μm in length. Given these, predictive capabilities had to include crack nucleation mechanisms as well as crack propagation mechanisms. This geometry was designed to obfuscate the location of crack nucleation and the path of crack propagation. This was desirable to avoid an obvious answer for the experienced analyst, yet allow the experimentalist to focus data collection at an appropriate location.

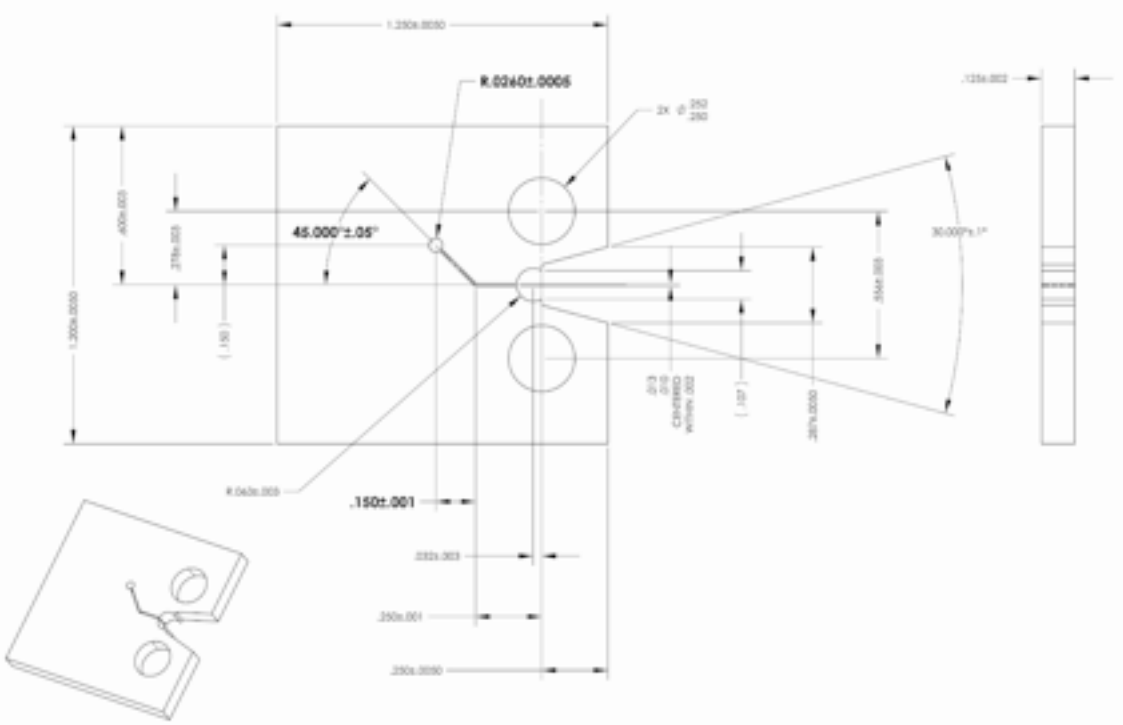

Figure C102. Specimen geometry.

The finite element model used the one plane of symmetry about the mid-thickness of the specimen, allowing only one half of the volume of material to be modeled. Four mesh

discretizations were used for the calculations. The meshes were progressively refined with a structured annular region near the stress concentrator. For each mesh, the elements on the surface of the keyhole had aspect ratios of 1.0. The element size on the key hole was 0.0104 inch, 0.0044 inch, 0.0024 inch, and 0.0012 inch for each progressively finer mesh. The meshes contained 3,392 elements, 23,112 elements, 125,184 elements and 1,015,812 elements. The three finest meshes are shown in Figure C103.

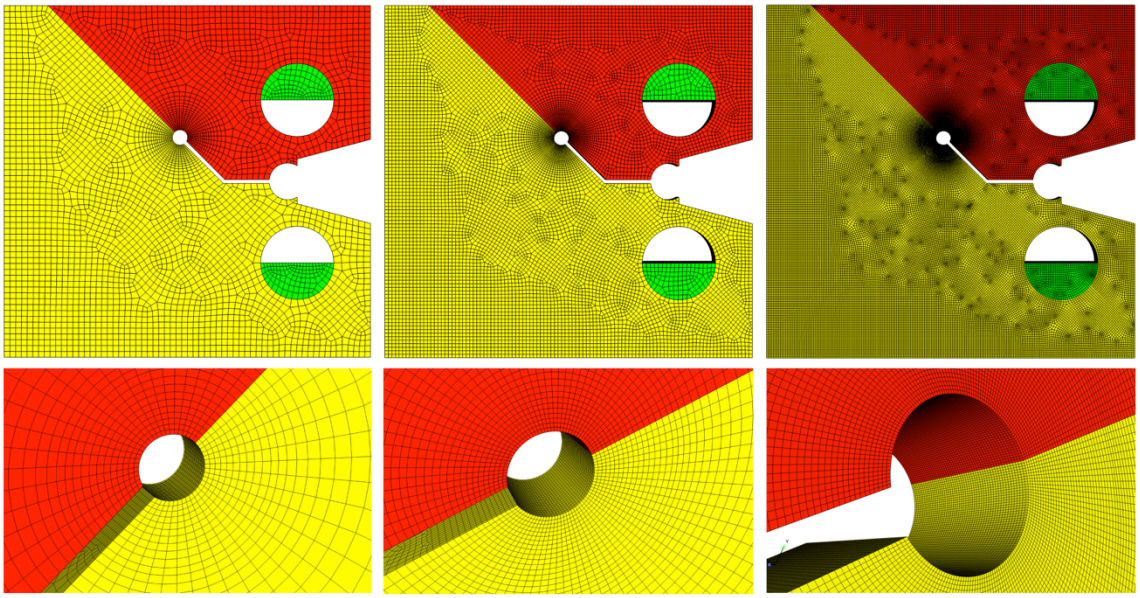

Figure C103. Discretizations employed in the analysis. The mesh size at the surface of the notch, s, is 120 μm, 60 μm, and 30 μm for meshes 02, 03, and 04, respectively.

In the finite element model, one half of the loading holes were filled with a semi-cylinder of rigid material to represent the loading pins. The kinematic boundary conditions were then applied to the nodes comprising the axis of the semi-cylinder allowing the loads to be appropriately distributed around the edge of the holes. Although it may have been more physical to use contact and friction between the rigid semi-pins and the fracture specimen, it was deemed unnecessary at this stage. Further, the mid-thickness plane of symmetry was restrained against out-of-plane deformation.

C1.4.2 Simulation results

Figure C104 shows a set of results for the three mesh sizes with the damage exponent set to six. In the top half of the figure, the first principal stresses are contour plotted on the mid-thickness face. In the bottom half of the figure, the accumulated damage on the fracture plane is contour plotted. As the mesh is progressively refined, the stress contour and accumulated damage show convergence in the mesh sizes 60 μm and 30 μm. The following uses the results from the 60 μm as they are considerably less computationally expensive and sufficiently accurate.

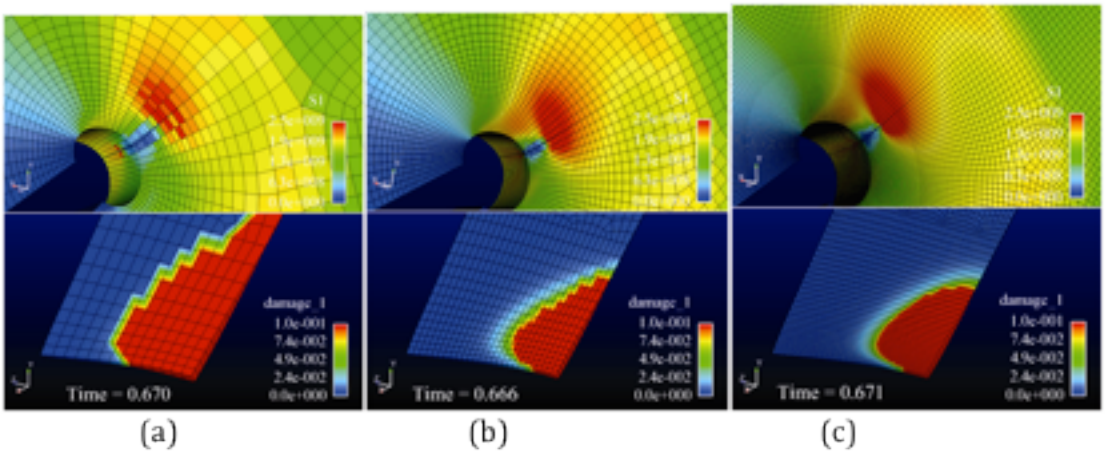

Figure C104. Contour plots of the first principal stress and accumulated damage at crack initiation showing convergence of the global and local fields as the mesh is refined for: (a) mesh size 120 μm; (b) mesh size 60 μm; and, (c) mesh size 30 μm.

Figure C105 shows additional detail for the analysis results with mesh size 60 μm and damage exponent equal to six. In Figure C105 (a), the first principal stress is contour plotted on the plane of mid-thickness. In part (b) of the figure, the first principal stress is contour plotted on the fracture plane. In part (c), the accumulated damage is contour plotted on the fracture plane. In part (d), the reaction force for one node in the top loading pin is plotted versus solution time. This set of plots was used to determine the applied loading at crack initiation which was said to occur when the first element in the hole had completely unloaded. Note, the calculations indicate a precipitous decline in the applied loading indicating that unstable crack growth rapidly follows crack initiation.

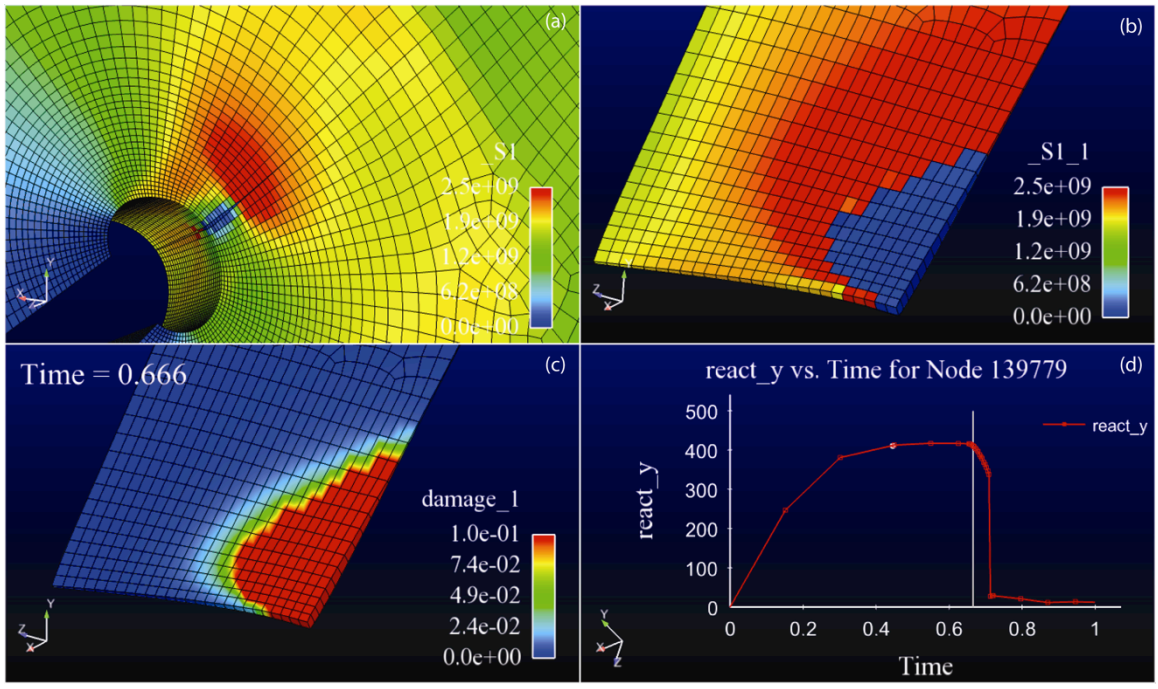

Figure C105. Graphical results for damage exponent m = 6 showing: (a) the principal stress contour plot at specimen mid-thickness; (b) the principal stress contour plot on the fracture plane; (c) the contour plot showing the accumulated damage on the fracture plane; and, (d) the

y-direction reaction force for one finite element node at the applied boundary condition plotted versus solution time.

Figure C106 provides an illustration of the gauge displacement reported. In the figure, the locations where gauge displacements were measured are indicated as ``gauge attachments''. In the undeformed, as manufactured configuration, the gauge opening measured ``*h*'', see figure inset. As deformation was applied, the gauge attachment points deformed with an x- and y-component, indicated as ``*dx*'' and ``*dy*'' in the figure. The total displacement is reported and was calculated as

$$\Delta_{gauge} = \sqrt{dx^2 + dy^2}. \tag{10}$$

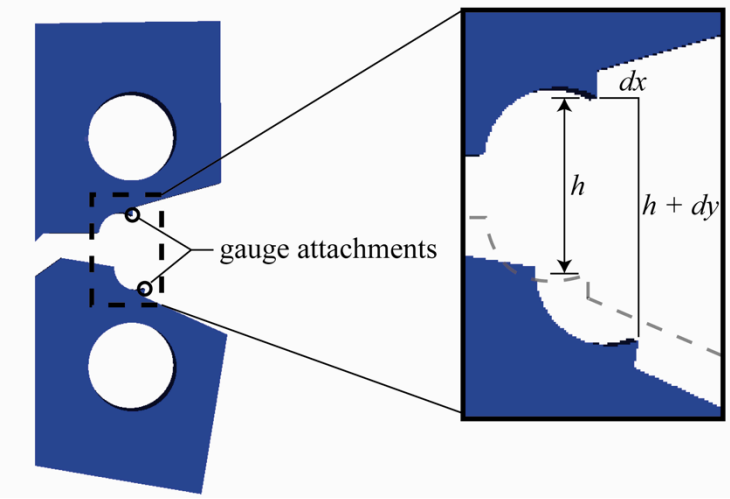

Figure C106. Gauge opening displacement measurement.

Figure C107 plots the global applied load versus gauge opening displacement for several sets of data. The solid black lines and blue lines plot experimental data. The black lines were from experiments run by [C1] while the blue lines represent experimental data from the laboratory of [C6]. These data were obtained at different loading rates with apparent affects. The data collected by Boyce was run at a constant loading rate of 0.0127 mm/s. The data collected by Cordova was run at a rate of 0.0027 mm/s up to an applied displacement of 2.03 mm when the rate was reduced to 0.00025 mm/s. From the plot, it is apparent that the simulation results with the damage exponent equal to five are the best fit to the slower rate data while something between five and six would nicely match the faster rate data. There is nothing in the simulation model to account for loading rate. This is an open area of investigation. The crack initiation with damage exponent equal to five occurred at an applied displacement of 2.52 mm.

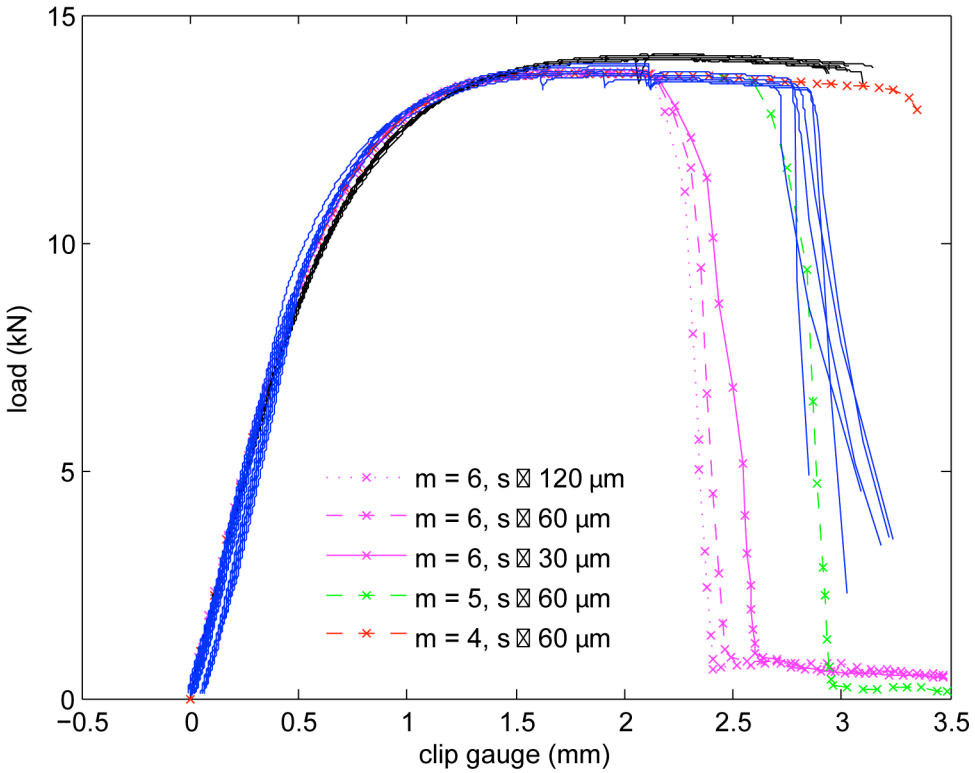

Figure C107. Gauge opening versus applied load. The solid black and blue lines plot the experimental results.

The solution was obtained with the quasi-static finite element code Adagio, part of the SIERRA/Solid Mechanics suite ([C11]). Adagio uses a nonlinear, preconditioned, conjugate gradient (CG) solution algorithm with a number of options for the preconditioning. The preconditioner used in these calculations was the FETI parallel scalable linear solver with fifty node-based smoothing iterations ([C8, C7]). With this preconditioner and prior to crack propagation, the norm of the residual was reduced by eight orders of magnitude (1.0e-08) in an approximate average of fifty-six iterations. For the mesh size of 60 μm with damage exponent of six, this performance occured at a constant time step of approximately 2.0e-03 seconds up to the crack initiation time of 0.666 seconds. The 120 μm and 30 μm exibited similar performance. Of the fifty-six iterations, fifty were the node-based smoothing iterations, which are very inexpensive, and only six iterations formed the full tangent matrix. Upon crack propagation, the adaptive load stepping algorithm had to reduce load increments and the simulation slowed down. Table summarizes the performance of the three meshes with the damage exponent equal to six on the Tri-Lab Linux Capacity Clusters (TLCC) at housed Sandia National Laboratories.

Table C2. Processing time on 2.2 GHz AMD quad core processors with 2 GB DDR2 SD RAM per processor with damage exponent equal to six.

mesh size (μ m)	element count	processor count	processing time (hh:mm)
120	23,112	64	01:39
60	125,184	128	06:19
30	1,015,812	256	70:40

References

[C1] Boyce, B. Personal communications (to be published), 2010.

[C2] Brown A.A., Kostka T.D., Antoun, B.R., Chiesa M.L., Bammann, D.J., Pitts, S.A., Margolis, S.B., O'Connor D., Yang Y.C.N. *Validation of Thermal Mechanical Modeling for Stainless Steel Forgings*, Proceedings of XI International Conference on Computational Plasticity, 2011.

[C3] Campbell, J.E. and Gerberich, W.W. and Underwood, J.H. *Application of fracture mechanics for selection of metallic structural materials*. American Society for Metials, Metals Park, OH, 1982.

[C4] Chiesa, M. Personal communications, 2010.

[C5] Cocks, A.C.F and Ashby, M.F. Intergranular fracture during power-law creep under multiaxial stresses. *Metal Science*, 14:395-402, 1980.

[C6] Cordova, T. Personal communications (to be published), 2010.

[C7] Farhat C., Lesoinne M., LeTallec P., Pierson K. and Rixen D. FETI-DP: A dual-primal unified FETI-method -- Part I: A faster alternative to the two-level FETI method. *International Journal for Numerical Methods in Engineering*, 50:1523-1544, 2001.

[C8] Farhat C., Lesoinne M. and Pierson K. A scalable dual-primal domain decomposition method. *Numerical Linear Albebra with Applications*, 7:687-714, 2000.

[C9] Hughes T. J. R. Generalization of selective integration procedures to anisotropic and nonlinear media. International Journal for Numerical Methods in Engineering, 15(9):1413–1418, September 1980.

[C10] Nagtegaal J. C., Parks D. M., and Rice J. R. On numerically accurate finite element solutions in the fully plastic range. Computer Methods in Applied Mechanics and Engineering, 4:153–177, 1974.

[C11] SIERRA Solid Mechanics Team. Adagio 4.16 User's Guide. Technical Report, SAND2010-3111, Sandia National Laboratories, Sandia National Laboratories, Albuquerque, NM, 2010.

[C12] Yang, Q. and Mota, A. and Ortiz, M. A class of variational strain-localization finite elements. *International Journal for Numerical Methods in Engineering*, 62:1013-1037, 2005.

C2. Follow-Up for Challenge 1A

C2.1 Initial X-prize predictions

1. Describe what material model you used for deformation (not crack initiation)? How did you calibrate that model against material properties? What parameters did you calibrate? Please specify what specific resources (datasets) you used to calibrate the parameters.
2. Describe what material model you used for crack initiation? How did you calibrate that model against material properties? What parameters did you calibrate? Please specify what specific resources (datasets) you used to calibrate the parameters.

We used a local damage model that provided the means for plasticity (deformation) and eventual crack initiation (via damage evolution). We fit the plasticity model to a single uniaxial stress-strain curve (taken from a tensile test prior to the jump). We did not initially address the jump in the load-displacement curve and it seems that this jump is actually critical to resolving smooth necking. We then assumed a length scale for the localization element ($h = 30\ mm$) and fit the damage parameter, m, through K-field simulations of the given plane-strain fracture toughness, K_{Ic}.

3. How was uncertainty captured in your simulation: (a) material variability, (b) uncertainty in the failure criterion?

For this initial attempt, we did not attempt to address material variability. The little data we do have indicates that the smooth tensile tests do not exhibit a tremendous amount of variability in deformation (plasticity) or displacement at failure. This is predicated on the fact that we extracted data prior to the jump in the load-displacement curves. Recent simulations indicate that this is important in modeling necking. We addressed uncertainty in the failure criterion through a simple parametric study based on K-field simulations.

4. Please summarize your examination (if any) of mesh dependency of your result.

While mesh convergence studies were also performed for the K-field simulations (with more documentation forthcoming), multiple meshes of the fracture specimen were considered. Elements at the notch for the coarse and finer mesh were on the order of s : 120 mm and s : 60 mm, respectively. A larger model is also being simulated with roughly 1 million elements and elements at the notch being s : 30 mm (with results forthcoming). While the process zone size at the crack tip probably merits the million element discretization (uniform refinement), the load-displacement behavior of both the coarse and finer mesh were convergent. We stress that we are using localization elements to regularize the evolution of damage so convergence in the far-field is expected.

5. Computational Efficiency. Estimate the node-hours and processor speed used to run one solution to the problem. Report a range if necessary, for example if you used different mesh sizes, report the time for each of the mesh sizes.

Simulations were run on a variety of platforms. Simulations of the fracture geometry were run on many processors (32--128) on both glory and thunderbird. Glory has 2.2 GHz AMD quad socket/quad core processors while thunderbird has Dual 3.6 GHz Intel EM64T processors.

Although glory might be a bit faster, our experience is that the difference is not marked. For m = 7 (this is an upper bound, m = 5, 6 exhibit faster simulation times).

Mesh 02 s ~ 120 mm: 64 processors on tbird ~ 78 minutes with a total system time (sum of all processors) of ~ 84 hours
Mesh 03 s ~ 60 mm: 128 processors on tbird~ 5 hours with a total system time (sum of all processors) of ~ 670 hours.

Note that in roughly 5 hours we simulated the entire failure process - not just initiation. This was completed under quasi-static conditions with extremely tight tolerances on equilibrium (quasi-statics).

6. What force (or range of forces) is predicted at a load line displacement of 0.01 in? 0.02 in? 0.03 in? 0.04 in?

In looking at cmod versus load, one can see that this exercise is probing the plasticity model, discretization, and applied boundary conditions. Because all damage parameters lie on a common curve for the indicated levels of the load line displacement, the below values are given for m = 5 but hold for m = 6 and m = 7.

0.01 in, 0.245 mm CMOD of 0.249 mm and a load of 4.83 kN
0.02 in, 0.508 mm CMOD of 0.503 mm and a load of 8.62 kN
0.03 in, 0.762 mm CMOD of 0.763 mm and a load of 10.97 kN
0.04 in, 1.016 mm CMOD of 1.032 mm and a load of 12.19 kN

7. Describe the strengths and weaknesses of your approach.

We are using a model that contains some of the relevant micromechanics for void nucleation, growth, and coalescence in ductile metals. The model is only for growth and depends heavily on the triaxiality. Shear lips are not well represented (see next slide). We currently seed a path for localization elements and are working on methods to make the path adaptive (and general). Other methods (nonlocal, gradient) do not suffer from this path issue but those methods are still in development. Although the method is currently not general (in either the physics or numerics), the simulations contained herein do show promise. The method is convergent and numerically robust. And while smooth tensile results are forthcoming, our approach is relatively straightforward. We do not stipulate a criterion. Rather, we simulate the evolution of a process and out of the process stems regularized initiation and propagation.

C2.2 Revised predictions

8. What force (or range of forces) is predicted at a load line displacement of 0.01 in? 0.02 in? 0.03 in? 0.04 in?

In looking at prior figure of load-cmod, one can see that this exercise is probing the plasticity model, discretization, and applied boundary conditions. Because all damage parameters lie on a common curve for the indicated levels of the load line displacement, the below values are given for $m = 6$.

0.01 in, 0.245 mm CMOD of 0.249 mm and a load of 4.98 kN
0.02 in, 0.508 mm CMOD of 0.502 mm and a load of 8.97 kN
0.03 in, 0.762 mm CMOD of 0.762 mm and a load of 11.55 kN
0.04 in, 1.016 mm CMOD of 1.029 mm and a load of 12.91 kN

C2.3 Source of discrepancies

9. What was the % difference of your predictions to the experimental values (maximum force prior to crack initiation and COD displacement at crack initiation)?

There was an error in our prior statement on maximum load. We reported the load at initiation to be 13.4 kN. The maximum load prior to failure was 13.7 kN. This essentially matches the lower bound of the data and is 2.1% off the average (13.95 kN). You can also clearly see in the experimental results that the lower bound of the load is essentially the rate-independent result. Consequently, we match the lower rates in Cordova's experiments (13.7 kN) quite well.

Our crack opening displacement error was larger. We predicted 2.16 mm and the lower bound was 2.83 mm. Given an average was 2.96 mm, the error in our calculation was 27.0%. We have included more analysis to illustrate the origins of this error and address this specifically in Question 3.

10. If you (or your team) submitted revised predictions, either after the initial due date, or after the comparison between modeling results, did your revisions bring the prediction closer to the experimental values?

Yes and no. We did improve our estimate of the maximum load after the initial due date because we took into account the extended hardening. Our peak load increased from 12.9 kN to 13.7 kN.

However, because we decided to not provide a span of a material property, $5 < m < 6$, and instead relied on a particular material property ($m = 6$), our prediction for the cod decreased. The upper bound moved from 2.60 mm ($m = 5$) to 2.16 mm ($m = 6$). The error on 2.60 mm is still substantial, 12.2%, but better than 27.0%. Note that the average measured cod was 2.96 mm. If we consider the difference from the lower bound (2.83 mm), the error is 8.1%.

Through revisiting K-field simulations and noting differences in the triaxiality between the smooth tension and x-prize geometries, we conducted additional simulations at $m = 5$ and $m = 4$. The cod for $m = 5$ and $m = 4$ are roughly 2.60 mm and 3.31 mm, respectively. Note that the bounds of the experimental data were 2.84 mm and 3.15 mm. Through additional simulation motivated by K-field findings, we now span the experimental findings. See included plots of the experimental and simulated data.

11. Describe the source(s) of discrepancy (if any) between your prediction and the experimental result. Where possible, provide quantitative estimates of how much your prediction might have improved if these sources were incorporated into the prediction. Discuss the ease or difficulty in incorporating such improvements in future work.

We did not predict the failure cod with tremendous accuracy. We believe that this reflects issues regarding the fitting of parameters. Although we did change the material hardening to adequately model the smooth tensile necking, we never revisited the K-field simulations. Consequently, the bounds for our damage parameter, m, were in error. Rather than $5 < m < 7$, we should have simulated $4 < m < 6$. In fact, we eventually settled on $m = 6$ because it matched the failure displacement in the smooth tensile test. Although this seemed logical, we were essentially tuning

our damage model to a lower triaxiality and hoping that it extrapolated to higher triaxialities. This was a bit naive. Hey, we got excited. We should know better. Simulations were conducted to prove these hypotheses. With some success, we have justified looking at different bounds for m. These new bounds allow us to span the experimental data. In addition, we make some attempts to examine fields of triaxiality in the three geometries (K-field, smooth tension, x-prize) and make sense of the arguments required for lumping dissipation in the K-field results. Two issues that were not revisited will be incorporated into future work. We need to eliminate all in-plane membrane forces generated by localization elements when bulk elements are on the order of h. Although the formulation does stipulate a thickness of h, the thickness is a modeling construct. Localization elements have zero thickness (in the simulation). This only matters when the bulk elements are on the order of h and the generated membrane forces affect field quantities. We have a fix in the works. We believe that this may, in fact, be causing issues in the K-field simulations. Also, we never varied h! We need to do this systematically and have begun this process. This is not terribly difficult. It just takes a little time.

12. Was this effort helpful for the development and evaluation of your modeling paradigm? How might we improve the challenges in the future?

This effort was extremely helpful in our development and the processes we use to model failure using localization elements. In fact, this provided the impetus to really put localization elements to work on a real boundary value problem.

1. Need nice tensile tests that have load-displacement information and the evolution of the necking geometry. We could match the final, necked geometry. We could also use compression testing to get a large portion of the finite deformation behavior. Might include a few rates. In the macroscopic x-prize tests, differences in displacement rates were noted. If one notices a strain-rate dependence in the macroscopic data, local fields might span many rates.
2. Fracture toughness tests. Any true measure of initiation stems from the evolution of a process that will employ some measure of propagation. Being able to clearly lump the dissipative mechanisms using a fracture toughness test rather than a book value for KIc would be helpful.
3. Notched tensile tests provide experimental information on intermediate triaxialities. If shear-lips dominate, other test geometries might be more helpful.
4. In addition to DIC, one might consider IR. It might be interesting to see if we need to include temperature and conduction.

C3. Predictions for Challenge 1B

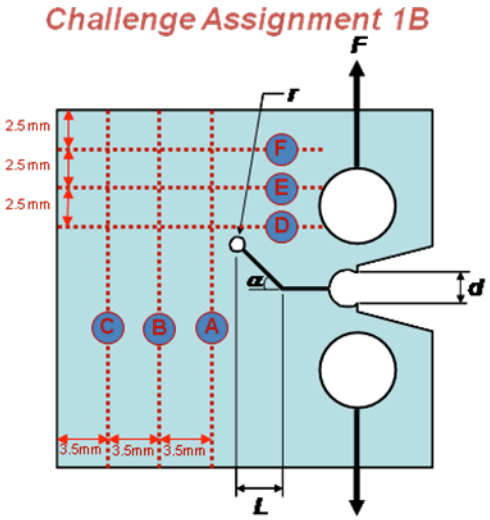

Challenge question 1B

1B.1 For a specimen as shown on the left, with geometry defined previously in Challenge 1A, what is the loadline displacement Δd needed to induce crack initiation (in inches) in aluminum alloy 2024-T3? What is the peak force *prior* to crack initiation?

1B.2 Six lines labeled A-G will be scribed prior to testing in the locations indicated. What is the order of crack propagation (e.g. A-B-D-C, etc.)?

1B.3 What is the force and displacement at which the crack reaches the 1st line?

1B.4 What is the force (kN) and loadline displacement (mm) at which the crack reaches line E (refer to previous drawing)?

Due date: Submit to Sharepoint Site by the end of Tuesday, August 31st

Please use the table below to report results. You can bound your answers if necessary.

		1B.1 Δd at crack initiation (mm)	1B.1 Peak force *prior* to crack initiation (kN)	1B.2 Crack path (e.g. D-E-F or D-A-E-B-F, etc.)	1B.3 Displacement Δd when crack reaches first line (mm)	1B.3 Force when crack reaches first line (kN)	1B.4 Displacement Δd when crack reaches line E (mm)	1B.4 Force when crack reaches line E (kN)
2024-T3	Upper bound	4.1815 mm			4.5755 mm	1.451 kN	5.0667 mm	0.575 kN
	BEST ESTIMATE	4.1181 mm	4.172 kN	D-A-E-F-B-fracture	4.4657mm	1.451 kN	4.8193 mm	0.575 kN
	Lower bound	4.0546 mm			4.4657 mm	1.138 kN	4.8193 mm	0.310 kN

Figure C108. Challenge 1B assignment

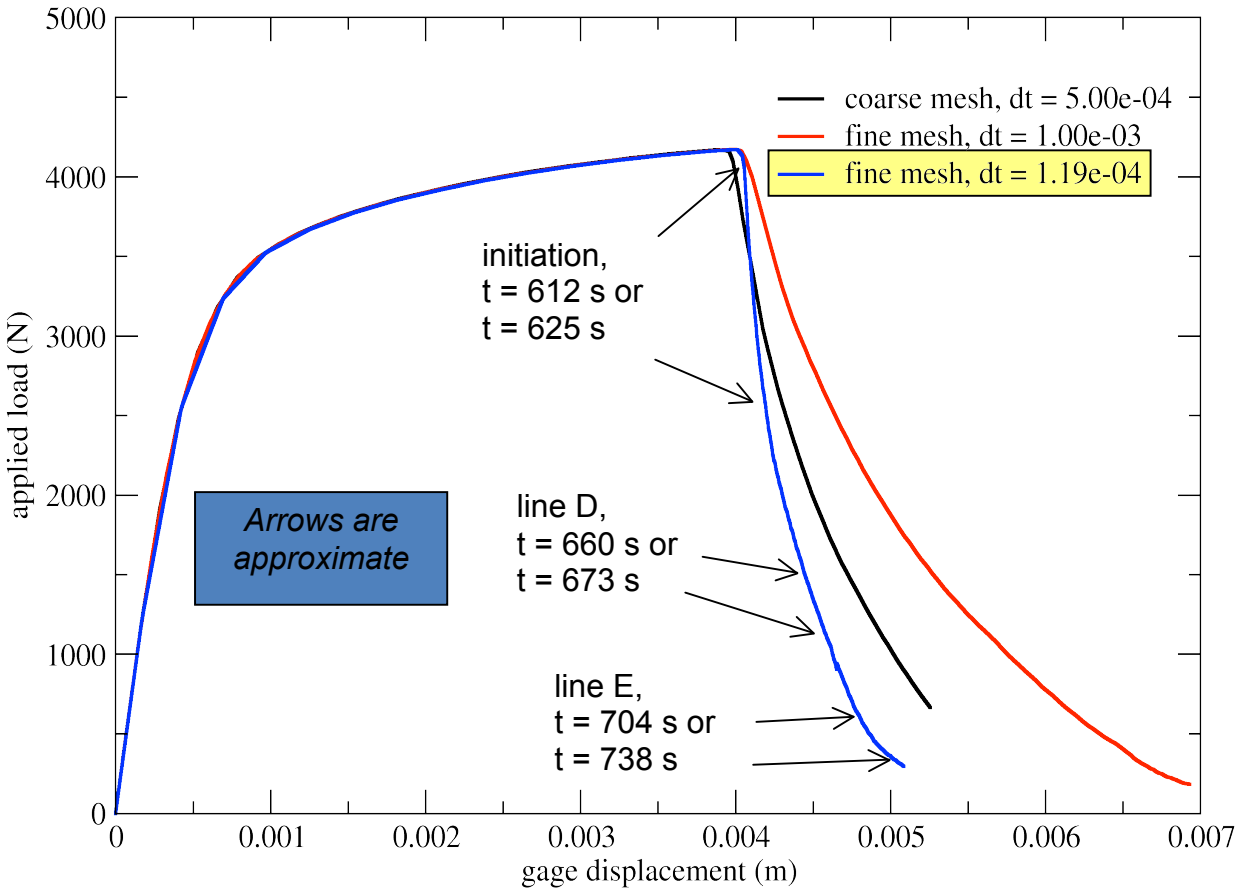

Figure C109. Load-displacement response predictions.

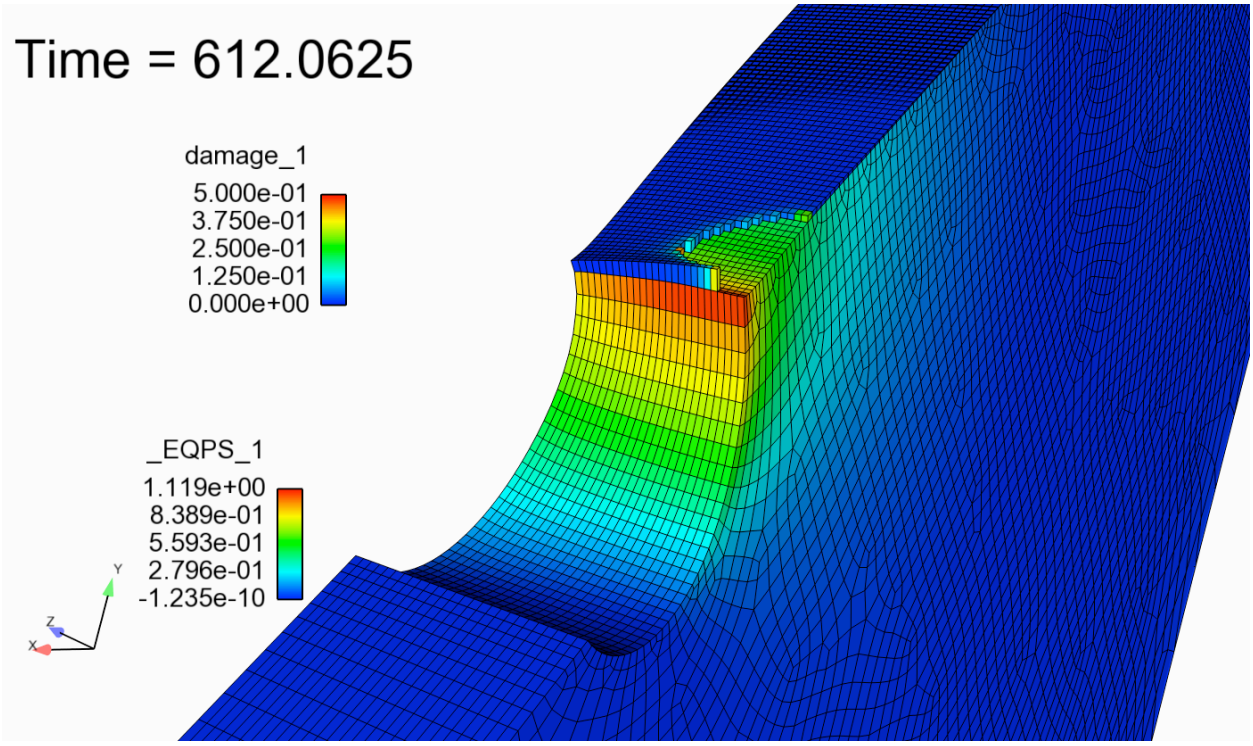

Figure C110. Damage and EQPS contours, Time=612.

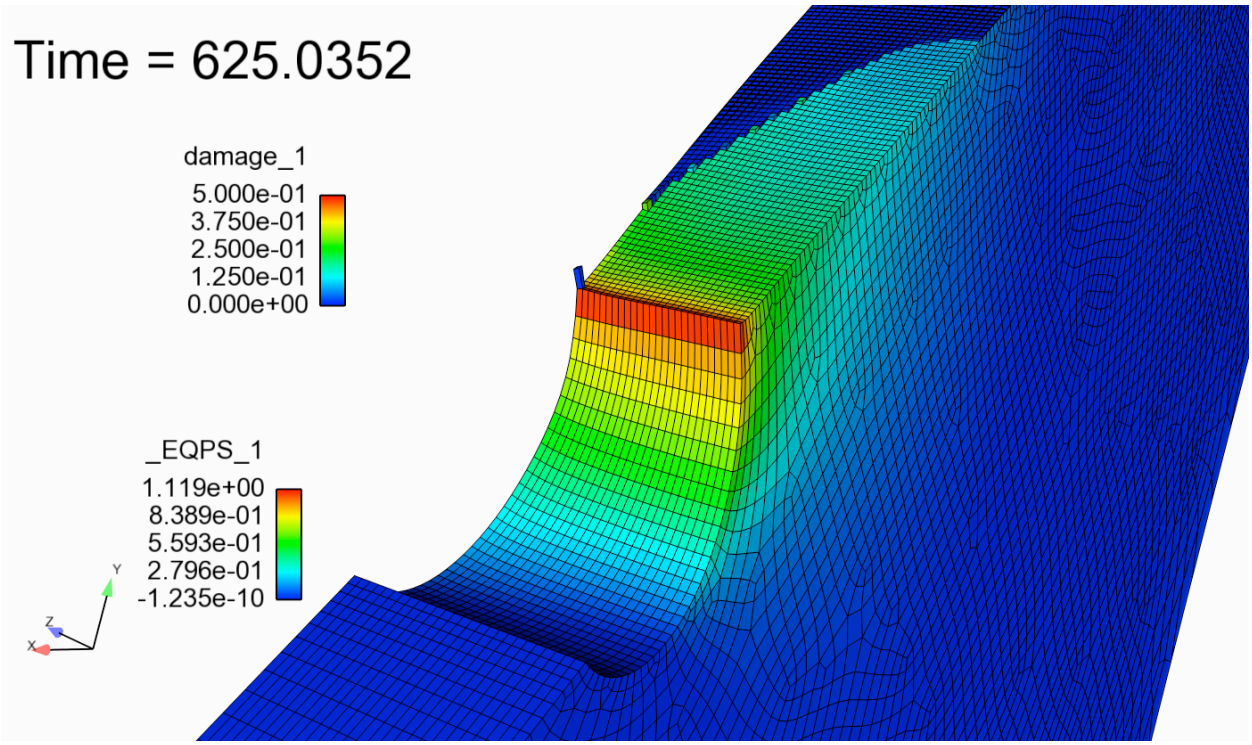

Figure C111. Damage and EQPS contours, Time=625.

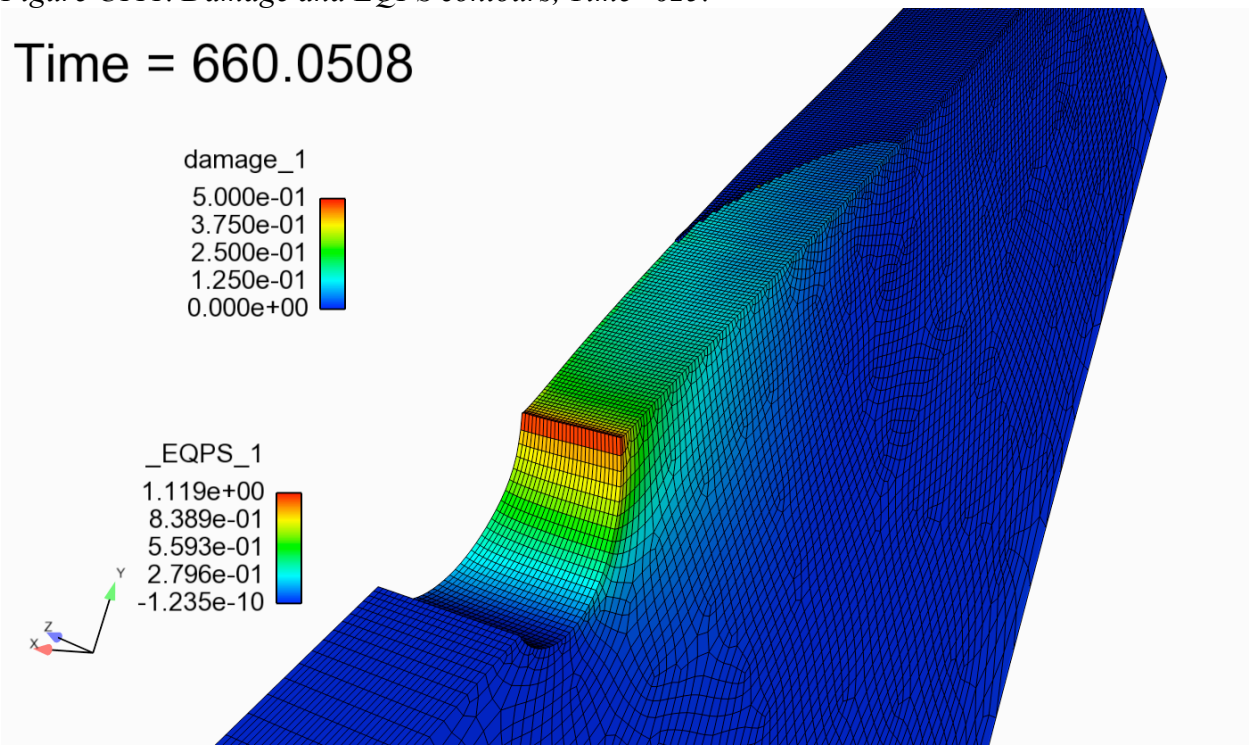

Figure C112. Damage and EQPS contours, Time=660.

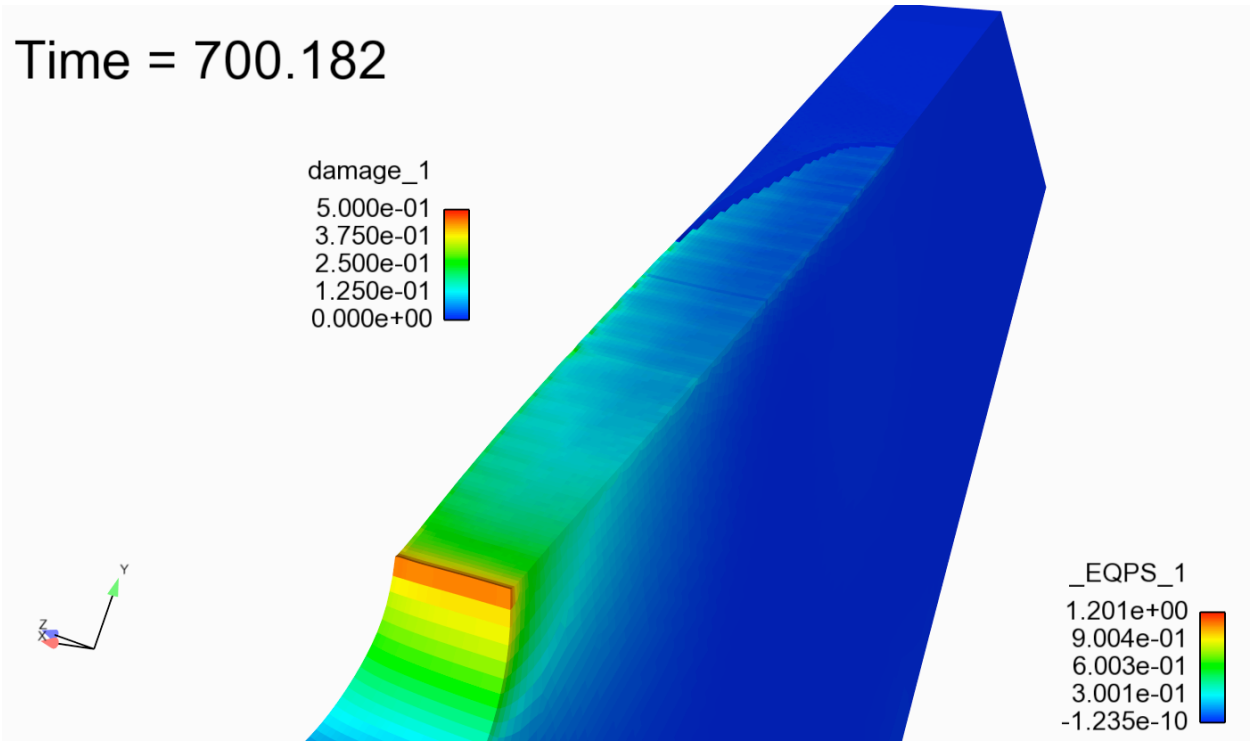

Figure C113. Damage and EQPS contours, Time=700.

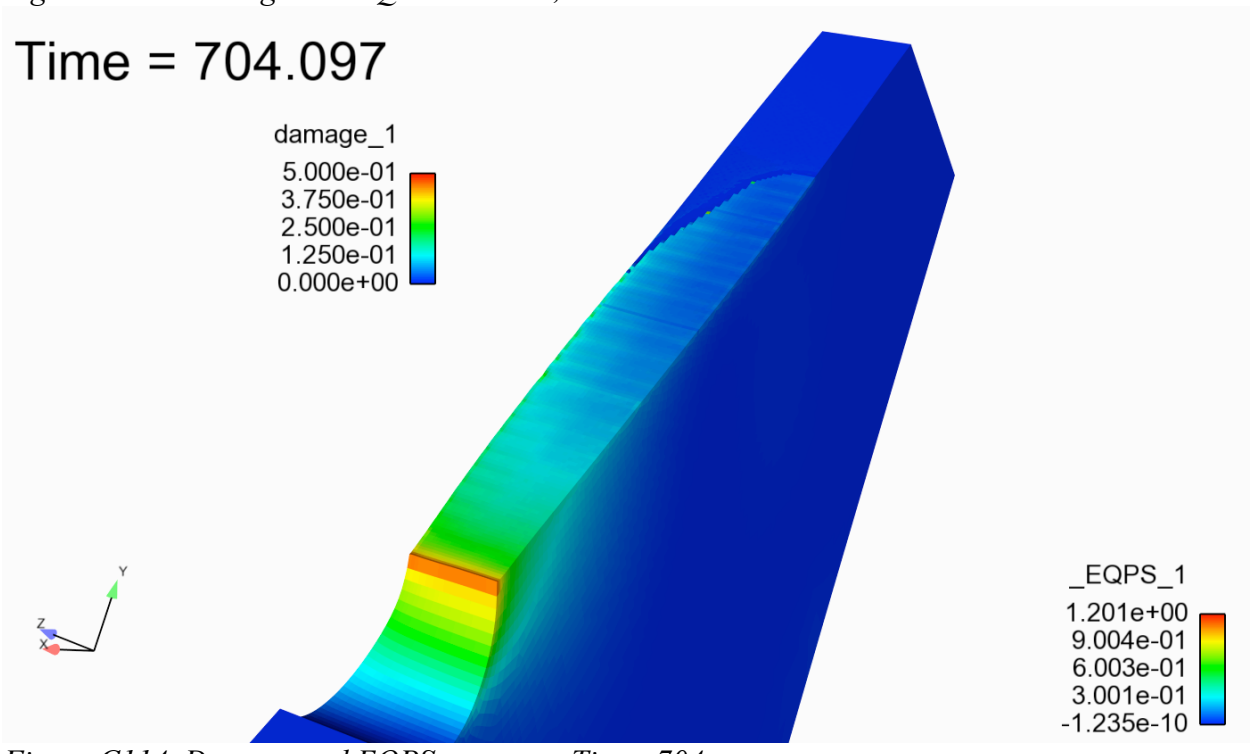

Figure C114. Damage and EQPS contours, Time=704.

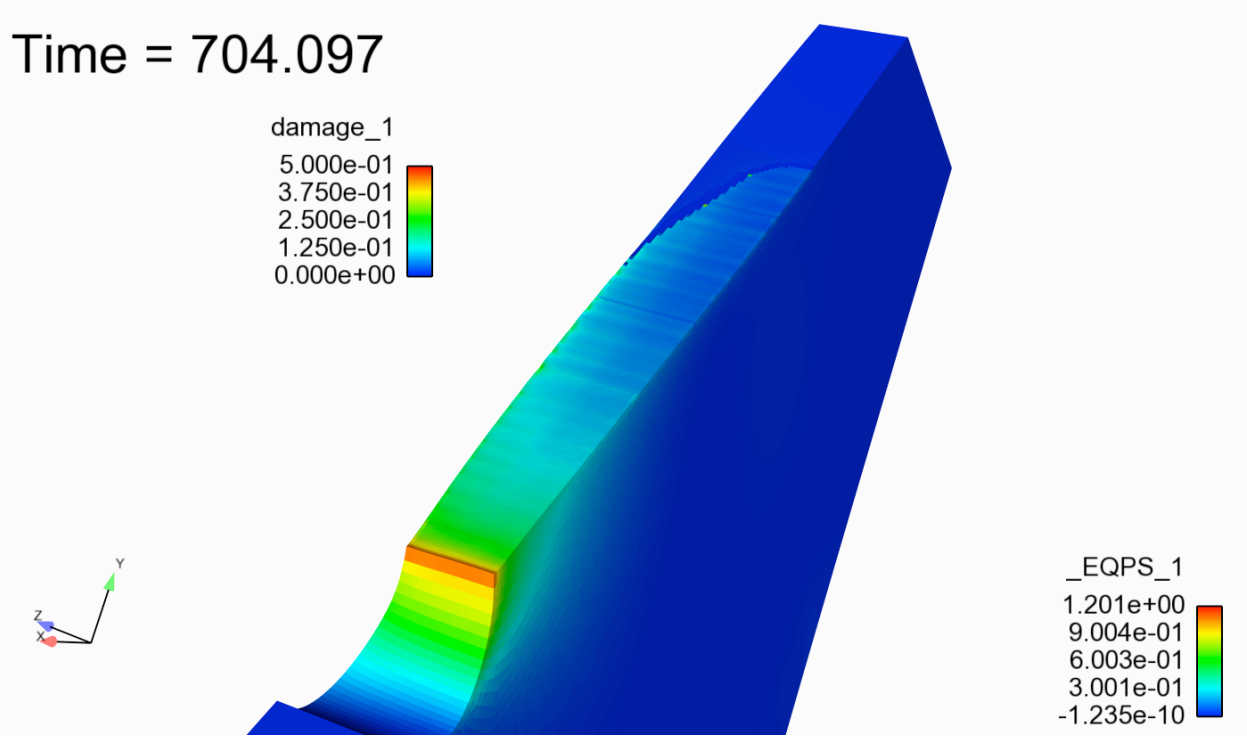

Figure C115. Damage and EQPS contours, Time=704.

C4. Follow-Up for Challenge 1B

Question: What do you believe were the most significant sources of error that produced discrepancy between your model and experimental results. Where possible, provide quantitative estimates of how much your prediction might have improved if these sources were incorporated into the prediction. Discuss the ease or difficulty in incorporating such improvements in future work.

We believe that the most significant errors are

1. Failure mode. We tune our triaxiality-dependent damage model to the plane strain fracture toughness and extrapolate that parameter to the X-Prize calculations. Brad has mentioned that fracture plane is slanted and we do not have the physics (or numerics) to represent the experimentally measured fracture plane which derives from lower constraint.
2. Fracture angle. We insert the plane at a give angle (51° to the mode I path). This will affect both initiation and propagation (the crack cannot curve). Angles are observed on the surface but one cannot really deduce the interior angle because the slanted nature of the crack will cause surface variations.
3. Material characterization. We employed a single tensile test to derive the deformational properties. Additional tests confirmed that the yield stress can vary by almost 10%. We did attempt to include this variation in additional X-Prize simulations and the corresponding K-field simulations which yield the damage parameter m. Figure C116 illustrates the effect on the load-displacement curve. While using a lower bound for the fracture toughness does push the evolution toward the experimental findings, these variations are not sufficient to bring our simulations into agreement. We could continue to raise the damage parameter to fit the data but we cannot justify those changes.

With regard to the numerics of localization elements, we have identified multiple sources of error and we are currently improving the implementation. Issues we are currently correcting include

1. An objective update scheme for the rate of deformation tensor. This update does filter out rigid body motions and we are currently testing the series expansion of $\log(F_{n+1}F_n^{-1})$. We have implemented this method and are currently debugging.
2. A revision to the multiplicative decomposition of the deformation gradient. We have derived that revision and have just implemented the new form into Sierra. It is our hope that it will further stabilize propagation.
3. Exclusion of the membrane forces. Because the length scale is on the order of the element size (60 μm), membrane forces generated by the methodology may be affecting crack tip fields. We have implemented this option, studied the effects, and reasoned that the elimination of the membrane forces is justified when the mesh size is on the order of the element size. However, when we do turn off those forces in the X-Prize calculations, the global calculation becomes unstable. We suspect this will be remedied by (1 & 2). In fact, the corrections given in (1) and (2) were motivated by the X-Prize calculations.
4. The probe for the pre-conditioner has been modified and may require additional debugging.

Regrettably, we cannot estimate the error associated with (1) and (2) without performing the simulations. These changes may enable convergence for (3) and significantly impact the

solution. We will revisit the X-Prize calculations for 2024 after the model changes have been verified.

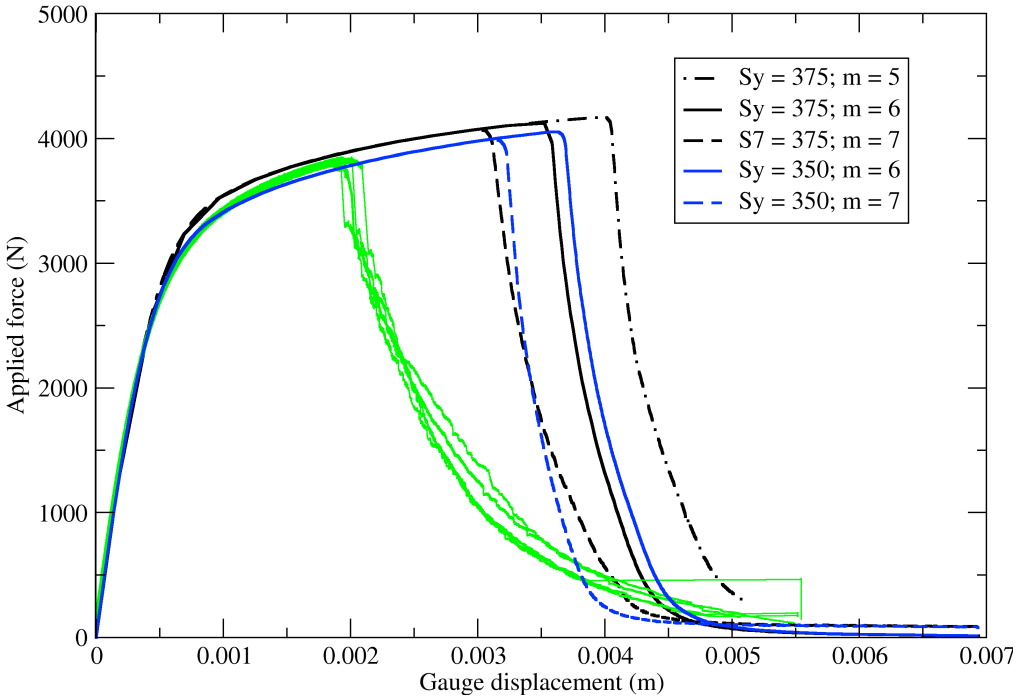

Figure C116. An examination of varying the exponent governing the evolution of damage m and the yield stress Sy.

The damage exponent was tuned to the fracture toughness of the material. For Sy = 375 MPa, m = 5 represents roughly 32 MPa√m and m = 6 corresponds to 27 MPa√m. For Sy = 350 MPa, m = 6 represents roughly 29 MPa√m and m = 7 corresponds to 26 MPa√m. An average toughness for 2024-T651 is roughly 30 MPa√m with a lower bound being near 27 MPa√m. These changes alone cannot explain the deviation from experimental findings.

C5. Predictions for Challenge 2A

C5.1 Background

Prior Challenge 2A, we reformulated the localization element and also derived a better approximation for the velocity gradient at Ln+1 from the deformation gradient at Fn and Fn+1. The prior formulation of the localization element was not objective (under rigid body motions). Small changes to the multiplicative decomposition ensure objectivity and also simplified the work conjugates. The prior method for calculating the velocity gradient was also not objective. This resulted in stresses being induced from rigid body motions. The new methodology derives from the Baker-Campbell-Hausdorff expansion and is more accurate than the strongly objective methodology currently employed for other element types.

C5.2 Determining material constants

Prior to beginning this work, we revisited prior findings and considered two variations in the large deformation behavior for 2024-T3. The first assumes that the yield stress is 375 MPa and allows for some hardening consistent with the experimental tensile stress-strain curve. Because aluminum has limited work hardening, another fit was also explored with a yield stress of 370 MPa and less work hardening. The plasticity is described through the constitutive model BCJ_mem in Sierra mechanics. We assume the hardening to be isotropic and to be of a hardening-recovery form, causing the effective stress to eventually asymptote at large strains. For the case with higher yield stress, the stress-strain curve asymptotes to approximately 640 MPa true stress at 60% true strain. Conversely, for the case with lower yield stress, the "plateau" case, the hardening is minimal and the stress-strain curve asymptotes to approximately 588 MPa at 33% true strain. Although we believe the first case to be representative of the material behavior and the second case to be a lower bound on the hardening, we do not have experimental data to justify our assumptions. Consequently, we carry both descriptions through both our fitting procedures and into the final calculations to understand the impact on our predictions. For all cases, the large-deformation behavior of 2024-T3 does not greatly impact our solutions because the specimen remains at, or near, the small scale yielding condition.

After fixing the two cases for large deformation plasticity, we need to develop a procedure for fitting both the exponent for the evolution of damage m and the length scale governing the localization element h. As in prior challenges, we employ the plane-strain fracture toughness. The literature indicates that the plane strain fracture toughness KIc in the LT direction varies from 27 MPa√m to 36 MPa√m with an average near 31 MPa√m. As in prior challenges, a K-field boundary condition is employed. Trying to match a range of values for the plane strain fracture toughness, we vary m and h to determine combinations that yield the proper resistance. This is ideal because we are prescribing the driving force and "recording" this resistance in a nearly criteria-free manner. The length scale h was chosen to be 30, 60, and 90 μm. The damage exponent m was varied from 4 to 8. Although the determination of h and m is not unique, clear

trends emerge from the analysis. The fracture toughness scales with h. This can actually be proven analytically for a given functional form. For the damage exponents chosen for this study, a length scale of 30 microns was insufficient to generate even the lower bound of the toughness. For the damage exponent, the toughness increases with decreasing m. As m increases the damage evolves more quickly and limits the resistance. With the plane strain, K-field boundary conditions, the crack propagates at the average resistance (32 MPa$\sqrt{m}$) for h = 60 μm, m = 5. Values greater than (m = 6) and less than (m = 4) represent the lower (27 MPa$\sqrt{m}$) and upper bound (41 MPa$\sqrt{m}$) of the resistance, respectively.

We should note a few things from these analyses. Determining when crack propagation in the simulations is subjective and requires the administration of a criterion. For this study, we have chosen to define propagation as the decay to zero of the normal stress for two elements in front of the original crack tip. This definition coincides with that of a cohesive zone approach to fracture. First the cohesive zone must form and then it will propagate. Also, the numerical convergence rate at the beginning of the simulations is slow and the solver must reduce the initial time step considerably. After an initial transient time period, the solution recovers and the time step is adaptively increased to the user- specified maximum. This behavior appears to be specific to the localization elements. We have changed the finite difference tangent of the localization element, resolving previous sources of error. More work is needed to understand the source of slow convergence, but a coding error cannot be ruled out at this time. We witnessed the same difficulty with the compact-tension cases, but we have been successful in driving down the residual to acceptable (and quite tight) tolerances. Finally, membrane forces are still an issue. We have investigated this before and need to revisit those calculations. We believe that the pressure field is being affected by membrane forces. Those pressures will affect local crack-tip fields and the resulting resistance. More study is needed to quantify the numerical implications of neglecting membrane forces. First and foremost, we have concentrated on solving issues with the standard formulation.

C5.3 Compact tension simulations

Having fit the material parameters through K-field simulations, we now can transition to predicting behavior for the side-grooved compact-tension specimen. We can, however, employ additional checks because the geometry has a sharp crack tip. Given the toughness of 2024-T3, we can actually apply fracture mechanics to the problem of interest and determine if the input resistance matches the global, far-field driving force at crack propagation. This can be accomplished via two methods. The easiest and most accurate approach is to apply the new J-integral capability in Sierra Mechanics. Employing the same mesh with a sharp pre-crack at a/W of 0.3, we need only select a node set on the crack front and a side set specifying the crack face. Using the same constitutive model without damage, we calculate the driving force as a function of simulation time, Figure C117. Note that the driving force is directly correlated with simulation time. Further, the driving force is independent of the two choices of plasticity parameters.

Next, following ASTM E399 9.1.1, we plot the global force versus displacement curve and the

secant line to determine the load at which the crack propagates, Figure C118. With this load we can determine the simulation time at which the crack propagated using Figure C119. Thus, because of the direct correlation between driving force and simulation time, we can determine the resistance as per ASTM E399. Ideally, the macroscopic crack propagates at the resistance "tuned" with the K-field simulation, indicating a direct correspondence between the idealized K-field simulations and the small-scale yielding solution at the centerline of the specimen. In practice, however, the correspondence shows the input resistance differs from the simulated resistance by 10%. More work is needed to understand that difference.

Following the procedure outlined above, for h = 60 μm, m = 5, the macroscopic crack propagates at a driving force of ~28 MPa√m while the tuned resistance was 32 MPa√m. Instead of h = 60 μm, m = 5 representing the average resistance, it is more closely aligned with a lower bound for the resistance. Additional simulations for h = 60 μm, m = 4.5 illustrate that the resistance at propagation is approximately 31 MPa√m, the average toughness from the literature. For h = 60, m = 4, the toughness is approximately 34 MPa√m, approaching the upper bound. We need to do more work to understand the discrepancy between the K-field tuning and the toughness as determined per E399. However, because we must provide a solution, we tend to side with the macroscopic simulations. Although the K- field simulations do yield insight and general trends, we are using the J-integral calculations for the actual specimen geometry to yield solutions that correspond to a near lower-bound, average, and upper-bound toughness.

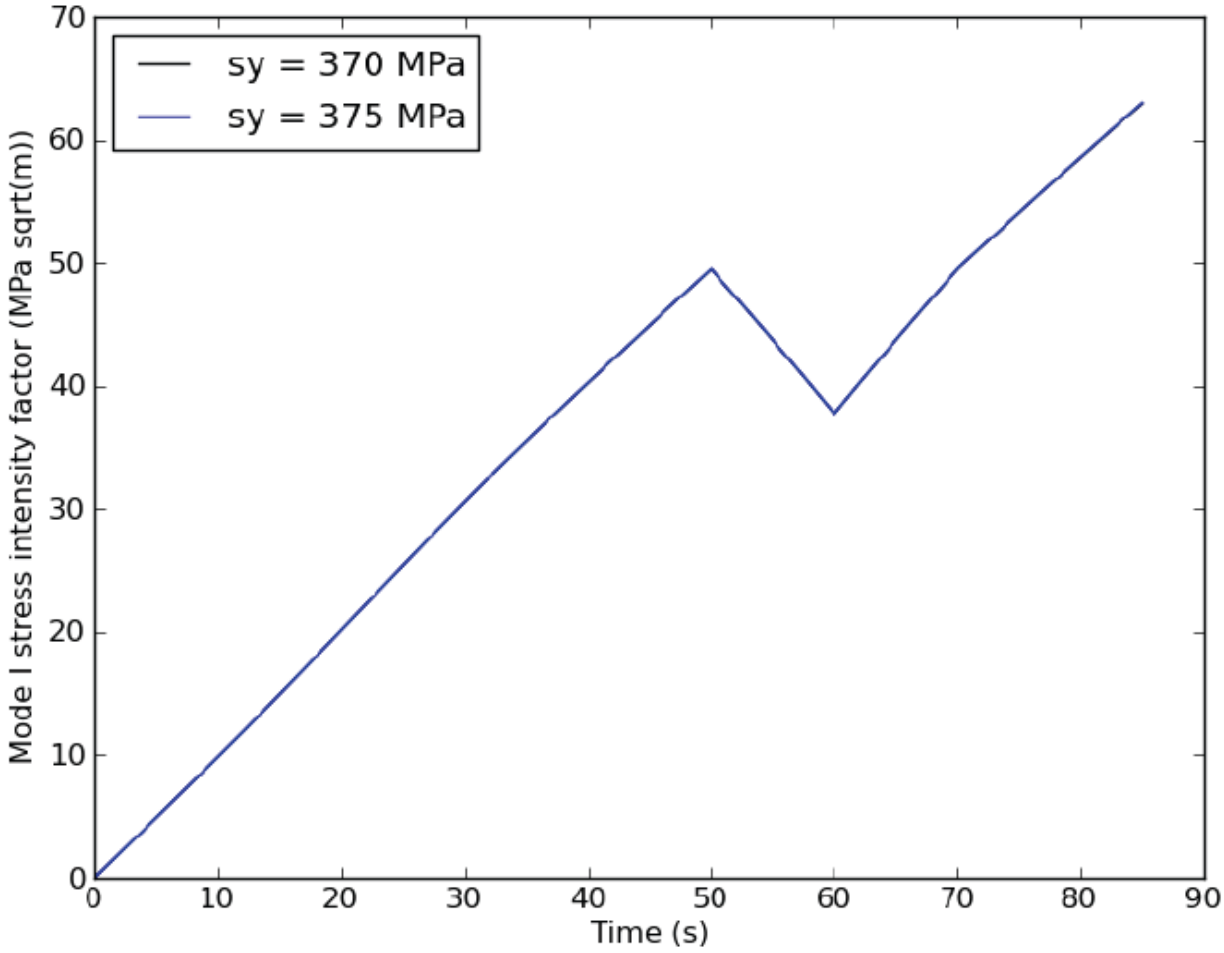

Figure C117. The computed driving force, mode-I stress intensity factor, versus time when the constitutive model is used with no damage.

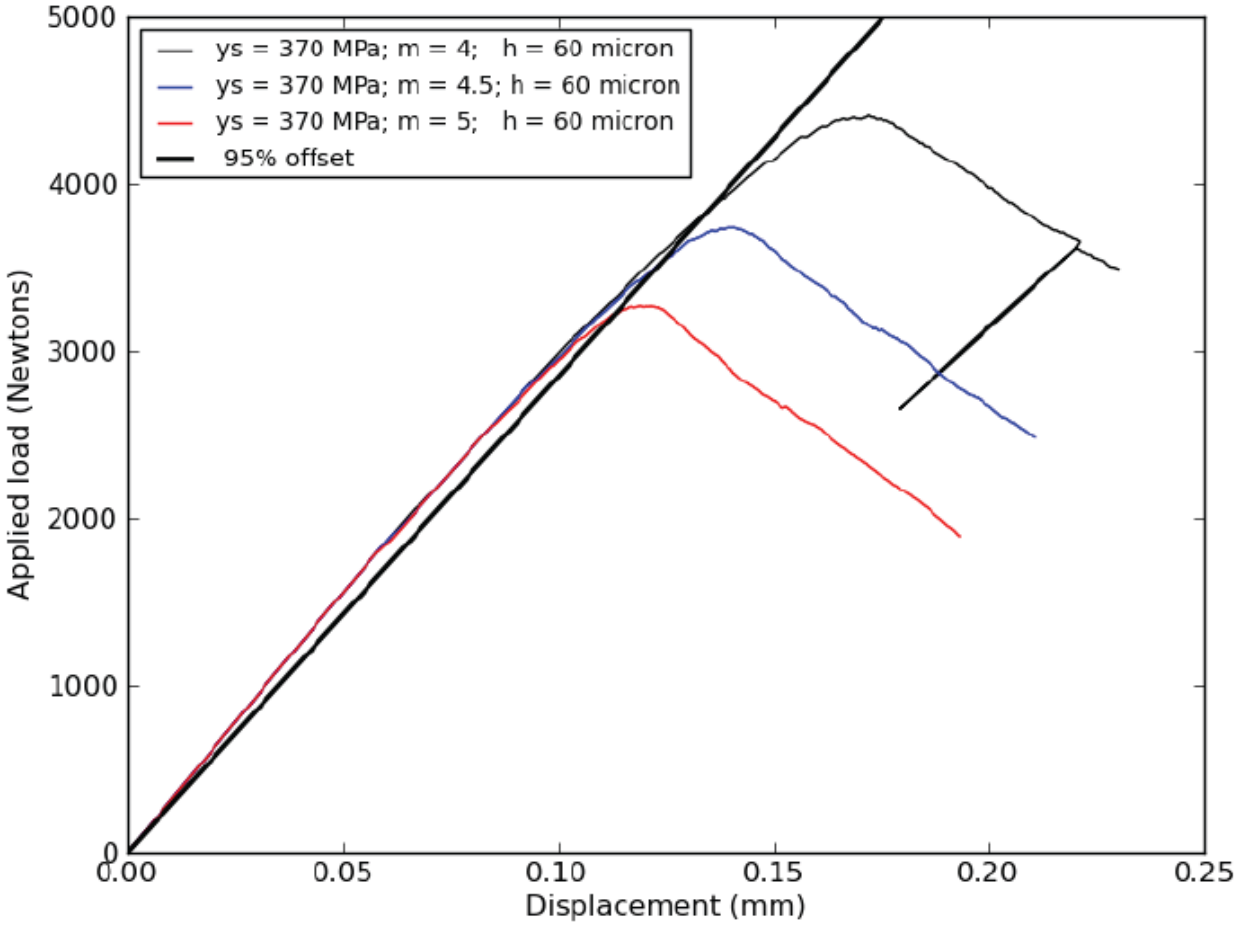

Figure C118. Force versus displacement for the compact tension specimen with the ASTM E399 straight line

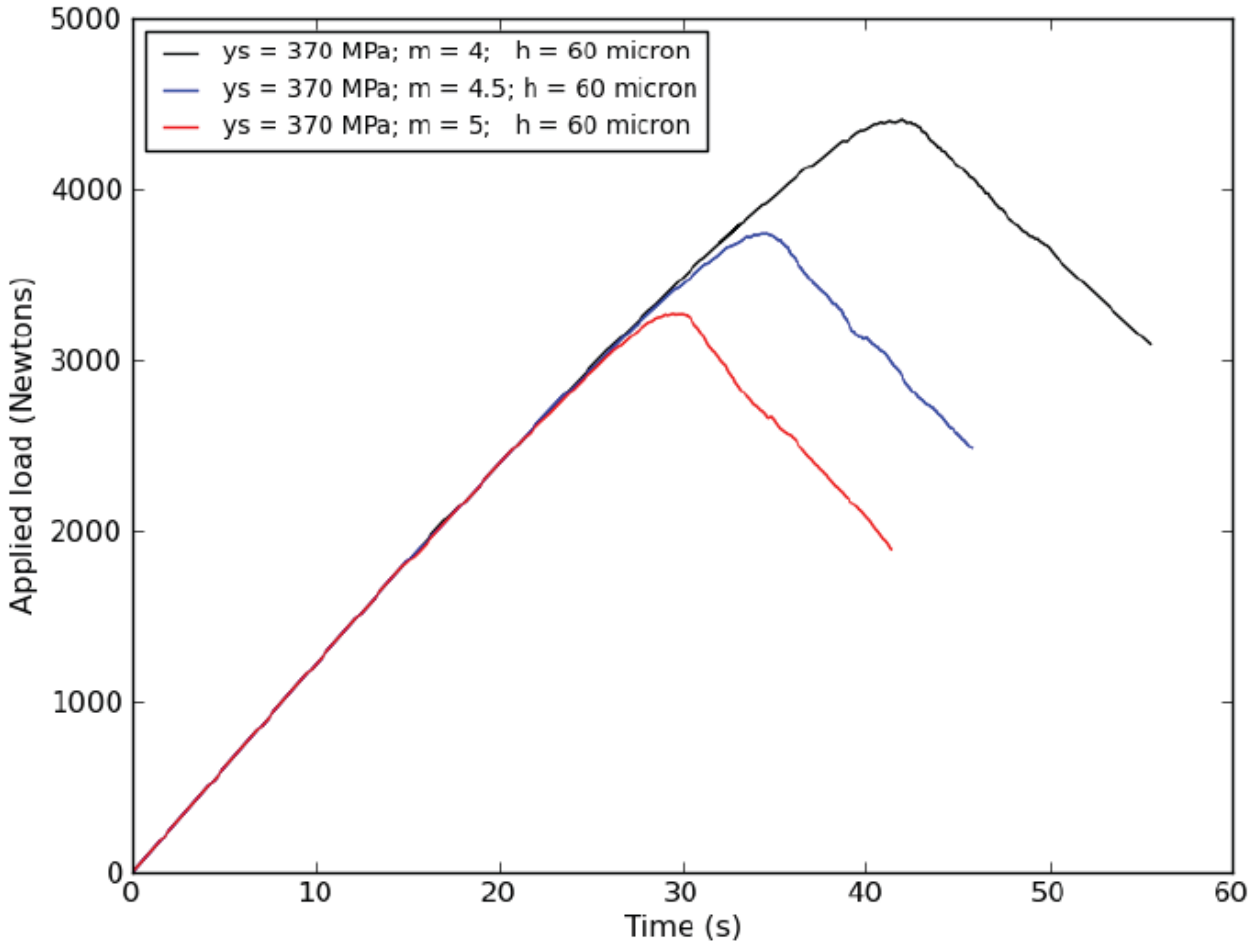

Figure C119. Force versus time for the compact tension specimen.

Note from Figure C117, time and driving force are directly correlated.

C5.4 Comparison to analytical solutions

Although we do rely on a computed driving force for the side--grooved specimen, we also compared driving force solutions from Sierra mechanics to the analytical solutions provided in ASTM standards. ASTM E399 was employed to find Kapp from the reaction force P. In order to compare with our computational solution, we also needed to employ a correction for the side grooves. That correction is given in ASTM E1820, Beff = (B Bnet)1/2. Rather than complete a full J-integral analysis per the standard, we only wanted to compare for small loadings. The computational and analytical solutions coincided for small loadings and slowly diverged near the first unloading. As expected, the computational prediction for the driving force (assuming a nonlinear elastic material through J2 plasticity) is slightly greater than the LEFM solution.

We also attempted to correlate our compliance solutions with those given in the literature. This turned out to be much more difficult than expected. Although one can obtain some agreement among solutions for the compliance, ASTM E399 should not be used as it does differ from other

solutions in later standards. Both ASTM E1820 and the fatigue standard, ASTM E647, employ the same solution for relating crack length to compliance. All 2-D solutions for compliance are given in plane stress as this stress state is generally more accurate for the displacement field while plane strain is employed for the driving force (ASTM E647). Finding the compliance from the crack length requires that one just find the root of a fourth-order polynomial. These solutions can also be related to Newman's solution (International Journal of Fracture, Vol. 17, No. 6, 1981) provided that you assume that 2VLL = Δ. Using E647, we find the initial stiffness (P/Δ) to be 2.37E7 while the stiffness calculated from simulation is
3.13E7 N/m. We ascribe some of the difference to the calculation of the effective width and the possibility that the heavily side-grooved specimen might more exhibit plane strain. The differences, however, are quite large and probably cannot be explained by these factors. These differences probably stem from how we load the specimen. We effectively "weld" a stiff elastic region into the pin location. This region has a stiffness of 200 GPa (steel) which is roughly three times the stiffness of the aluminum. This might cause significant deviations in stiffness for all a/W. One can seek to minimize the error by placing a small elastic region at the top of the pin and the increased stiffness would not greatly contribute to the overall beam stiffness (or compliance). Future calculations will consider this change in the applied loading and determine the effect on the compliance.

C5.5 Results

Figure C120 shows the global response of the compact tension specimen for the various material properties used in our simulations. This demonstrates the strong dependence on the choice of the damage exponent, m, with peak load ranging from 3268 N to 4401 N for m = 5 to m = 4, respectively. The early post-peak response appears to be relatively independent of the damage exponent; however, the unloading compliance and latter stages of the response do exhibit dependence on the exponent. Also, the solid and dotted red curves for m = 5 results reflect both model fits and show that there is no dependence on the choice of plasticity model in the global response. Hence, the results reported in Tables 1 and 2 (below) are only for the plasticity model with yield stress of 370 MPa and the lower-bound, mean and upper-bound values of the damage exponent, m = 5, m = 4.5, and m = 4, respectively.

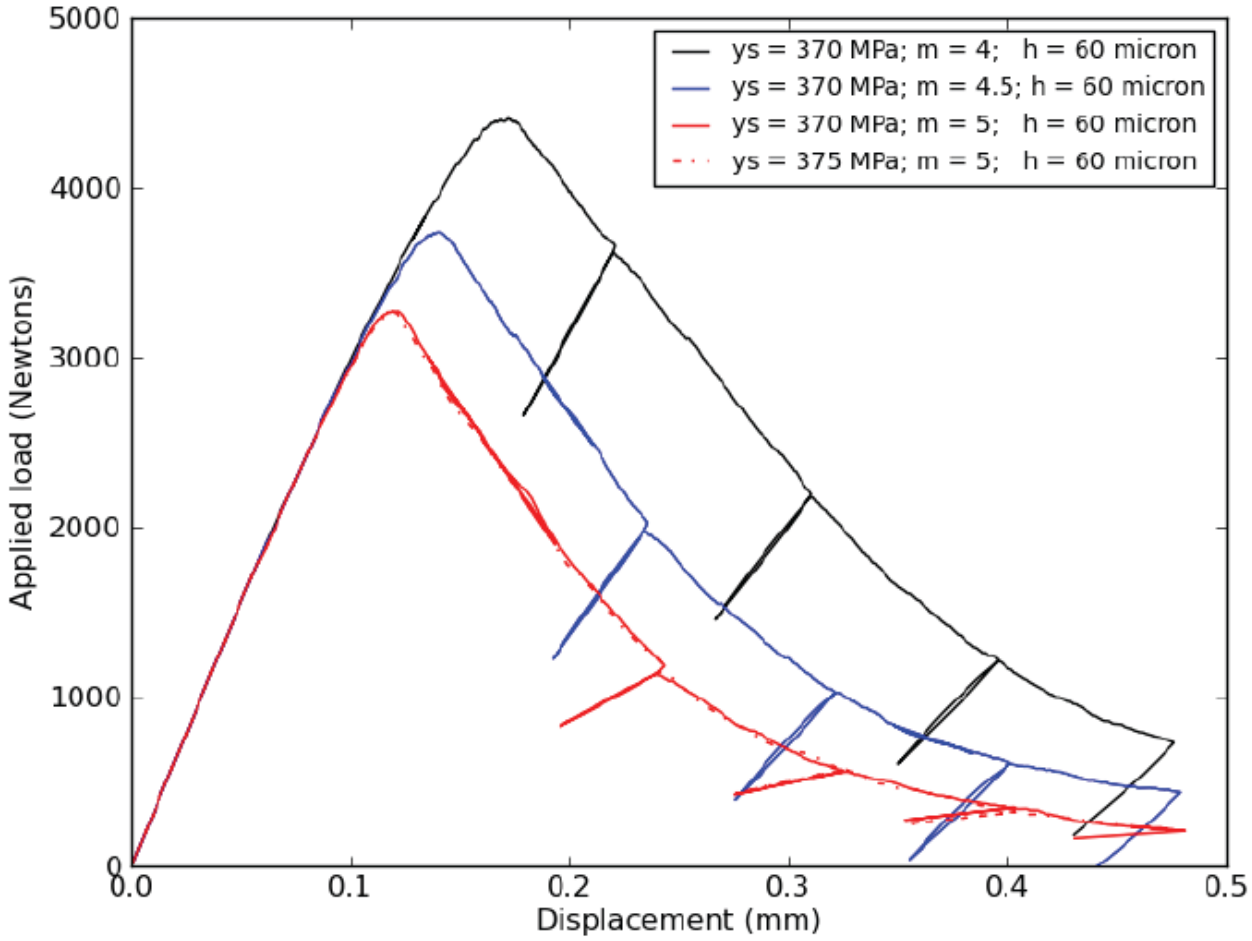

Figure C120. Force versus displacement curve for various material properties.

We should not that that although the displacement shown in Figure C120 is crack mouth opening displacement at the load line, we are controlling the simulation through load-line displacement. During the latter portion of propagation the load-line displacement (and longer crack lengths) can be correlated with the crack mouth opening displacement. However, for the first 45two unloadings, substantial errors are incurred. These errors also scale with the damage parameter because smaller values of m results in shorter cracks for a given load-line displacement. The difference between the controlling load-line displacement at the pin and the measured crack-mouth opening displacements below the pin are illustrated in Figure C121.

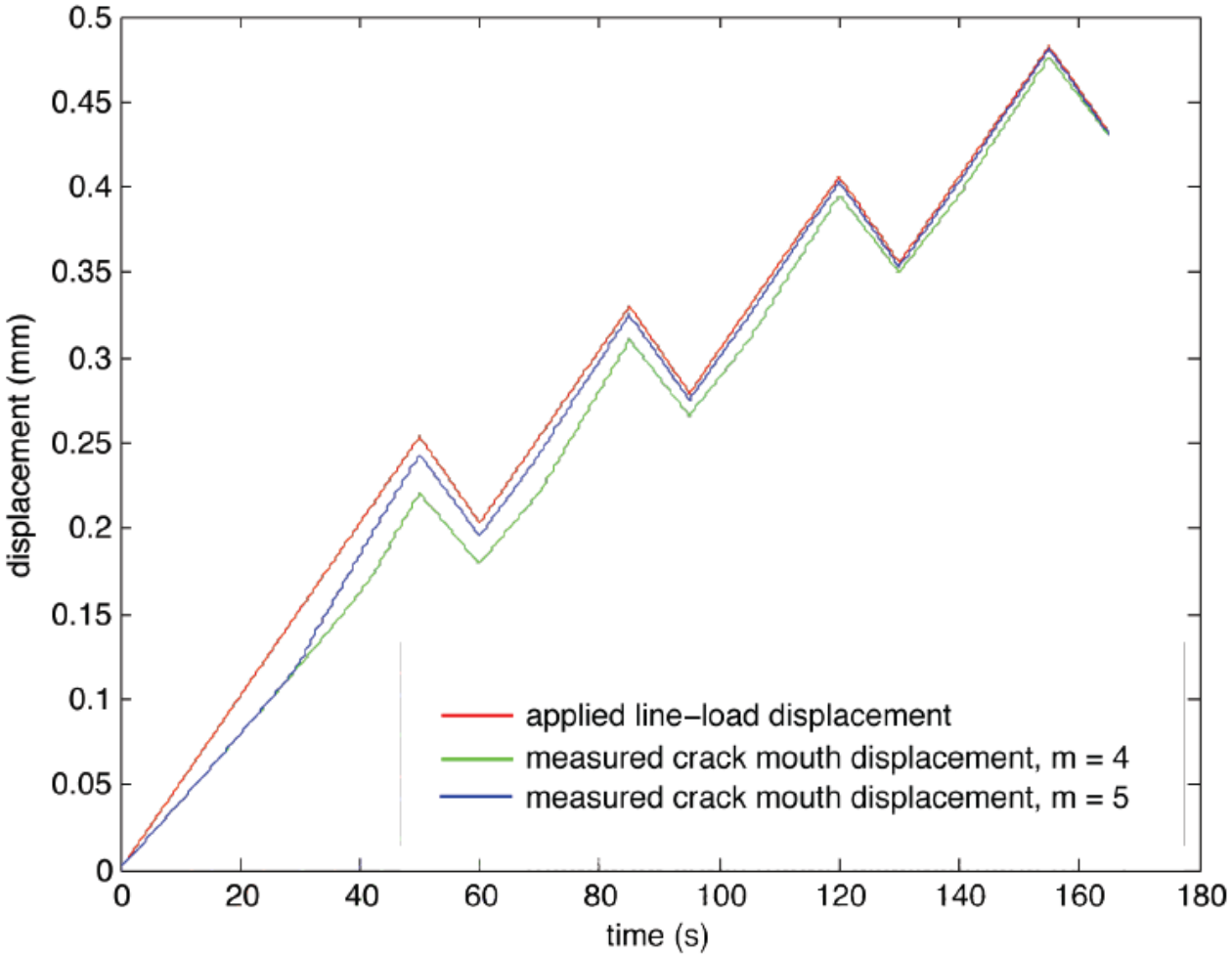

Figure C121. Differences between the applied load-line displacement and the measured crack-mouth opening displacement along the load line. Although the differences for small long crack lengths are minimized (m = 5), shorter crack lengths (m = 4) at t = 60 s do generate significant errors.

Table C3 through Table C5 tabulate the results of crack length and compliance for the four unloading programs. Included in the table are the time of unload, the total crack length at the peak associated with unload, the change in crack length associated with the peaks, the a/W ratio (W = 25.4 mm), the stiffness of unloading/reloading and the compliance of unloading/reloading. The crack length that is reported is the total crack length and includes the initial 7.62 mm crack length (initial a/W = 0.3). The change in crack length reported represents the amount of crack propagation leading up to the peak in loading. The compliance reported is merely the inverse of the stiffness. The stiffness was computed by a least squares fit to the data in the unloading portion of the curve. Finally, Table 4 merely compares all the results for varying toughness.

Table C3. Results for lower-bound material properties, m = 5.

Unload	Time (s)	crack length (mm)	Δ a (mm)	a/W	Stiffness (N/mm)	compliance (mm/N)
-	0	7.62	-	0.3	-	-
A	50	16.36	8.74	0.64	7170	1.39e-04
B	85	19.47	11.85	0.77	2830	3.53e-04
C	120	20.89	13.27	0.82	1510	6.64e-04
D	155	22.02	14.40	0.87	836	1.20e-03

Table C4. Results for average material properties, m = 4.5.

Unload	Time (s)	crack length (mm)	Δ a (mm)	a/W	Stiffness (N/mm)	compliance (mm/N)
-	0	7.62	-	0.3	-	-
A	50	14.18	6.56	0.56	18100	5.53e-05
B	85	17.90	10.28	0.71	13900	7.21e-05
C	120	20.02	12.40	0.79	12300	8.16e-05
D	155	21.15	13.53	0.83	11300	8.88e-05

Table C5. Results for upper-bound material properties, m = 4.

Unload	Time (s)	crack length (mm)	Δ a (mm)	a/W	Stiffness (N/mm)	compliance (mm/N)
-	0	7.62	-	0.3	-	-
A	50	10.69	3.071	0.42	23600	4.23e-05
B	85	14.71	7.089	0.58	16500	6.06e-05
C	120	17.80	10.18	0.70	13200	7.57e-05
D	155	19.73	12.11	0.78	11700	8.57e-05

Table C6. Comparison of a/W for the upper-bound, average, and lower-bound toughness

Unload	Time (s)	a/W KIc = 34 MPa√ m m = 4	a/W KIc = 31 MPa√ m m = 4.5	a/W KIc = 28 MPa√ m m = 5
-	0	0.3	0.3	0.3
A	50	0.42	0.55	0.64
B	85	0.58	0.71	0.77
C	120	0.70	0.79	0.82
D	155	0.78	0.83	0.87

C5.6 Sources of error

We have identified multiple sources of error. We have attempted to rank these errors but some have not been quantified and we can only reference analytical solutions without additional simulations.

1. We must rely on literature values for the toughness. Consequently, we provide an upper bound, average, and lower bound solution for a fracture toughness of 34 MPa√m, 31 MPa√m, and 28 MPa√m, respectively.

2. We did not match the compliance from linear elastic fracture mechanics. Late in the

assignment we began to check our solutions with LEFM solutions of the compliance (ASTM E1820, ASTM E647, literature) and determined that we did not match the initial compliance. We note that we did match the LEFM solutions for the driving force but the compliance is more sensitive to the methodology in which we are applying the loading. Specifically, we believe that our welded, steel pins are increasing the specimen stiffness and contributing to this error. We can apply the load through a local elastic region at the top of the pin but those studies were not completed. Thus, our solution for the compliance has been polluted for all a/W.

3. We did not follow a crack mouth opening displacement (CMOD) profile. Instead, we followed a load-line displacement profile. This difference is minimal for large a/W but does impact the result for smaller a/W.

4. Smaller values of m lead to cracks that are not straight. The curving crack front leads to an increased stiffness for an equivalent value of a/W for larger m. In this sense, the compliance is a 3-D quantity because it does reflect a curved front. We term this an error because we believe that the front is curved a bit more than one can physically justify. Even if the crack length is reflective of the experiment the compliance will be less than physically justified and provides additional motivation for increased physics in our damage models.

C6. Follow-Up for Challenge 2A

After our predictions, the experimental load-displacement curves and compliances were shown. Our predictions could have been much better and we sought to determine major sources of error.

C6.1 False assumptions

Prior work assumed that the macroscopic driving force could be equated to the plane strain toughness of the material. Because our extrapolation was not robust, we tuned our material parameters to the driving force calculated through a J-integral calculation. The driving force does converge in the center of the specimen and we believed the center of the specimen to be under plane strain. While this seemed logical at the time, it was, in fact, erroneous in that the given specimen was not fully constrained. Even with the large side grooves, the specimen thickness is much smaller than the plane-strain thickness that would be employed to generate a valid plane-strain fracture toughness. J-integral calculations can be converged and "flat" for specimens not in plane strain. Tuning to the plane strain fracture toughness resulted in our simulation propagating at lower driving forces and hence, smaller loads.

To avoid future issues, we need to rectify our extrapolation procedure from the plane strain fracture toughness to the specimen geometries. In the last few weeks, we have explored two potential areas of concern. First, we wanted to examine the membrane forces and their contribution to crack-tip fields. Second, we are working with Arthur Brown to implicitly integrate the damage evolution within the material model. This is still in progress. We are still employing the old integration scheme and, in some cases, chasing our tail. We emphasize that future work will remedy this issue so that we can be assured that the model is properly integrated and assumptions regarding volumetric strain are consistent with void growth and coalescence. It is our hope that modification of the membrane forces and a robust integration scheme will enable us to tune to the damage model to the plane-strain fracture toughness and extrapolate to lower constraint geometries.

C6.2 Rectifying membrane forces

We spent time after reporting results to determine if membrane forces. In addition to verifying the implementation, we systematically investigated the role of the membrane forces on the generated toughness. The study was encouraging. In the absence of membrane forces, the computed fields are smooth and look correct. In addition, unlike prior studies, the resistance did not significantly change with mesh size and varies smoothly (relatively) with both the damage exponent m and the characteristic length h. Finer meshes should yield increasing resistance but converge (asymptotically) with subsequent refinements. One difficulty with having membrane forces off is that it leads to a nonsymmetric stiffness matrix. With significant effort, we have made great strides to overcome this and we are able to solve those systems using a different scheme (newton with a line search) with different iterative and direct solvers (ML and SuperLU).

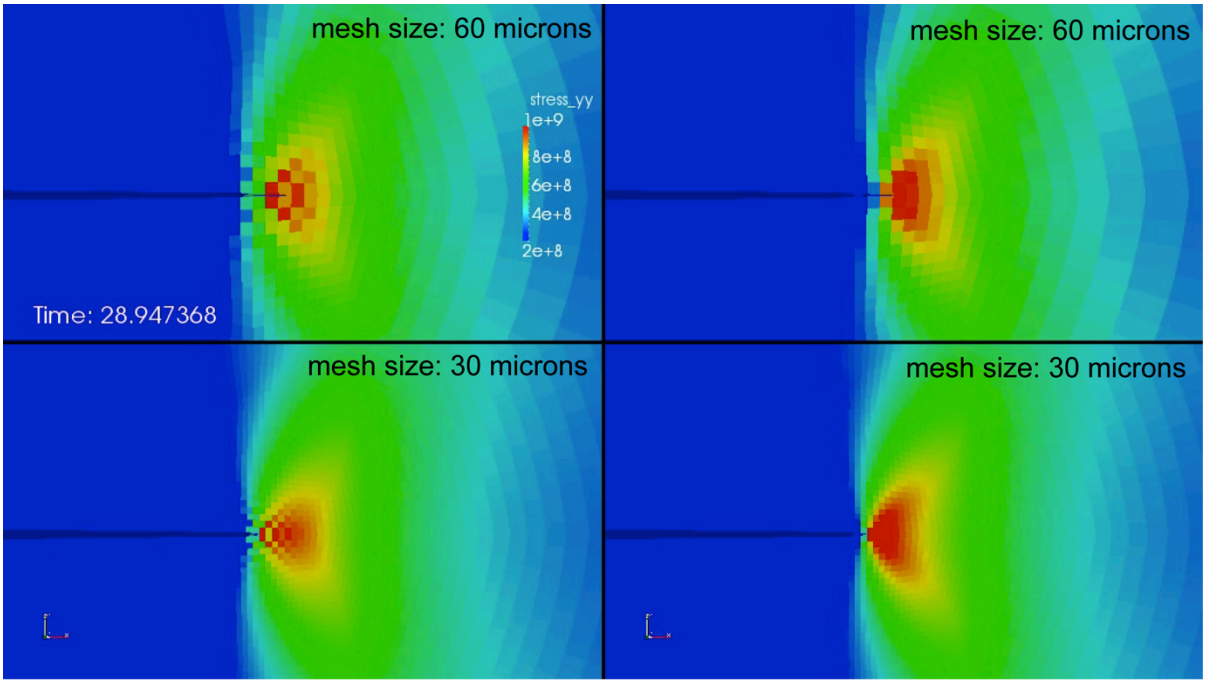

Figure C122. Effect of the membrane forces on the stress field

When h is on the order (or greater) than the element size, membrane force can corrupt crack tip fields. In this specific case, the "tiling" of the stress field hampers crack propagation. Turning off the membrane forces enables smooth fields and permits crack tip blunting.

C6.3 Integration scheme of BCJ_mem

Time step studies conducted in prior work motivated us to re-examine the integration scheme for BCJ_mem. Arthur Brown has moved to an implicit scheme for pressure and damage and we are currently debugging the implementation for X-Prize. While we are very close, a few issues emerged that we need to consider. If one assumes dilute void growth, should the dilatational strain continue to grow with increasing porosity? Because coalescence will occur, large volumetric strains are non-physical and will affect the boundary value problem in unexpected ways. We are currently considering this matter. We also should note the obvious - the need to move to an implicit integration scheme. We still are having issues with the prior, explicit implementation. Large, nonphysical triaxilities develop in the localization elements prior and during crack propagation. This complicates both the fitting process and ultimately the reliability of our X-Prize predictions. We hope to be using an implicit scheme in the very new future and we will revise both our fitting procedures and our predictions with the new scheme.

C6.4 Issues with the compliance

We investigated the role of specimen compliance and its impact on our predictions. Included in our original report, we asserted that our assumed boundary conditions would be artificially rigid and, therefore, would reduce the initial compliance. To test the hypothesis, a new set of boundary conditions was applied which removed the rigid plugs from the loading holes and applied the displacements at the distal edges of the loading holes. Figure C123 plots the load versus displacement for the experiments and three simulation results.

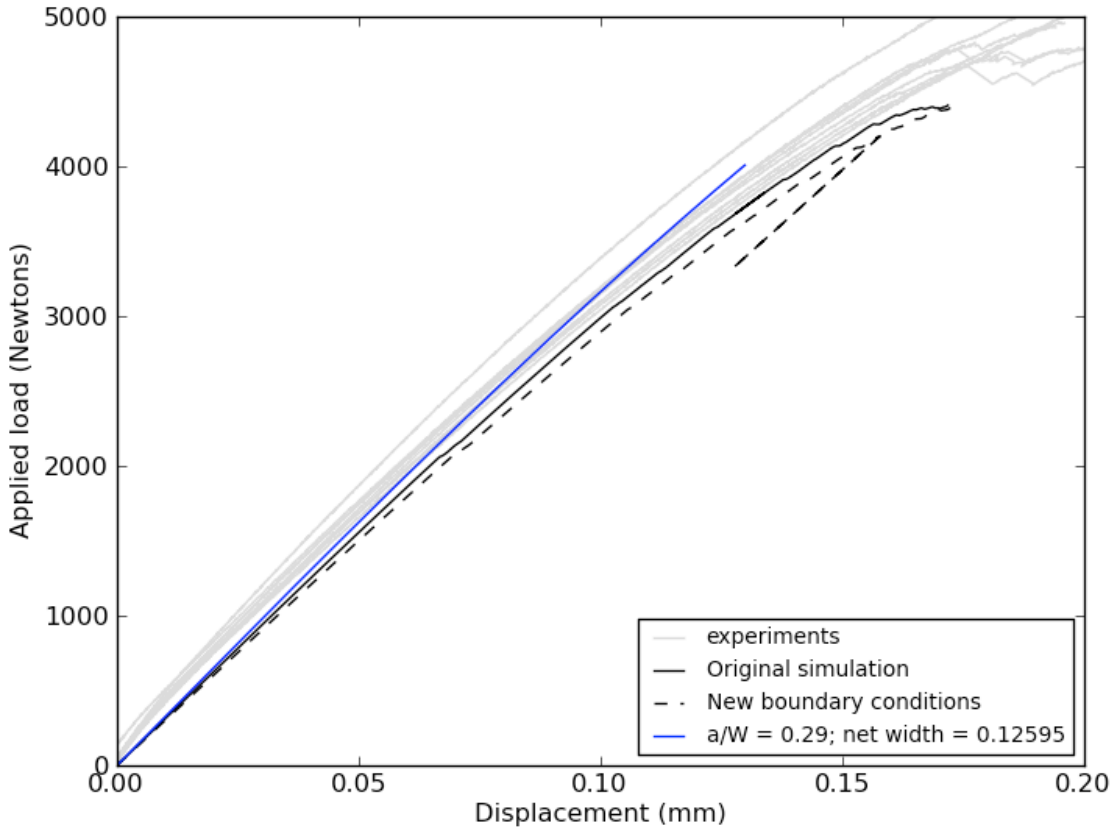

Figure C123. Load versus displacement prior to crack propagation showing the experimental observations plotted with three simulation results: a) the original simulation with geometry exactly matching specimen drawings and assumed pin-loading boundary conditions; b) an alternate boundary condition focusing the applied load at the top (and bottom) of the loading holes; and, c) an alternate geometric arrangement reflective of the average "as-built" geometry of the experiments.

In the figure, the solid black line shows the original prediction while the gray lines are the experimental observations. It is noted that the initial compliance of the experimental specimens is not adequately captured in the original simulation. The dashed black line is the simulation result with the modified boundary conditions. By design, this set of results is less stiff than the original simulation and represents a greater deviation from the experimental findings. The possible sources of this discrepancy are initial geometry and materials properties because there is no crack propagation in this early stage of loading. Upon request, Brad Boyce quickly provided a micrograph of a failed specimen which clearly illustrates the fatigue pre-crack. Closer observation of the fatigue pre-crack revealed that the initial crack depth was smaller than per the design drawing.

Figure C124 shows the experiment observation and measurement of the crack depth (courtesy B. Boyce).

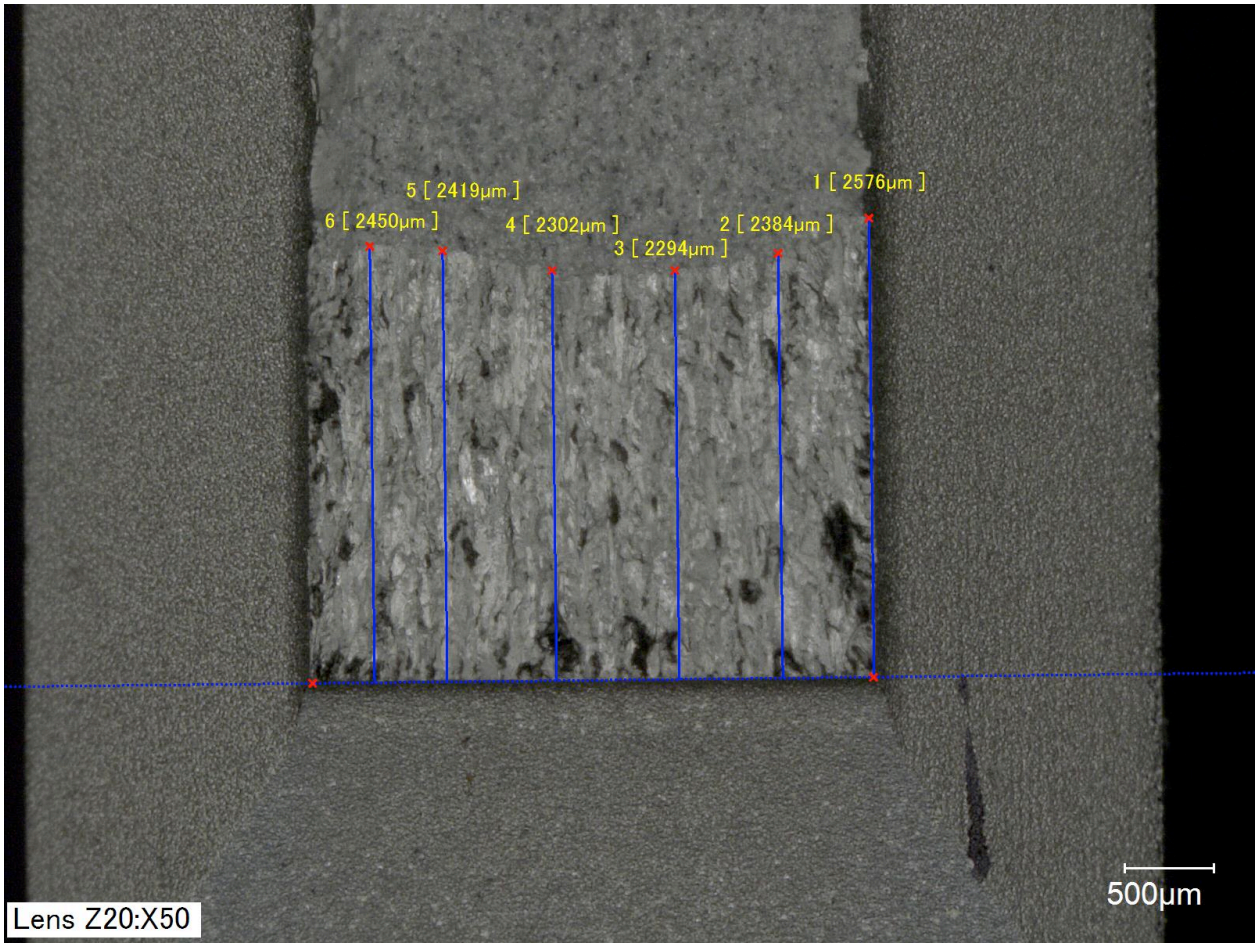

Figure C124. The fatigue pre-cracked surface of one of the experimental specimens.

Furthermore, in the experimental records, the net section width was recorded. The average of these was 0.12595", which is 0.00195" greater than the design drawing. These differences are small; however, they do make a noticeable difference in the initial compliance. In Figure C123, the solid blue line shows the simulation result with the original boundary condition, but with the geometry modified to accommodate the small perturbations in the observed geometry.
One can see that the small changes in the geometry and boundary conditions make significant differences in the initial compliance. These differences are dramatically escalated in the driving force. Figure C125 plots the driving force calculation for the original simulations and the modified boundary conditions (with the calculation for the modified geometry/modified boundary condition yet completed). For the difference in initial stiffness between the original boundary conditions and the modified boundary conditions, the difference in the driving force is large. This will likely be larger for the as-built geometry.

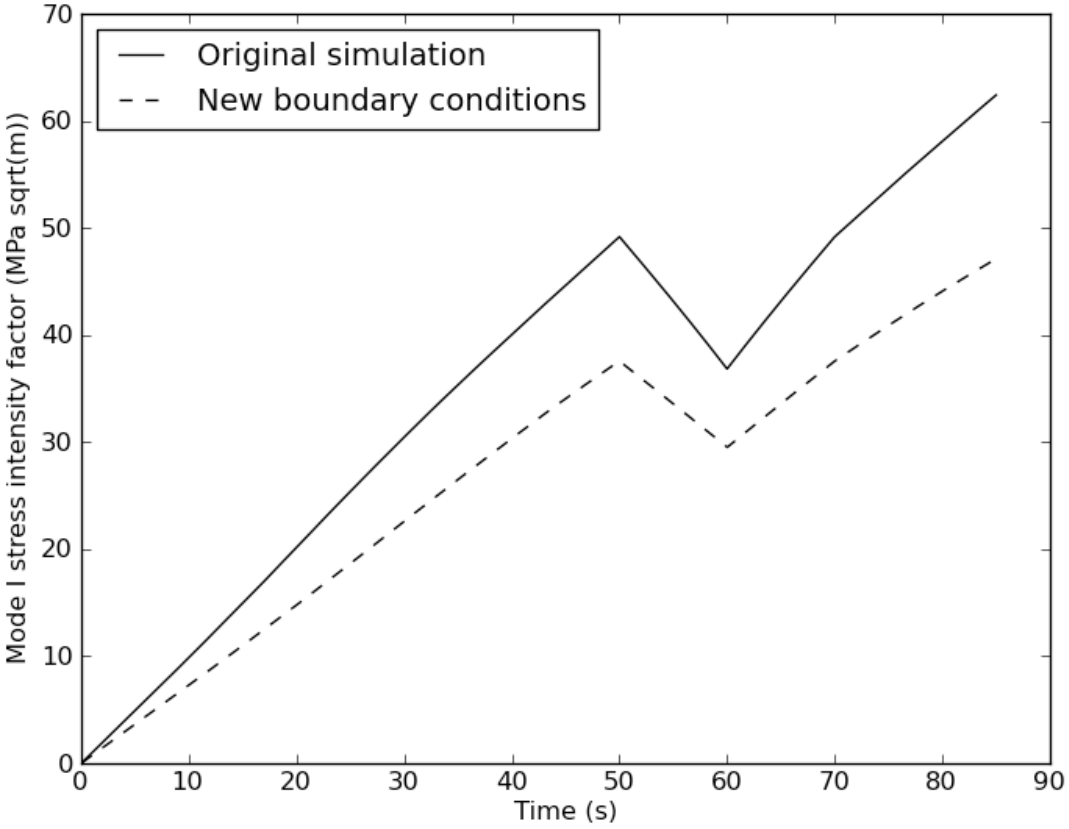

Figure C125. The driving force for the original results and for the simulation with modified boundary conditions.

In summary, we are still pushing ahead on multiple fronts to better understand both the methodology and our ability to tune and predict crack initiation and propagation for the given geometry with our given physics.

APPENDIX D: XFEM

Jim Cox (1524), Ben Spencer (1542), and David Littlewood (1435)

D1. Predictions for Challenge 1A

The X-Prize XFEM group analyzed the 1A challenge using finite element modeling with elastic-plastic material models and a failure criterion based on equivalent plastic strain. Two analysis codes were used: Abaqus and Sierra Mechanics. In both cases, model calibration was carried out against experimental data provided by Jerry Wellman. In neither case was the stress triaxiality considered. A criterion that does account for the triaxiality, the tearing parameter (Wellman), has been used in Sierra with success. Other criteria that treat the bound on equivalent plastic strain as a function of the stress triaxiality are given in the literature by *e.g.* Wiezbicki *et al.*

The calibrated models and failure criterion were then applied to the 1A problem. The resulting predictions are:

Table D1. Predictions for Challenge 1A.

Software	Load-Line Displacement	Reaction Force
Abaqus	0.09 inches	3100 pounds
Sierra Mechanics	0.086 inches	3080 pounds

Details regarding the analyses are provided below. For both codes, additional analyses have been completed since the January 4th submission. The analyses carried out with Abaqus include a mesh refinement (which reduced the load-line displacement from approximately 0.1 to 0.09 inches). The analysis carried out with Sierra Mechanics contains several improvements, specifically, changing the element type to the nodal-based tetrahedron and explicitly modeling the loading pins.

D1.1. Introduction

Extended finite element method (XFEM) capabilities are in a research and development state both at Sandia and within commercial FEA codes. This is reflected in the results obtained for this first challenge problem. To "predict" crack initiation two "XFEM approaches" were taken – one using Abaqus, and the other using Sierra mechanics. Neither code is equipped yet with the ability to apply general initiation criterion and to introduce a strong discontinuity in an arbitrary position within the domain – though both are quickly approaching this goal. While Abaqus (version 6.9) has 2d and 3d XFEM capabilities, its crack initiation criteria for XFEM are limited to upper bounds on the maximum principal stress or elastic strain. Sierra mechanics can not yet initiate an XFEM crack based upon mechanics. Note that because the codes' limitations, the more meaningful results presented do not use XFEM to represent the kinematics of a crack but rather answer the question of when the crack would initiate at a point if it were based upon equivalent plastic strain. Overviews of some the Abaqus and Sierra mechanics results are presented in the two sections below.

D1.2. Abaqus XFEM Results

Jim Cox (1524)

The table below summarizes the candidate initiation states highlighted in Figure D126. The underlined results are those reported in January. Since measures of elastic strain are not commonly used for crack initiation for ductile fracture, only the states of equivalent plastic strain are considered useful; even these predictions do not address the stress triaxiality. After the first mesh refinement a better prediction is Δd~0.09 in. and F~3100 lbs, but Figure D126 suggests that while the load may not change much with mesh refinement Δd might. However, the omission of making the initiation criterion dependent of the stress triaxiality may be a bigger factor than the mesh density.

Table D2. Candidate crack initiation7 states.

Initiation Criterion	Mesh 1 Δd (in)	Mesh 1 F (lbs)	Mesh 2 Δd (in)	Mesh 2 F (lbs)
$\max(\varepsilon^{ep})>0.81$	0.09920	3119	0.08928	3086
$\max(\varepsilon^{ep})>0.815$	0.09965	3118	0.08977	3085
$\max(\varepsilon^{ep})>0.852$	<u>0.10324</u>	<u>3113</u>	0.09325	3080
$\max(\varepsilon^{e}_{max})> 0.0113$	<u>0.2462</u>	<u>2801</u>	0.13577	2981

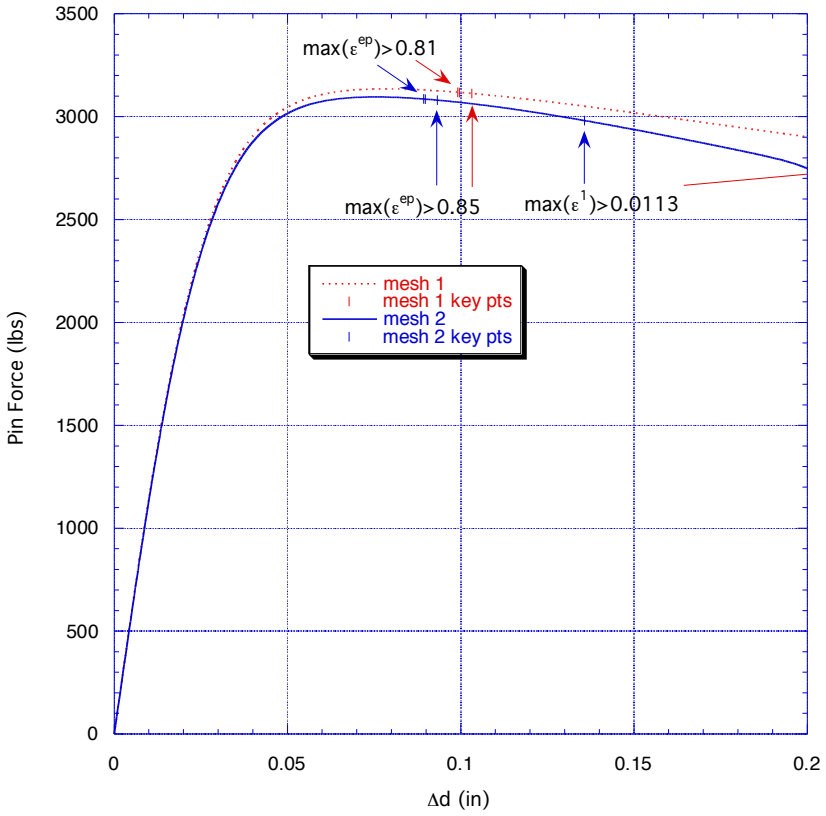

Figure D126. Challenge 1A solutions for 2 meshes.

D1.3. Sierra Mechanics "XFEM Results"

Ben Spencer (1542) and David Littlewood (1435)

The load line displacement and pin reaction force at the onset of cracking in the 1A challenge problem have been reevaluated using explicitly modeled pins and the nodal-based tetrahedron

element type available in Sierra Mechanics. The XFEM capabilities in Sierra are operable only with single-integration-point four-node tetrahedron elements, of which there are two types: the standard four-node tetrahedron, and the nodal-based tetrahedron. The standard four-node tetrahedron was used for the initial analysis of the 1A challenge problem (submitted January 4th). The results from the initial analysis, however, exhibited signs of overly stiff material response, which is characteristic of the standard four-node tetrahedron. A secondary analysis using the nodal-based tetrahedron yielded improved results. Further improvements were achieved by explicitly modeling the loading pins, as opposed to applying loading directly to a node set on the inner portion of the loading holes.

Using nodal-based tetrahedron elements, the Sierra Mechanics simulation predicts crack initiation at:

Load line displacement = 0.086 inches
Force = 3080 pounds

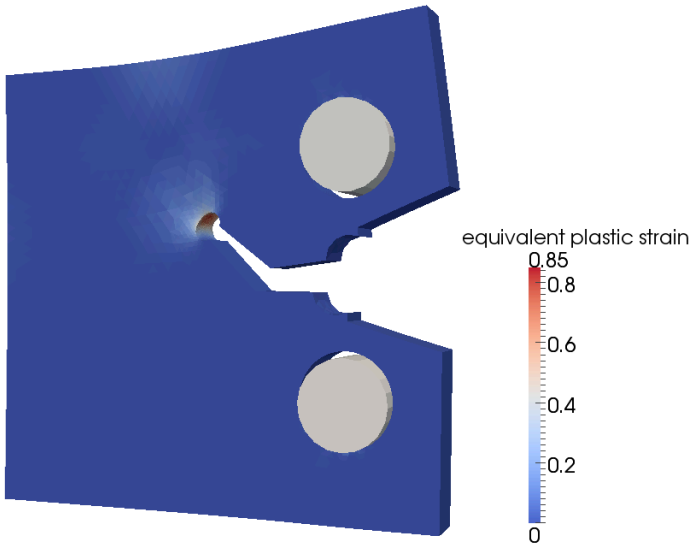

Figure D127. Sierra Mechanics simulation at failure.

D2. Follow-Up for Challenge 1A

D2.1 Abaqus XFEM

The questions given in January are first answered followed by the main results. The results submitted in January were limited to single meshes. After the initial submission, additional work on mesh convergence was conducted and presented here (mesh 2).

1. *Describe what material model you used for deformation (not crack initiation)? How did you calibrate that model against material properties? What parameters did you calibrate? Please specify what specific resources (datasets) you used to calibrate the parameters.*

Abaqus's isotropic hardening plasticity model was applied to the problem. To calibrate the plasticity model, I modeled the gage length region of a tensile specimen (mesh provided by John Emery), and then fit a piecewise linear hardening function to match the engineering stress versus nominal strain results. The experimental data used to calibrate the model were those provided by Jerry Wellman from tests performed in Theresa Cordova's structural mechanics lab for three round bars (labeled on the share-point site as ph13-8-h950-test*N*-smooth.dat). The FEA model consisted of a half model axially and a twenty-degree section radially.

Additional details:
The elastic properties were taken from the Carpenter 13-8 stainless data sheet: E=28.3e6 psi, ν=0.28.

Figure D128 shows the first 3 calibrations for the hardening functions. The first hardening function came from the sharepoint file labeled handbook-tru.dat. Figure D129 shows how the first three calibrations affect the predicted specimen response and compares them with experimental test 3. Figure D130 and Figure D131 shows the results for the fourth calibration. Calibration 4 made the predicted tensile test behavior closer to the average of the three tensile tests – biased less to test 3. As such the slope of the hardening curve was reduced in the last line segment. Calibration 5 extended the hardening to larger values of effective plastic strain. Without extending the hardening curve, the plastic response was perfectly plastic after the last line segment.

2. *Describe what material model you used for crack initiation? How did you calibrate that model against material properties? What parameters did you calibrate? Please specify what specific resources (datasets) you used to calibrate the parameters.*

Abaqus's crack initiation criteria for XFEM are limited to upper bounds on the maximum principal stress or elastic strain. Thus each criterion requires a single parameter – the corresponding bound. Since these criteria are not expected to be very useful for ductile fracture, I also examined the state at which the equivalent plastic strain reached critical values observed in the tensile specimen (crack initiation and specimen failure). The same data used to calibrate the plasticity model was used to calibrate the initiation models. The end of the curves in the experimental data was assumed to be the failure point for the specimens. Similarly the lack of convergence in the FEA model was

assumed to be the point where the specimen would fail (*i.e.*, the elastic strain energy exceeded the energy needed to create the new surface). Numerically convergence fails, as it is very difficult to capture the dynamic response under displacement control alone. A caveat here is that cohesive crack model was not calibrated for the material, rather a low fracture energy was attributed to the interface. While not usable in the Abaqus XFEM implementation yet, critical values of equivalent plastic strain were also recorded to determine when the crack might initiate based upon these values.

Additional details:
Figure D131 shows two model responses, the only difference of which was the criterion used for the crack initiation. One was tuned for the maximum principal stress criterion (s_{max}= 393 ksi) and the other for the maximum principal elastic strain criterion (ε^{e}_{max}=0.0113). The calibrations for the crack initiation occur nearly at the same state and fall within the experimental scatter. (Considering that neither are expected to be accurate, matching them closely is like putting a $1000 saddle on a $10 horse.) Note that the equivalent plastic strain at these failure points is approximately 0.852.

The motivation for extending the hardening in calibration 5 was that the initiation criteria were not being satisfied with a 3D model of the challenge specimen, even when the loading appeared to be extreme. The equivalent plastic strain in the tensile specimen exceeded the last segment of the hardening function, and thus perfect plasticity was occurring at some points in the specimen. The only perceptible change in the tensile specimen modeled response with the change in calibration was when the crack initiated and failed. Figure D132 shows that failure occurred earlier with the change of calibration. All of the initial material calibration work was done using Abaqus's c3d8r element – an 8-node brick that uses reduced integration. The initial models of the challenge specimen had used the c3d8 element – an 8-node brick that uses selectively reduced integration. While the element type had some effect on when failure occurred (run 10 *vs*. run 11), it was less significant than the change in calibration (run 9 *vs*. run 11). Figure D133 shows that the initiation criterion for principal elastic strain can be calibrated to give good results for plasticity model calibration 5; in this case the criterion was ε^{e}_{max}=0.01122. For simplicity, since I don't expect the strain initiation criterion to be useful, I used ε^{e}_{max}=0.0113 for both plasticity model calibrations. Note that using the XFEM capability there is a distinction between when the crack initiates and when the specimen fails. The maximum equivalent plastic strain is about 0.81 at initiation and about 0.85 at failure – both values are later considered.

The initial submission results did not include a mesh convergence study for the material calibration. Figure D134 shows the original calibration mesh and a refined mesh (*h*->*h*/2). Figure D135 shows the results for both meshes indicating excellent convergence. The only noticeable difference is when the specimen fails. These results are for strain initiation when ε^{e}_{max}=0.0113. For mesh 2 the specimen fails at an engineering strain of about 0.003 less.

3. *How was uncertainty captured in your simulation: (a) material variability, (b) uncertainty in the failure criterion?*

Uncertainty was not explicitly modeled, as statistical data for the material and failure criterion was not readily available. While one could examine the effects of varying the initiation criterion within

the experimental bounds, it didn't seem like that fruitful of an exercise with an experimental population of 3.

4. Please summarize your examination (if any) of mesh dependency of your result.

The only mesh dependence of these results is that associated with having a sufficiently fine mesh to obtain convergence. Another mesh refinement for the challenge problem would be useful in evaluating the "closeness to convergence." Since this initiation study did not examine the development of the crack until it reached the outer surface of the specimen "pathological mesh dependence" was not an issue. As discussed in more detail below, this type of mesh dependence is a key concern in modeling failure and is overcome by the XFEM formulation.

Additional details:
Typically when the phrase "mesh dependency" is used in the context of failure modeling, it is referring to the classic "pathological mesh dependence" that occurs when softening is explicitly included in the constitutive response and is not defined to be dependent on the element size. For this type of mesh dependence, the response during softening is "pathologically dependent" upon the mesh size – pathologically in the sense that the energy required to create a new surface in a quasi-brittle tensile specimen will approach zero with mesh refinement (*i.e.*, convergence is to a physically meaningless solution). The cohesive crack idealization kinematically represents the failure response by a strong discontinuity in displacement. As such the failure region is idealized by the surface over which these jumps occur, and the corresponding softening is described in terms of these jumps. The cohesive crack formulation includes a length scale associated with the failure via the cohesive crack law, and inherently does not have pathological mesh dependence. The XFEMs considered in this study adopt a cohesive crack formulation and thus do not have a pathological mesh dependence either.

5. *Computational Efficiency. Estimate the node-hours and processor speed used to run one solution to the problem. Report a range if necessary, for example if you used different mesh sizes, report the time for each of the mesh sizes.*

All analyses reported below were run using a single processor on the new blade workstation (Processor speed: 2.93 GHz).

Analysis details – Final Time: 0.902, Pin displacement at Final time: 0.2 inches, Maximum time increment: 2e-3. The analysis did not reach the final time with mesh 2, as noted below.

Table D3. Computational efficiency.

Mesh	No. Nodes	No. Els	No. Vars	Time increments	Time completed	Total CPU Time (hrs)
1	15,589	6134	46,767	451	0.902	0.48
2	109,886	49,072	329,658	434	0.848	7.3

6. What force (or range of forces) is predicted at a load line displacement of 0.01 in? 0.02 in? 0.03 in? 0.04 in?

Table D4. Predicted force.

Load line Displacement (in)	Mesh 1 Force (lbs)	Mesh 2 Force (lbs)
0.01	1145	1133
0.02	2037	2018
0.03	2602	2577
0.04	2905	2877

7. Describe the strengths and weaknesses of your approach.

Weaknesses

- Initiation criteria that can be use the XFEM capabilities are limited to maximum principal stress and elastic strain. Use of a criterion that bounds equivalent plastic strain as a function of the stress triaxiality is supposed to be available in the next release. For now, simple bounds on the equivalent plastic strain were examined.
- I did not have meaningful cohesive crack properties; arbitrary, small values were used for the fracture energy.
- Initiation of crack did not account for propagation to the outer surface where it would be observed in the experiment.
- Additional mesh convergence studies for the challenge specimen were not completed.

Strengths

- XFEM allows the crack to be explicitly represented by a crack surface. The value of this will be more apparent with crack propagation.

D2.1.1 Main Results

What is the loadline displacement, Δd, needed to induce crack initiation (in inches)? What is the peak force F applied to the sample prior to crack initiation (in pounds)?

The emphasis this first quarter in using Abaqus was to evaluate what its current capabilities are and to start applying it to the challenge problem. John Emery's coarse mesh was used in the initial analyses (Figure D136) and designated as "mesh 1." This month one mesh refinement analysis was completed (mesh2), which contained the first mesh and has 8x as many elements. Both plane stress, plane strain, and 3D models were examined, but initial lack of agreement in the analyses suggested that a 3D analysis was necessary for the challenge specimen. The plane strain model (with strain initiation) did give a maximum load of about 3300 pounds – in the "ball park" of the 3D results (~3100). The necking is significant in the region where the crack should initiate, suggesting the need for 3D analyses. Most of the 3D results given below are for calibration 5.

Using plasticity calibration 4 and the principal stress initiation criterion the specimen did not fail for an applied pin relative displacements of 0.3". Since the equivalent plastic strain was very high, this criterion was assumed to not be physically meaningful.

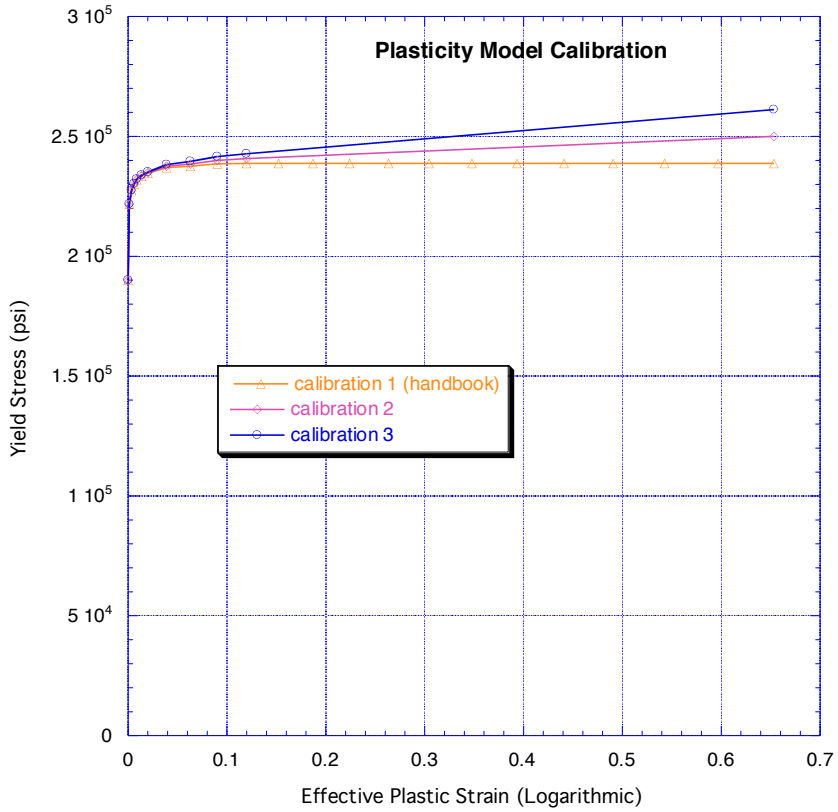

Figure D128. First 3 calibrations of the hardening function.

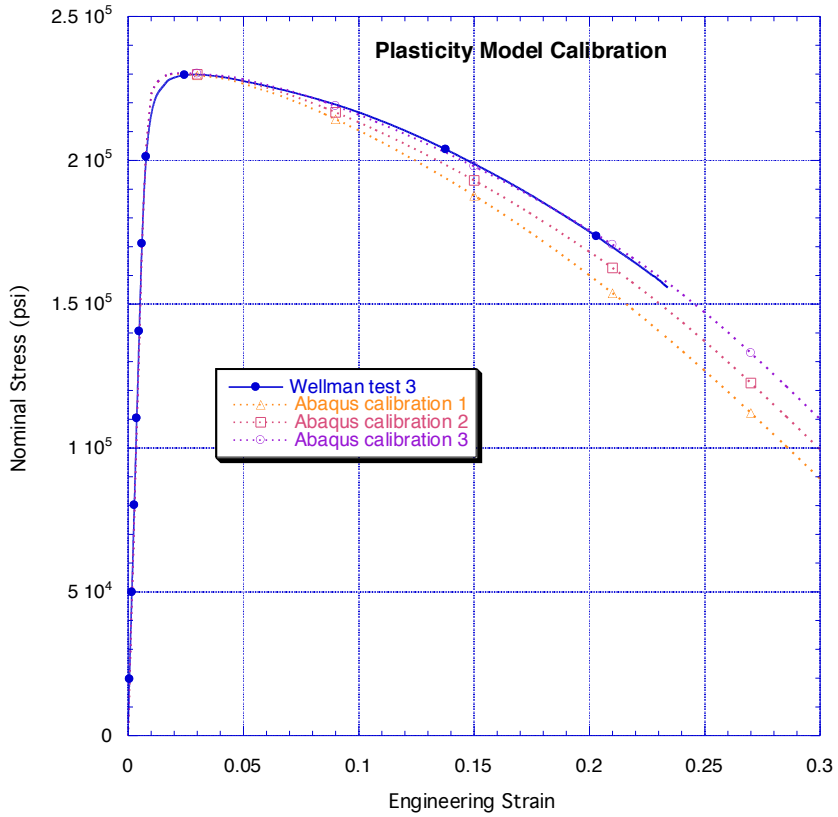

Figure D129. Abaqus plasticity model calibrations 1-3 compared with test 3.

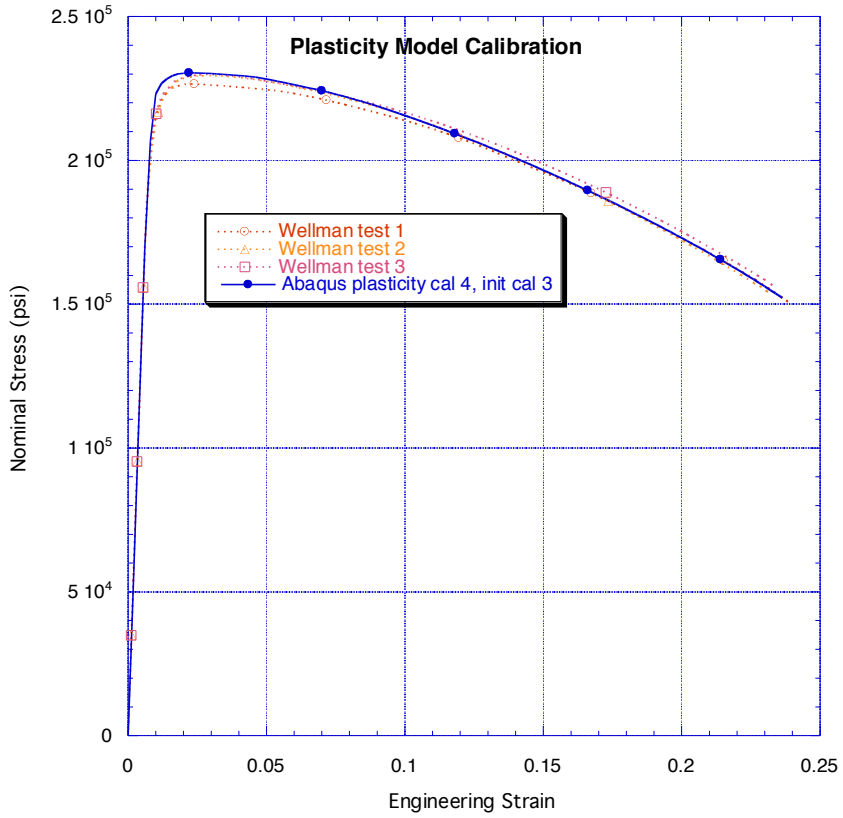

Figure D130. Plasticity calibration 4 versus 3 experimental tests – full range.

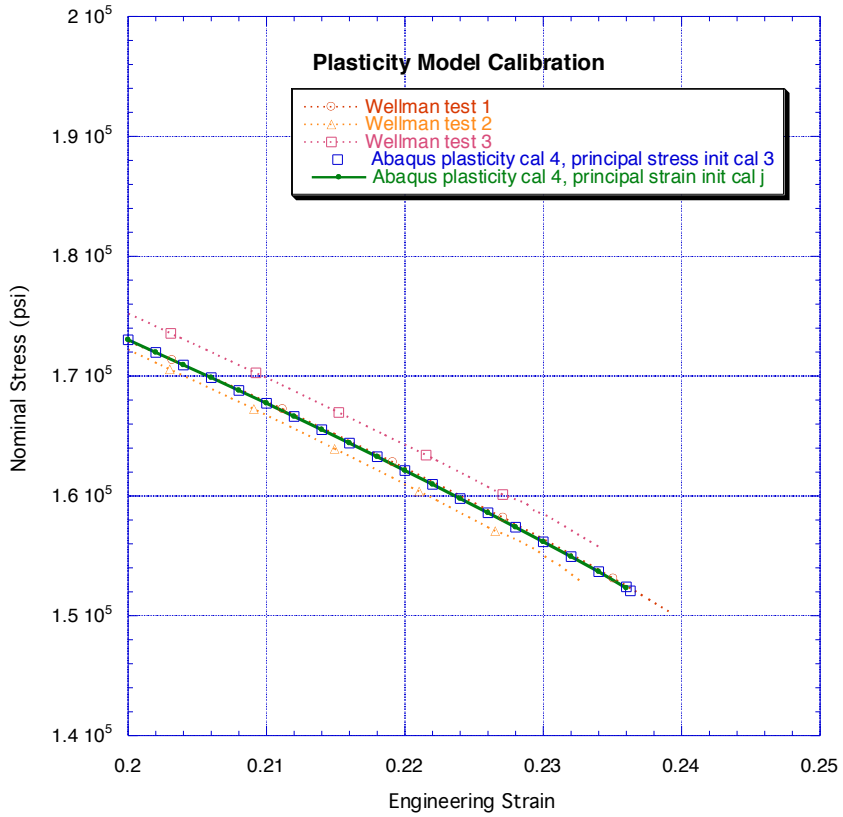

Figure D131. Plasticity calibration 4 versus 3 experimental tests – near failure.

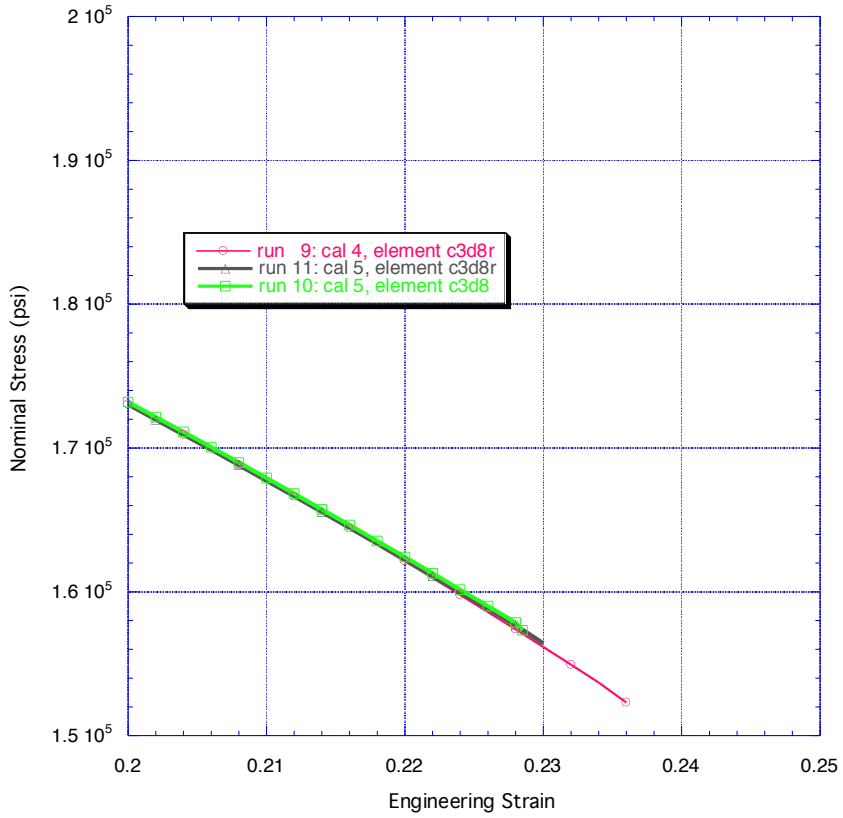

Figure D132. Effect of extending the hardening (cal 5) and different elements.

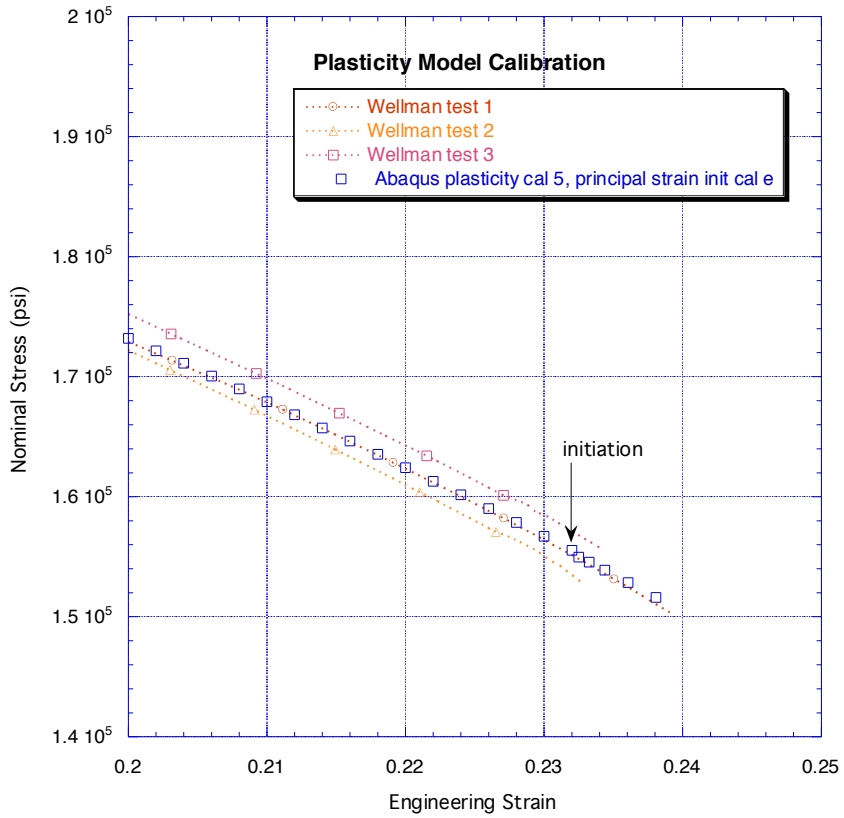

Figure D133. Calibration of initiation strain for plasticity model calibration 5

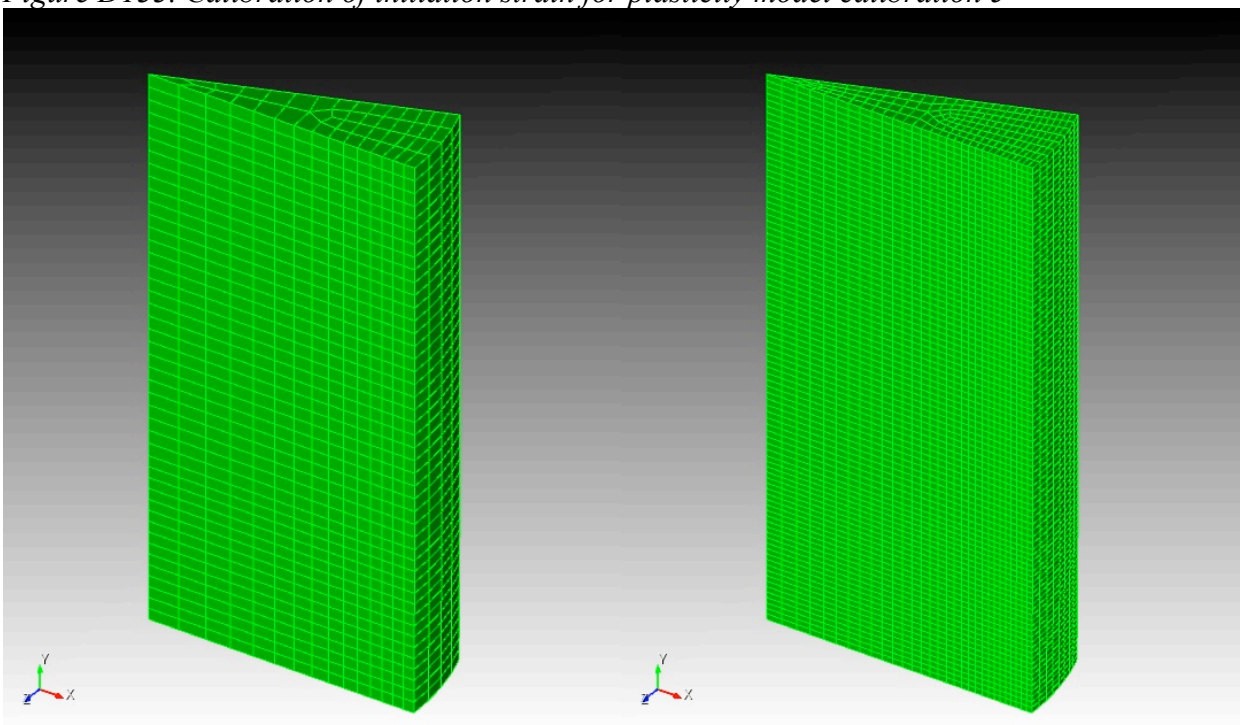

(a) mesh 1 (2070 elements) (b) mesh 2 (16,560 elements)

Figure D134. Material model calibration meshes.

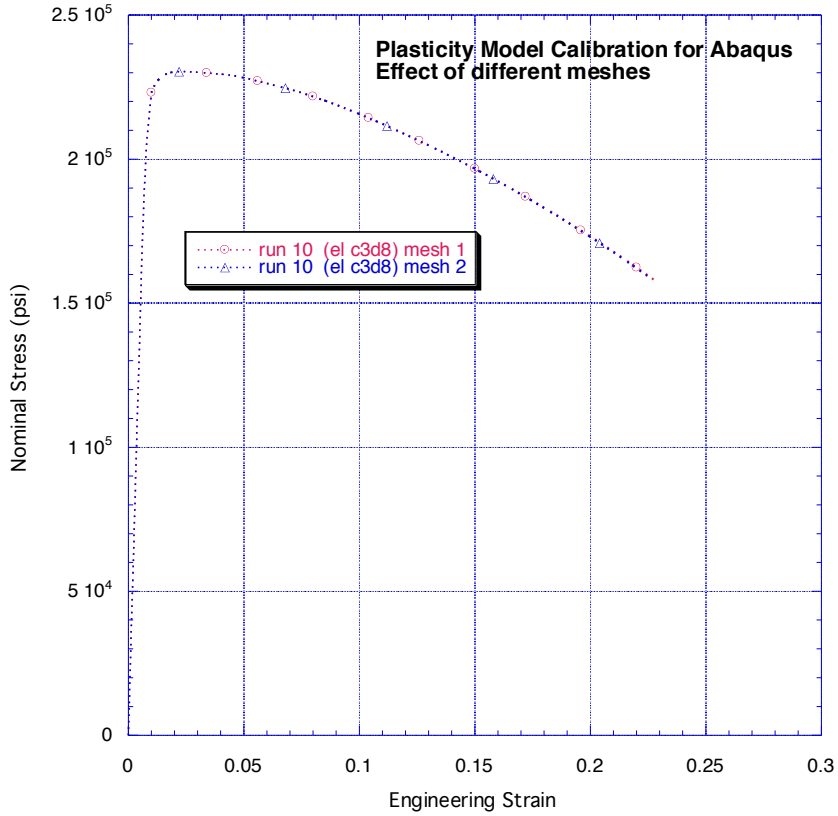

Figure D135. Calibration 5, mesh convergence test.

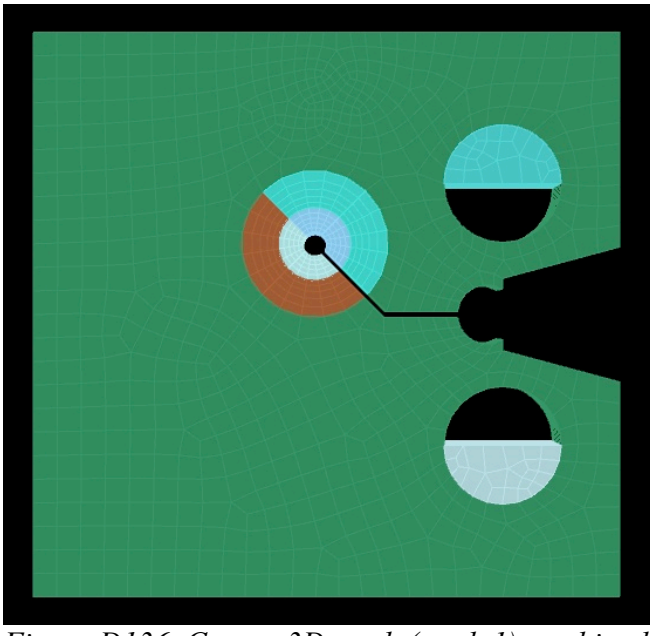

Figure D136. Coarse 3D mesh (mesh 1) used in challenge 1A solution

D2.2 Sierra XFEM

1. *Describe what material model you used for deformation (not crack initiation)? How did you calibrate that model against material properties? What parameters did you calibrate? Please specify what specific resources (datasets) you used to calibrate the parameters.*

The material model selected for modeling PH13-8Mo H950 is the Multilinear Elastic-Plastic Hardening Model available in Sierra. Initial model parameters were selected based on the calibration provided by John Emery. The parameters for the piecewise linear hardening curve were then further refined by comparing the results of a tensile test simulation to the response curves provided by Jerry Wellman from tests performed in Theresa Cordova's structural mechanics lab (ph13-8-h950-test-1.cl.txt, ph13-8-h950-test-2.cl.txt, and ph13-8-h950-test-3.cl.txt).

The finite element model used in the calibration process is shown below. For computational efficiency, only $1/8^{th}$ of the tensile test specimen was modeled and symmetry boundary conditions were applied.

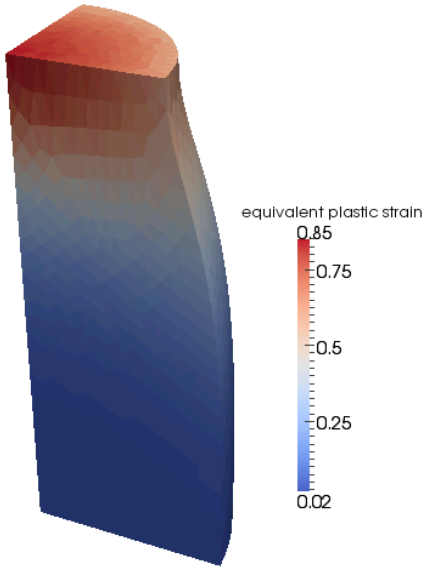

Figure D137. Tensile test simulation used for model calibration.

The calibration process involved matching the response curve of the simulated tensile test to the experimental response curves provided by Jerry Wellman. The response curve for the final calibration is shown below along with the experimental data.

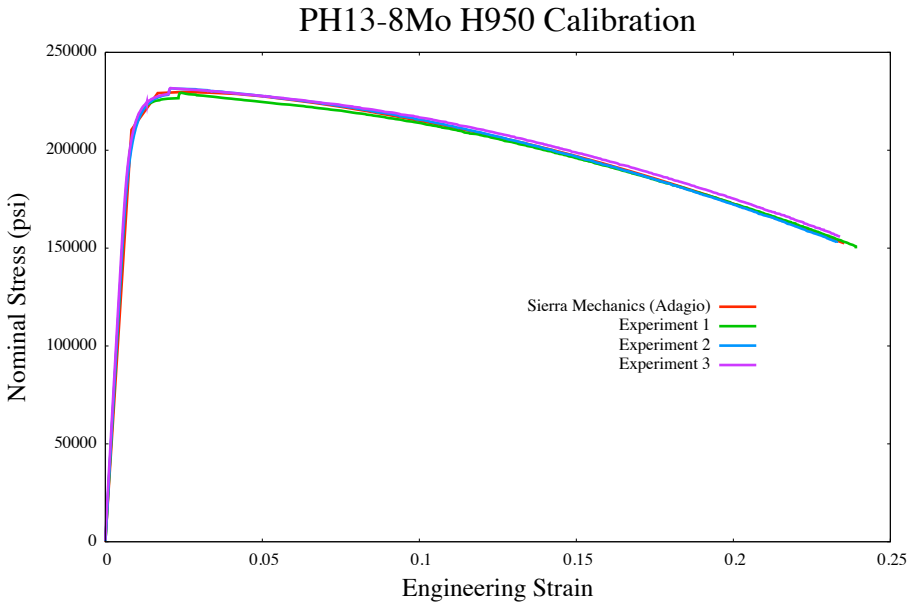

Figure D138. Calibration curves. Good agreement was achieved between the Sierra Mechanics simulation and experimental results.

The calibrated material data are:

Table D5. Calibrated material constitutive properties.

Density	7.34e-4 lb·s^2/in^4
Young's modulus	28.3e6 lb/in^2
Poisson's ratio	0.28
Yield stress	190.0e3 lb/in^2
Beta	1.0 (isotropic hardening)

The hardening curve is defined by the following points (truncated for brevity):

Table D6. Hardening curve.

0.0	190000.0
0.001248	221768.5
0.003581	227461.8
0.006150	230200.0
0.008695	232150.0
0.013682	233770.0
0.020178	235180.0
0.038934	238170.0
0.062976	239540.0
0.09	241500.0
0.2	246000.0
0.3	249000.0
1.0	258000.0

A plot of the hardening curve is given below:

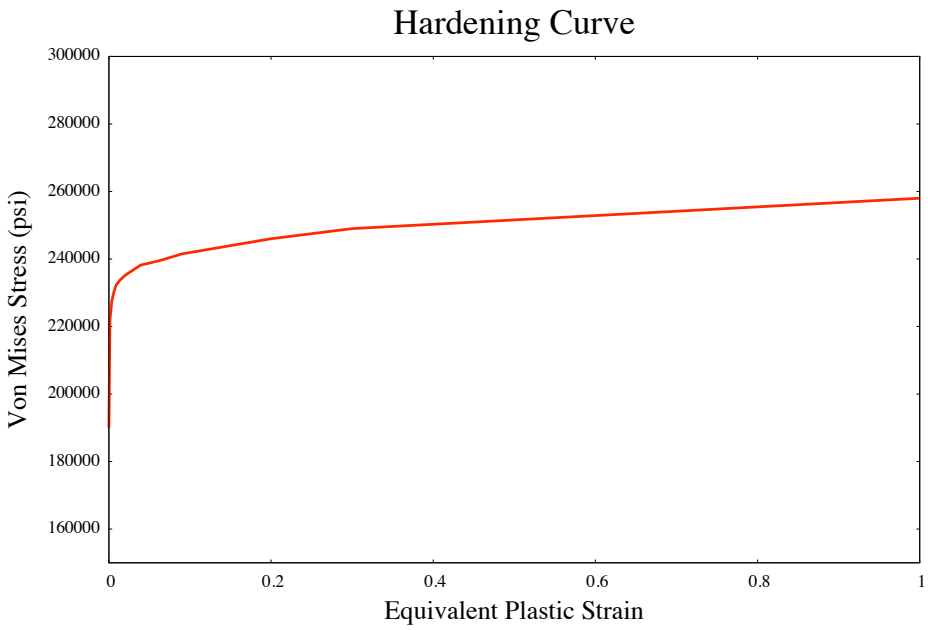

Figure D139. Calibrated hardening curve for the elastic-plastic material model.

2. *Describe what material model you used for crack initiation? How did you calibrate that model against material properties? What parameters did you calibrate? Please specify what specific resources (datasets) you used to calibrate the parameters.*

Crack initiation was defined based on a critical value for equivalent plastic strain. The critical value was determined using the calibration described in the response to question 1, above. As illustrated in the deformed image of the test specimen, the maximum value of equivalent plastic strain at the point of failure was calculated to be 0.85. This point corresponds to the right-most point in the calibration plot, at which point the experimental specimens failed.

3. *How was uncertainty captured in your simulation: (a) material variability, (b) uncertainty in the failure criterion?*

The modeling approach taken is deterministic in nature and model uncertainty was not quantified. It is certainly true that material variability and uncertainty in the failure criterion, along with additional uncertainties in the modeling process, lead to uncertainty in the predicted load-line displacement and reaction forces in the pins. However, in the absence of a large pool of experimental data, it is difficult to make meaningful approximations of the uncertainly in the present approach.

One possible approach to estimating uncertainty is to run a series of simulations in which the material properties and failure criterion are perturbed. This would provide an estimate of the sensitivity of the predicted values for load line displacement and reaction force to uncertainty in

the material model parameters. This approach, however, requires knowledge of the statistical variability of the material properties and requires a relatively large amount of analysis time.

Uncertainty in the failure criterion is most likely the largest source of uncertainty in the prediction of crack initiation. Equivalent plastic strain is a commonly used metric for the failure of ductile metals. It is difficult to determine the extent to which this metric is applicable to the 1A challenge problem, however. Calibrating against a small set of data under relatively simple loading conditions, as was done in this study, is a potentially large source of error considering the more complex loading conditions present in the 1A challenge problem.

Furthermore, mesh convergence in the sense of a consistent maximum value for equivalent plastic strain in the neighborhood of anticipated material failure under a given set of loading conditions proved difficult to achieve. Convergence of the maximum value of equivalent plastic strain was examined through a series of simulations using meshes that exhibited convergence of load line displacement and reaction force. These simulations showed inconsistencies in maximum equivalent plastic strain with variations of approximately 0.15 with no clear trend toward convergence. When defining failure based on a critical value of equivalent plastic strain, these inconsistencies resulted in variations in load line displacement at failure of approximately 0.01 inches and variations in the corresponding reaction force of approximately 10 pounds.

4. Please summarize your examination (if any) of mesh dependency of your result.

Mesh dependence was addressed with a series of mesh convergence simulations, both for the calibration specimen and the 1A challenge specimen.

Mesh convergence results for the calibration simulation are illustrated below. A uniform mesh was applied in each case. The response curves show convergence for all but the coarsest model.

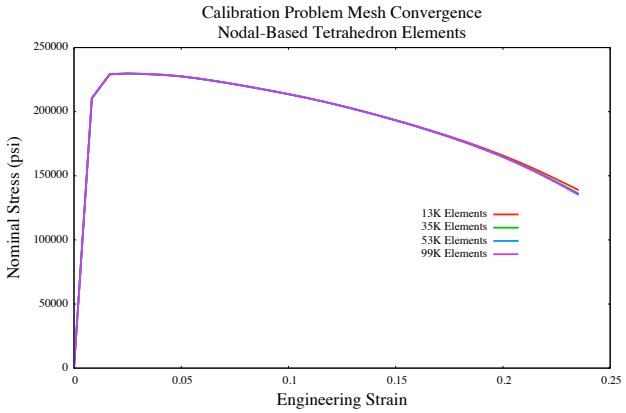

Figure D140. Mesh convergence results for the calibration model.

Mesh convergence results for the 1A challenge problem are presented below via plots of load line displacement versus reaction force. For the 1A problem, mesh refinement was concentrated near the point of anticipated crack initiation and in the neighborhood of applied loading. Note that the mesh convergence study for the 1A model problem was carried out with loading applied directly to an inner portion of the loading holes (pins were not modeled).

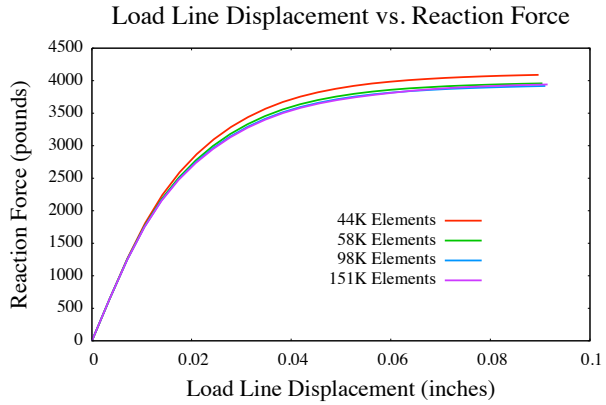

Figure D141. Mesh convergence results for the 1A challenge problem

Based on the 1A mesh convergence study, the mesh containing 98K elements, shown below, was selected for the predictive simulation.

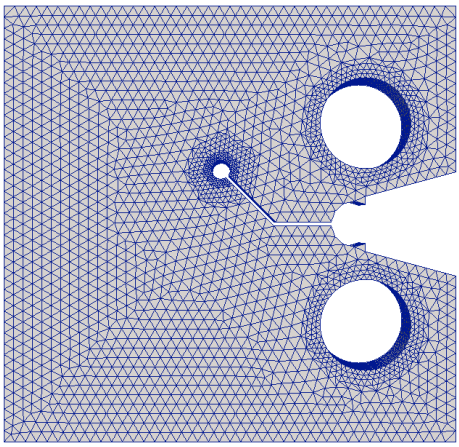

Figure D142. 1A mesh without pins

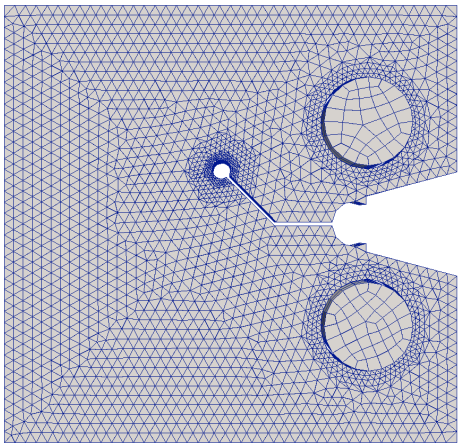

Figure D143. 1A mesh with pins.

5. *Computational Efficiency. Estimate the node-hours and processor speed used to run one solution to the problem. Report a range if necessary, for example if you used different mesh sizes, report the time for each of the mesh sizes.*

Calibration specimen mesh convergence study:

Table D7. Computational Efficiency.

Number of Elements	Total CPU Time
13314	0:44:00
32562	2:14:28 (mesh convergence achieved here)
53313	4:48:20
98859	8:42:44

1A model mesh convergence study (Adagio quasi-static model without pins):

Number of Elements	Total CPU Time
43926	1:51:06
57627	2:41:14
97963	6:08:35 (mesh convergence achieved here)
150632	10:26:34

1A model predictive simulation (Presto explicit dynamic model with pins):

Number of Elements	Total CPU Time
98368	57:30

6. *What force (or range of forces) is predicted at a load line displacement of 0.01 in? 0.02 in? 0.03 in? 0.04 in?*

The predicted forces are:

Table D8. Force predictions for displacements from 0.01 to 0.04 inches.

Displacement	Force
0.01 inches	1100 pounds
0.02 inches	1990 pounds
0.03 inches	2540 pounds
0.04 inches	2850 pounds

A displacement versus force plot is given below, ending at the point of predicted failure (equivalent plastic strain > 0.85).

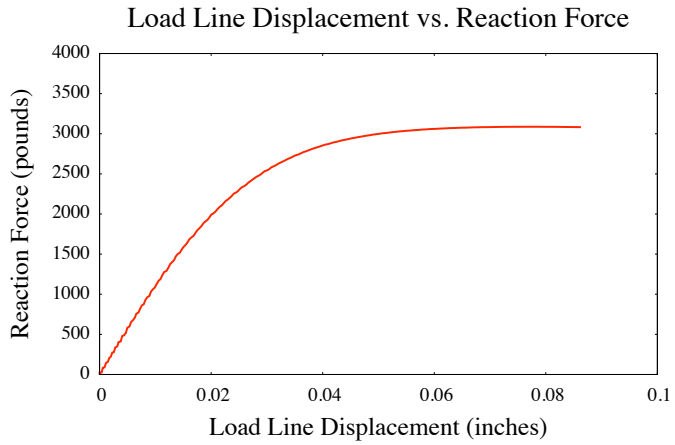

Figure D144. Load line displacement versus force (plot ends at predicted failure).

7. Describe the strengths and weaknesses of your approach.

The approach taken for the prediction of crack initiation in the 1A model has a number of strengths in comparison to alternative approaches. Most importantly, the approach taken can be directly extended in future X-Prize challenges to include the XFEM capabilities in Sierra Mechanics for modeling crack propagation. The approach taken in the 1A challenges is centered on the Multilinear Elastic-Plastic Hardening Model and the selection of equivalent plastic strain as the crack initiation criterion. Defining material failure based on equivalent plastic strain does not require predetermination of the location of failure, as may be required in alternative approaches. Both the constitutive model and the failure criterion are relatively simple approaches for simulating ductile material response and have the advantage of being easily calibrated against the experimental response curves presented above. In the absence of additional experimental data and knowledge of the underlying physics of crack initiation in PH13-8Mo these approaches offer a sound approach to the 1A challenge problem.

A disadvantage of the approach taken is the uncertainty surrounding the choice of equivalent plastic strain as the failure criterion. Crack initiation is a complex process involving material microstructure and chemistry in addition to complex local deformation fields. It is impossible to determine the extent to which the critical value for crack initiation found in the calibration simulation can be applied to the more complex deformation state found in the 1A challenge problem.

Wrap-Up Questions

1. What was the % difference of your predictions to the experimental values (max force prior to crack initiation and COD displacement at crack initiation)?

In previous discussions, we noted that we used three distinct types of analyses each based upon a different crack initiation criterion: (a) maximum principal stress, (b) maximum principal elastic strain, and (c) maximum equivalent plastic strain. The first two reflected the limitations of

Abaqus's initiation criterion for that version of the code and were not expected to yield good quantitative results. As such the only results discussed here are those for criterion (c). The results for Abaqus and Sierra were in good agreement in the revised predictions and both were in good agreement with the initial Abaqus results.

The prediction of the maximum force fell within the experimental scatter.

The prediction of the COD at crack initiation was approximately 15 percent less than the lower bound of the experimental results.

2. *If you (or your team) submitted revised predictions, either after the initial due date, or after the comparison between modeling results, did your revisions bring the prediction closer to the experimental values?*

Initial results with Abaqus and Sierra differed significantly, but we were not able to resolve the source of the differences for the initial submission. Upon further analysis, we determined that the initial results for Sierra used standard four-noded tetrahedron elements yielding a model that was overly stiff and incorporated an approximate boundary condition for the pins that was inaccurate. The Sierra model was revised to use nodal-based tetrahedron elements and explicitly modeled the pin contact. The Abaqus model was revised to examine the effects of element type and mesh refinement. Revised predictions with both Sierra and Abaqus were in good agreement with the initial Abaqus results. The Sierra results were significantly improved by the revisions.

3. *Describe the source(s) of discrepancy (if any) between your prediction and the experimental result. Where possible, provide quantitative estimates of how much your prediction might have improved if these sources were incorporated into the prediction. Discuss the ease or difficulty in incorporating such improvements in future work.*

Crack initiation was defined experimentally by the state at which a crack reached the surface specimen and had a length of 100-500 mm. Since neither code could both initiate and propagate the crack to the surface of the specimen using an equivalent plastic strain criterion, we took initiation to be the state at which the equivalent plastic strain reached the critical value defined

Comment [J1]: Based on an estimate of the experimental value of 2.7 mm and a model value of 0.09" (~2.29 mm)

by the tensile specimen. As such, our under-prediction of the COD is consistent with the differences in the definitions of initiation (i.e., the COD would increase as the crack propagated to the surface of the specimen). Until the codes can address the propagation based upon equivalent plastic strain, we can't further quantify the difference caused by the differing definitions of initiation. Hopefully both codes will have advanced enough to examine the effect for the next challenge.

4. *Was this effort helpful for the development and evaluation of your modeling paradigm? How might we improve the challenges in the future?*

The first challenge was helpful in being able to examine how well equivalent plastic strain can be used to predict initiation, but it leaves the issue of dependency upon the stress triaxiality open. To be frank we were surprised to have done so well when not incorporating this effect. For future tests that are likely to address propagation more data on the fracture behavior of materials will be necessary to effectively utilize a cohesive zone idealization.

D3. Predictions for Challenge 1B

Summary

The X-Prize XFEM group analyzed the 1B challenge using finite element modeling with elastic-plastic material models and a failure criterion based on equivalent plastic strain or maximum principal logarithmic strain. Two analysis codes were used: Abaqus and Sierra Mechanics. For this challenge, a single model calibration was carried out against the experimental data provided (Modern Industries Inc. test of 7/6/10). As in challenge 1A, the affect of stress triaxiality on crack initiation was not considered, because it was not available in our models. A criterion that does account for the triaxiality, the tearing parameter (Wellman), has been used in Sierra with success. Other criteria that treat the bound on equivalent plastic strain as a function of the stress triaxiality are given in the literature by *e.g.* Wiezbicki *et al.*

The calibrated models and failure criterion were then applied to the 1B problem. The "development state" of both codes has limited what could be modeled for this problem, but "state of the codes" results are presented separately below.

Abaqus

Table D9. Abaqus predictions for Challenge 1B.

		Δd at crack initiation $^{\alpha}$	Peak force prior to initiation	Crack Path	Δd when crack reaches 1st line $^{\alpha}$	Force when crack reaches 1st line
	"Upper bound"	0.059 in	853 lb			
2024-T3	3D (best est.)	0.041 in	812 lb	D-E-A-F	0.348	548 lb$^{\Xi}$
	2D			D-E-F-A		

* Note that the best estimate value used for initiation corresponds to when the crack would first initiate based upon equivalent plastic strain. This would not yield a visible crack, but it was the measure used in challenge 1a that was relatively accurate. The upper bound value is based upon when the crack was first visible on the surface of the specimen, which can only be based upon total strain in Abaqus. The upper bound value includes the effect of crack cohesion.

$^{\Xi}$ This value is expected to be low, since cohesion would increase the value. The value based on a cohesive crack will be reported if Abaqus staff can correct the convergence problem.

$^{\alpha}$ Δd values here are based upon the u_y displacements alone – a projected length. If the measurement is for the total distance between the points, these must be recalculated.

D3.1 Introduction

Extended finite element method (XFEM) capabilities are in a research and development state both at Sandia and within commercial FEA codes. This is again reflected in the results obtained for this second challenge problem. To "predict" crack initiation (and continued propagation) two "XFEM approaches" were taken – one using Abaqus, and the other using Sierra mechanics. Neither code is equipped yet with the ability to apply general initiation criterion and to introduce a strong discontinuity in an arbitrary position within the domain – though both are quickly approaching this goal. (The beta version of Abaqus, which we now have, allows the initiation/propagation criterion to be defined by a user subroutine, but we received it too late to

develop a user subroutine for this challenge problem.) While Abaqus (version 6.10) has 2d and 3d XFEM capabilities, its crack initiation criteria for XFEM are limited to upper bounds on the maximum principal stress or logarithmic strain. Version 6.9 (challenge 1A) used maximum principal elastic strain, so at least the total strain measure includes the plastic deformation. Sierra mechanics can not yet initiate an XFEM crack based upon mechanics, so a preliminary analysis was used to seed an initial crack. Overviews of some the Abaqus and Sierra mechanics results are presented in the two sections below.

D3.2 Plasticity Model Calibration

Jim Cox (1524)

Abaqus's isotropic hardening plasticity model was used for the model calibration. To calibrate the plasticity model, I modeled the gage length region of a tensile specimen (mesh provided by John Emery), and then fit a piecewise linear hardening function to match the engineering stress versus nominal strain results. The FE model used symmetry with respect to each coordinate plane. The tensile specimen was 2"x1/2"x1/8". The triple-symmetry model used for calibration was 64x16x4 elements, thus each element was a cube measuring 1/64" on each side. The specimen model had a taper of 0.002" over its length with an average width of 0.505".

Several iterations were used to calibrate the hardening of the plasticity model. Figure D145 shows 3 such iterations. The hardening used for run 11 was used for all of the following results. The point where run 11 intersects the experimental response prior to the last drop was the state used to initiation cracking. Two measures of this state were used: (1) the maximum principal value of the total logarithmic strain (ε_1), and (2) the equivalent plastic strain (ε^{eq}). Abaqus used ε_1 for all crack initiation and propagation calculations. I still used ε^{eq} to estimate initiation in the results. For Sierra ε^{eq} was used for all initiation and propagation calculations.

The fracture energy of the material was initially estimated from a fracture toughness value of about 29.1 ksi-in$^{1/2}$ (Aerospace Specification Metals Inc.). The estimated fracture energy value for plane strain conditions was about 87 lb/in. Unfortunately, most of the results were obtained without incorporating the effect of the fracture energy. Many attempts were made to incorporate it in the Abaqus analyses, but the analyses failed to converge before the crack could reach the first lines.

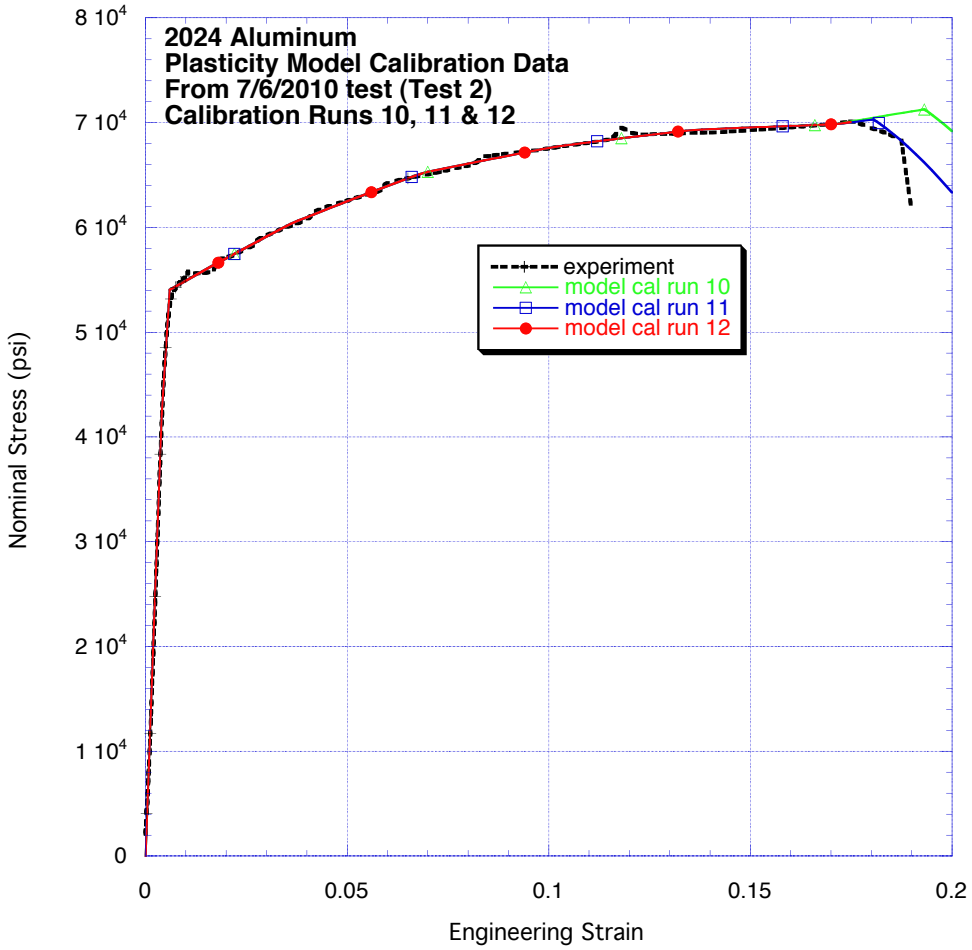

Figure D145. Material calibration results for 3 trial iterations.

D3.3 Abaqus Results

Meshes created by John Emery and Jerry Wellman were used in the Abaqus analyses. Figure D146 shows the coarser mesh created by John Emery. I quickly refined this mesh, for 2D analyses, by doubling the mesh density in each direction. Because the meshing was graded in two concentric rings, the refined mesh is ugly but works. The Wellman mesh is slightly coarser near the "initiation hole" but is finer over much of the crack path. A caveat in using the Wellman mesh is that is assumed symmetry through the thickness of the specimen. Unfortunately, I later found that Abaqus does not maintain the symmetry conditions for cracked elements. The effect of this "error" upon the results has not been investigated, but it is expected to reduce the plane strain effect near the center of the crack depth. Formal mesh convergence studies were beyond the scope of the study, as I was struggling just to get some results.

Figure D147 presents results from 4, 3-dimensional analyses. The figure compares the results for two different meshes and with and without fracture energy included. Unfortunately, the results with fracture energy will not converge for longer crack lengths, but the fracture energy appears to have a significant affect upon the results. As such, I anticipate that the load levels

predicted by the Γ=0 analyses are likely to under predict those of the experimental results, but that's all we can currently obtain. I will submit the convergence problems to Abaqus to see if they can extend the prediction. Figure D148 shows the predicted crack results for the Emery mesh with Γ=0.

While the 3d results indicate that a plane stress approximation is a gross approximation for this problem, 2d analyses were used to supplement our results. In particular, one analysis cracked most of the way through the specimen, giving a more complete crack path result. Figure D149 shows this 2d model. A problem with Abaqus that significantly affected our ability to obtain results in 2d, was that when a crack path intersected an element edge at a very shallow angle, the crack stalled on that edge and plastic deformation increased ahead of the crack. This occurred in the case shown in Figure D148, but in this case the analysis was almost complete.

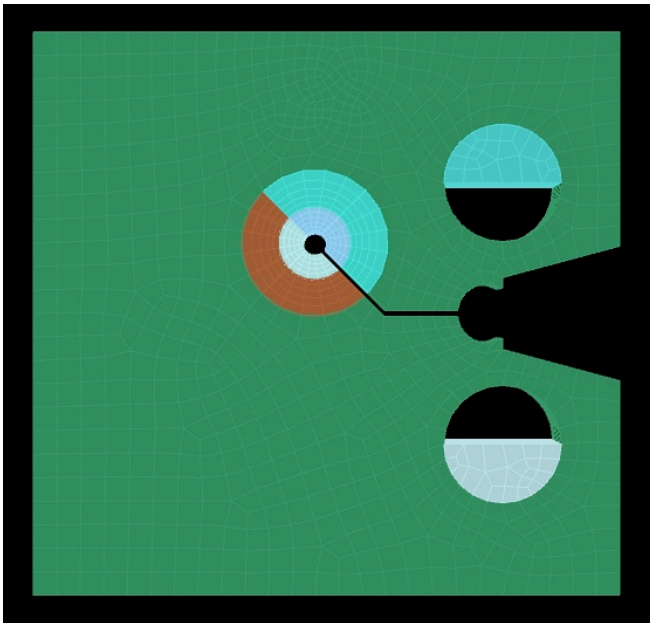

Figure D146. Coarse 3D mesh (mesh 1) used in challenge 1B solution.

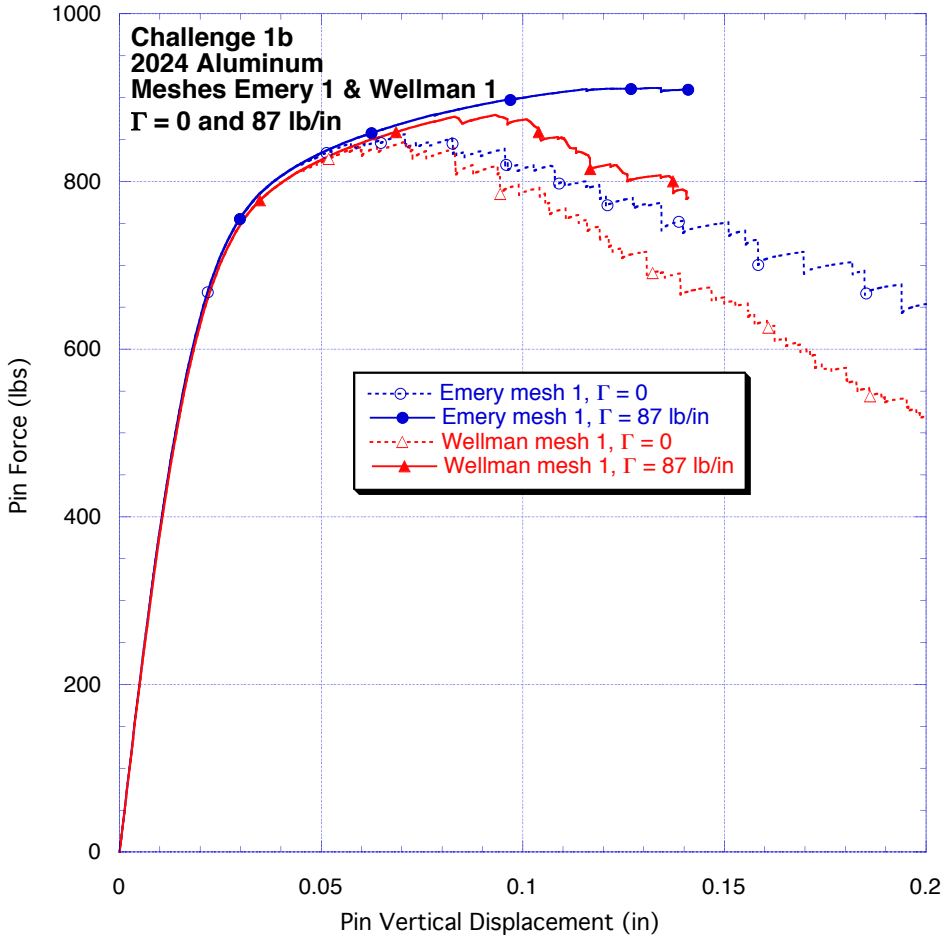

Figure D147. Specimen 1b model results for two mesh and fracture energy cases.

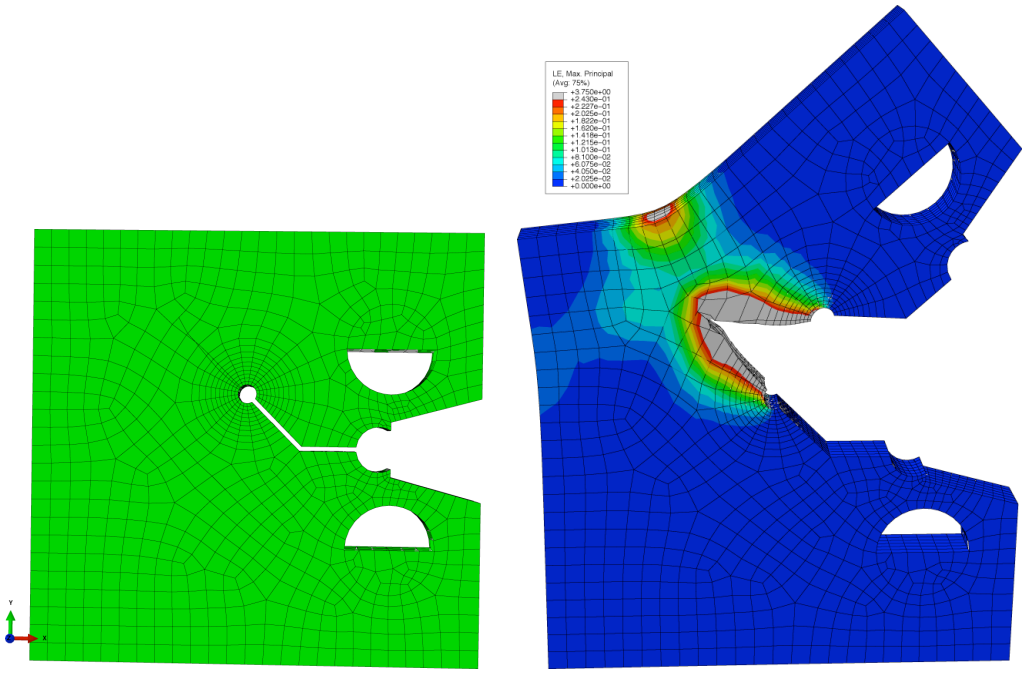

(a) undeformed body (b) deformed body

Figure D148. Predicted crack in a 3d analysis of the specimen (Emery mesh, Γ=0).

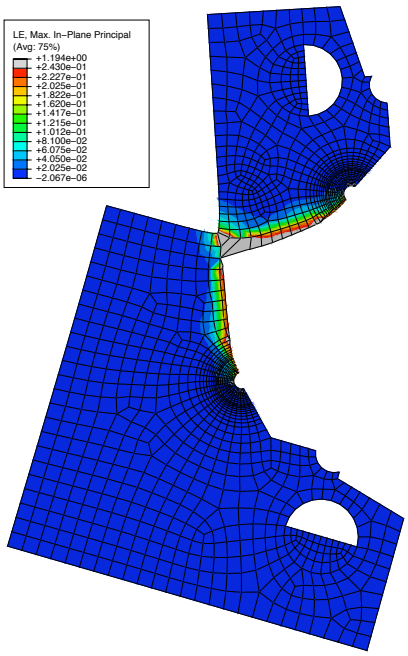

Figure D149. Predicted deformed structure for a 2d model with Γ=0.

D4. Follow-Up to Challenge 1B

What do you believe were the most significant sources of error that produced discrepancy between your model and experimental results? Where possible, provide quantitative estimates of how much your prediction might have improved if these sources were incorporated into the prediction. Discuss the ease or difficulty in incorporating such improvements in future work.

While further study is needed, we expect that the component of the model that had the greatest impact on the inaccuracy of our results was the criterion for crack initiation and propagation. There are many empirical criteria in the literature that incorporate additional parameters like stress triaxiality and that might allow one to obtain better results. This will be further investigated to see if their inclusion in the code(s) might improve our results for the next challenge problem. The usefulness of these empirical models, however, must be in their ability to capture the progressive fracture response (in terms of macroscopic variables) under significantly different conditions. Simply having enough "knobs to turn" to match an individual experiment is only a calibration exercise – not prediction.

To better evaluate the most significant source of error would require us to have software that is more mature than its current state. Both Sierra and Abaqus are showing advancements but neither is in a state to facilitate extensive parameter studies. Below is a list of factors that we would like to investigate to determine how they affect the results:

Plasticity model and its calibration
Cohesive model and its calibration
Initiation model
Crack propagation direction model
Mesh density
Dynamic effects with higher rate of loading (in original Sierra analyses)

Limited discussions of these factors are presented below. In addition to these factors that directly affect the accuracy of the calculations, factors affecting the computational efficiency of the codes come into play was well because they prevented us from performing more complete studies (especially with finer meshes). Advances in the capabilities (particularly in Sierra SM) that will facilitate future studies are also discussed.

D4.1 Plasticity model and its calibration

Comparing the model results with the experiments, the XFEM models exhibited significantly more ductility after crack initiation. This could be a result of the plasticity model, the cohesive zone models, or the crack initiation/propagation model. For the Abaqus runs convergence errors occurred much earlier in the analysis when cohesion was included, and the reported model results did not even include interface cohesion. Since the "tearing parameter" results exhibit a more brittle response, we compared the hardening model calibration with those of "tearing parameter model." Figure D150 shows that the models do not differ significantly, especially considering they were calibrated with different models for the tensile specimen, different elements, and different implementations of isotropic hardening plasticity.

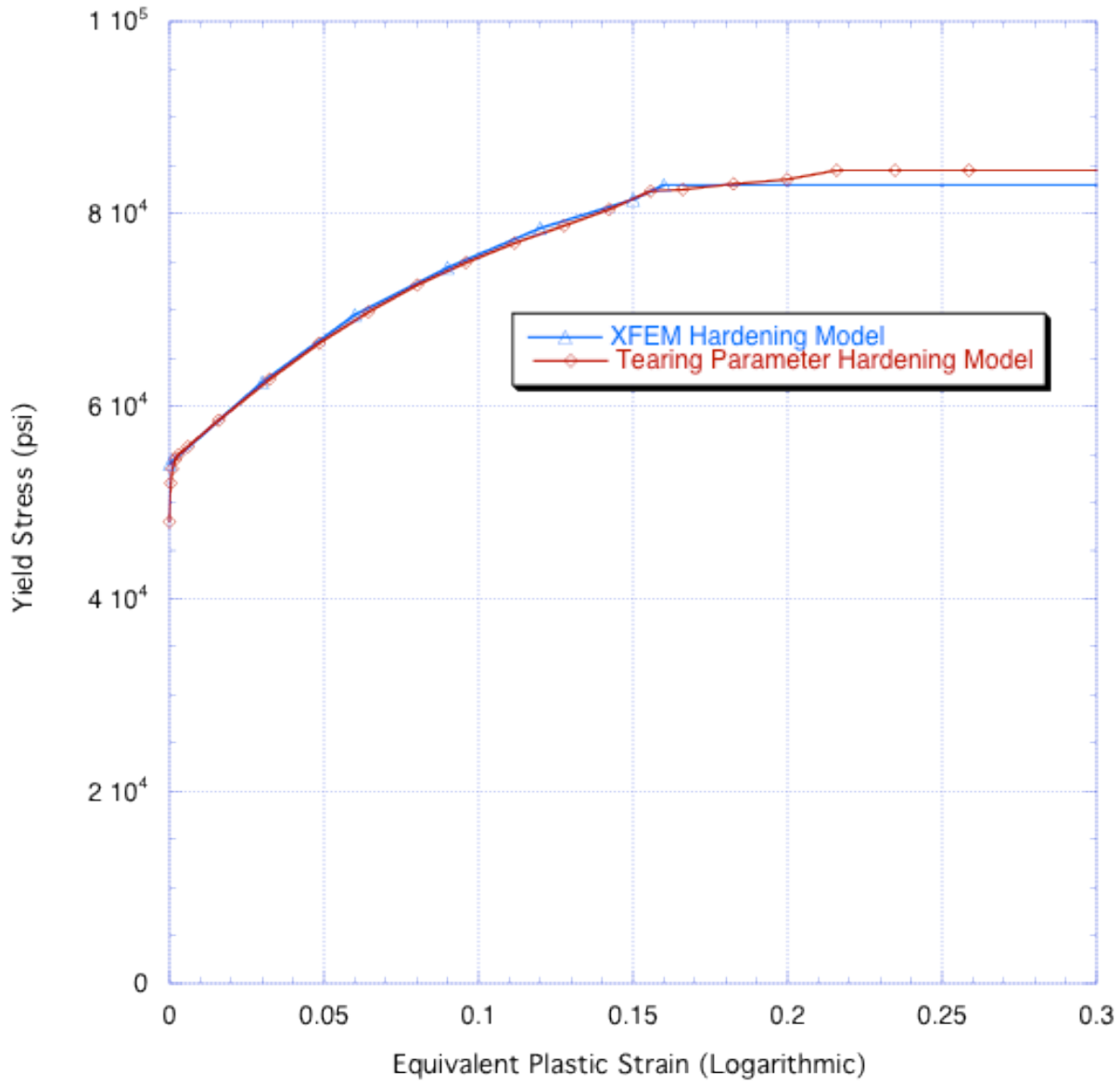

Figure D150. Hardening models.

D4.2 Abaqus

Most additional analyses used a modified version of the meshes from Jerry Wellman, mainly because he had three different mesh densities available. The modification was that a symmetry plane was not assumed and thus the meshes modeled the full thickness of the specimens. Previous analyses using the original meshes did not satisfy the symmetry boundary conditions along the crack.

Most of the force-displacement plots presented here use the pin displacement rather than the measured COD. This was just a matter of time constraints. Either is fine for reflecting changes in ductility that might occur due to model changes.

D4.3 Cohesive model and its calibration

No additional analyses were conducted to examine the effect of the cohesive zone model, because as mentioned above cohesion was not included in the reported results. Figure D151. Shows earlier results using two different meshes, reflecting the obvious trend that including cohesion yields a more ductile result.

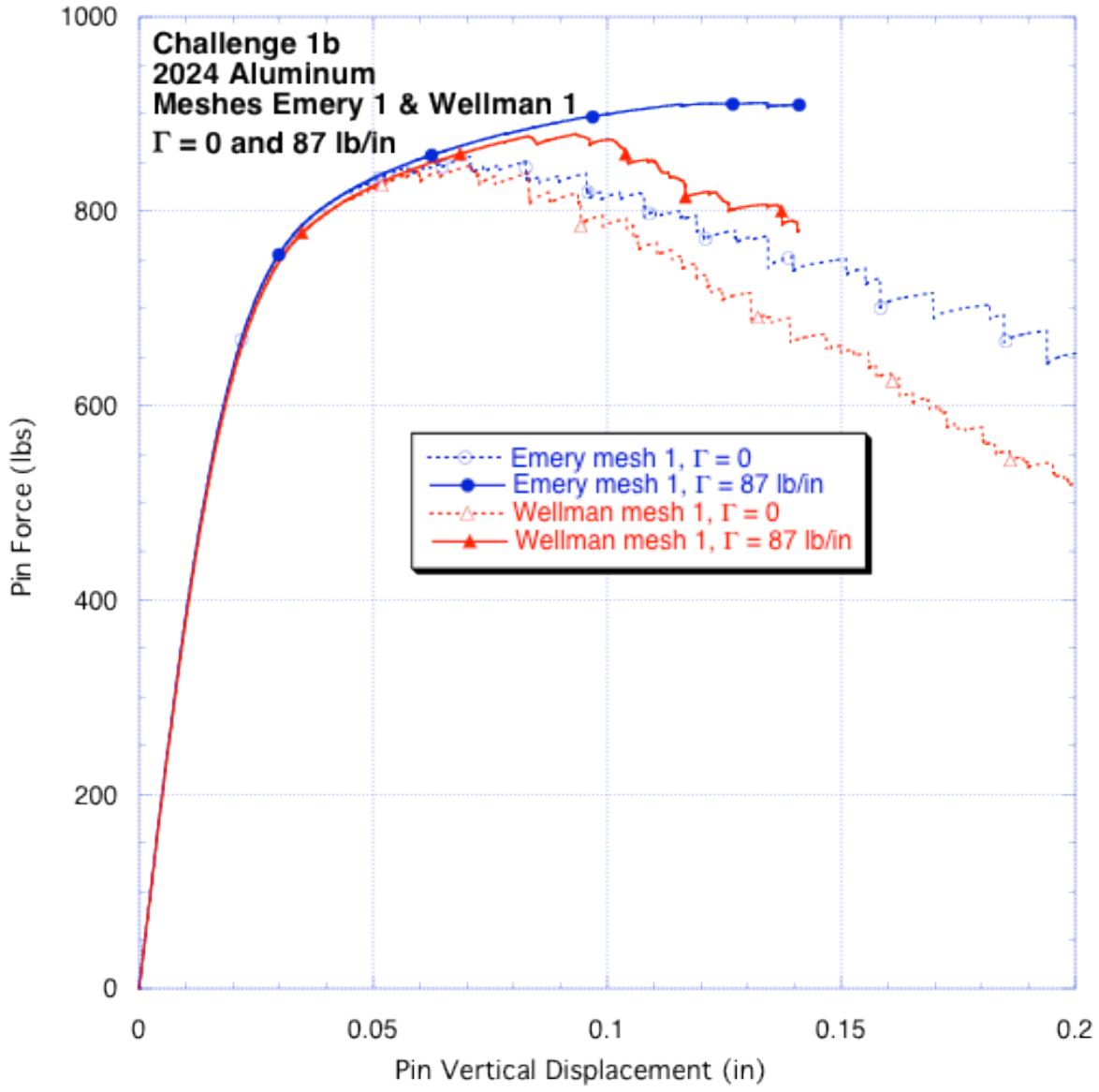

Figure D151. Effect of cohesion on earlier results.

D4.4 Initiation model

For this challenge problem, Abaqus only had two choices for initiation (and continued crack propagation): maximum principal stress, and maximum principal strain. After the blind study, we were able to use a beta version of Abaqus that included the ability to define a user subroutine for initiation. The user subroutine also allows one to define the model for the crack direction which will be discussed some below. Figure D152 compares a force-displacement prediction using the original criterion (maximum principal strain) with that given by two models using maximum equivalent plastic strain. The second analysis used a crack direction base upon the principal stress. The differing crack geometry (reference the next section) appears to have increased the ductility of the specimen response.

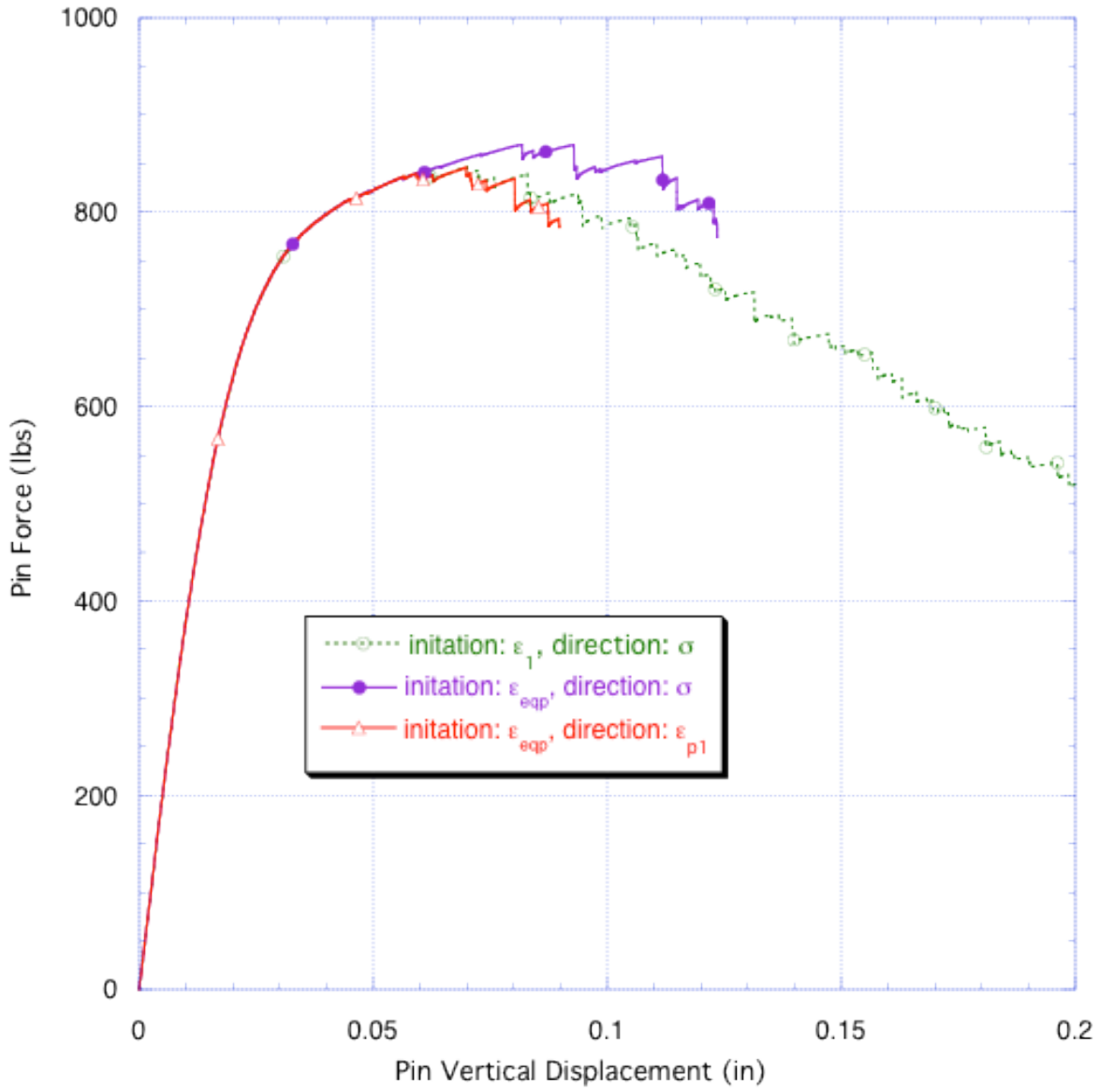

Figure D152. Results for both total strain and equivalent plastic strain initiation models.

D4.5 Crack propagation direction model

The results shown here include cohesion, and thus "do not live very long," but the same trends are observed when cohesion is omitted. Figure D153 and Figure D154 show the initial crack geometries when two different models are used for crack direction – maximum principal σ and ε^p, respectively. The latter more closely resembles the crack directions obtained experimentally. For both cases equivalent plastic strain was used for initiation.

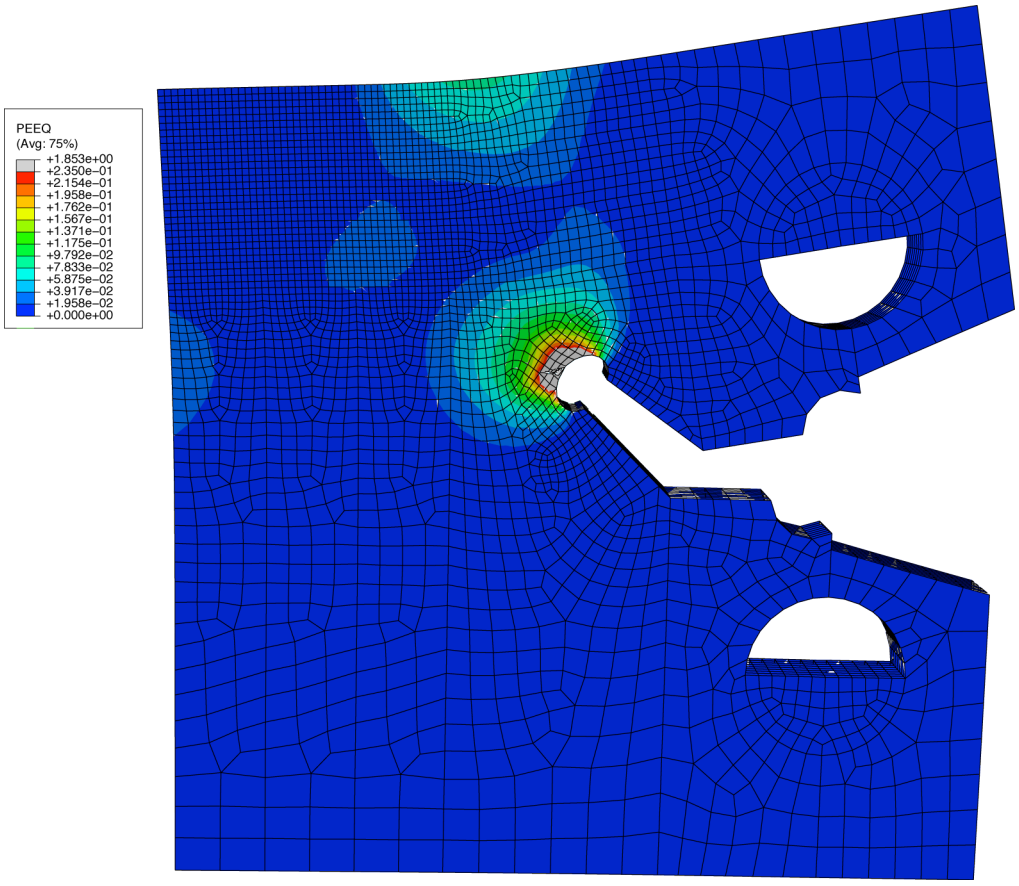

Figure D153. Early cracking when using ε_{eqp} for initiation and σ_1 for direction.

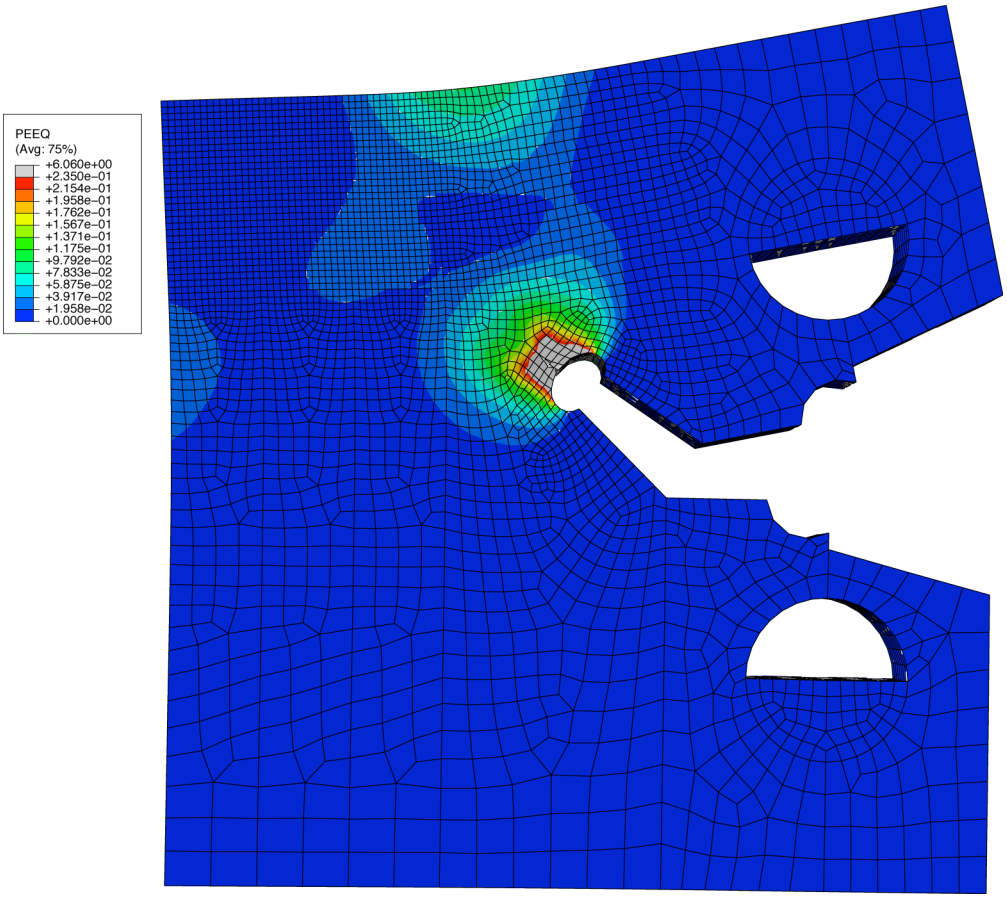

Figure D154. Early cracking when using ε_{eqp} for initiation and ε_1^p for direction.

D4.6 Mesh density

Figure D155 compares analyses with two different meshes. The refined mesh, relative to that used in previous analyses, is denoted as W2_ns (Wellman mesh 2 without a symmetry plane). While refinement of the mesh did reduce the ductility some, the effect was small relative to the differences with the experimental results.

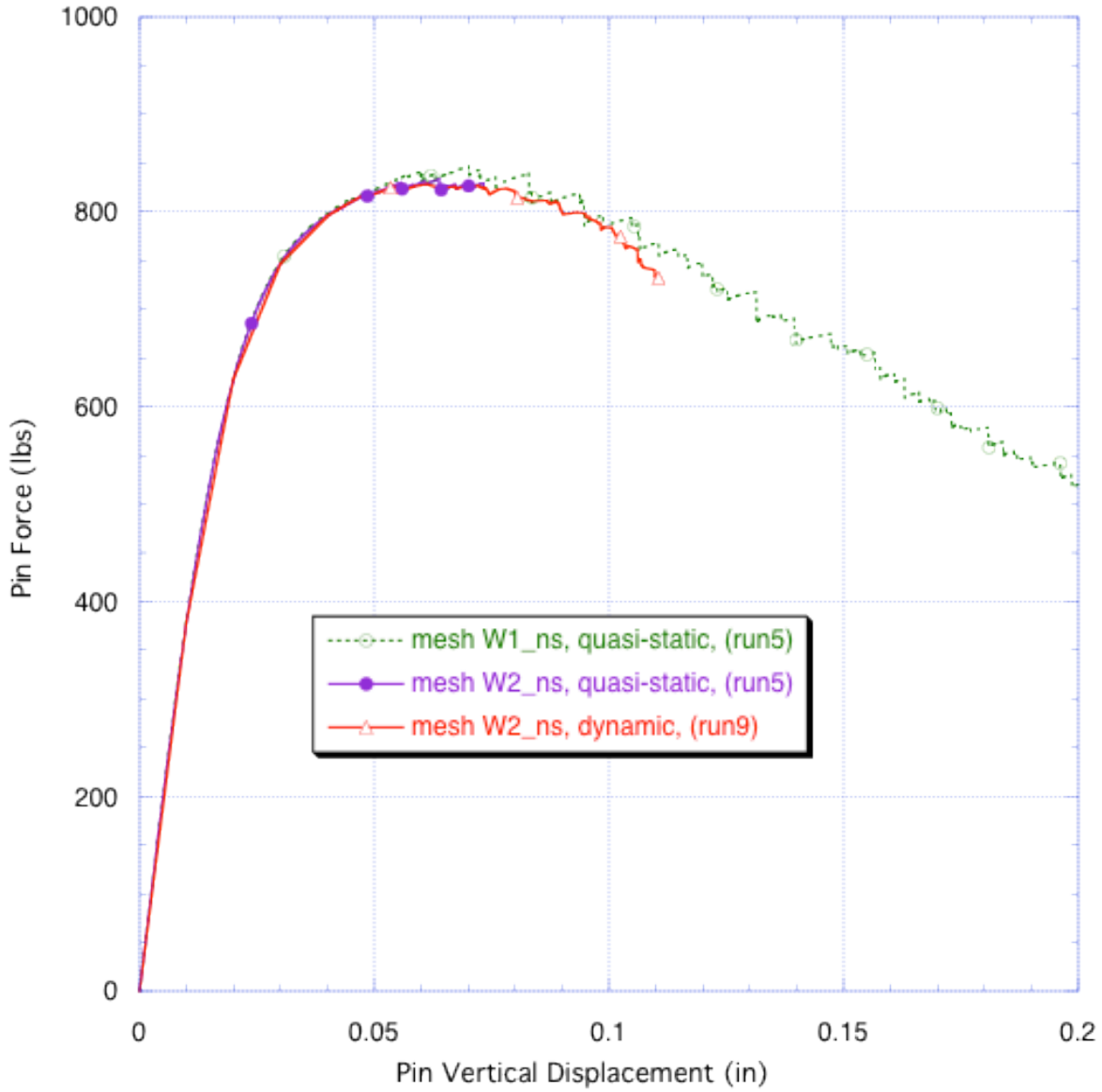

Figure D155. Effect of mesh refinement on force-displacement response.

The analysis using the finer mesh did not show converge much past the peak response when run with quasi-statics. Using implicit dynamics, the analysis went further but drove the time step extremely small and stopped making progress. With the finer mesh the tendency of the crack to exhibit "tunneling" behavior is represented better. Figure D156 and Figure D157 show the cracked specimen and the geometry of the crack alone.

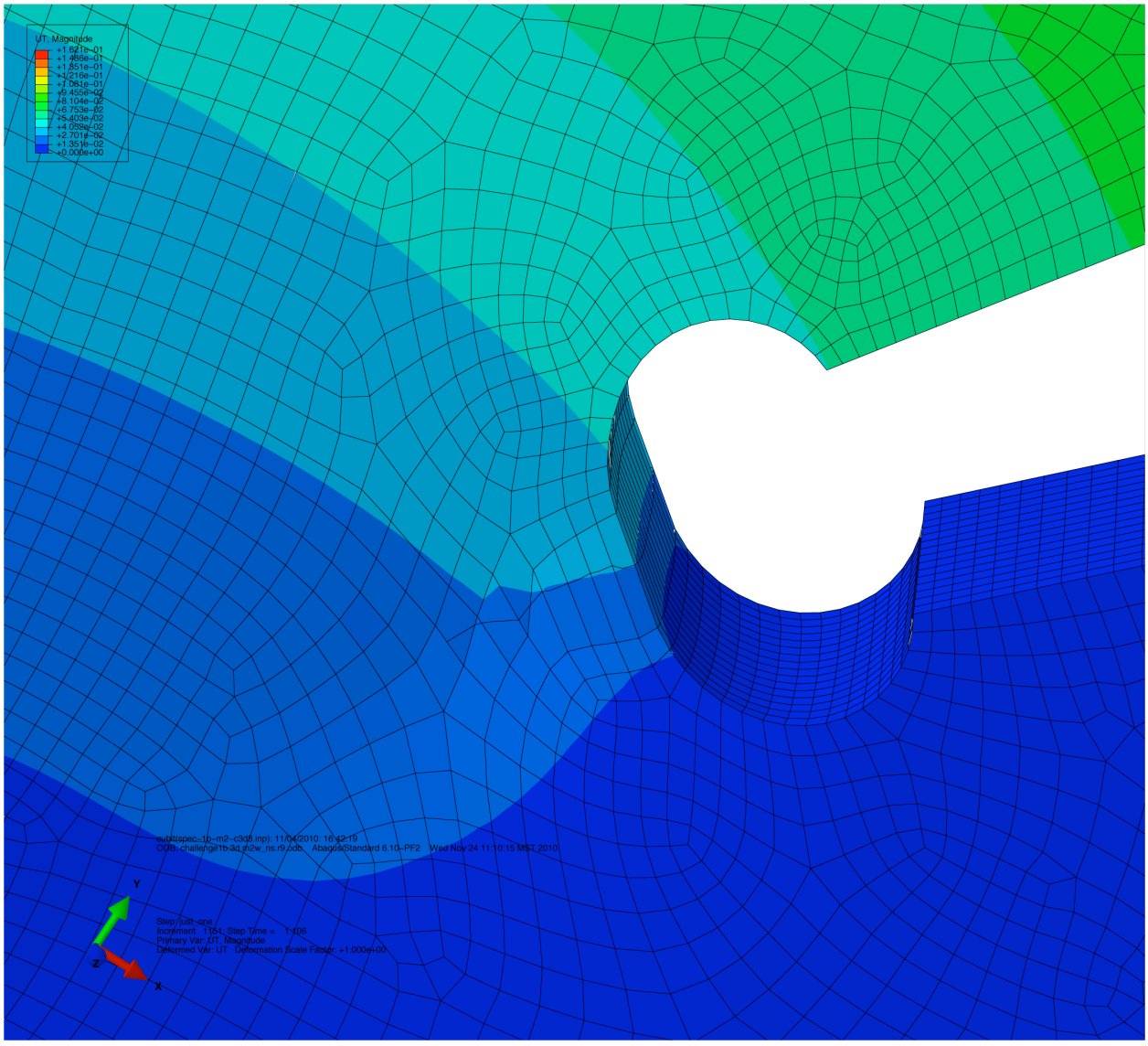

Figure D156. Cracked specimen for refined mesh model.

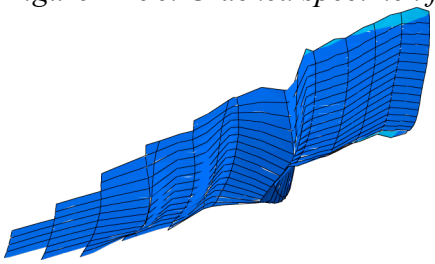

Figure D157. Geometry of Crack alone for refined mesh model.

D4.7 Sierra

The implementation of XFEM in Sierra is very new and under active development, and as a result, still has many limitations that will be resolved as it matures. These limitations affected both the ability to run analyses in a timely manner and the ability to include the appropriate physics.

D4.8 Explicit Dynamic Time Integration

One of the most severe limitations for analyzing X-Prize problem 1B was that Sierra's XFEM implementation could only be run with explicit time integration. Explicit dynamics is used to efficiently solve high rate dynamic problems with many small time steps. It can be used to solve quasistatic problems such as the X-Prize problem by applying the loading at a low rate that minimizes dynamic effects. That is what was done for the original analysis submitted for this problem.

The dynamic effects from the loading rate used for the prediction had a significant effect on the results. The Sierra XFEM prediction indicated crack propagation at a small angle above the horizontal direction. This was significantly different from the test results, which indicated that the crack should initially propagate at roughly at 45-degree angle from the horizontal, and then turn to a nearly vertical direction. After the test, analyses were performed at lower loading rates, and the crack propagated at a higher angle, so it appears that the inertial effects from the dynamic loading were at least partly responsible for the poor prediction of the crack path.

A major drawback to running explicit dynamic XFEM simulations currently is that the cracked elements cause the stable time step to drop dramatically, which results in very long run times. Even with the very coarse mesh used in the pretest analysis, the model took around 3 weeks to run on a single processor. There are currently code issues that prevent the use of XFEM in parallel that need to be resolved. These constraints led to the use of the high loading rate that produced errors in the results.

D4.9 Implicit Time Integration

Because of the problems mentioned above, it was clear that it would be very difficult to do a reasonable study of the sensitivity of the model to various parameters if it takes several weeks to do a single simulation. An implicit time stepping scheme is much better suited to analysis of this problem because the loading rate in the experiment is quasistatic. In the time since the test was conducted, an initial capability to run XFEM with a quasistatic implicit solver was developed to facilitate further work. This has enabled much more efficient solution of this problem without the errors due to inertial effects seen in the explicit dynamic solution.

The quasistatic capability was only recently developed, so a very limited number of analyses have been performed on the X-Prize 1B problem. The same mesh used in the pretest analysis was used, except that the method for modeling the pins was changed. The pins were modeled with half-cylinders contiguously meshed with the test specimen, and boundary conditions were applied to the row of nodes along the axis of the cylinder to allow the specimen to rotate about the pins. This was done to avoid convergence issues associated with contact in an implicit solver. In addition, a preliminary analysis using a more refined mesh was also performed, although this model has not yet been run to completion. The run times have gone down from weeks to hours, so future parameter studies will be greatly facilitated by this new development.

Figure D158 shows the front and back faces of the coarse mesh with the crack path from the quasistatic run. Figure D159 shows the final deformed shape of the same model. The run ultimately terminated because the crack path got tangled, which is a challenge with XFEM. Figure D160 shows a detailed view of the tangled crack path. The model locks up when the crack path gets tangled. Work is currently underway to address this problem.

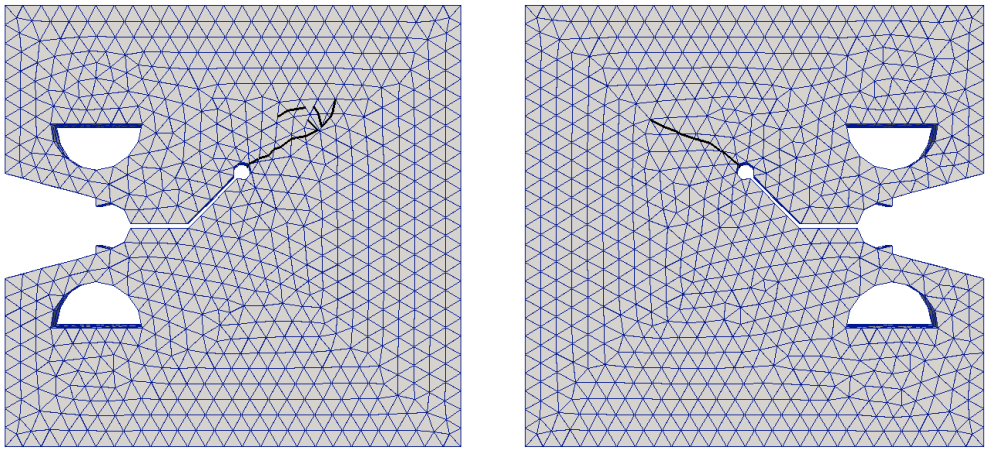

Figure D158. Crack path on undeformed mesh for coarse mesh run quasistatically

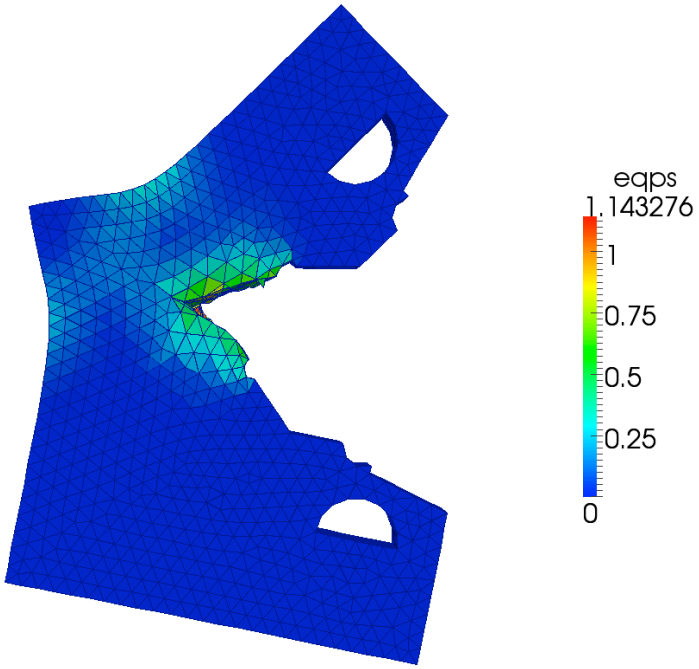

Figure D159. Deformed mesh from coarse quasistatic model

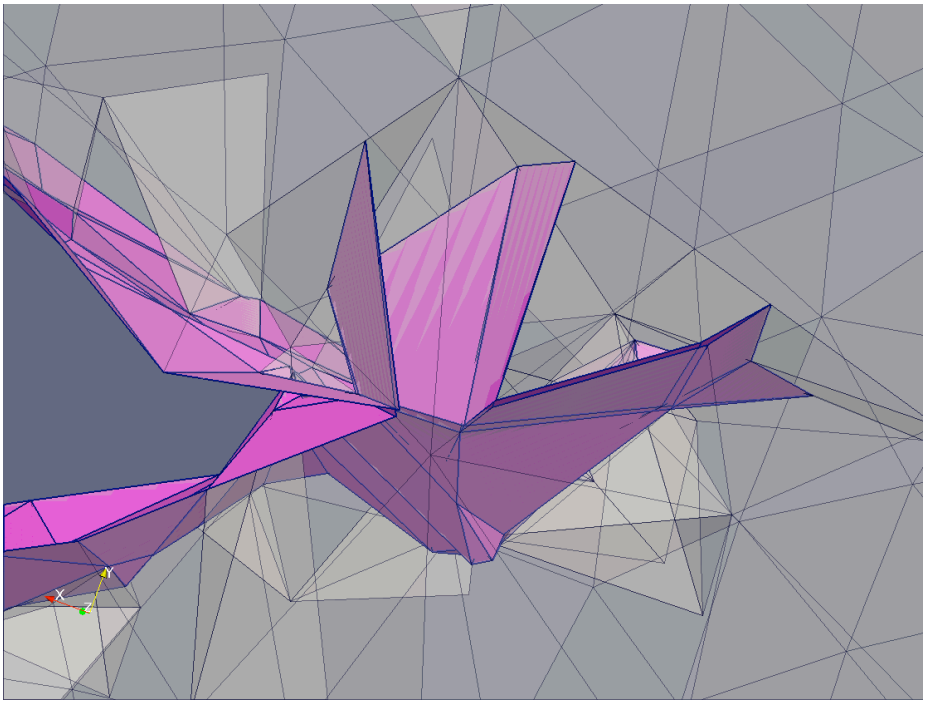

Figure D160. Tangled crack path on coarse model

Figure D161 shows the load-displacement response of the coarse model run quasistatically compared with the earlier explicit dynamic run of the model. The quasistatic run is stiffer because it was run with standard tetrahedral elements rather than the node-based tetrahedral used in the explicit run. This was done because there are still limitations with the quasistatic solver and node-based tetrahedra.

Early-time results from a more refined mesh, also run quasistatcally, are shown along with the coarse mesh results in Figure D161. Figure D162 shows the cracked region of the finer mesh in the region of crack initiation. This model was not run to completion, but it clearly demonstrates that the response will be significantly softer with a more refined mesh. The coarse mesh used in this work is clearly a significant source of error.

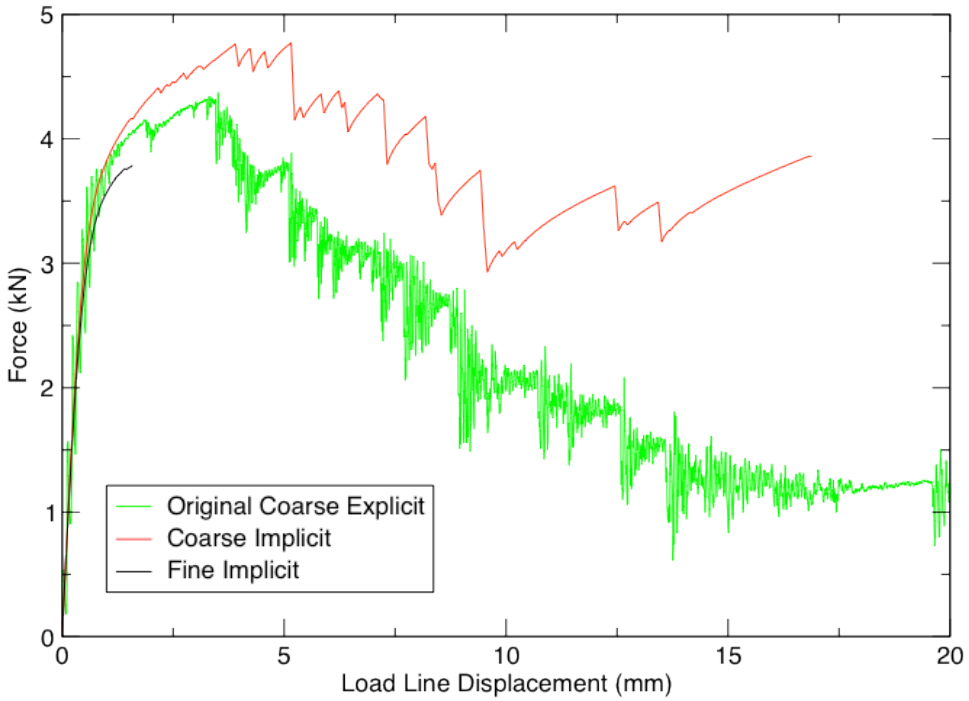

Figure D161. Crack path on undeformed mesh for coarse mesh run quasistatically

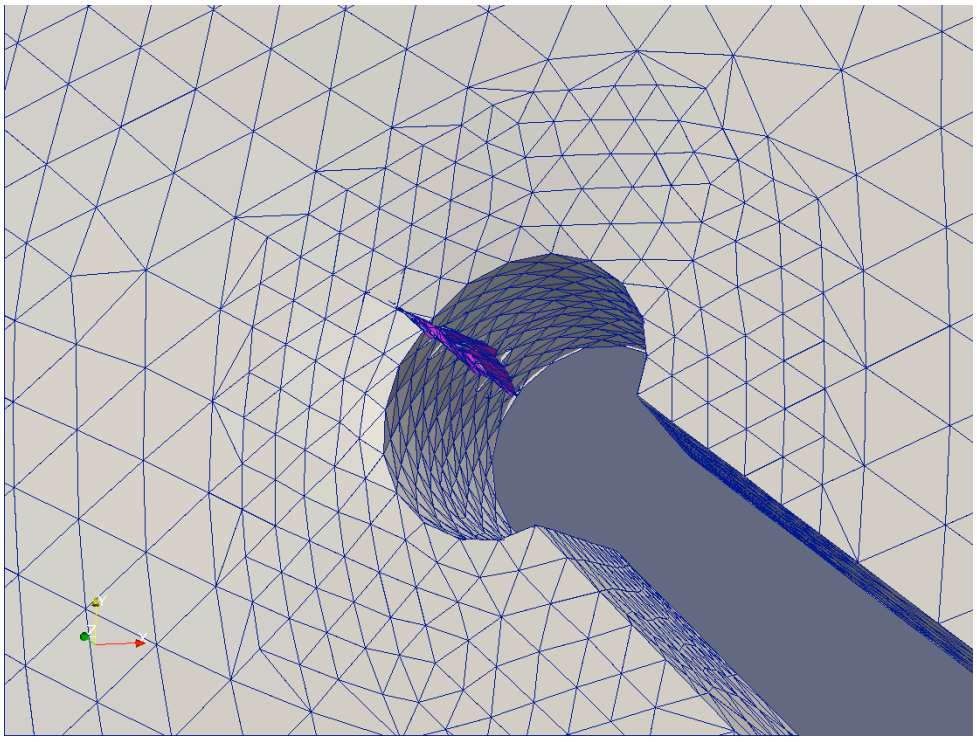

Figure D162. Cracked initiation region with fine mesh

D4.10 Other potential sources of error

Because the option to run the model quasistatically was only recently added to the XFEM implementation in Sierra, there was not sufficient time to explore the influence of other parameters. The mesh refinement and inertial effects due to dynamic loading have been shown above to significantly influence the results. Material parameters, especially the criterion for crack propagation, are certainly important and will be investigated further.

D5. Predictions for Challenge 2A

Summary

The X-Prize XFEM group analyzed the 2A challenge using finite element modeling with elastic-plastic material models and a few different failure criteria. Two analysis codes were used: Abaqus and Sierra Solid Mechanics. For this challenge, two plasticity model calibrations were examined, our own and Jerry Wellman's from challenge 1B. I used the former and Ben the latter. Unlike previous challenges, in this one, we put more emphasis upon the initiation/propagation criteria, for two reasons: (1) we determined that to be our weakest model component in the last challenge and (2) this is not a problem particularly suited to the strengths of XFEM since the crack path is known and could be addressed with a simpler approach, *e.g.*, using interface elements. Results for a few criteria were examined but only two are presented. The ability to examine different criteria was in part due to access to the beta version of the Abaqus code which allowed the initiation/propagation criterion (including crack direction) to be defined by a user subroutine.

Insufficient data was available to calibrate the initiation criterion implemented for the Abaqus analyses, so those results are not predictive in nature but do demonstrate the application of a new criterion. For the Sierra/SM analyses the tearing parameter was applied with XFEM. To simplify the analyses in Sierra the crack plane was defined *a priori*, while it was adaptively defined in Abaqus. Using the tearing parameter the extent of the cracking "predicted" in Sierra was considerably larger than that "predicted" in Abaqus using a newly implemented criterion.

D5.1 Introduction

Extended finite element method (XFEM) capabilities are in a research and development state both at Sandia and within commercial FEA codes. This is again reflected in the results obtained for this third challenge problem. To "predict" crack initiation (and continued propagation) two "XFEM approaches" were taken – one using Abaqus, and the other using Sierra mechanics. The beta version of Abaqus, which we now have, allows the initiation/propagation criterion to be defined by a user subroutine. This capability was used in this challenge to examine a few different criteria, with a strong emphasis upon the criteria proposed by Xue and Wierbicki [2005]. Sierra was modified to allow the tearing parameter to be used for initiation and propagation. An XFEM model consists of a few different component models, models to: (1) predict crack initiation, (2) predict continued crack propagation, (3) predict the incremental crack direction, (4) represent the kinematics of the localization, and (5) predict the response of the cohesive crack. Only component (4) is strictly unique to the XFEM approach. A true strong discontinuity in the displacement is introduced by modifying the basis of the approximation on the fly with functions that include a discontinuity but without remeshing. Both Abaqus and Sierra are currently limited to enriching this class of problems with Heaviside functions. For both codes model components (1) and (2) are synonymous, though conceptually there is no reason they can't be defined separately.

Sierra mechanics can not yet initiate an XFEM crack based upon mechanics, but for this problem that is not a limitation, since the specimen has a pre-existing fatigue crack. Abaqus did not allow

a pre-existing crack to be defined for an imported mesh (created in cubit), so the initial crack was simply defined by a plane of "missing elements." The "development state" of both codes has limited what could be modeled for this problem, but "state of the codes" results are presented separately below.

D5.2 Abaqus Analyses

The initiation criterion examined the most for Abaqus was that due to Xue and Wierbicki [2005]. It has five parameters, one of which can be related to the hardening exponent. In this work we treat all 5 parameters as requiring calibration. In the paper by Wierzbicki et al. [2005] seven different models for ductile fracture are compared, using 15 distinctly different test specimens. In this study both the tensile specimen and specimen 1b were used as calibration tests, but there was still a 3-dimensional space of parameter combinations to choose from. As such the presented results are not considered to be predictive. In fact the parameters for which we did not have any calibration data for, may be controlling the growth of the crack significantly by restraining the crack growth in the middle of the thickness. While the particular calibration of the Xue and Wierbicki [2005] model matches the tensile specimen failure and better represents the challenge 1b failure than our previous results, I expect (attempting to get into Brad's head) that it significantly underestimates the extent of cracking in this challenge. Convergence problems, which were only overcome recently, prevented extensive parameter studies with the model parameters, but a few analyses were conducted to investigate how the results changed with the "uncalibrated parameters." Without additional data, these three parameters simply serve as three additional "knobs" whose "correct settings" are unknown.

D5.2.1 Xue and Wierzbicki "Fracture Model"

Xue and Wierzbicki [2005] refer to their model and others as "fracture models." In the terminology we have used to describe our results we would refer to it as a crack initiation/propagation model, similar to the tearing parameter model. While it is used to determine when a crack should initiate or further propagate, the complete model can also include a cohesive zone model to characterize the energy required to create a new surface. Of course lumping this energy into a cohesive zone description is artificial since significant energy is dissipated in the bulk material near the crack as well. For brevity we will refer this model as the *X-W initiation model*.

D5.2.2 Model Form

Johnson and Cook postulated that the equivalent strain at fracture (for constant strain rate and temperature) was a function of the stress triaxiality (η), in the form (ref. X-W [2005])

$$\bar{\varepsilon}_f = C_1 + C_2 \exp\left(C_3 \eta\right) \tag{1}$$

where

$$\eta = \frac{\sigma_m}{\bar{\sigma}} \tag{2}$$

σ_m ~ mean stress, and $\bar{\sigma}$ ~ equivalent or Mises stress.

Wierzbicki *et al.* [2005] indicate that Xue [2005] showed that the equivalent plastic strain at fracture "is always bounded by two lines corresponding to the axisymmetric stress state and the plane strain state." The two bounds were expressed in a form similar to (1) as

$$\bar{\varepsilon}_f^{axi} = C_1 \exp\left(-C_2\eta\right) \quad \text{and} \quad \bar{\varepsilon}_f^{ps} = C_3 \exp\left(-C_4\eta\right) \tag{3a,b}$$

States between these bounds are expressed in terms of the deviatoric state parameter (ξ) defined as

$$\xi = \frac{27}{2}\frac{J_3}{\bar{\sigma}^3} \tag{4}$$

where J_3 ~ third invariant of the deviatoric stress tensor.

Note that for axisymmetry, ξ=1, and for plane strain ξ=0. In general, one seeks to express the equivalent plastic strain at fracture as a function of (η,ξ), *i.e.*, $\bar{\varepsilon}_f = F\left(\eta,\xi\right)$. In their formulation, they express the normalized drop in the failure strain from the axisymmetric bound and ξ as an elliptic function (reference Wierzbicki *et al.* [2005] for additional details). Solving for equation for $\bar{\varepsilon}_f = F\left(\eta,\xi\right)$ gives

$$\bar{\varepsilon}_f = F\left(\eta,\xi\right) = \bar{\varepsilon}_f^{axi}\left(\eta\right) - \left[\bar{\varepsilon}_f^{axi}\left(\eta\right) - \bar{\varepsilon}_f^{ps}\left(\eta\right)\right]\left(1-\xi^{1/n}\right)^n \tag{5}$$

where (η) explicitly denotes the functional dependence of the bounds upon η. The above form, in concept, could be used directly and the authors do so for calibration using average values of the invariants (η,ξ) over the history. To account for the stress history in a more detailed manner they apply it as a weighting function for the equivalent plastic strain integration as

$$\int_0^{\bar{\varepsilon}_f} \frac{d\bar{\varepsilon}}{F\left(\eta,\xi\right)} = 1 \tag{6}$$

which denotes (for our application) that fracture initiates/propagates when the integral reaches the critical value of one. This criterion was implemented as a user subroutine for Abaqus to study a more complex phenomenological criterion for ductile crack initiation/propagation. The integration is approximated using the trapezoidal rule over each time step. At the very least, its use of the stress invariants to characterize the effect of the stress state history is potentially more likely to match the response of differing tests specimens than simply placing a bound on the equivalent plastic strain. The question is whether it is inherently more "predictive" in nature because of its phenomenological form, or whether it simply provides more knobs to turn. In this study we do not have an optimum ensemble of tests for a given material to calibrate the model with, so even the calibration is questionable.

D5.2.3 Model Calibration

To calibrate the model we had two tests available: the tensile test and challenge 1b. Since the model has five parameters, the two tests only limit our unknowns to a three-dimensional space. Table 1 shows the parameter values for several calibrations. Calibration *EQPS* corresponds to using an upper bound on the equivalent plastic strain (independent of the stress state history), as used in challenge 1b. Wierzbicki *et al.* [2005] calibrated the model for the aluminum alloy 2024-T351; this calibration is denoted as *X-W*. The remaining calibrations used this known calibration for as a starting point.

Table D10. X-W Calibration Parameters

Calibration	C_1	C_2	C_3	C_4	n	1b Runs
EQPS	0.2351	0	0.2351	0	∞	
X-W	0.87	1.77	0.21	0.01	6	
1	0.424	1.77	0.102	0.01	6	11
2	0.87	3.924	0.21	2.164	6	12
3	0.328	1.0	0.102	0.01	6	13
4	0.278	0.5	0.102	0.01	6	14
5	0.260	0.3	0.102	0.01	6	15
8	0.278	0.5	0.05	0.01	1	
9	0.260	0.3	0.05	0.01	1	

Figure D163 shows the approximate range of the stress invariants (η,ξ) for the tensile test, challenge 1b, and challenge 2, in the element in which the crack initiates (or further propagates the fatigue crack) just prior to propagation, and three curves for plane strain, axisymmetry, and plane stress.

For the tensile specimen, ξ~1 and η~1/3. Using equation (5), the authors' calibration values would give $\bar{\varepsilon}_f$ = 0.4819. This value is greater than the observed value of 0.2351. The first calibration for this study was obtained by scaling C_1 and C_3 to match $\bar{\varepsilon}_f$ = 0.2351, with C_2, C_4, and n unchanged from the X-W calibration. The second calibration, conversely, was obtained by changing C_2 and C_4 to match $\bar{\varepsilon}_f$ = 0.2351, with C_1, C_3, and n unchanged from the X-W calibration. Figure D164 shows the axisymmetric and plane strain bounds (equations 3) for the first two calibrations. Since ξ~1 corresponds to the axisymmetric case, the axisymmetric bounds both pass through the point $\bar{\varepsilon}_f$ = 0.2351 where η~1/3. As such the calibration changes for the plane strain bound do not affect the comparison.

Figure D165 shows the axisymmetric and plane strain bounds (equations 3) for calibrations 5 and 6. Note that when the bounds cross their meaning is contradicted, and as such the actual η values in the analysis should remain smaller than the intersect value. This motivated the reduction in C_3 in calibrations 8 and 9, since sampled η values in challenge 2 suggest it might have exceeded the intersect value of calibration 4. Since these last calibrations were defined late in the study, they were not used to re-examine the tensile specimen or challenge 1b. Certainly for the tensile specimen, they would have little effect due to the stress invariant state at failure.

For challenge 1b, ξ∈(0.884,0.942) and η~0.55, so again the axisymmetric bound has the greatest affect upon the response. The monotonic decrease of $\bar{\varepsilon}_f^{axi}$ for the first two calibrations (Figure D164) indicates that the X-W criterion will result in earlier crack initiation (lower $\bar{\varepsilon}_f$) for challenge 1b than obtained by using constant equivalent plastic strain as a criterion. As the previous results for challenge 1b gave more ductility than the experiments, the decrease would appear to be the right trend, but as shown in Figure D166 these calibrations seem to fail too early.

For challenge 2 the stress state near the middle of the section (i.e., through the thickness) has a value of ξ close to a ½. As such, $\bar{\varepsilon}_f^{ps}$ can affect the results more, and thus the values C_3, C_4, and n are significant. The last two calibrations (8 and 9) were defined to examine the effects of two of these parameters. Note that the original value 6 for n, tends to almost eliminate the effect of $\bar{\varepsilon}_f^{ps}$ except when a plane strain state is almost exactly reproduced. The value of 1 for n, linearly interpolates between the axisymmetric and plane strain bounds.

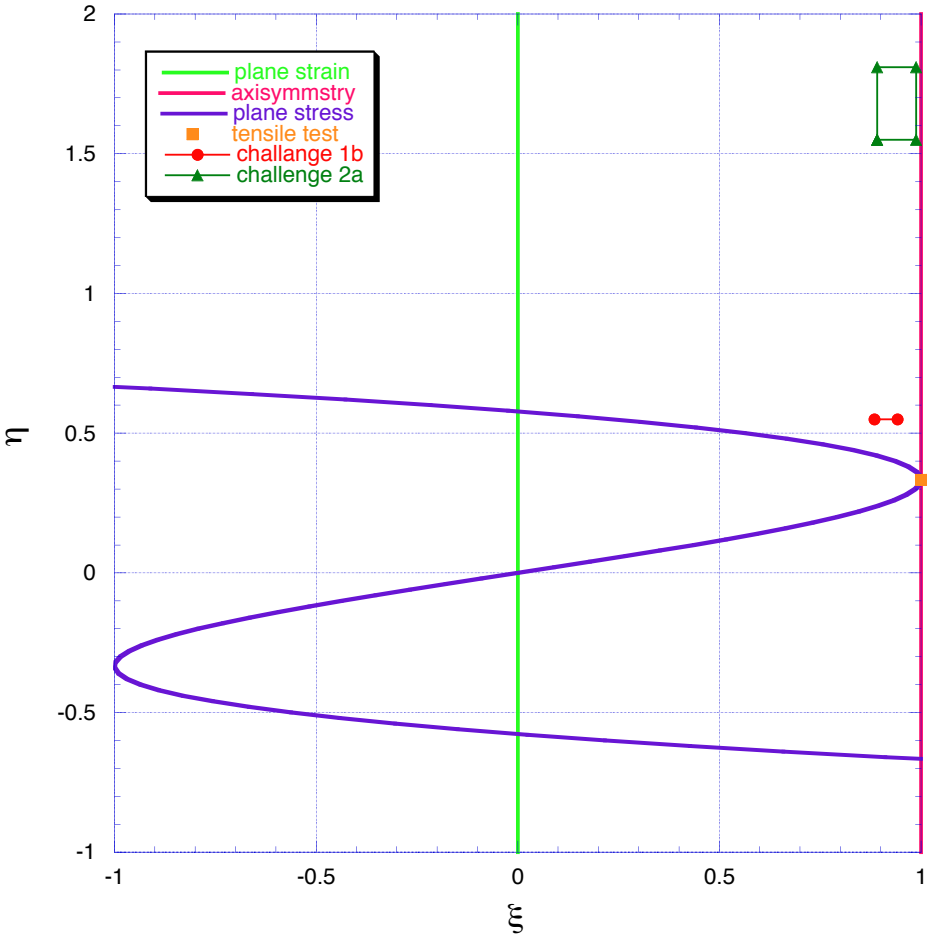

Figure D163. Invariants of the critical element just prior to initiation.

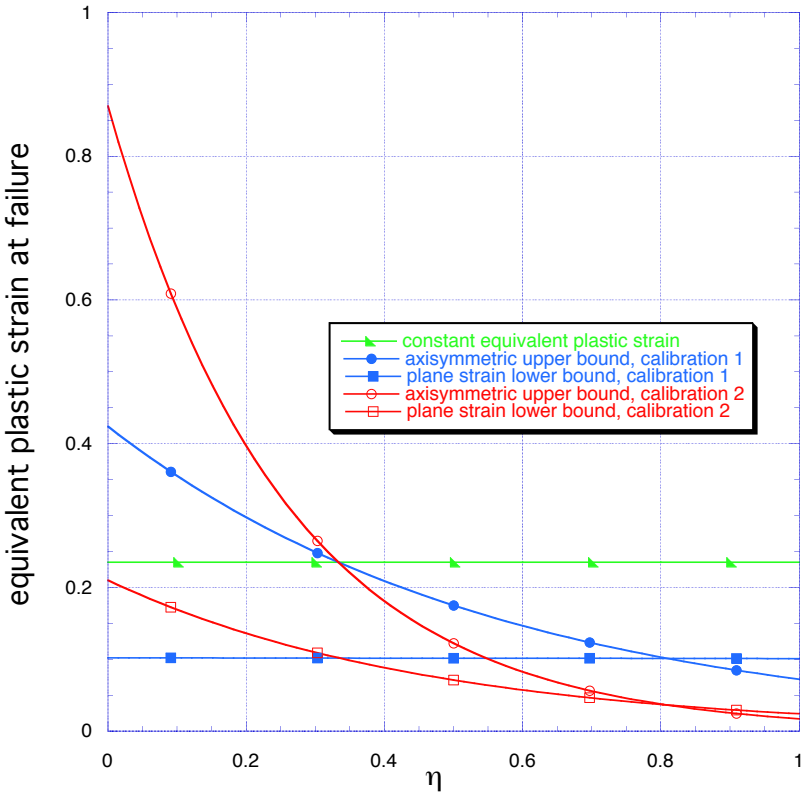

Figure D164. Axisymmetric and plane strain bounds for first two calibrations.

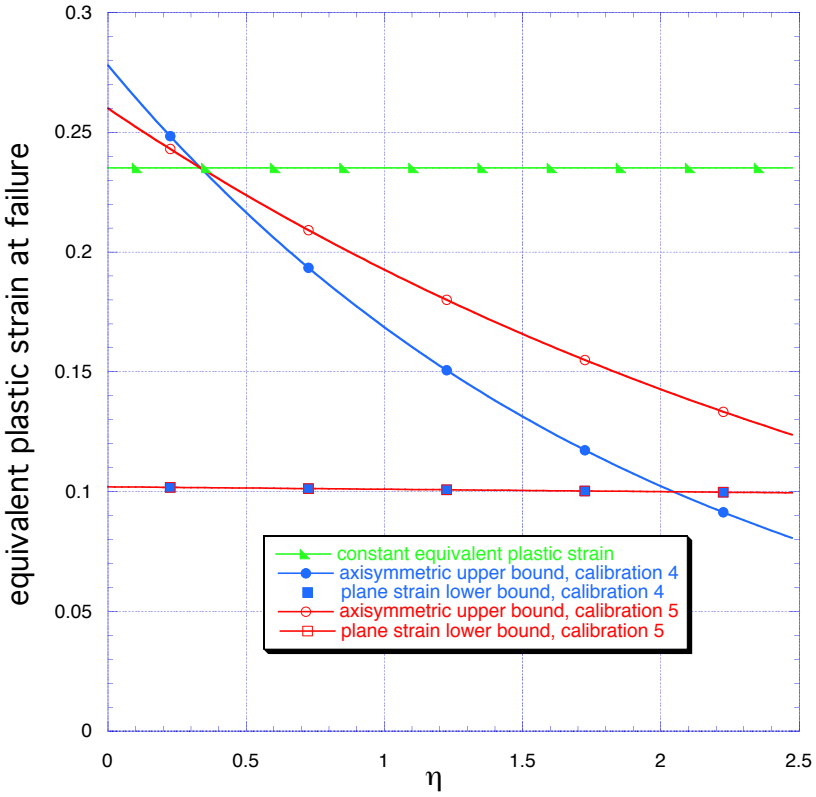

Figure D165. Axisymmetric and plane strain bounds for calibrations 4 and 5.

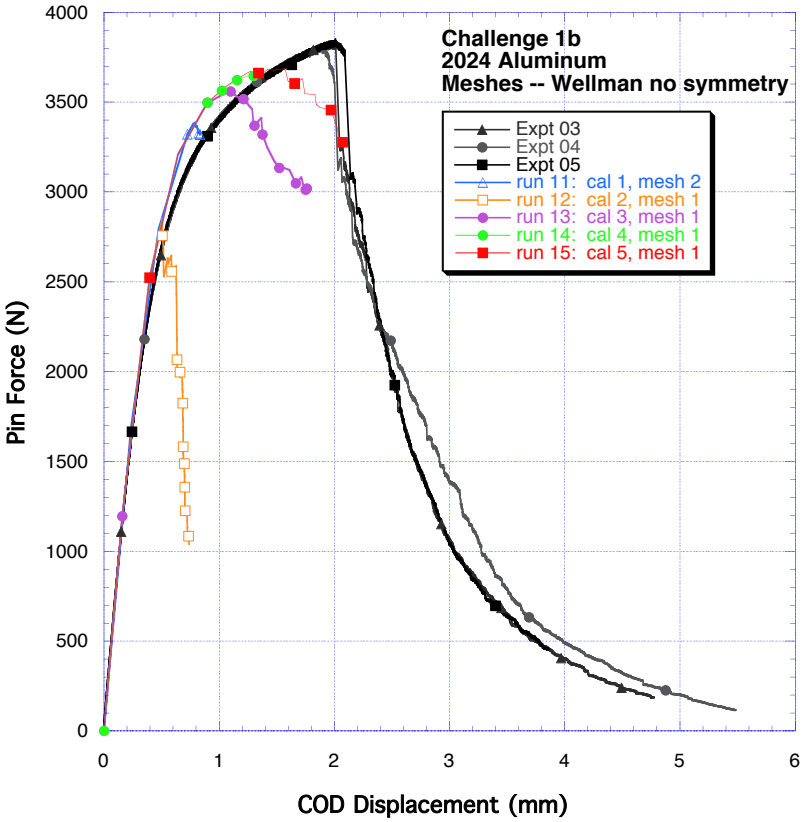

Figure D166. Challenge 1b results for several X-W calibrations.

For calibrations 3-5, C_2 was successively reduced and C_1 was calculated to match the tensile specimen. While calibration 5 is closest to the experimental results, it does not reflect the abrupt drop in strength exhibited in the experimental results. The effect of mesh refinement for challenge 1b was examined for several cases but found to be small.

While challenge 2a has a significantly different stress state (Figure D163), with respect to ξ it is still closer to the axisymmetric bound for the first element to fail. Unfortunately the first element to fail (on the specimen edge) has a very different stress state than those near the middle of the thickness. Near the middle of the specimen just prior to failure, $\xi \in (0.435, 0.514)$ and $\eta \in (2.15, 2.43)$. The shift to the left in the invariant space implies C_3 and C_4 would have a significant effect on the predictions for this challenge. The net effect, as will be seen in the next section, is that the crack growth is severely restricted in the middle of the cross-section thus inhibiting the growth of the whole crack.

D5.2.4 Challenge 2 Results

A few different initiation criteria were used for this test, but the simpler ones like a bound on equivalent plastic strain gave very little crack growth. The results shown here are limited to those obtained using the X-W initiation criterion. Figure D167 shows the coarser mesh used in most of the analyses.

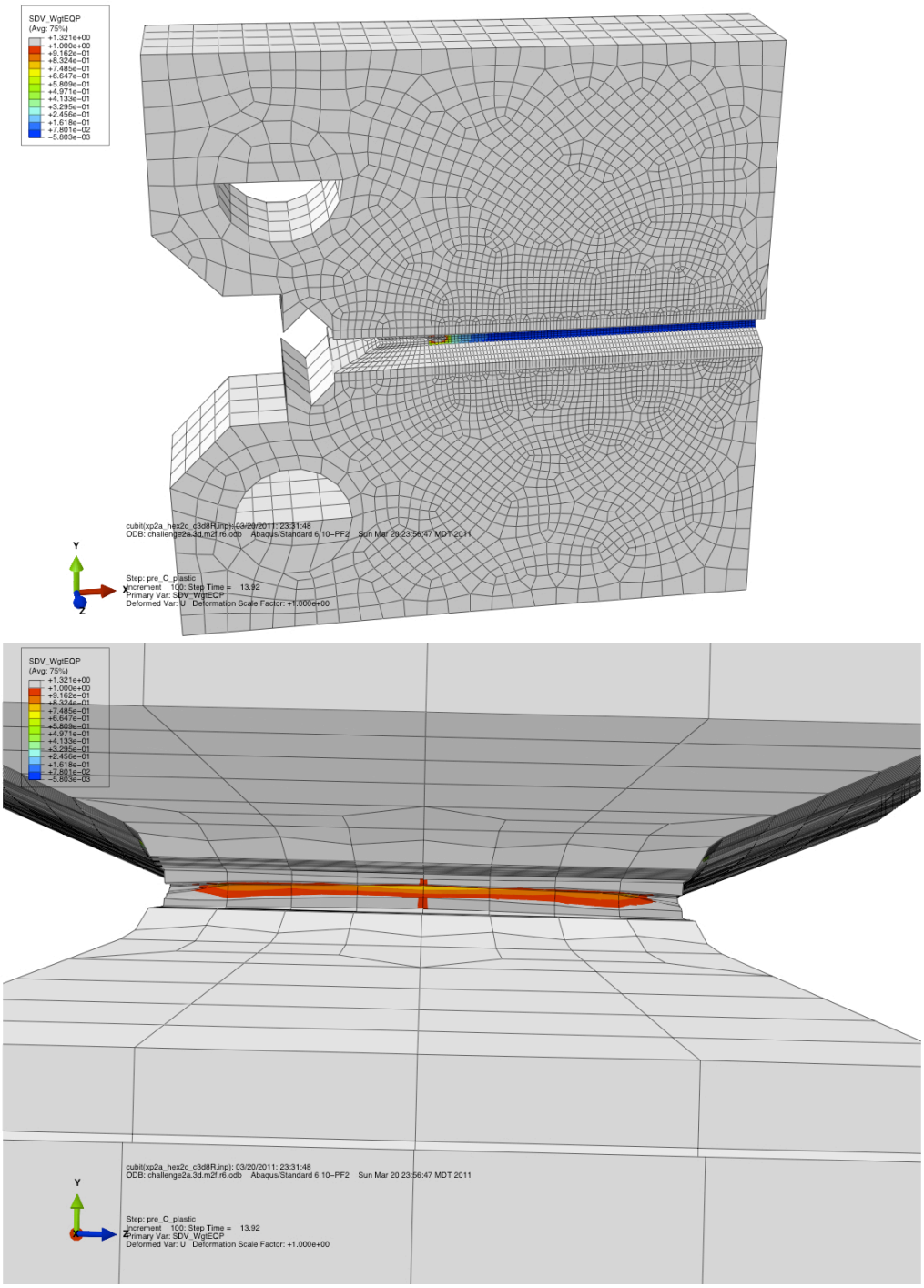

Figure D167. Coarse mesh – lower view looking toward the initiating crack

In this problem the boundary conditions are not prescribed explicitly but must be defined to produce the measured gage displacement. While one could algorithmically adjust the boundary conditions to match the gage displacements, it is not clear if this could be done easily in Abaqus, so instead I took a "simpler approach." First I applied the measured gage displacement history to the pin and determined the corresponding gage displacement. This is depicted in Figure D168. Roughly, the ratio U_{gage}/U_{pin} varied from about 0.78 to 0.85. As a correction to applying the gage displacements to the pin, in the subsequent analysis the data of Figure D168 was used to determine U_{pin} for a prescribed U_{gage}, and the boundary conditions were modified accordingly.

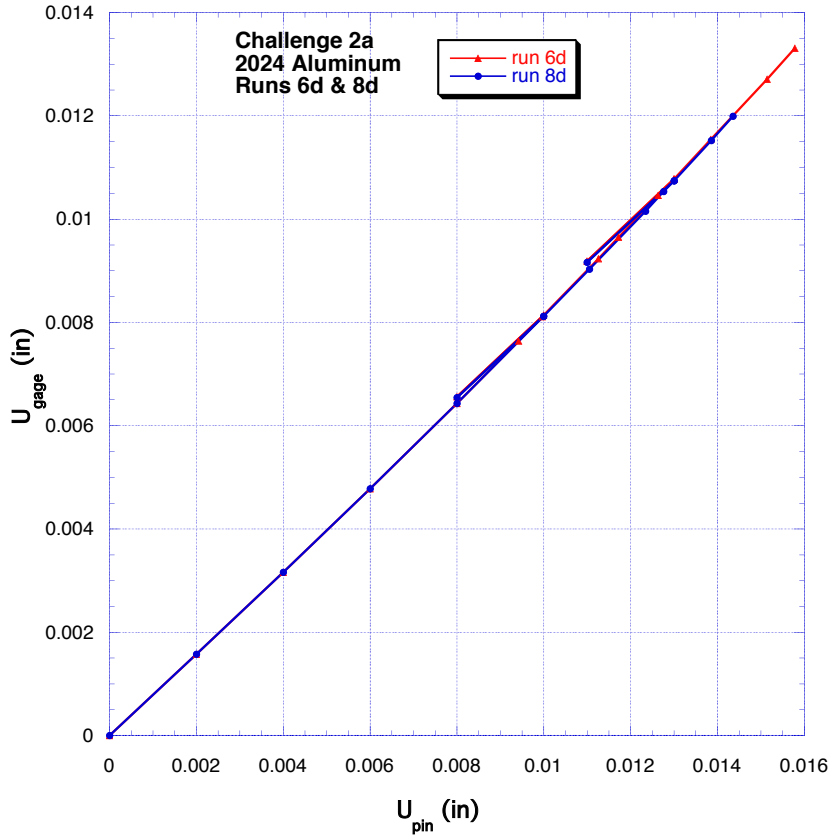

Figure D168. Measured relative displacement vs. pin displacement.

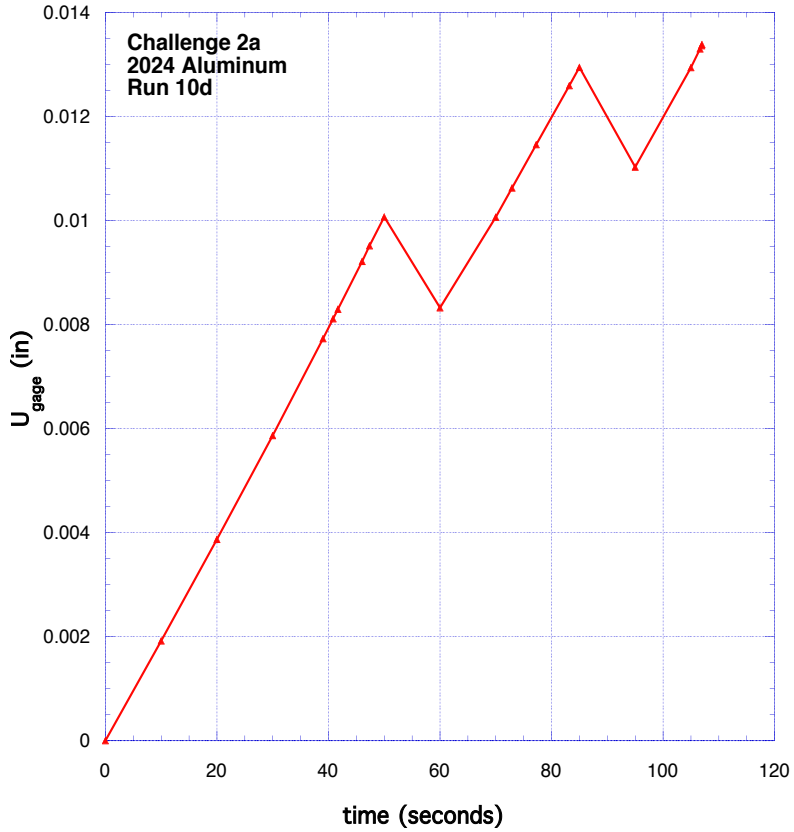

Figure D169. Measured displacement for 1st revision of boundary conditions

Figure D169 depicts the resulting history of the gage displacement to the state that most of the analysis would die at. While not perfect I expect the accuracy is much better than our crack predictions, and as such sufficient.

Table D11 correlates the analysis or run designation with the differing parameters and gives the crack lengths (in terms of uniformly sized elements) at different states. For all of the analyses shown implicit dynamics was applied, and the fracture energy was zero. In challenge 1b, using implicit dynamics in the simulation instead of quasi-statics sometimes improved how far an analysis could go before encountering convergence problems. In this challenge it appeared to have little effect as both types of analyses died at the same states. In most cases, including the fracture energy reduces the range over which convergence could be obtained.

Table D11. Run designations.

Run	Initiation Calibration	Convergence tolerance	Cracked surface els at A	Cracked surface els at death	Cracked surface els at B	Cracked surface els at death	Cracked surface els at C	Cracked surface els at death	Cracked surface els at D
10d	4	defaults	1		3	5			
18d	4	looser	1		3		9	10	
19d	5	looser	1		2		6		11
22d	8	looser	7	11					

23d	9	looser	5		13	16			

To get the results in analyses 18d – 23d the convergence tolerances were loosened significantly, but comparisons with results for analyses with the default convergence tolerances for states A and B indicate the accuracy was good. Figure D169 shows the pin force vs. gage displacement for the two calibrations.

The requested results are given in Table D12. Figure D170 shows the corresponding load displacement results for the 4 calibrations. The expected trends between calibrations 4 and 5 are consistent with those seen in challenge 1b; calibration 4 allows cracking to occur more easily. For both calibrations the crack grows much more readily along the surface than through the middle of the specimen. As previously noted this is due to the difference in the stress invariants through the thickness of the member. Figure D171 shows the crack profile at the end of run 19d. The crack growth near the middle of the specimen appears to restrict the growth of the whole crack.

Clearly we can "improve" upon the predicted results, because we still have "three knobs to turn," but the improved results will not constitute a prediction without additional data upon which to base the calibration. Table D12 and Figure D172 shows that in changing the calibration the extent of cracking can be increased. While convergence problems limited the results, Figure D170 shows changing the parameters reduced the peak load and thus compliance at each state after cracking initiated. Further reduction in key parameters would be required to shift the "unloading responses" to the specimen softening regime as obtained in the Sierra analyses.

Table D12. Requested results.

State A	**Calibration 4 (run 10d/18d)**	**Calibration 5 (run 19d)**	**Calibration 8 (run 22d)**	**Calibration 9 (run 23d)**
Crack length (mm)	2.74	2.73	3.80	3.44
Crack length change (mm)	0.196	0.193	1.26	0.901
Stiffness (N/mm)	31,200	31,700	30,000	30,500
State B			n/a	
Crack length (mm)	3.09	2.91		4.87
Crack length change (mm)	0.548	0.371		2.33
Stiffness (N/mm)	30,600	30,900		28,600
State C			n/a	n/a
Crack length (mm)	4.15	3.62		
Crack length change (mm)	1.62	1.08		
Stiffness (N/mm)	29,200	29,900		
State D	n/a		n/a	n/a
Crack length (mm)		4.51		
Crack length change (mm)		1.97		
Stiffness (N/mm)		29,000		
State *Death*	<D	n/a	<B	<C
Crack length (mm)	4.33		4.57	5.41
Crack length change (mm)	1.79		2.03	2.87

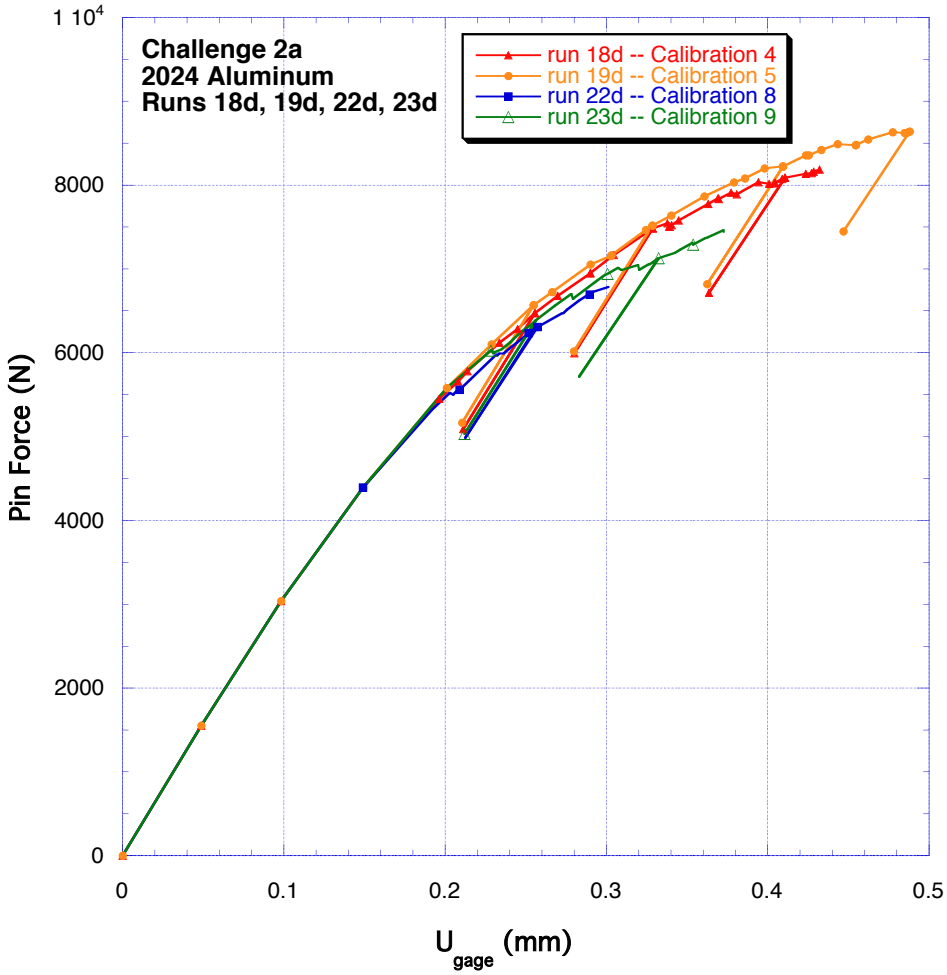

Figure D170. Load vs. displacement response for four calibrations.

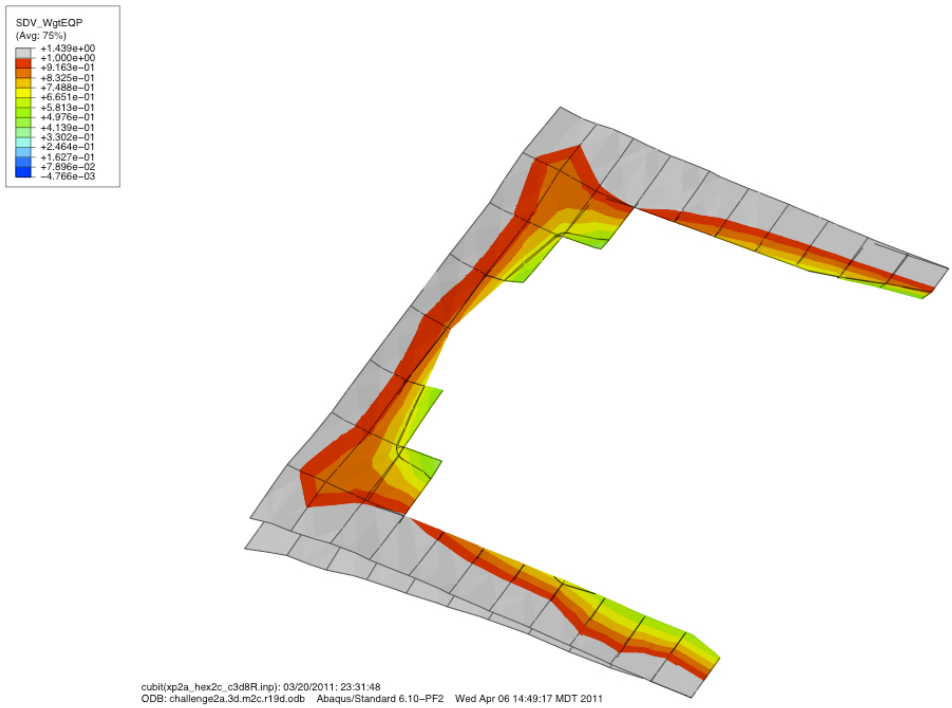

Figure D171. Crack at end of run 19d (calibration 5).

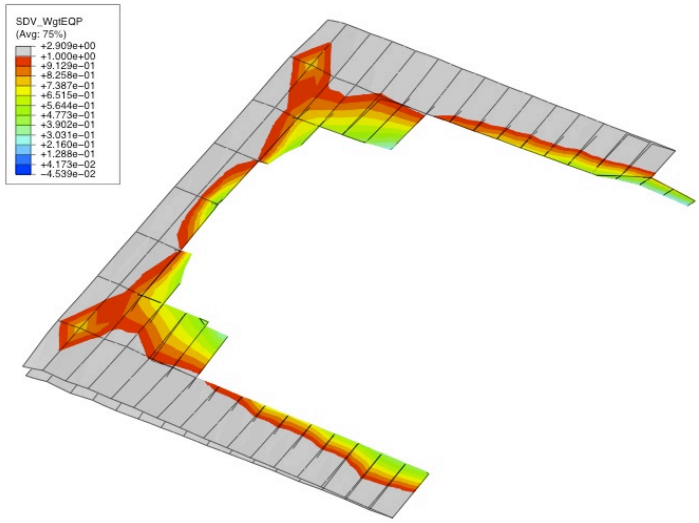

Figure D172. Crack at end of run 23d (calibration 9).

D5.3 Sierra/SM Analyses

The Challenge 2a problem was also run using the XFEM capability in Sierra/SolidMechanics (Sierra/SM), which is still under active development. Because this capability is under development, running this problem uncovered a number of bugs in that code implementation. As a result, there was not sufficient time to do model calibration, and the mesh used was not as highly refined as would be ideal for this problem.

For this analysis, the multilinear_ep_fail material model was used with the same parameters that were used by the team using element death for Challenge 1b. Those parameters were calibrated against the tensile pull specimen. In the Challenge 1b problem, that set of parameters resulted in excessively rapid load shedding. It is likely that the load shedding is too rapid for this problem as well. With more time, the parameters could be better tuned. The tearing parameter was used as the criterion for propagation of the crack into a new element. The multilinear_ep_fail model is typically set up to soften when the tearing parameter is reached. Since the softening is modeled by inserting a crack in this case, the material model was set up to never soften.

Sierra/SM's XFEM capability is currently based on tetrahedral elements. Figure D173 shows the finite element mesh used for this analysis. The model has 15000 nodes and 77400 elements. The mesh is very coarse in the region away from the mesh, but is refined in the region of the machined notch. The elements in the notch zone have a size of approximately 0.08 in (0.2 mm). The pins are modeled by inserting semi-circular blocks of material in the holes. Displacement is prescribed on a line of nodes at the center of that semi-circle.

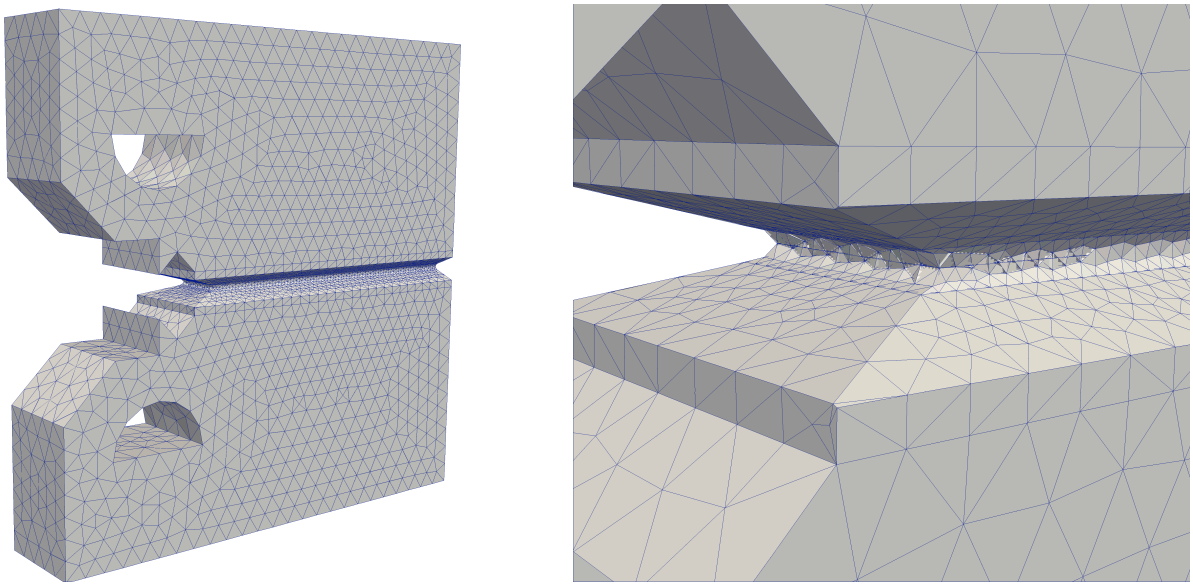

Figure D173. Finite element mesh used for Sierra/SM analysis, showing fatigue crack detail

In the experiment, the displacement is measured at the lips near the tip of the initial notch. That displacement is different from the pin displacement. It is difficult to prescribe the displacement

in terms of this gage displacement in the analysis. Prescribing the gage displacement would require an iterative process. No attempt was made to prescribe the gage displacement for this effort. The specified displacement history was simply applied at the pins, and the difference was noted. Figure D174 shows the difference between the pin and gage displacement over time. As the crack propagates, the two displacements grow closer together because the two halves of the specimen behave more as rigid bodies. Figure D175 shows the gage displacement plotted as a function of pin displacement. The two displacements are not dramatically different, so this is not expected to have a major effect on the results.

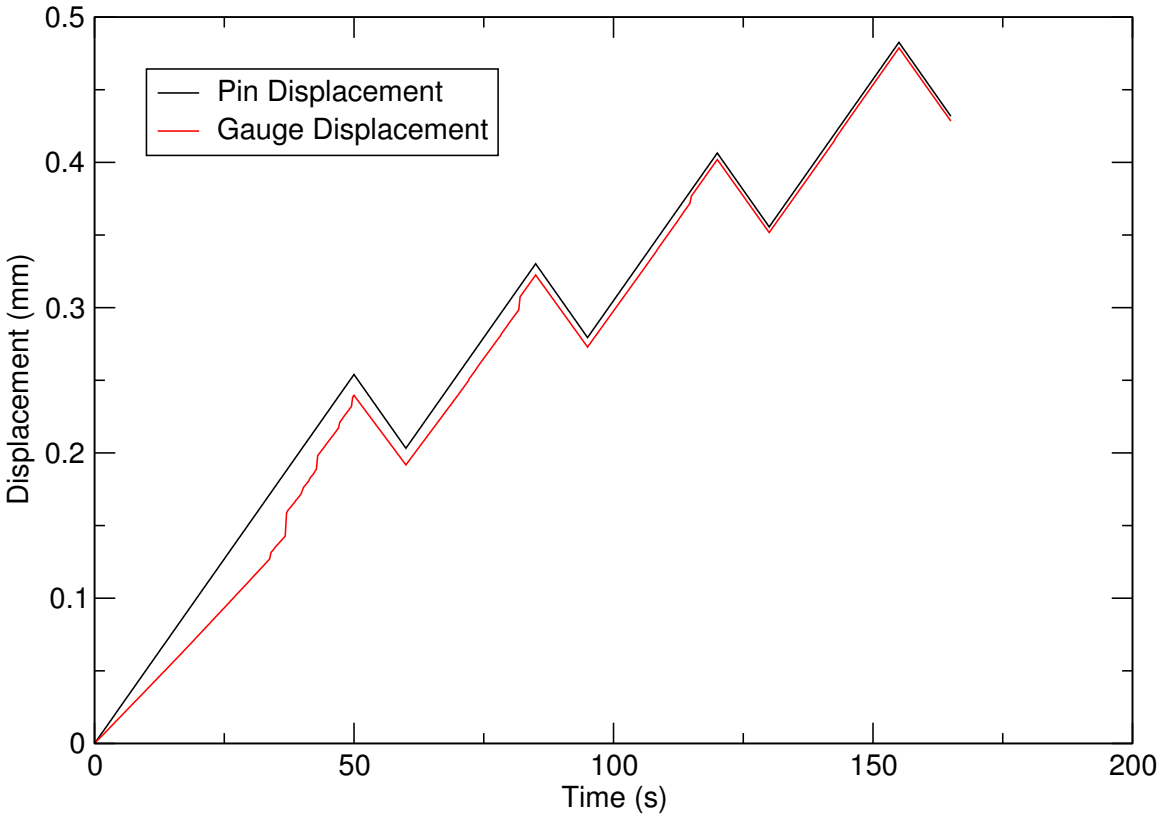

Figure D174. Pin Displacement and Gage Displacement vs. Time

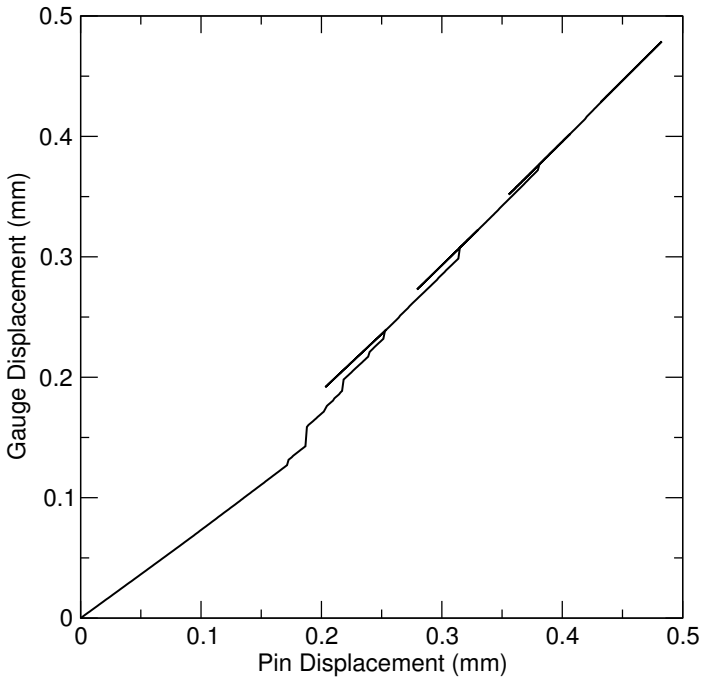

Figure D175. Gage Displacement vs. Pin Displacement

Figure D176 shows the history of the force vs. displacement. This is shown both in terms of the pin and the gage displacement. The four unloading/reloading curves are annotated in the plot. The stiffness at these points was measured using the gage displacement. In this analysis, Peak A in the displacement history occurred well past the point where peak load was reached. There was a notable decay in the stiffness as the loading progressed.

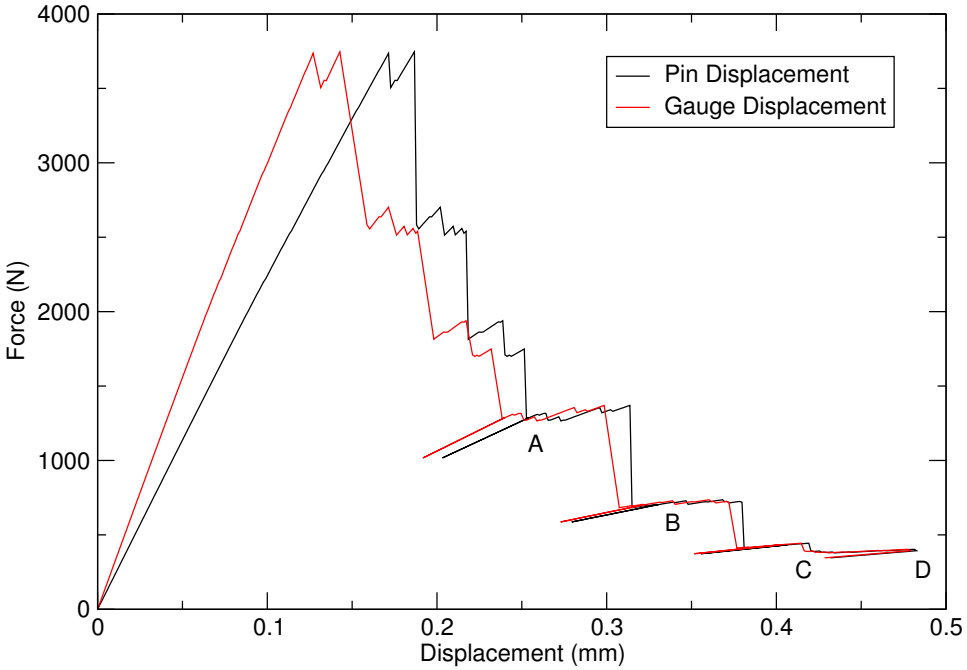

Figure D176. Force vs. Displacement

Figure D177 shows the deformed mesh with the crack surface (highlighted in pink) at the four peaks. The crack advanced most rapidly during loading up to the first peak. Figure D178shows a history of the crack surfaces created by XFEM at the four peaks. These are shown against a scale using units of inches measured from the center of the loading pins. The initial fatigue crack started out at a distance of 0.1 inches from the tip of the machined notch, or 0.3 inches from the center of the loading pins.

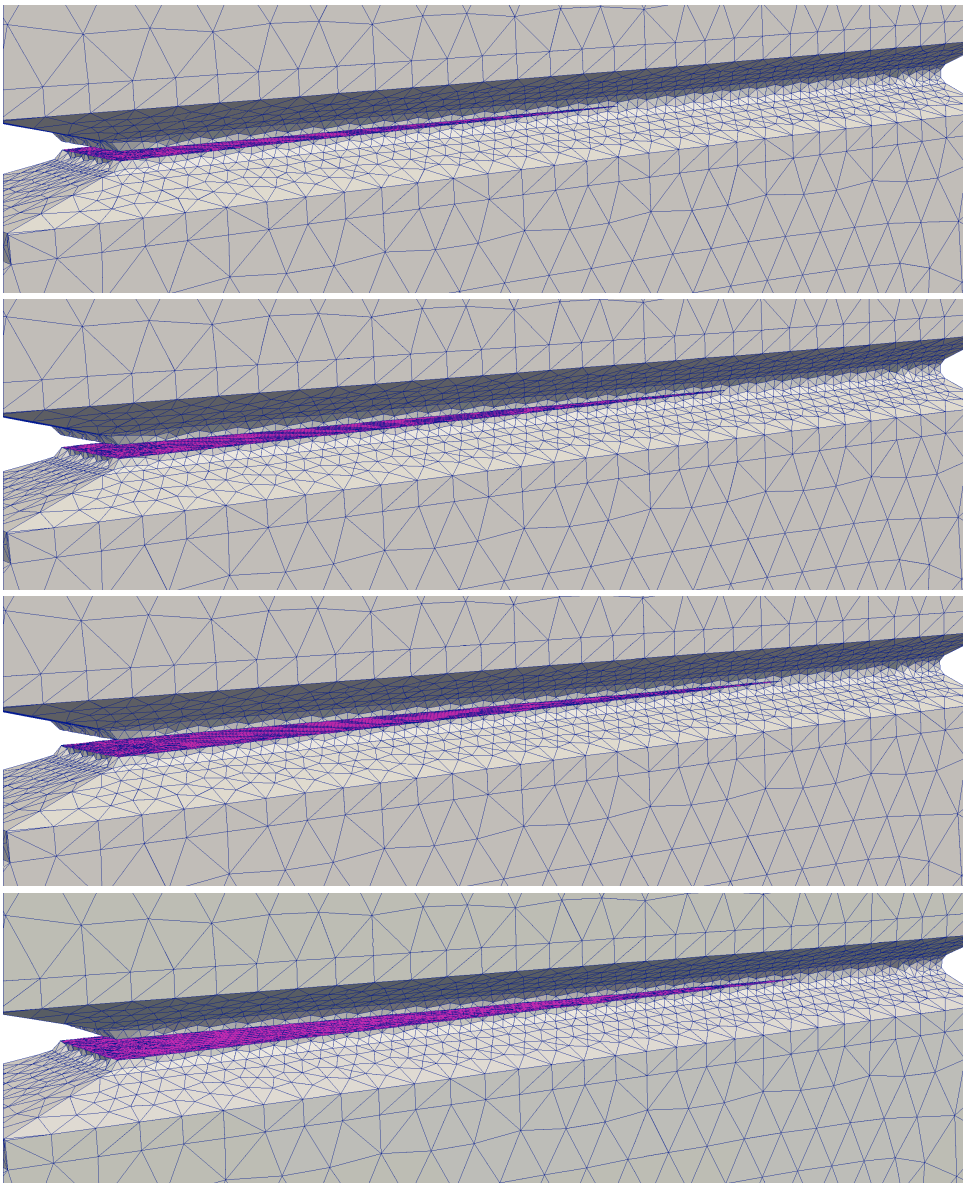

Figure D177. Deformed cracked mesh at Peaks A, B, C, and D

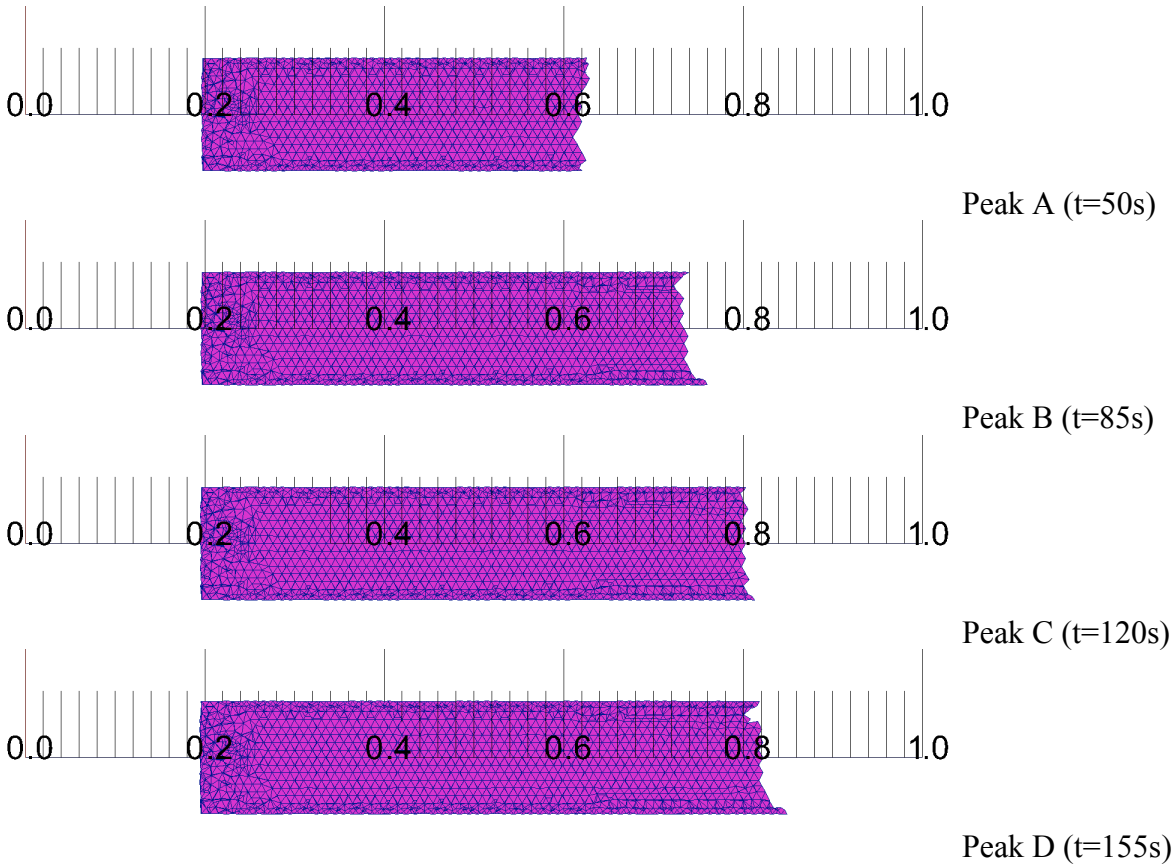

Figure D178. Deformed cracked mesh at Peaks A, B, C, and D (lengths in inches)

Table D13 shows a summary of the state at each of the four peaks. The gage displacements at the peak and at the subsequent trough are reported, along with the corresponding force at the peak and trough. The stiffness computed from the change in force and gage displacement is reported. In addition, the crack length is reported at each peak. The crack length is reported relative to the tip of the initial fatigue crack. The initial fatigue crack was 0.1 in (2.5 mm) deep, so the crack lengths relative to the tip of the machined groove can be calculated by adding 2.5 mm to these values.

Table D13. Results at Four Peaks

Peak	Peak Disp (mm)	Trough Disp (mm)	Peak Force (N)	Trough Force (N)	Stiffness (N/mm)	Crack Length (mm)
A	0.2396	0.1918	1286	1017	5628	8.1
B	0.3225	0.2730	703.0	586.8	2348	10.9
C	0.4020	0.3517	433.0	373.1	1191	12.7
D	0.4789	0.4284	393.6	345.5	952.5	13.2

D6. Follow-Up to Challenge 2A

D6.1 Introduction

The pre-test analysis of the X-Prize 2a problem using the XFEM implementation in Sierra reasonably predicted the load-displacement response prior to crack initiation and the point where softening started to occur. However, it dramatically under-predicted the load after that point.

D6.2 Modifications to Analysis Approach

Since the time that pre-test analysis was completed, two important improvements have been made to XFEM in Sierra that have resulted in a significantly improved simulation of that test. The first is that the capability to use cohesive zone elements on the XFEM cut plane in implicit analyses has been added. The original analysis simply cut elements when a failure criterion was reached, and provided no cohesive strength after cracking.

The second improvement made to Sierra's XFEM implementation is that node-based tetrahedral elements can now be used with XFEM for implicit calculations. The original analysis was performed using standard linear tetrahedral elements, which are well known to suffer from locking problems in conditions of near incompressibility, which is the case for material that is yielding in advance of the propagating crack for ductile fracture problems.

Introducing cohesive zones on the fracture planes was the most important of these two changes in the modeling approach. A Tvergaard-Hutchinson interface cohesive model was used. This model has a linear hardening curve, a flat plateau, and linear softening. This model takes as parameters the maximum traction, normal and tangential relative displacements at which traction has completely decayed, and the points at which the stiffening branch ends and at which the softening branch starts. The important parameters used here were peak traction of 120000 psi, and normal and tangential relative displacements for complete decay of 0.005in. Ideally, the peak traction should be set based on the stress in the parent element at the point of initiation, but that cannot yet be done in our code. There is still more work to do in this area. Aside from the cohesive zone parameters, all of the parameters used in the original model were kept the same.

D6.3 Results

Figure D179 shows a plot of the load-displacement curve for the post-test analysis shown compared to the pre-test analysis and experiment. From this, it is clear that including the cohesive strength has a significant effect on the load-displacement response. In the post-test work, I simply applied monotonic loading rather than unloading and reloading. The points where the model was unloaded and reloaded in the original analysis were off from the actual experimental points in the original analysis because they were based on the pin displacement rather than the gage displacement. Since we can't directly impose the gage displacement, the unloading and reloading needs to be specified based on an initial monotonic analysis. The unloading and reloading does not appear to significantly affect the overall load-displacement curve. The post-test model can be modified to include the unloading to obtain the stiffness, but that has not yet been done.

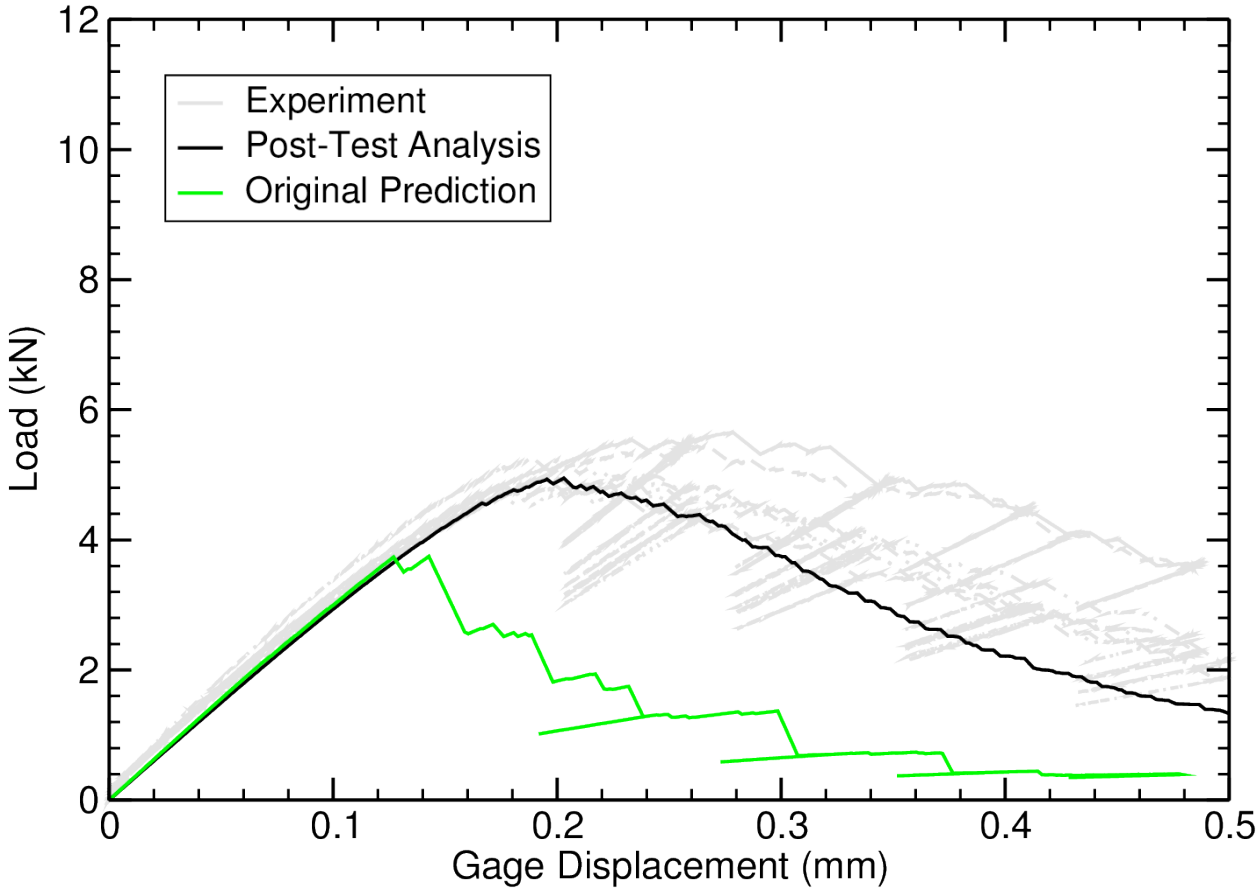

Figure D179. Comparison of experimental results, original prediction post-test analysis load-displacement curve for X-Prize 2A

To show the effect of using the node-based tet element on this problem, the model was run using three levels of mesh refinement using both the linear tet and the nodal tet. Figure D180 shows a comparison of the load-displacement curves for all of these analyses. In this convergence study, the fine mesh was the same mesh used in the original pre-test prediction. The medium mesh is twice as coarse as the fine mesh in the region of crack growth, and the coarse mesh is twice as coarse as the medium mesh in that region.

From this plot, it can be seen that the nodal tetrahedron consistently produces a softer response than the standard linear tetrahedron. The results produced by the nodal tetrahedron are roughly equivalent to those produced by the linear tetrahedron with a mesh with twice the refinement. This convergence study indicates that the fine mesh used here is still likely not sufficiently refined to produce a converged solution.

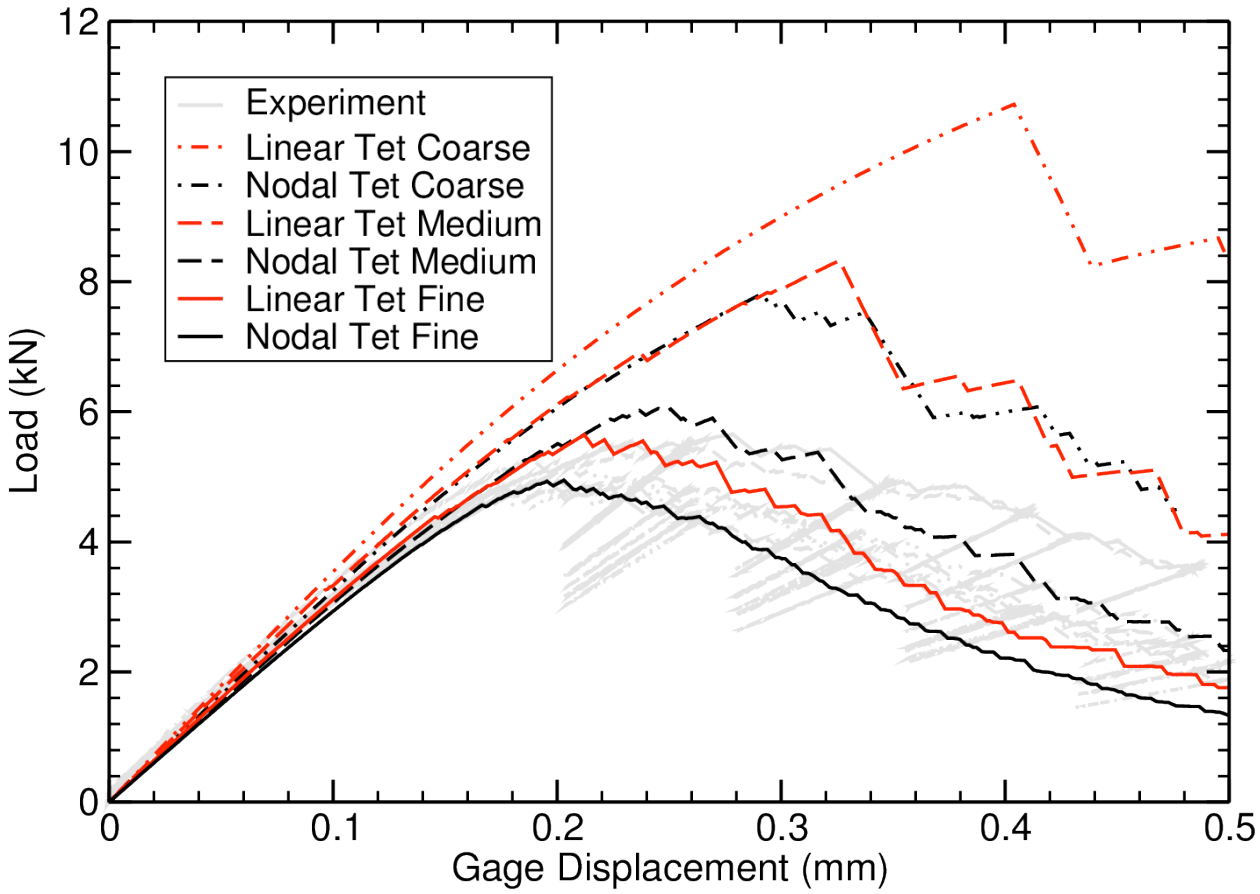

Figure D180. Load-displacement curves for X-Prize 2a problem comparing convergence of linear tetrahedral elements with nodal tetrahedral elements

Figure D181 shows plots of the crack progression at Peaks A, B, C, and D, and Table 1 shows the crack lengths and forces at these four points. Cohesive zones are introduced when the failure criterion is reached. As can be seen from this figure, the fracture process zone where the material still has some cohesive strength has a fairly significant length. The crack lengths reported in Table D 14 are based on the point where the cohesive zone has lost all of its strength (i.e. the transition from dark blue to cyan in Figure D181).

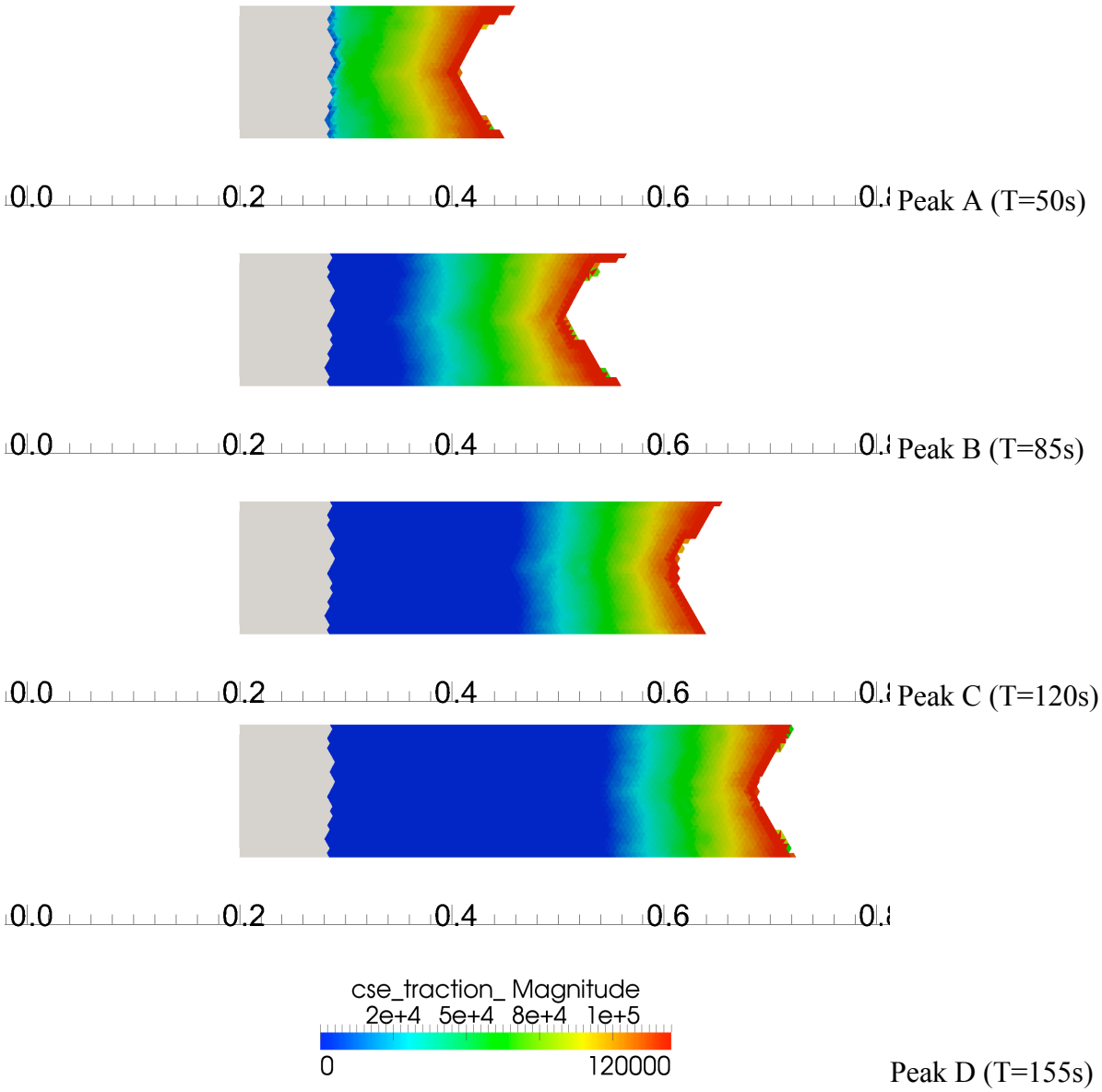

Figure D181. Deformed cracked mesh at Peaks A, B, C, and D (lengths in inches)

Table D 14. Results at Four Peaks

Peak	Peak Disp (mm)	Peak Force (N)	Crack Length (mm)	Crack Length (normalized A/W)
A	0.2396	4610	0.0	0.30
B	0.3225	3290	2.0	0.38
C	0.4020	2210	4.8	0.49

D	0.4789	1480	6.9	0.57

D6.4 Summary

The XFEM capability in Sierra is a work in progress, and as features are being added to this capability, its ability to model ductile fracture problems is improving. The addition of cohesive zones on the XFEM cut planes and the use of nodal tetrahedral elements have both significantly improved upon the original pre-test prediction of the X-Prize 2A problem. The lessons learned here will be valuable for future modeling of ductile fracture problems.

APPENDIX E: EXPERIMENTAL RESULTS

The purpose of this appendix is to provide supplementary details regarding the experimental outcomes for the X-Prize assessment. These experiments were designed to be relatively easy to perform with little ambiguity in the outcome of the tests, aside from natural material variability. The test geometries, test material, and test conditions were chosen so that these were very accessible experiments, readily performed by nearly any materials mechanics or structural mechanics laboratory. All three challenges required a simple pin-loaded clevis grip arrangement, a Crack Opening Displacement (COD) gage, and some sort of high-resolution optical imaging with measurement capabilities. Some of the additional details provided in this appendix can be used in addition to the results presented in the main section of this report to validate models in the future, albeit no longer blind validation. Geometric measurements were made of the test samples to ensure that they conformed to the desired test geometry within the tolerances specified in the machining drawings. Since the test samples conformed to the machining tolerances, those details are omitted here.

E1. Experiments for Challenge 1A

A total of 14 specimens were tested to measure the peak force prior to crack initiation and the loadline crack opening displacement at the crack initiation (crack size > 100 μm). The testing was performed in two separate labs: 6 tests in one lab and 7 tests in another to confirm reproducibility. The labs were provided the machined samples and given the same challenge assignments as described in Chapter 3. There was no additional stipulations placed on the method that the lab chose to execute the tests. Independently, the labs actually chose two very different load train configurations: one lab utilized a load train that was fully constrained (rigid) against lateral deflection, whereas the other lab utilized a load train with a universal joint that permitted two degrees of freedom for lateral deflection. Nevertheless, in spite of these very different boundary conditions, the two labs reported values that were within ~2% of one another. The results are tabulated in Table E1.

Finally, the surface strain field was measured by 3D digital image correlation on one test specimen (specimen 3) using Vic3D from Correlated Solutions. This DIC technique measures all three components of surface strain, xx, yy, and xy. A progression of ~100 images was collected throughout the deformation experiment prior to fracture. The resulting strain fields taken in the final frame just before fracture are shown in Figure E182. While these results were not the focus of the X-Prize effort, it is hoped that future validation efforts will also afford direct comparison of the models' predicted strain fields to observed strain fields. In that same spirit, the surface profile of the fracture surface was measured after fracture. The fracture surface was very 3-dimensional due to the presence of significant shear lips on both sides of the sample, as shown in Figure E183 and Figure E184. This complex fracture surface highlights phenomenology that is not currently represented in any of the X-Prize codes.

Table E1. Experimental results from the two test labs. Note that the observed peak load prior to crack initiation occurs before *the reported COD displacement values at crack initation.*

Test Lab	Sample ID	Peak Load *prior to crack initiation* (kN)	Load Line Displacement *at crack initation* using COD gage (mm)
Boyce/Crenshaw	**Sample 1**	**14.14**	**2.947**
	Sample 2	**14.01**	**3.088**
	Sample 3	**14.02**	**2.935**
	Sample 4	**14.04**	**2.939**
	Sample 5	**14.14**	**3.146**
	Sample 6	**14.05**	**3.029**
	Sample 7	**14.08**	**3.012**
	Sample 8	**14.13**	**3.031**
Cordova/Laing	**S1**	**13.71**	**2.865**
	S2	**13.78**	**2.934**
	S3	**13.87**	**2.888**
	S4	**13.72**	**2.944**
	S5	**13.94**	**2.847**
	S6	**13.74**	**2.835**
maximum		**14.14**	**3.146**
minimum		**13.71**	**2.835**
average		**13.95**	**2.960**
std. dev.		**0.16**	**0.091**

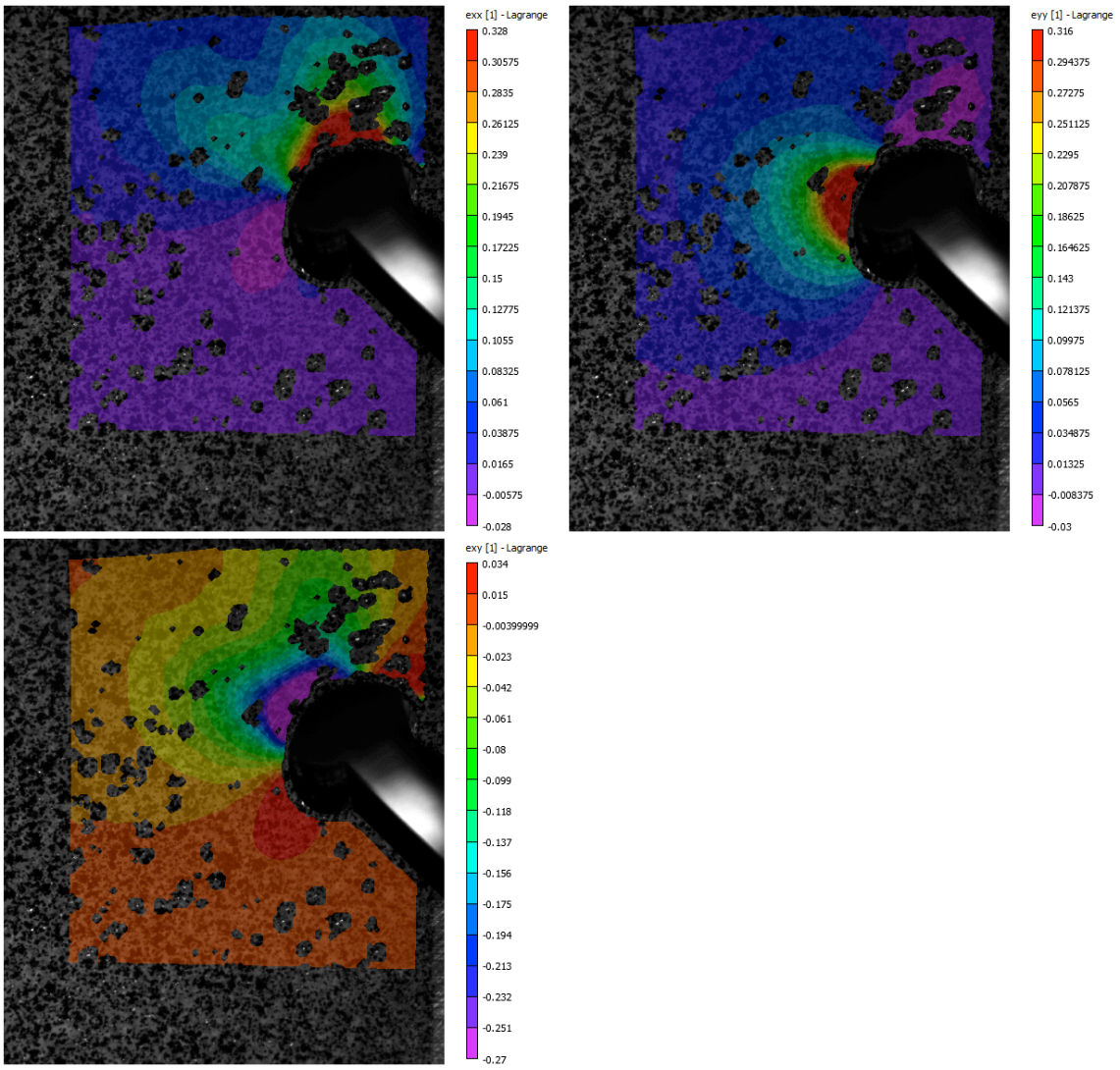

Figure E182. Surface strain contours immediately prior to crack initiation for the three surface components of strain, xx, yy, and xy. Not surprisingly, the crack nucleated in the region of maximum shear stress.

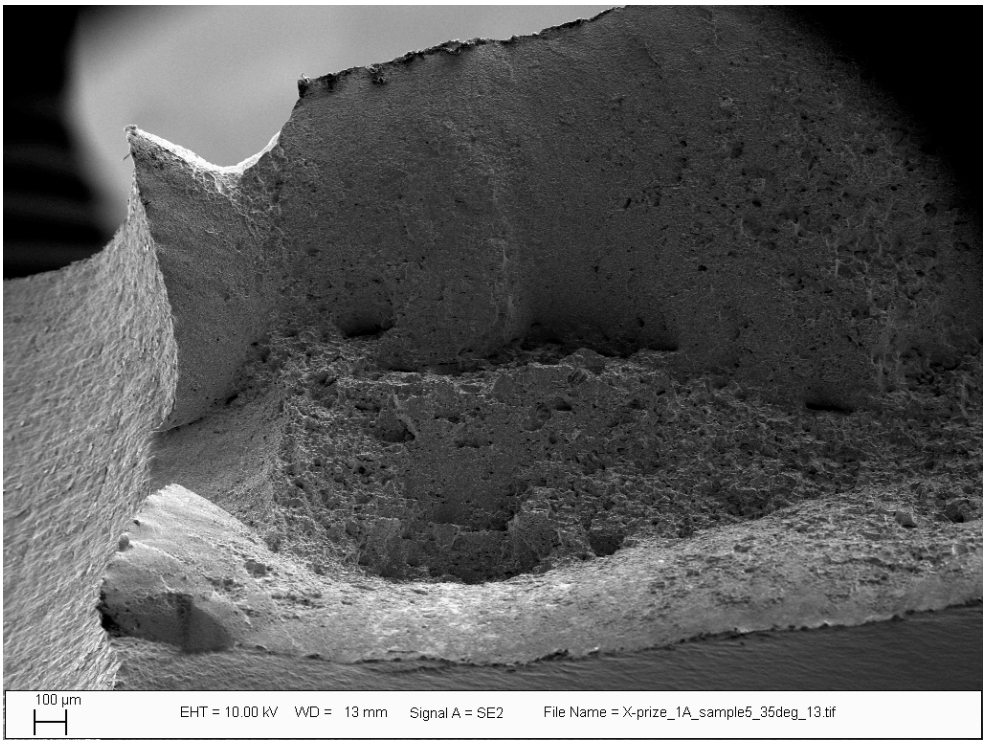

Figure E183. Scanning electron microscope image of the 3-Dimensional nature of the fracture surface. The crack initiated near the left side of the image, and propagated from left to right.

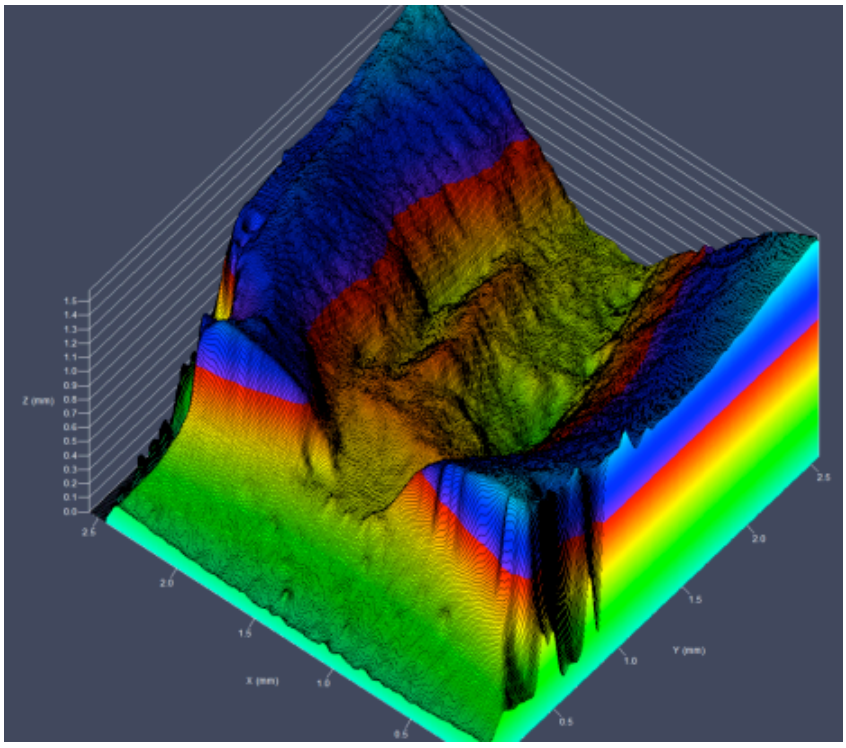

Figure E184. Confocal microscope image measuring the surface profile of the crack. The crack moved from lower left to upper right. The machined cylindrical hole is green in the lower left portion of the image.

E1.1 Details of Experimental Method and Results for Challenge 1A tests in the Structural Mechanics Lab

Theresa Cordova (1522)

E1.1.1 Introduction

Six 1.2” x 1.25” x 0.125” PH13-8Mo specimens similar to a compact tension specimen were quasi-statically testing in the Structural Mechanics Laboratory (SML) in March 2010 to support an X-prize challenge proposed by Brad Boyce for purposes of comparing four predictive fracture codes used by Sandia national Laboratories. The study was a double blind study with experimental participation from the Multiscale Metallurgical Science & Technology lab and the Structural Mechanics lab. Only SML test methodology and results for Challenge 1A of the X-prize test series are discussed in this memorandum. Overarching analytical information and comparison between experiment results are discussed in a SAND report to be completed by the end of FY11.

E1.1.2 Test Setup and Methodology

Eight H950 PH13-8Mo samples with geometry of that shown in Figure E185 were provided to the SML for quasi-static, displacement controlled testing. Data acquisition and servo-hydraulic control were provided by an MTS FlexTest GT system. The nomenclature given to the CT specimens was S1 through S8. In addition, two incorrectly heat treated specimens were provided to the lab for test setup purposes. The incorrectly heat treated samples are referred to as D1 and D4.

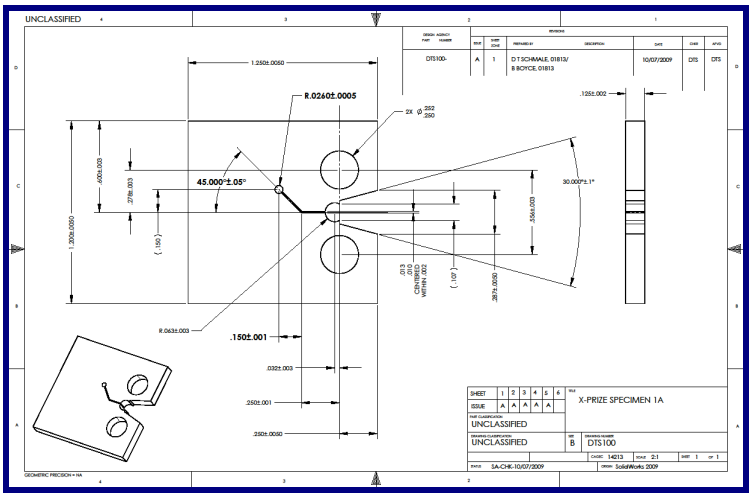

Figure E185. CT-like specimen used for Challenge 1A

Measurements of each sample were recorded prior to testing using a calibrated caliper for length measurements and a calibrated micrometer for thickness measurements. Measurement locations and values are noted in Figure E186 and Table E2, respectively.

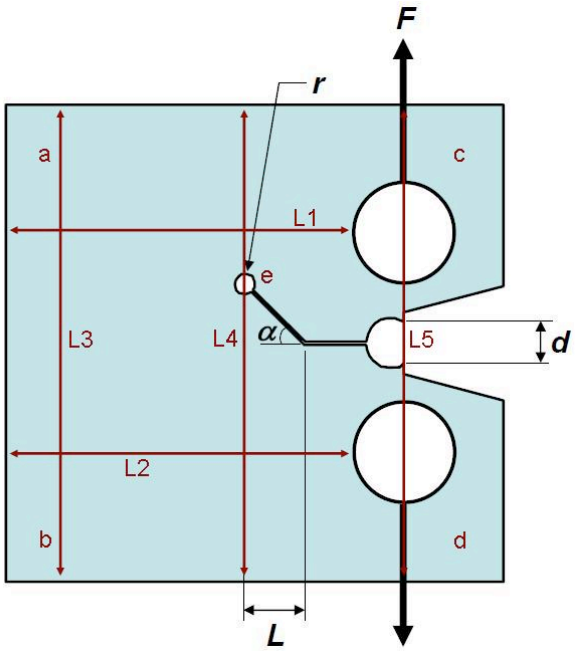

Figure E186 - Measurement Locations for CT Specimens

Table E2. Dimensional measurements corresponding to Figure E186 - Measurement Locations for CT Specimens.

Specimen ID	Thickness Measurements using QuantuMike by Mitutoyo (in.)					Length Measurements using Mitutoyo Absolute Digimatic (in)				
	a	b	c	d	e	L1	L2	L3	L4	L5
*D1**	*0.12180*	*0.12185*	*0.12270*	*0.12230*	*0.12245*	*0.8740*	*0.8745*	*1.1990*	*1.1990*	*1.1990*
*D4**	*0.12325*	*0.12495*	*0.12340*	*0.12275*	*0.12285*	*0.8780*	*0.8770*	*1.2025*	*1.2035*	*1.2005*
1	0.12345	0.12375	0.12450	0.12340	0.12375	0.8805	0.8770	1.2015	1.2020	1.2015
2	0.12385	0.12365	0.12390	0.12415	0.12400	0.8785	0.8770	1.2010	1.2020	1.2015
3	0.12390	0.12430	0.12470	0.12415	0.12435	0.8780	0.8770	1.2015	1.2015	1.2010
4	0.12345	0.12395	0.12360	0.12380	0.12380	0.8780	0.8780	1.2005	1.2010	1.2010
5	0.12440	0.12450	0.12430	0.12445	0.12445	0.8780	0.8775	1.2010	1.2020	1.2020
6	0.12375	0.12405	0.12280	0.12220	0.12345	0.8765	0.8765	1.2010	1.2015	1.2015
7	0.12375	0.12370	0.12275	0.12360	0.12340	0.8760	0.8760	1.2010	1.2010	1.2010
8	0.12410	0.12440	0.12405	0.12320	0.12420	0.8765	0.8760	1.2000	1.2010	1.2010
Average	0.12383	0.12404	0.12383	0.12362	0.12393	0.87775	0.87688	1.20094	1.20150	1.20131
Standard Deviation	0.000297	0.00031	0.000686	0.000664	0.000368	0.001346	0.00065	0.000464	0.000433	0.000348

The notch diameter at location e was measured with a microscope available in the Multiscale Metallurgical Science & Technology laboratory. The resolution of the calipers was 0.5 mils with repeatability within ± 1 mil. Likewise, the micrometer had a resolution of 0.05 mils and an accuracy of ± 0.05 mils.

The goal of the experimental work was to uniaxially load the specimen, simplifying loading conditions to a two-dimensional plane. It was desired to detect a crack of 100-500 μm in length and record the peak load prior to crack initiation. The overall test setup is pictured in Figure E187.

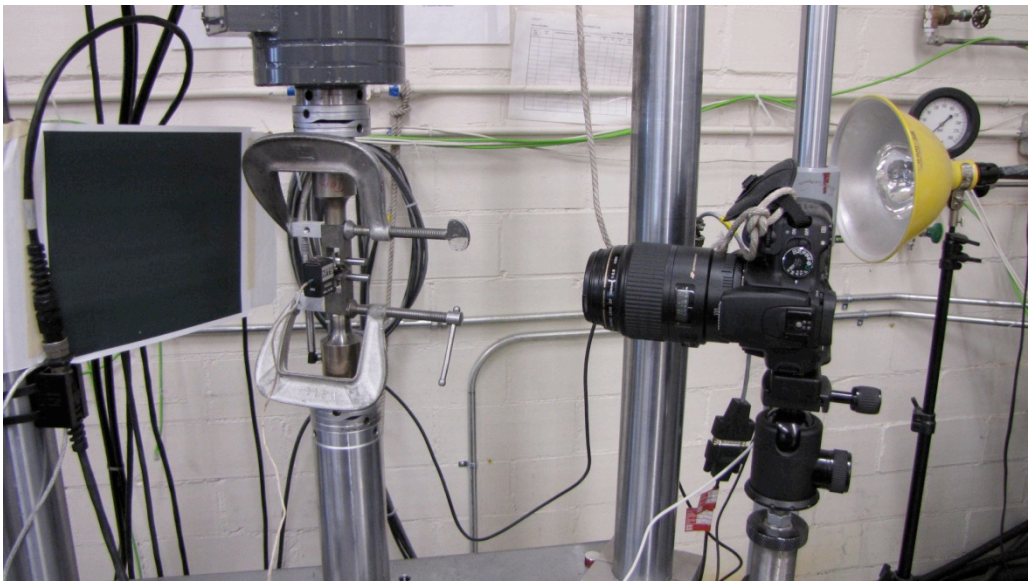

Figure E187. X-Prize Challenge 1A SML Test Setup

A calibrated 22 kip load cell and calibrated actuator stroke integral to the load frame were used for force and stroke measurements, respectively. Optical measurements were taken with a digital Cannon SLR Rebel xTi. A horizontal and vertical resolution of 0.5 mils/pixel and 0.4 mils/pixel, respectively, were obtained for the given camera position. Images were taken throughout the test. The CT specimen was vertically constrained by a clevis set that was rigidly connected to the load frame via thread reducing fixtures. Horizontal constraints on the CT specimen were achieved by placing bushings on both sides of the top and bottom pin holes in the CT specimen, centering the test specimen within the clevises (Figure E188).

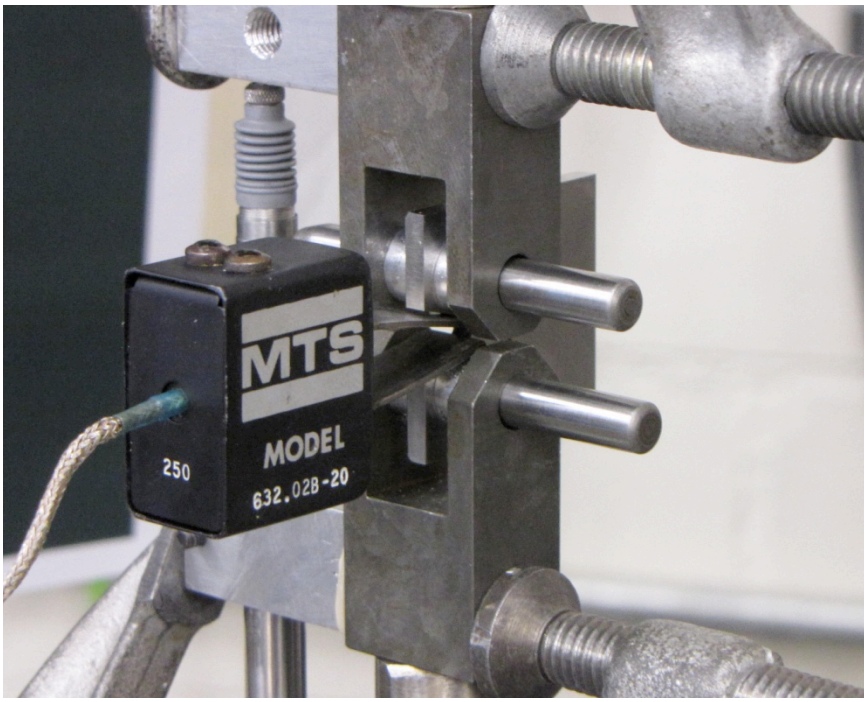

Figure E188. Close-up of CT Specimen Setup

Bushings were marked so that their position in the setup was the same between tests. A Crack Opening Displacement (COD) gage was positioned at the radiused notch located at the opening of the CT specimen. A linear variable differential transformer (LVDT) measured the clevis set displacement and was used for displacement control of 0.1 mil/sec rate. Load frame compliance was measured by subtracting the local LVDT displacement from the overall load frame actuator displacement when a load of 1 kip was applied to the rigid metal plate shown in Figure E189.

Figure E189. Rigid Metal Plate Used for Load Frame Compliance Measurements

Holes were drilled into the rigid metal plate at a distance of approximately 0.556" from center to center, to match the hole separation of the CT specimens. Although load frame compliance compensation was applied to the entire loading sequence, the compensation factor looked only at the difference between displacement measurements at a single load point and did not account for the relationship between the load frame actuator and LVDT as load increased. Error associated with this method of compensation was not quantified, but runs on specimens D1 and D4 demonstrated that the compensation more closely related the LVDT and actuator stroke than if compensation was not used. This displacement compensation technique was applied to the clevis LVDT for test specimen S6 to match the COD measurement in an effort to better control the failure of the specimen.

Specimens D1 and D4 were instrumented with strain gages on both CT faces to monitor strain behavior and provide confidence that loading through the thickness was not present. Pictures of both D4 faces are shown in Figure E190 as an example of strain gage locations

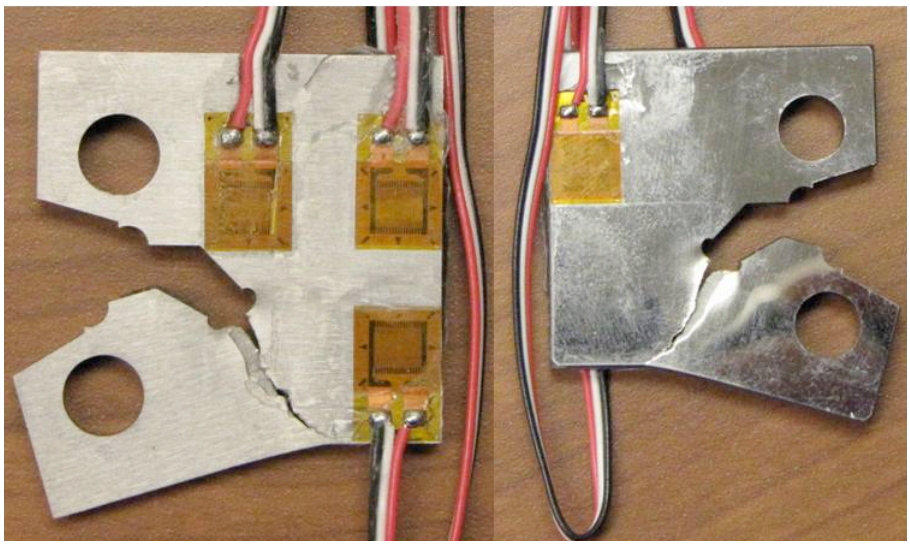

Figure E190. Gaged CT Specimen

Strain readings did not indicate that out of plane bending was present during the test. It was noted that a single strain gage reading would increase dramatically with respect to other strain gages prior to fracture in the eventual direction of crack growth, predicting the crack path.

Four seating cycles were applied to each test specimen prior to loading the specimen to failure. Each seating cycle increased load by 500 lb_f with a hold at the targeted load for ten seconds. The purpose of the seating cycles was to reduce any gaps present in the system and essentially "seat" the system and thus establish a repeatable elastic behavior.

E1.1.3 Test Results and Conclusions

The CT specimens failed in a much more brittle manner than was anticipated. A slow 0.1 mil/sec LVDT displacement rate was used for specimens S1 through S5 during the test in an effort to control and capture fracture of the specimens. The load dip in Figure E191 demonstrates a load relaxation for the steady displacement rate. A linear relationship between compensated displacement and the COD reading is apparent from the figure, deducing that the COD did not suddenly open when the load dropped and thus a crack did not initiate.

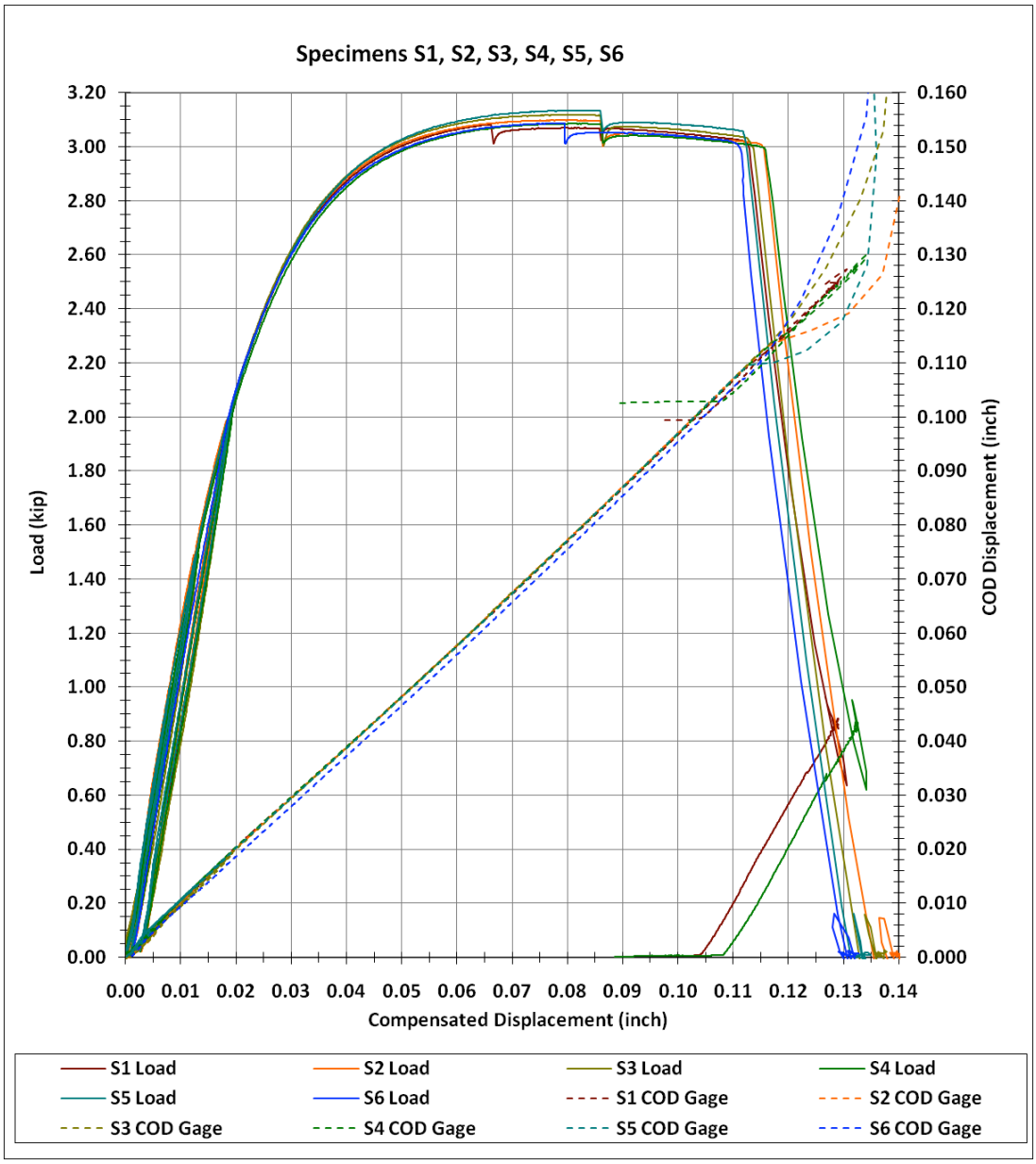

Figure E191. Load Behavior of H950 PH13-8Mo CT Specimens

Load is represented by the solid lines in Figure E191 and the COD response is shown with dashed lines. Compensated displacement removed load frame compliance from the displacement measurement. A calculated compensated displacement was used for displacement control on S6. The idea on test S6 was to keep the displacement control rate lower than the relaxation rate and encourage stable crack growth in the specimen. The failure of the CT specimens occurred so rapidly, however, that imaging was not able to track crack propagation as the crack grew despite the use of a compensated displacement control. Thus, neither the arrest nor detection of a 100 – 500 µm crack length was obtained. It was determined that the servo-control rate of the load frame was insufficient to keep up with the elastic energy loaded into the specimen. An example of the changes observed in a CT specimen during testing are captured in Figure E192.

Figure E192. CT Specimen Images Captured During Testing

The center image in the figure above was taken immediately before the crack visibly initiated on the outer surface of the material. It can be seen that significant yielding had occurred around the blunt notch prior to failure. Each CT specimen was lightly sanded prior to testing to produce the visible vertical lines shown in Figure E192. The vertical lines produced pixel variation necessary for optical measurements. Using optical measurements, it was noted that a lateral displacement of approximately 55 mils was present during testing. This lateral force may have contributed to the repeated failure paths of the "S" specimens shown in Figure E193.

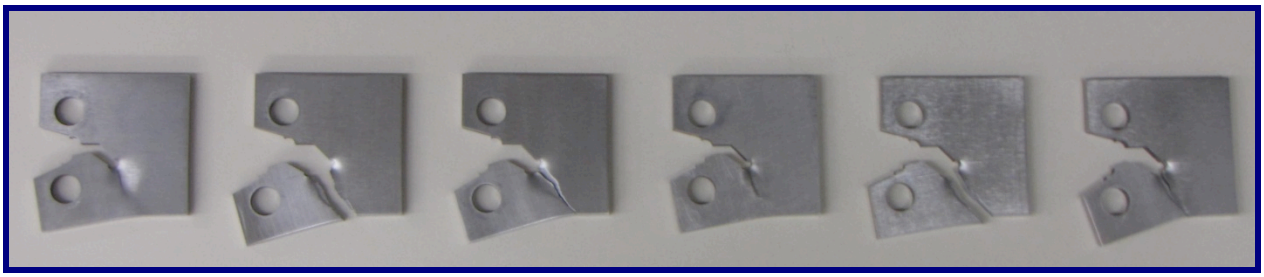

Figure E193. Post-test Image of S-specimens

A summary of the associated loads and displacements measured at three critical points during testing for each S-specimen are presented in Table E3.

Table E3. Summary of Three Critical Points During Testing of S-specimens

	Load			CompDisp at Loading Condition		
Specimen	**Max**	**Transition**	**Rupture**	**Max**	**Transition**	**Rupture**
	(kip)	(kip)	(kip)	(inch)	(inch)	(inch)
S1	3.082	3.018	3.002	0.066147436	0.112320	0.112790
S2	3.099	3.010	2.997	0.080844471	0.114870	0.115530
S3	3.118	3.031	2.992	0.08037203	0.112590	0.113660
S4	3.085	2.995	2.989	0.081634604	0.115650	0.115880
S5	3.134	3.057	3.040	0.081160312	0.111720	0.112090
S6	3.088	3.016	2.974	0.07935127	0.110080	0.111570
S7	-	-	-	-	-	-
S8	-	-	-	-	-	-
Mean	**3.101**	**3.021**	**2.999**	**0.078**	**0.113**	**0.114**
Std Dev.	**0.018875**	**0.019265**	**0.020281**	**0.005459618**	**0.0018804**	**0.001632**

Since the specified 100 - 500 μm crack was not caught, two points of interest in the realm of crack propagation were defined. The transition point was defined as the last point on the linearly decaying load versus compensated displacement curve. Rupture was the sudden load drop in the load versus compensated displacement curve after the maximum load had been reached. A scatter of the transition and rupture points is presented in Figure E194.

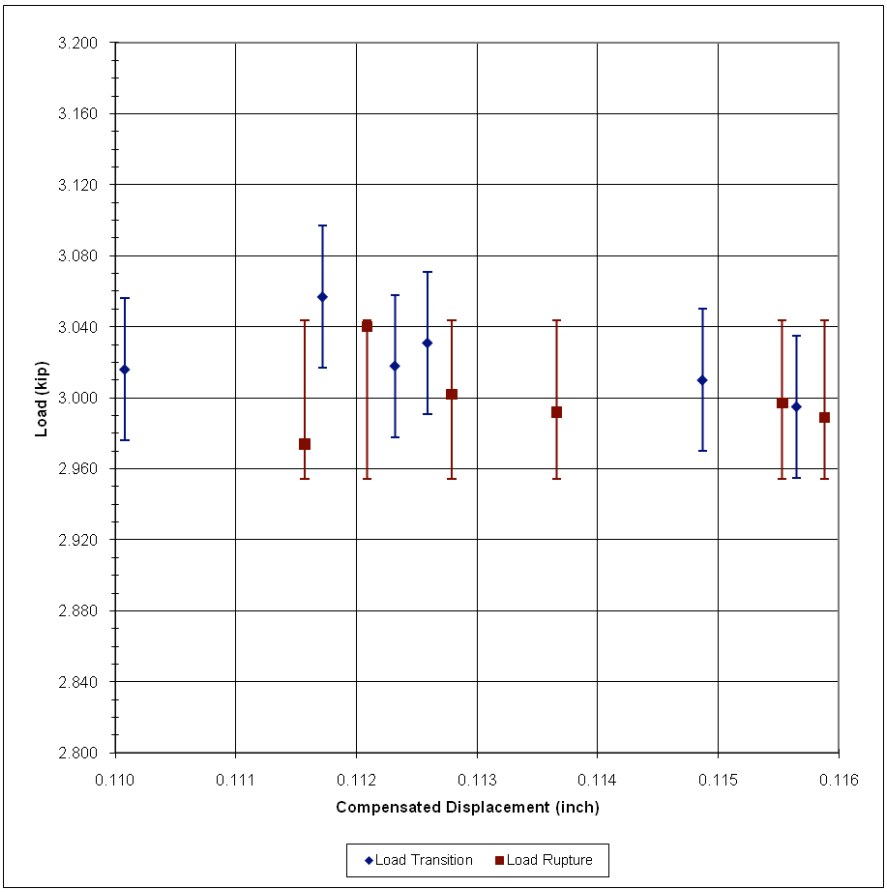

Figure E194. Transition and Rupture Scatter for CT Specimens

A bound on where crack initiation likely occurred is captured in Figure E194. From the plotted scatter, crack initiation may have occurred between a load value of 2,974 lb_f and 3,057 lb_f and a compensated displacement of 0.11 and 0.116 inches.

Specimens S7 and S8 were not tested for Challenge 1A. A determination was made to use these specimens as baseline tests for the next x-prize follow-up challenge. Since a repeatable load behavior was obtained for the given setup and the CT specimens tested, S7 and S8 would be used to determine the affects test setup improvements had on the subsequent test series. Unfortunately, funding constraints prevented further testing in the SML.

E1.1.4 Recommendations and Future Work

It is highly recommended that future work include participation from a minimum of two experimental labs to gain insight into experimental test methodology and better determine the strategies that best work for a variety of tests. There is a lot to be gained by sharing of information between experimental labs and a huge benefit to customers of these labs.

A repeat of this test could be performed on a more ductile material with improvements made to the test setup. Samples tested up to a specified load could be provided for CT scans so that additional information on tunneling within the specimen, not visible to the naked eye

may be obtained. Material properties from tensile tests of the same material lot is necessary to accurately characterize the material for modeling purposes and compare against those properties already in material databases.

Future work should also quantify the uncertainties associated with test measurements.

Photos, data, and other documents associated with this test have been stored in the SML archive under SML499 for future reference.

E2. Experiments for Challenge 1B.

Challenge 1B focused on crack propagation from the same inclined blunt notch geometry of Challenge 1A, but this time manufactured from alloy 2024-T3. Due to funding limitations, only a single laboratory (Boyce/Crenshaw) participated in Challenge 1B and 2A. Fiduciary lines A-F were scribed onto the surface of the sample by first painting permanent marker ink onto the region of interest, and subsequently scribing the surface with a sharp tungsten stylus using a motorized XYZ stage. The stage was feedback controlled with linear glass-scale encoders to ensure that the lines were accurately placed. An example of the fiduciary lines is shown in Figure E195. An example of the subsequent measurements, performed with a Keyence VHX-1000 digital microscope, is shown in Figure E196.

Two Keyence digital microscopes were positioned in-situ during the tests to observe crack propagation at high magnification during the tests. This allowed the operator to determine the force and displacement conditions at which the crack crossed each fiduciary line. An example of the high-resolution images used to determine surface crack position is shown in Figure E197. An example of a fully cracked specimen is shown in Figure E198. The observed crack was not flat, but rather inclined at an angle, akin to a shear lip. For this reason, the crack did not intersect both side faces of the sample at the same location. On one side of the specimen, the crack may run nearly straight and intersect lines D-E-F, whereas on the other side of the specimen, that same inclined crack may curve more and intersect lines A-D-E-F. A compilation of the crack paths from both sides of the first four tested specimens is shown in Figure E199. Due to the inclined crack path and the significant material variability, the most useful fiduciary lines were lines D and E. The observed forces and displacements for all five test samples as the crack reached lines D and E are included in Table E4 and Table E5, respectively.

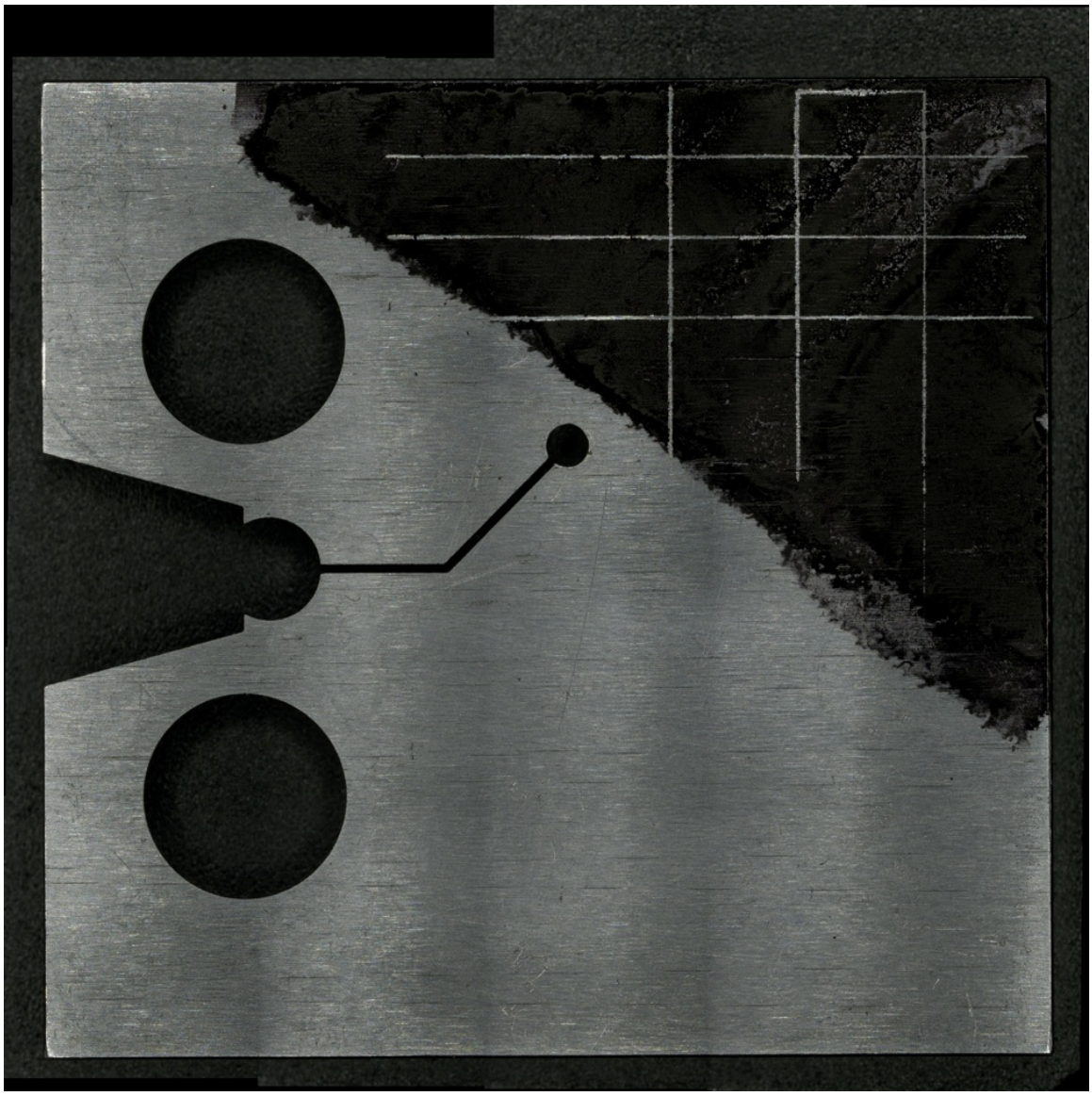

Figure E195. Optical image of a Challenge 1B specimen with marked fiduciary lines.

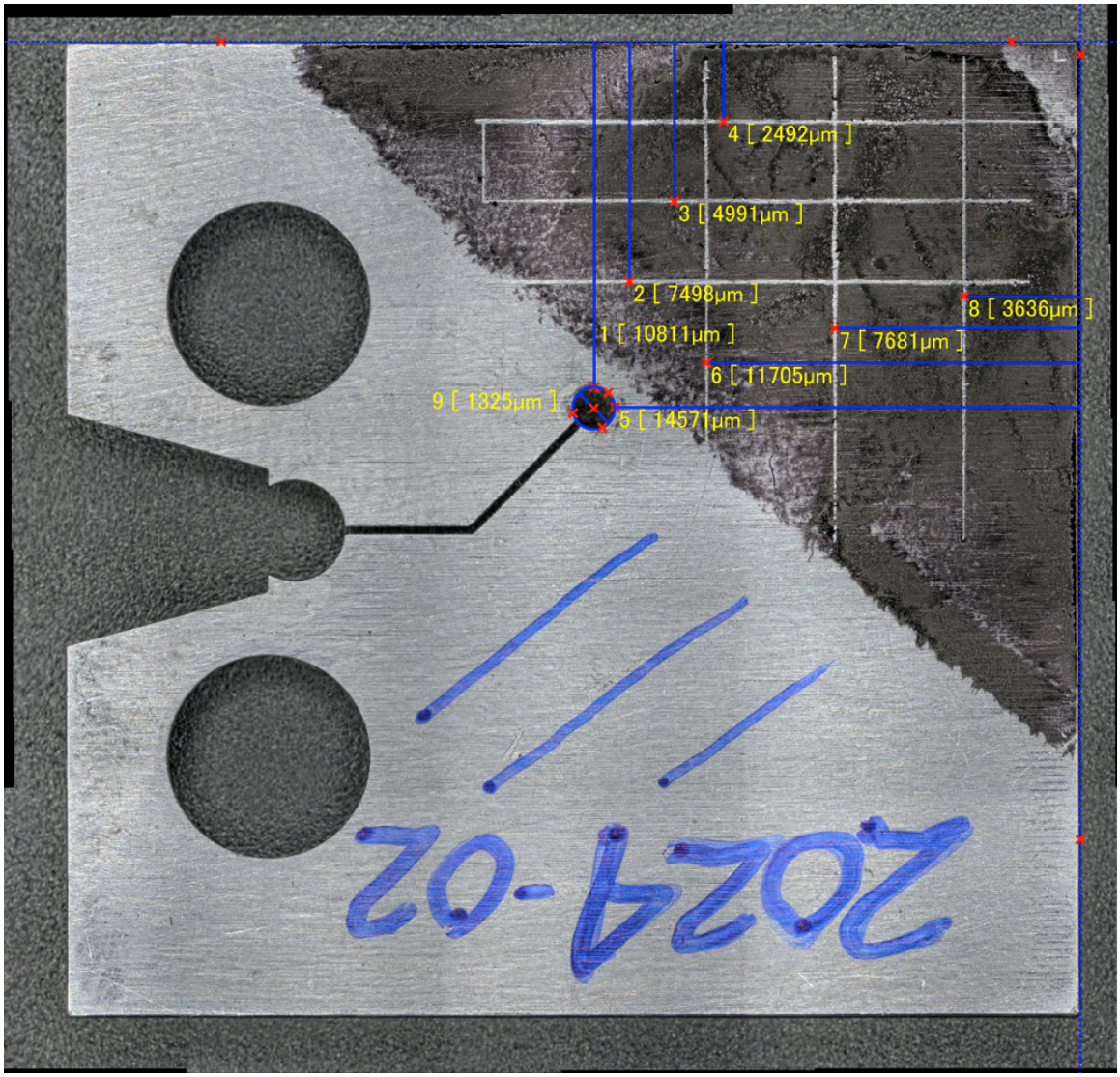

Figure E196. Example of measurements taken on each side of each test specimen to confirm that the fiduciary lines were properly positioned (within ~20 µm).

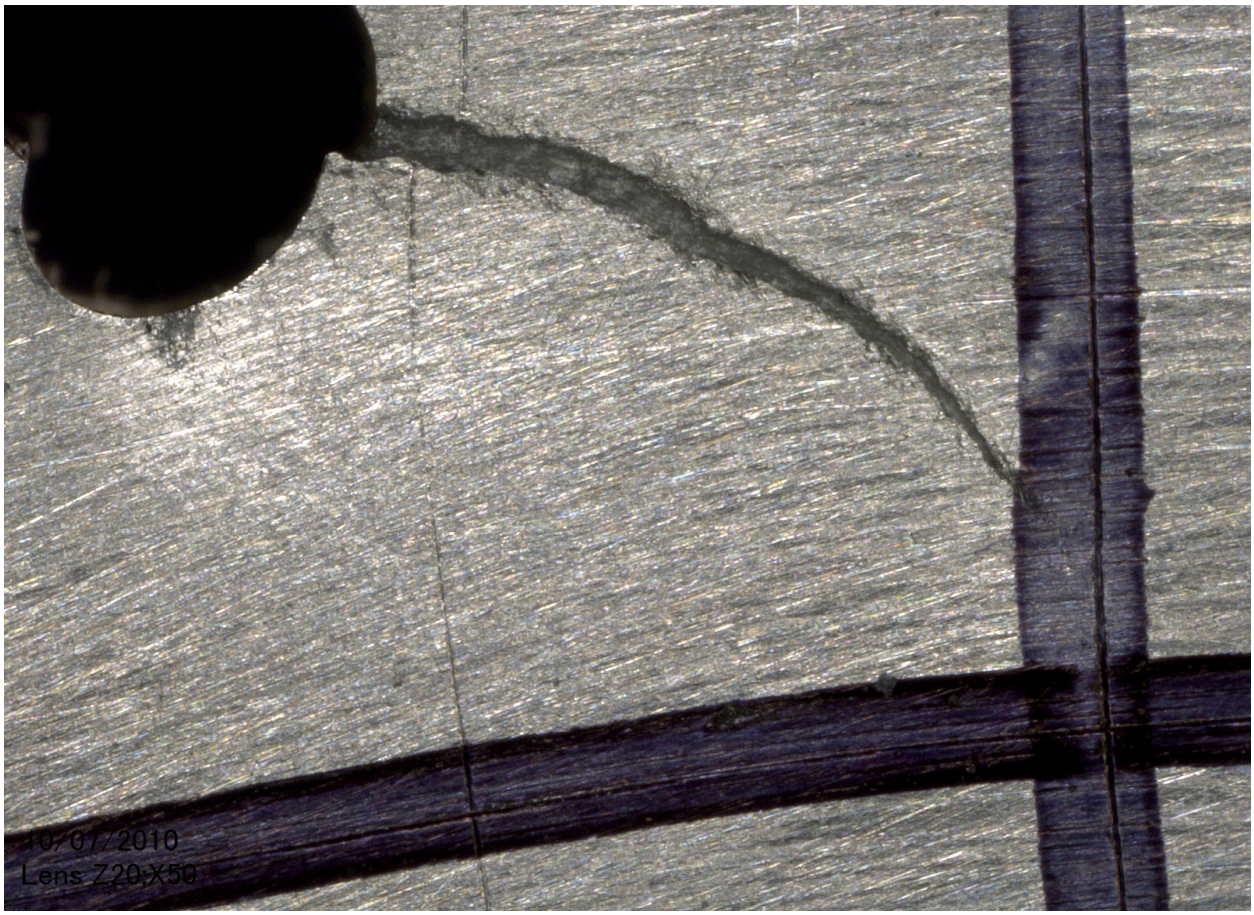

Figure E197. An example of the crack nearing the first vertical fiduciary line as viewed in-situ during testing using a digital microscope.

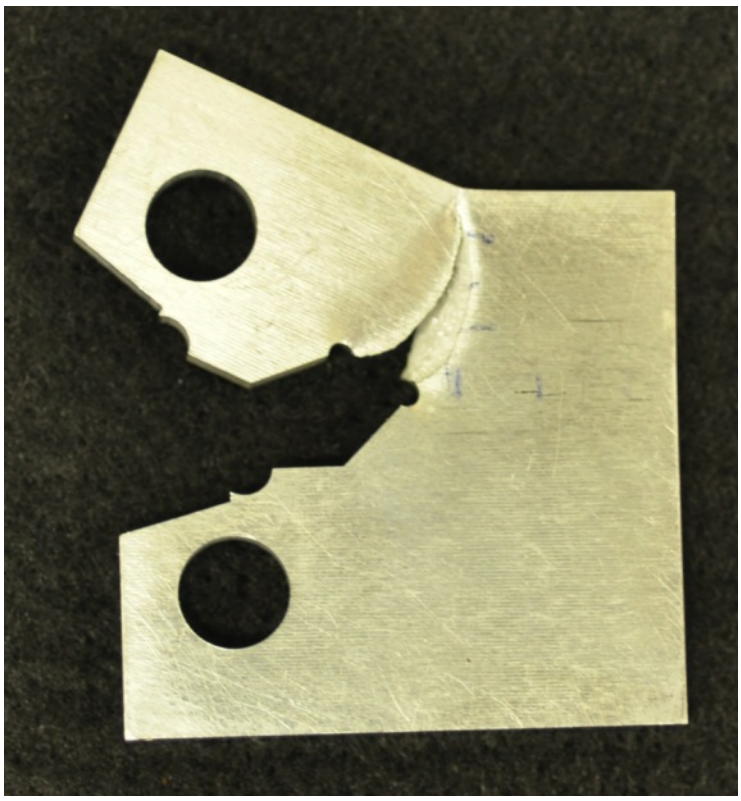

Figure E198. An example of the crack propagation direction in one test sample.

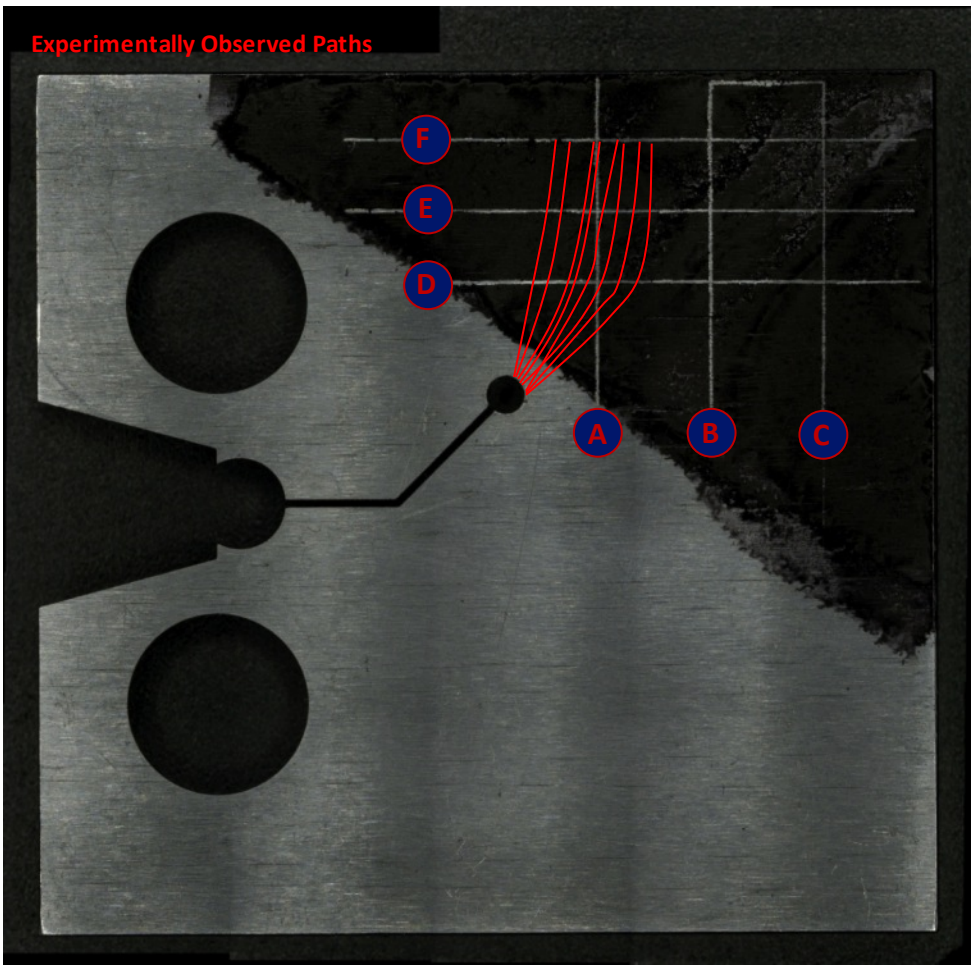

Figure E199. The observed crack paths on both sides of the specimen for samples 3, 4, 5, and 6. Sample 8 also followed a similar path, within the bounds of these first four observations.

Table E4. Force and displacement conditions at which the crack reached fiduciary line 'D'. Note that the 'a' and 'b' designations for the 5 test specimens represent the front and backside of the specimens.

Specimen	Force (N)	COD (mm)
3a	1996.0	2.4900
3b	1382.0	2.7800
4a	1387.0	3.0160
4b	1356.0	3.0600
5a	1993.0	2.5160
5b	1620.0	2.6400
6a	1391.0	2.8930
6b	1470.0	2.8100
8a	2251.6	2.3375
8b	1416.2	2.7534

Table E5. Force and displacement conditions at which the crack reached fiduciary line 'E'. Note that the 'a' and 'b' designations for the 5 test specimens represent the front and backside of the specimens.

Specimen	Force (N)	COD (mm)
3a	935.00	3.1200
3b	594.00	3.5400
4a	848.00	3.4400
4b	631.00	3.7000
5a	768.00	3.2800
5b	705.00	3.4000
6a	613.00	3.7600
6b	499.00	3.9500
8a	949.00	3.0800
8b	670.00	3.4000

E3. Experiments for Challenge 2A.

Challenge 2A involved predicting crack propagation behavior (so-called R-curve behavior) from a sharp fatigue pre-crack in a side-grooved compact tension specimen, again from alloy 2024-T3. The fatigue pre-cracking was performed consistent with ASTM E399, with manual ΔK-shedding to minimize the plastic zone at the tip of the pre-crack. As with challenge 1B, two horizontal digital microscopes provided imaging of both side faces of the sample to observe the crack on both surfaces independently. The starting crack lengths of the fatigue precracks are shown in Table *E6*, both from surface measurements taken prior to subsequent fracture testing, and from subsurface measurements taken after fracture. Note that the subsurface crack was ~5-7% shorter than the surface crack. The observed load-displacement response, including the four unloading compliance curves, is shown in Figure E200. In addition, several tabulated values are reported. The observed crack length, in normalized a/W units at each of the four unloading peaks is shown in Table E7. The observed force at each of the four loading peaks is reported in Table E8. Finally, the unloading stiffness corresponding to each of the four peaks is shown in Table E9.

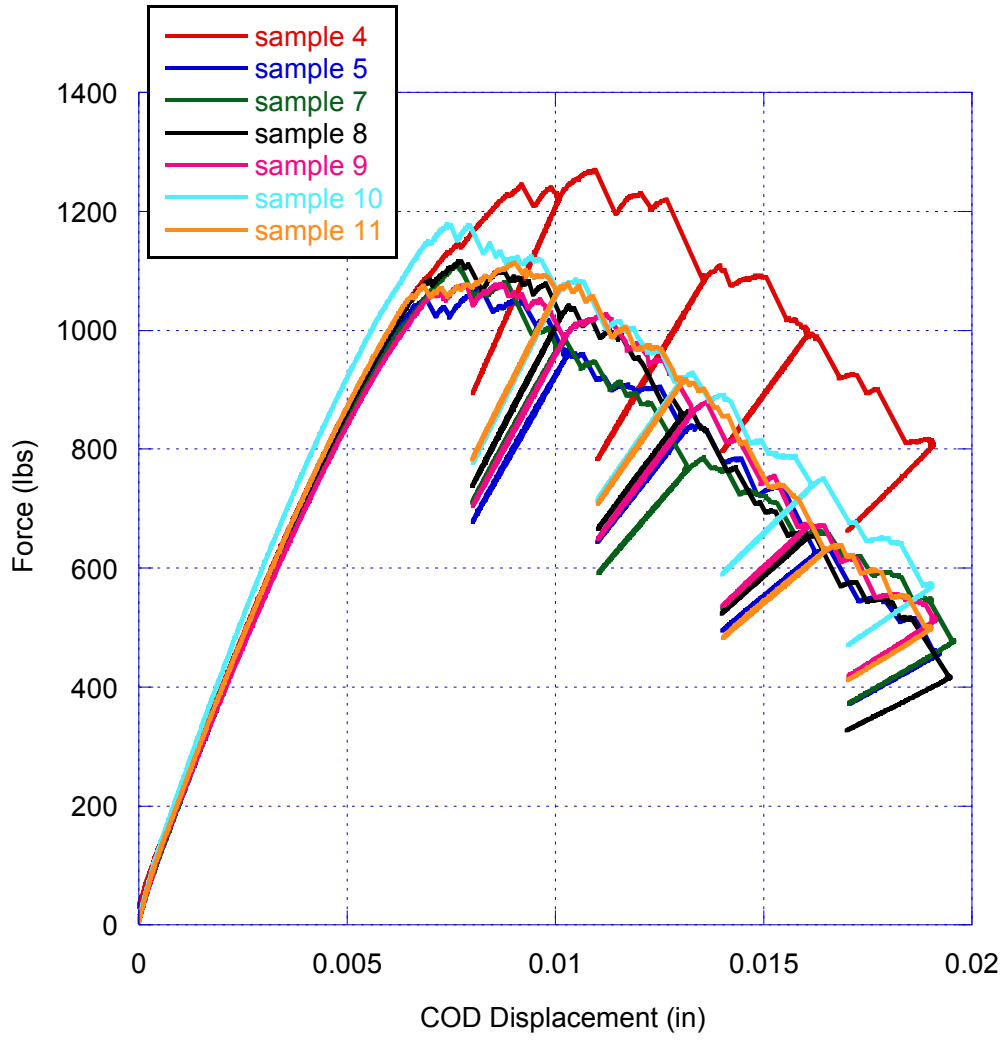

Figure E200. Observed force-displacement profile for the X-Prize Challenge 2A tests. Note that each test included four partial unloads corresponding to peaks A-D.

Table E6. Surface crack length a/W taken from measurements of the crack intersecting the side groove of the sample ('from side'); internal crack length taken from fracture surfaces after fracture ('crack front'); and sample thickness measured between the side-grooves on either side of the sample.

Sample	a/W_o From side	a/W_o crack front	Thickness Average front to back
3	0.299	0.287	0.127
4	0.304	0.287	0.127
5	0.300	0.281	0.126
6	0.300	0.294	0.126
7	0.300	0.286	0.126
8	0.300	0.284	0.126
9	0.300	0.290	0.126
10	0.300	0.269	0.126
11	0.299	0.279	0.126

Table E7. Crack length (in normalized a/W units) at each of four peaks.

Specimen ID	**Peak A**	**Peak B**	**Peak C**	**Peak D**
4	0.321	0.38	0.426	0.449
5	0.363	0.429	0.532	0.586
6	0.332	0.395	0.455	0.512
7	0.365	0.446	0.514	0.598
8	0.331	0.412	0.491	0.587
9	0.361	0.439	0.501	0.558
10	0.324	0.422	0.472	0.536
11	0.368	0.424	0.512	0.576
avg	**0.345625**	**0.418375**	**0.487875**	**0.55025**
stdev	**0.020311**	**0.022057**	**0.034958**	**0.050070**
max	**0.368**	**0.446**	**0.532**	**0.598**
min	**0.321**	**0.38**	**0.426**	**0.449**

Table E8. Force at each of four peaks (in N).

Specimen ID	**Peak A**	**Peak B**	**Peak C**	**Peak D**
4	5408.768	4834.976	4421.312	3585.088
5	4287.872	3696.288	2788.896	2028.288
6	5346.496	4674.848	3998.752	3567.296
7	4319.008	3393.824	2917.888	2126.144
8	4554.752	3798.592	2895.648	1845.92
9	4403.52	3843.072	2975.712	2286.272
10	4732.672	4065.472	3282.624	2530.912
11	4737.12	4061.024	2793.344	2210.656
avg	**4723.776**	**4046.012**	**3259.272**	**2522.572**
stdev	**437.890**	**488.227**	**617.046**	**679.592**
max	**5408.768**	**4834.976**	**4421.312**	**3585.088**
min	**4287.872**	**3393.824**	**2788.896**	**1845.92**

Table E9. Unloading stiffness in N/mm at each of the four peaks.

Specimen ID	Peak A	Peak B	Peak C	Peak D
4	27502.3	20427.53	16741.29	12158.45
5	21385.42	15531.23	10069.29	6775.32
6	26866.62	19716.55	14408.72	12196.98
7	22022.85	14198.58	10659.44	7088.781
8	23332.74	16275.48	10799.53	6183.42
9	22241.75	16321.01	11335.4	7792.756
10	24556.81	17308.67	11948.31	8473.965
11	24138.28	17651.91	10302.2	7531.83
avg	**24005.85**	**17178.87**	**12033.02**	**8525.187**
stdev	**2239.078**	**2083.374**	**2347.211**	**2354.863**
max	**27502.3**	**20427.53**	**16741.29**	**12196.98**
min				

Distribution

Qty.	Mail Stop	Name	Org.
5	MS0889	Brad Boyce	1831
1	MS0825	Joel Lash	1510 (electronic copy)
1	MS9042	Mike Chiesa	8249 (electronic copy)
1	MS0110	Justine Johannes	1220 (electronic copy)
1	MS0372	H. Eliot Fang	1524 (electronic copy)
1	MS1322	John Aidun	1425 (electronic copy)
1	MS0824	John Pott	1525 (electronic copy)
1	MS1411	R. Allen Roach	1823 (electronic copy)
1	MS0889	F. Michael Hosking	1831 (electronic copy)
1	MS0384	Duane. Dimos	1500 (electronic copy)
1	MS0847	Peter Wilson	1520 (electronic copy)
1	MS0885	Terry Aselage	1810 (electronic copy)
1	MS0824	Joseph Bishop	1525 (electronic copy)
1	MS9042	Arthur Brown	8249 (electronic copy)
1	MS0555	Theresa Cordova	1522 (electronic copy)
1	MS0824	James Cox	1524 (electronic copy)
1	MS0889	Thomas Crenshaw	1831 (electronic copy)
1	MS0372	Kristin Dion	1525 (electronic copy)
1	MS0372	John Emery	1524 (electronic copy)
1	MS9042	James Foulk III	8246 (electronic copy)
1	MS1322	David Littlewood	1444 (electronic copy)
1	MS9404	Alejandro Mota	8246 (electronic copy)
1	MS9042	Jake Ostein	8246 (electronic copy)
1	MS1322	Stewart Silling	1444 (electronic copy)
1	MS0372	Gerald Wellman	1525 (electronic copy)
1	MS0889	Corbett Battaile	1814 (electronic copy)
1	MS1411	Chris Weinberger	1814 (electronic copy)
1	MS1411	Elizabeth Holm	1814 (electronic copy)
1	MS0889	Joe Puskar	1822 (electronic copy)
1	MS0899	Technical Library	9536 (electronic copy)


Sandia National Laboratories